



UNIVERSIDAD DE CHILE
FACULTAD DE CIENCIAS FÍSICAS Y MATEMÁTICAS
DEPARTAMENTO DE GEOLOGÍA

REASSESSING THE ROLE OF ORGANIC MATTER IN STRATABOUND Cu-(Ag) DEPOSITS, NORTHERN- CENTRAL CHILE

TESIS PARA OPTAR AL GRADO DE DOCTORA EN CIENCIAS, MENCIÓN GEOLOGÍA

ANDREA PAOLA HERAZO MERCADO

PROFESOR GUÍA:
MARTIN REICH MORALES

PROFESOR CO-GUÍA:
FERNANDO BARRA PANTOJA

MIEMBROS DE LA COMISIÓN:
DIEGO MORATA CÉSPEDES
IRENE DEL REAL CONTRERAS

Este trabajo ha sido financiado por el Núcleo Milenio Trazadores de Metales (NMTM) NC130065, el Centro de Excelencia de Geotermia de los Andes (CEGA) y los proyectos FONDECYT #1140780 y #1190105

SANTIAGO DE CHILE
2021

RESUMEN

RE-EVALUACIÓN DEL ROL DE LA MATERIA ORGÁNICA EN LOS DEPÓSITOS ESTRATOLIGADOS DE CU-(AG), NORTE-CENTRO DE CHILE

Los depósitos estratoligados de Cu-(Ag) representan la tercera fuente más importante de cobre en Chile después de los pórfidos cupríferos y los depósitos IOCG. Estos depósitos, de edad Jurásica a Cretácica Inferior, ocurren en un cinturón que se extiende por ~1000 kms a lo largo de la Cordillera de la Costa del centro-norte de Chile. En los depósitos del Cretácico Inferior, la mineralización se encuentra albergada en rocas volcánicas íntimamente asociada con bitumen. La estrecha asociación espacial entre mineralización y bitumen ha sido interpretada como evidencia de la precipitación de sulfuros de Cu y Fe inducida por la materia orgánica a través de procesos de oxidación-reducción. Sin embargo, el rol específico de los hidrocarburos en la mineralización de Cu-(Ag) es aún incierto y no ha sido investigado en profundidad.

Sobre la base de recientes estudios experimentales y empíricos que reconocen la capacidad los hidrocarburos de transportar metales y ligantes, es que la presente investigación tiene por objetivo re-evaluar el rol de la fase orgánica (hidrocarburo) durante las etapas de mineralización en los depósitos estratoligados de Cu-(Ag) del centro-norte de Chile.

Con el propósito de evaluar el rol de la fase orgánica en estos depósitos estratoligados de Cu-(Ag), esta investigación contempló un estudio micro-analítico detallado de las asociaciones de bitumen y sulfuros de Fe-Cu. Estos estudios incluyeron observaciones a través de (FE)-SEM, análisis de elementos mayores, menores y trazas mediante EMPA y LA-ICP-MS, y mapeo elemental utilizando μ -XRF. Además, se investigó el estado redox del azufre en el bitumen mediante métodos espectroscópicos por luz sincrotrónica (μ -XANES), y se determinó la signatura isotópica del azufre en pirita utilizando técnicas in situ mediante SIMS.

Los resultados presentados en esta tesis muestran evidencia que los sulfuros de (Fe)-Cu y pyrobitumen están íntimamente asociados en las dos etapas de mineralización: pre-mineral y de mineralización principal de Cu. Observaciones texturales en estos depósitos, evidencian que múltiples pulsos de un fluido acuoso e hidrocarburos estuvieron involucrados en la formación de estos depósitos. Además, los análisis de microsonda electrónica (EMPA) y μ -XRF revelaron que el bitumen alberga decenas a miles de ppm de metales bases (Fe, Cu, V) y ligantes (Cl, S) alcanzando en algunos casos niveles de porcentaje en peso (% peso). El azufre es el elemento más abundante en el bitumen y los datos de μ -XANES muestran que este se encuentra presente con diferentes estados de oxidación, siendo tiofeno y sulfona las especies más probables. Datos geoquímicos de elementos traza en estos depósitos revelan que la pirita asociada al bitumen hospeda concentraciones significativas de Cu, As, Mn, Pb, Tl, Co, Ni, V y Mo, que oscilan desde unos pocos ppm a niveles de porcentaje en peso. Además, la pirita se caracteriza por presentar razones bajas de Co/Ni (~0.1 a 10) y Co/Cu (~0.0001 a 10) y altos valores de las razones Ag/Co (~0.001 a 10), lo que sugiere que la pirita se formó a temperaturas relativamente bajas (100 a ~300 °C), condiciones reducidas y con una fuerte componente sedimentaria. Adicionalmente, datos isotópicos de azufre en pirita en los distintos depósitos muestra un rango amplio de valores (-30 a +60‰) que apuntan a fuentes predominantemente sedimentarias para el azufre, y sugieren mecanismos de fraccionamiento isotópico modulados por reducción incompleta de sulfato en un sistema parcialmente cerrado e interacción sulfato-metano anaeróbico.

Los datos presentados en esta tesis entregan nuevos antecedentes geoquímicos e isotópicos que confirman un rol relevante de la fase orgánica en la formación de los depósitos estratoligados de Cu-(Ag) en el centro-norte de Chile, validando un modelo genético en el cual fluidos hidrotermales acuosos de origen externo y mixto interactuaron con el bitumen, gatillando la precipitación de sulfuros. Finalmente, los datos obtenidos destacan el potencial de la fase orgánica como una fuente, al menos en parte, de metales y azufre para la mineralización de Cu-(Ag) en depósitos estratoligados.

ABSTRACT

REASSESSING THE ROLE OF ORGANIC MATTER IN STRATABOUND CU-(AG) DEPOSITS, NORTHERN-CENTRAL CHILE

Stratabound Cu-(Ag) deposits represent the third most important source of copper in Chile after porphyry Cu and IOCG deposits. These Jurassic to Lower Cretaceous deposits occur in a belt that extends for ~1000 km along the Coastal Range of northern and central Chile and are host to high grade Fe-Cu-(Ag) sulfide mineralization. In deposits hosted by Lower Cretaceous volcanic rocks, the sulfides are intimately associated with bitumen. The close spatial association between ore mineralization and bitumen has been interpreted as evidence of redox-induced mineral deposition by the organic matter. However, the specific role of liquid hydrocarbons on the processes leading to Cu-(Ag) mineralization remains highly controversial and has not been investigated in-depth.

Based on new experimental and empirical studies that recognize the ability of natural crude oils to mobilize metals, this work aims to re-evaluate hydrocarbon in ore formation in bitumen-bearing stratabound Cu-(Ag) deposits.

In order to evaluate the role of the organic phase in these stratabound Cu-(Ag) deposits, this research involved a detailed micro-analytical study of the bitumen-Cu-(Fe) sulfides assemblages. These studies included (FE)-SEM observations, major, minor and trace element analyses obtained by using EMPA and LA-ICP-MS, and elemental mapping using μ -XRF and synchrotron light. Furthermore, sulfur speciation within bitumen was determined by using synchrotron light spectroscopic techniques (μ -XANES), and in-situ sulfur isotope analysis in pyrite were carried out using SIMS.

The results presented in this thesis reveal that Cu-(Fe) sulfides and pyrobitumen are intimately associated in stratabound Cu-(Ag) deposits. In these deposits, two main stages were identified: a pre-ore and a main Cu ore stage. Textural observations of mineralized samples from these deposits indicate the presence of pyrobitumen in both stages, evidencing that multiple pulses of aqueous and hydrocarbon fluids were involved in the deposit formation. Further, electron microprobe analysis (EMPA) and μ -XRF analyses revealed that bitumen hosts 10's to 1000's ppm of base metals (Fe, Cu, V) and ligands (Cl, S), reaching in some cases weight percent (wt.%) levels. Sulfur is by far the most abundant element in bitumen and exploratory X-ray absorption near-edge structure spectroscopy (XANES) analysis shows that sulfur is present with different oxidation states, with thiophene and sulfone, the most probable species. Trace element geochemistry data reveal that pyrite hosts significant concentrations of Cu, As, Mn, Pb, Tl, Co, Ni, V, and Mo that range from a few parts per million (ppm) to weight percent (wt.%) levels. Furthermore, pyrite is characterized by distinctively lower Co/Ni (~0.1 to 10) and Co/Cu ratios (~0.0001 to 10) and higher Ag/Co values (~0.001 to 10); suggesting that pyrite was formed at relatively low temperatures (100 to ~300 °C), reducing conditions, and with a strong sedimentary component. In addition, sulfur isotope data in pyrite from different deposits show a wide range of values (-30 to +60 ‰) indicating a predominantly sedimentary source for sulfur and suggest isotopic fractionation mechanisms by incomplete sulfate reduction in a partially closed system and sulfate-anaerobic methane interaction.

The data presented in this thesis provide new geochemical and isotopic insights that corroborate the role of the organic phase in the formation of stratabound Cu-(Ag) deposits in northern-central Chile, and further support a genetic model, in which aqueous hydrothermal fluids of external and mixed origin interacted with bitumen, inducing sulfide precipitation. In addition, the reported results highlight the importance of bitumen as a potential source, at least in part, of metals and sulfur for the Cu-(Ag) mineralization in these deposits.

A mis grandes amores

AGRADECIMIENTOS

Hoy, quiero agradecer a los miembros de mi comisión: Martin Reich, Fernando Barra y Diego Morata por ser apoyo y guía constante durante todos estos años. Me considero, realmente afortunada de haber podido trabajar y formarme bajo estos investigadores tan extraordinarios, que me ayudaron a valorar y a sentir la ciencia. A todos, gracias por las oportunidades, por los comentarios, las correcciones y todo el tiempo dedicado durante esta estancia. Quiero agradecer de manera especial a Martin, por su inigualable trabajo como profesor guía, por los años de aprendizaje, por su preocupación y apoyo en llevar a cabo cada trabajo realizado en este tiempo. Martin eres un verdadero mentor y agradeceré siempre la confianza que depositaste en mí desde el inicio, cuando llegue a tu oficina con escasos antecedentes pero con ansias de superación y crecimiento. Gracias por ser ejemplo e inspiración, siempre admiración por ti.

También me gustaría extenderle mis más sinceros agradecimientos a la miembro externa de mi comisión Irene del Real por su apoyo y ayuda durante todo este proceso y a mis co-autoras Anais Pagès y Laure Martin; quienes no solo me brindaron comentarios y discusiones reflexivas sino que también han sido inspiración para mí. De igual manera, deseo expresar mis agradecimientos a quienes contribuyeron en la obtención de datos durante la ejecución de alguna técnica analítica durante este estudio, a Owen Neil por mis análisis de microsonda en bitumen en Washington State University; a Laure Martin por toda su guía en el montaje de las muestras y por la realización de los isotopos de azufre “in-situ” en pirita, en The University of Western Australia; a Santiago Tassara por acompañarme en las noches en vela durante mis análisis de sincrotrón en LNLS, Brasil; a Rurik Romero por su apoyo en los análisis de LA-ICP-MS; y al laboratorio LAMARX de la Universidad Nacional de Córdoba, Argentina por mis análisis de microsonda en bitumen y sulfuros en sus instalaciones. De igual forma, agradezco a las compañías mineras Las Cenizas y Carmen Bajo porque de manera desinteresada nos permitieron el acceso a sus instalaciones y nos compartieron muestras. De manera muy especial agradezco al profesor Marcos Zentilli, por su disposición y por compartir conmigo las muestras de El Soldado.

Agradezco también a Maritza, Blanca, Karin, William, a Mauricio del NMTM y a todos los administrativos del departamento de Geología que siempre estuvieron dispuestos a colaborar o guiarme frente a un trámite o a cualquier requerimiento.

Un especial agradecimiento a mis padres por su eterno amor, por ser mi mayor inspiración, por impulsarme día a día, por enseñarme que el cielo es el límite y por regalarme alas para volar y ser feliz. A Adri, gracias por su compañía constante, por ser mi oído y también mi polo a tierra. A Fernando gracias por su amor, por creer en mí, por su apoyo incondicional, por sus palabras acertadas, por su compañía en este camino y por saber y sentir que este logro es nuestro.

No puedo dejar de agradecer a todas las personas maravillosas que conocí durante este período en el NMTM, todos ellos hicieron mis días amenos, y a cada uno de ellos gracias por las conversaciones livianas y las discusiones profundas. Siempre llevaré conmigo las enseñanzas que sin notarlas cada uno de ustedes me dejó.

Finalmente reconozco y agradezco el apoyo financiero del Núcleo Milenio Trazadores de Metales (NMTM), del Centro de Excelencia en Geotermia de los Andes (CEGA), de los FONDECYT #1140780 y #1190105; de ANID por mi beca de Doctorado (21171385) y a la Society of Economic Geologists por la beca Hugh McKinstry.

CONTENT

CHAPTER 1 – Introduction	1
1.1. Overview and Motivation.....	1
1.2. Geological Setting of Stratabound Cu-(Ag) Deposits.....	5
1.3. Research Objectives and Hypothesis	7
1.4. Methodology	7
1.5. Previous Studies	9
1.6. Publications Resulting from this Thesis.....	10
CHAPTER 2 – Assessing the role of bitumen in the formation of stratabound Cu-(Ag) deposits: Insights from the Lorena deposit, Las Luces district, northern Chile	12
2.1. Introduction	13
2.2. Geological Background.....	15
2.2.1. Upper Jurassic and Lower Cretaceous stratabound Cu-(Ag) deposits.....	15
2.2.2. The Lorena stratabound Cu-(Ag) deposit.....	16
2.3. Samples and Methods	17
2.3.1. SEM, FE-SEM and EMPA methods.....	17
2.3.2. XRF elemental mapping.....	18
2.3.3. Sulfur X-ray absorption near edge structure (XANES) spectroscopy	18
2.4. Results	19
2.4.1. Variations with depth.....	19
2.4.2. Hydrothermal alteration and mineralization	20
2.4.3. Pyrobitumen inclusions in pyrite and chalcocite	21
2.4.4. Elemental composition and pyrobitumen textures	21
2.4.5. Pyrobitumen XRF maps.....	22
2.4.6. Sulfur XANES data	22
2.5. Discussion	23
2.5.1. Paragenetic sequence and ore-forming processes	23
2.5.2. Evidence for hydrocarbon-hydrothermal fluid emulsions	25
2.5.3. Key metals in bitumen.....	26
2.5.4. Pyrobitumen as source of organic sulfur.....	28
2.6. Genetic model and concluding remarks	30
2.7. Acknowledgements	31
2.8. References	31
2.9. Figures	40

CHAPTER 3 – Trace element geochemistry of pyrite from bitumen-bearing stratabound Cu-(Ag) deposits, northern Chile	58
3.1. Introduction.....	59
3.2. Geological Background.....	60
3.3. Samples and methods.....	62
3.4. Results.....	63
3.4.1. Micro-textural observations.....	63
3.4.2. Chemical composition of pyrite.....	64
3.5. Discussion.....	64
3.5.1. Trace element incorporation in pyrite from stratabound Cu-(Ag) deposits.....	64
3.5.2. Comparisons with IOA and IOCG deposits within the Coastal Cordillera.....	67
3.6. Concluding remarks.....	68
3.7. Acknowledgements.....	69
3.8. References.....	69
3.9. Figures.....	79
CHAPTER 4 – Sulfur isotope and trace element signature of pyrite from bitumen-bearing stratabound Cu-(Ag) deposits, northern Chile: Implications for fluid sources and mineralization processes ...88	
4.1. Introduction.....	89
4.2. Geological Background.....	91
4.2.1. Las Luces district.....	91
4.2.2. Copiapó district.....	91
4.2.3. El Soldado district.....	92
4.3. Samples and methods.....	93
4.3.1. LA-ICP-MS.....	93
4.3.2. In-situ sulfur isotope analysis - Secondary-ion mass spectrometry (SIMS).....	94
4.4. Results.....	95
4.4.1. Chemical composition of pyrite.....	95
4.4.2. Sulfur isotope composition of pyrite.....	95
4.4.3. LA-ICP-MS and SIMS transects.....	96
4.5. Discussion.....	96
4.5.1. Pyrite textures and geochemical variations.....	96
4.5.2. Source(s) of sulfur and fractionation processes.....	97
4.5.3. Implications for ore mineralization processes.....	99
4.6. Final remarks.....	101

4.7. Acknowledgements	101
4.8. References	101
4.9. Figures	113
4.10. Tables	121
CHAPTER 5 – Conclusions	125
BIBLIOGRAPHY	128
ANNEXES	134
ANNEXES A: Supplementary Material of Chapter 2	134
A.1. Sulfur K-edge spectra for sulfur standards (Bolin et al., 2016)	135
A.2. Representative electron microprobe analyses (EMPA) data (wt.%) of bitumen in Lorena deposit carried out at the Peter Hooper GeoAnalytical Laboratory of Washington State University (WSU), USA and LAMARX Laboratory of the Universidad Nacional de Córdoba, Argentina. b.d.l: below detection limit. Detection limits (wt.%) are shown below each element analyzed	136
A.3. Concentration boxplot for selected minor elements in pyrobitumen from Lorena. Electron microprobe analyses (EMPA) including all data are plotted in weight percent (wt.%) on a vertical logarithmic scale. In the boxplot, mean and median concentrations are shown. A circle outlier is a data point above $1.5 \times (75\text{th percentile} - 25\text{th percentile})$ while a square outlier is above $3.0 \times (75\text{th percentile} - 25\text{th percentile})$	139
A.4. Boxplot showing the concentration of Fe, Cu, S, Cl, Ag and Au in pyrobitumen plotted as a function of sample depth (LO-62, LO-7-1 and LO-15: intermediate-shallow samples, LO-24: deep sample). All EMPA data are plotted in weight percent (wt.%) on a vertical logarithmic scale. In each boxplot, mean concentrations are marked. A circle outlier is above $1.5 \times (\text{quartile 3} - \text{quartile 1})$ while a square outlier is above $3.0 \times (75\text{th percentile} - 25\text{th percentile})$	140
ANNEXES B: Supplementary Material of Chapter 3	141
B.1. Electron probe microanalysis (EPMA) data of pyrite from stratabound Cu-(Ag) deposits, Chile. Concentrations are reported in weight percent (wt.%). Detection limits (in wt.%) are shown below each element. LO: Lorena deposit; MTCUL: La Culebra deposit; MTC: Manto Cobrizo deposit. b.d.l: below detection limit.	142
B.2. Laser ablation inductively coupled plasma mass spectrometry (LA-ICP-MS) analyses of Ag, Au, Cu, Bi, Hg, Tl, Pb, Zn, Se, Te, As, Sb, Ge, Cd, In, Sn, Co, Ni, Mn, Cr, V and Mo of pyrite from stratabound Cu-(Ag) deposits, Chile. Concentrations are reported in parts per million (ppm). Detection limits (in ppm) are shown below each element. LO: Lorena deposit; MTCUL: La Culebra deposit; MTC: Manto Cobrizo deposit. b.d.l: below detection limit.	147
ANNEXES C: Supplementary Material of Chapter 4	150
C.1. BSE images showing pyrite grains from Lorena deposit analyzed by SIMS. In-situ sulfur isotope values are shown.	151

C.2. BSE images showing pyrite grains from La Culebra deposit analyzed by SIMS. In-situ sulfur isotope values are shown.....152

C.3. BSE images showing pyrite grains from Lorena deposit analyzed by SIMS. In-situ sulfur isotope values are shown.....153

FIGURES

- Figure 1.** Schematic representation of the main pathways of petroleum and bitumen generation (modified from Gaupp et al., 2008)3
- Figure 2.** Location of stratabound Cu-(Ag) deposits in the Coastal Cordillera of northern-central Chile. AFS: Atacama Fault System.....4
- Figure 3.** Location of representative Jurassic and Cretaceous stratabound Cu-(Ag) deposits of the Coastal Cordillera of northern-central Chile. The extension of Jurassic and Lower Cretaceous belts and the NS-trending Atacama Fault System (AFS) are also shown.....40
- Figure 4. A)** Location of the Lorena deposit, Las Luces district. **B)** Geologic map of the Las Luces district (modified from Detlef, 2002). **C)** Satellite image of the Lorena (underground) mine showing the location of the sub-vertical DDH15LO-05 drill hole collar.41
- Figure 5.** Representative pyrobitumen-bearing andesitic host rock samples from the Lorena deposit. **A)** and **B)** Pyrobitumen filling vesicles has a black color, glassy luster and conchoidal fracture. **C)** Pyrobitumen associated with hypogene chalcocite. **D)** Pyrobitumen in contact with Cu oxides formed by in-situ oxidation of hypogene sulfides.....42
- Figure 6.** Schematic illustration of drill core DDH15LO-05 from the Lorena deposit showing lithological variations (center) and images of representative samples along the drill core. The orange line indicates the average Cu grade from the top to the bottom of the drill core. **A)** Andesite with ~5-30 modal percentage of plagioclase phenocrysts. **B)** Afanitic andesite with scarce plagioclase phenocrysts (<5 modal percentage). **C-D)** Backscattered electron (BSE) images of globular pyrobitumen filling a vesicle in a sample from the intermediate section. **E-F)** Backscattered electron (BSE) images of angular pyrobitumen. This textural type is dominant in the deep zone. Angular pyrobitumen grains vary in size and is commonly observed in brecciated zones.....43
- Figure 7.** Transmitted and reflected polarized light microscopy photomicrographs of representative alteration minerals at Lorena. **A)** Prehnite and pumpellyite in vesicles with albite microcrysts. **B)** Albitized plagioclase with minor sericite. **C)** Vesicle infilled with prehnite with minor pyrobitumen at the edges. **D)** Reflected light image of **(C)** where copper sulfides (chalcocite and digenite) are observed in close association with pyrobitumen. **E)** Albitized plagioclase phenocrysts cross-cut by thin calcite veinlets. **F)** Calcite and chalcocite amygdale in volcanic host rock.....44
- Figure 8.** Reflected polarized light microscopy images of pre-ore and ore stage assemblages from the Lorena deposit. **A)** Euhedral pyrite (Pyrite I) from the pre-ore stage, **B)** Pyrite overgrowths from on pre-existing euhedral pyrite core, forming elongated and sub-rounded clusters. **C)** Rosette-shaped pyrite aggregates (Pyrite II). **D)** shows the magnified image of the yellow rectangle in **(C)**, highlighting the finer structures of the pyrite aggregates. **E)** Set of rosette-shaped pyrite aggregates. **F)** Chalcopyrite grain replaced by digenite and covellite. **G)** Pyrobitumen/chalcocite association

replaced by late digenite. **H)** Droplet-shaped, micrometer-sized pyrobitumen inclusions within chalcocite.....45

Figure 9. Backscattered electron (BSE) images showing pyrobitumen in association with pyrite. **A)** Subhedral pyrite grains with pyrobitumen interspersed or filling fractures. **B)** Rosette-shaped pyrite, showing pyrobitumen inclusions and in simple contact with pyrobitumen grains46

Figure 10. A-D) Field emission scanning electron microscopy (FE-SEM) images revealing the presence of micro- to nano-sized pyrobitumen inclusions within Pyrite I. Pyrobitumen inclusions usually have droplet-like shapes and show a regular distribution following crystallographic planes. Pyrobitumen grains are also observed in fractures or near crystal.....47

Figure 11. Detailed FE-SEM images of micro- to nano-sized pyrobitumen inclusions in Pyrite I. **A)** Elongated, sub-rounded pyrobitumen inclusions within a pyrite grain. Pores are also observed. **B)** Detail view of nano-sized pyrobitumen droplet in pyrite inclusion observed in image (A). **C)** Rounded and elongated pyrobitumen nano-inclusions from image (A). **D)** Pyrobitumen inclusions bordering a fracture in the center of a pyrite grain. **E)** Detail view of pyrobitumen inclusions observed in (D). **F)** Al- and Si-bearing nanoparticles within a pyrobitumen droplet48

Figure 12. Backscattered electron (BSE) images showing pyrobitumen in association with chalcocite. **A)** Angular pyrobitumen in close proximity to anhedral chalcocite grains. Also observed is pyrobitumen filling fractures in chalcocite. **B)** Rounded and randomly oriented inclusions of pyrobitumen within chalcocite. **C)** Angular pyrobitumen is observed in contact with and partially surrounded by chalcocite. Rounded pyrobitumen inclusions in chalcocite are also present. **D)** Chalcocite grain in contact with pyrobitumen and magnetite in a calcite amygdale. Pyrobitumen droplets within chalcocite are also observed.....49

Figure 13. Concentration boxplot for selected minor elements in pyrobitumen from Lorena. Electron microprobe analyses (EMPA) are plotted in weight percent (wt.%) on a vertical logarithmic scale. In the boxplot, mean and median concentrations are shown as well as the number of analyses above detection limit for each element (displayed in or outside of each box). A circle outlier is a data point above $1.5 \times (75\text{th percentile} - 25\text{th percentile})$ 50

Figure 14. Boxplot showing the concentration of Fe, Cu, S, Cl, Ag and Au in pyrobitumen plotted as a function of sample depth (LO-62, LO-7-1 and LO-15: intermediate-shallow samples, LO-24: deep sample). EMPA data are plotted in weight percent (wt.%) on a vertical logarithmic scale. In each boxplot, mean concentrations are marked and the number of analyses above detection limit for each element is displayed inside/outside of each box. A circle outlier is above $1.5 \times (\text{quartile } 3 - \text{quartile } 1)$ while a square outlier is above $3.0 \times (75\text{th percentile} - 25\text{th percentile})$51

Figure 15. XRF elemental maps of pyrobitumen grains from Lorena obtained by desktop (**B-J**) and synchrotron (**L-R**) μ -XRF. **A, F, K)** Backscattered electron (BSE) images of the analyzed pyrobitumen grains. See text for discussion52

- Figure 16.** Wavelength dispersive spectrometry (WDS) EMPA X-ray maps (Fe, Cu, S) of pyrobitumen grains within andesite host rock. The WDS maps show a high concentration of S and a low concentration of Cu in pyrobitumen. Slight variations in the S concentration are observed in the pyrobitumen grains, whereas Cu appears more homogeneous. No Fe was detected in the analyzed grains53
- Figure 17.** Sulfur speciation in pyrobitumen obtained using synchrotron XANES. Several analyses were performed and merged to achieve each spectrum. XANES data of pyrobitumen from the Lorena deposit indicate the presence of thiophene and sulfone species (LO-24-SP4). Sample LO-24-SP1, on the other hand, shows peaks associated with elemental sulfur and sulfate54
- Figure 18.** Paragenetic sequence for the Las Luces deposit. The thick bars represent more abundant phases (dashed line, thin line and thick bar indicate low, moderate and abundant, respectively)55
- Figure 19.** FE-SEM BSE images showing micro- to nano-sized Cu-Fe sulfide inclusions within pyrobitumen. The BSE image on the right (**B**) shows a magnified view of the ~250-500 nm Cu-Fe sulfide nanocrystals56
- Figure 20.** Summary figure showing key processes that led to the formation of the bitumen-bearing Lorena stratabound Cu-(Ag) deposit. **A) and B)** The first stage involves hydrocarbon generation from a sedimentary rock source. Petroleum was mobilized as immiscible droplets in an aqueous fluid through permeability zones. At the same time, hydrocarbon gases are emitted (e.g., CH₄ and CO₂) and pyrite grains are bound by coalescence into the petroleum phase. **C) and D)** Migrated hydrocarbons were injected into the andesite rocks filling vesicles (OM1) and pyrite crystals grew in the presence of hydrocarbons (e.g., OM2). **E) and F)** External Cu-rich fluids circulated through the andesite host rock. The pyrobitumen-fluid interaction triggered Cu sulfide precipitation and a second pulse of hydrocarbon or remobilization event is evidenced by the presence of angular pyrobitumen (OM3) in close association with chalcocite (which can also show bitumen inclusions, OM2). At the same time, the organic phase is affected by thermal cracking, resulting in chemical bond breakage and leading to a slow, gradual released of sulfur as pyrobitumen becomes more aromatized. See text for details57
- Figure 21.** **A)** Location of stratabound Cu-(Ag) deposits in the Coastal Cordillera of northern-central Chile. Iron oxide-apatite (IOA) and iron oxide-copper-gold (IOCG) deposits are also shown. **B)** Map showing the geology of the Lorena/Las Luces district (modified from Detlef, 2002). **C)** Geological map of the Copiapó district, including the La Culebra and Manto Cobrizo deposits (modified from Arévalo et al., 2009). AFS: Atacama Fault System.....79
- Figure 22.** Reflected polarized light microscopy photomicrographs of representative sulfide ore assemblages from the Lorena and Copiapó stratabound Cu-(Ag) deposits. **A)** Subhedral pyrite grains associated with bitumen. **B)** (Sub)-euhedral pyrite grains in contact with bitumen. Late Cu sulfides are also observed. **C)** Euhedral pyrite grain associated with bitumen **D)** Chalcopyrite grain replaced by chalcocite. **E)** Pyrite grains replaced along fractures by chalcopyrite, bornite and chalcocite/digenite. Late tennantite is also observed. **F)** Cu-(Fe) sulfides (chalcocite-bornite)80

Figure 23. Backscattered electron (BSE) images showing pyrite in association with bitumen (pre-ore stage). **A)** Sub-euhedral pyrite grains with droplet-shaped micrometer-sized inclusions of bitumen. **B)** Pyrite in close association with bitumen. **C)** Elongated pyrite grains in association with bitumen. Aggregates of fine euhedral pyrite crystals are also observed. **D)** Aggregates of pyrite forming a rosette-like texture. **E)** Rounded pyrite grains in close contact with bitumen. **F)** Euhedral to subhedral pyrite grain in contact with bitumen.....81

Figure 24. Concentration boxplot for selected minor and trace elements in pyrite from Lorena and the Copiapó stratabound Cu-(Ag) deposits. EMPA and LA-ICP-MS spot analysis data are included and shown as dotted lines and boxplots, respectively. Data are plotted in parts per million (ppm) on a vertical logarithmic scale. In each boxplot, minimum, median and maximum concentrations are indicated. The horizontal dashed line marks the mean detection limit (mdl) of EPMA analyses for all elements. A circle outlier is above $1.5 \times$ (quartile 3- quartile 1) while a square outlier is above $3.0 \times$ (75th percentile - 25th percentile).....82

Figure 25. Concentration boxplot for selected minor and trace elements in pyrite from stratabound Cu-(Ag) deposits (Lorena, La Culebra and Manto Cobrizo). Only LA-ICP-MS spots data are included. Data are plotted in parts per million (ppm) on a vertical logarithmic scale. In each boxplot, minimum, median and maximum concentrations are marked83

Figure 26. Representative LA-ICP-MS depth-concentrations profiles (time vs. intensity) for Sselected isotopes (^{55}Mn , ^{63}Cu , ^{107}Ag , ^{123}Sb , ^{205}Tl and ^{208}Pb) in pyrite from stratabound Cu-(Ag) deposits. See text for discussion.....84

Figure 27. Elemental concentration scatterplots for pyrite from stratabound Cu-(Ag) deposits. **A)** Tl vs As. **B)** Au vs As. **C)** As vs S. In (A) the dotted lines corresponds to a Tl/As = 1.0. The dashed curve in (B) represents the solubility limit of Au as a function of As concentrations, as determined by Reich et al., 2005. Concentrations are reported in parts per million (ppm) in (A) and (B), while in (C) are in weight percent (wt.%).....85

Figure 28. Elemental concentration scatterplots for pyrite from stratabound Cu-(Ag), IOA and IOCG deposits. **A)** Co vs Ni. **B)** Co vs As. **C)** Ni vs As. **D)** Cu vs Ag. **E)** Cu vs As. **F)** Ag vs As. All concentrations are reported in parts per million (ppm).....86

Figure 29. Ag/Co vs Co/Cu scatterplot diagram for pyrite from stratabound Cu-(Ag), iron oxide-apatite (IOA) and iron oxide-copper gold (IOCG) deposits from northern Chile. Data are plotted on a logarithmic scale. Data (SIMS and LA-ICP-MS) for the Los Colorados IOA and Candelaria IOCG deposit were obtained from Reich et al., 2016 and del Real et al., 2020, respectively87

Figure 30. **A)** Location of representative Jurassic and Cretaceous stratabound Cu-(Ag) deposits of the Coastal Cordillera of northern-central Chile. The extension of Jurassic and Lower Cretaceous belts and the NS-trending Atacama Fault System (AFS) are also shown. **(B)** Map showing the geology of the Lorena/Las Luces district (modified from Detlef, 2002). **(C)** Geological map of the Copiapó district, showing the location of the La Culebra deposit (modified from Arévalo et al., 2005). **(D)** Map showing regional geological configuration from the El Soldado deposit (adapted from Boric et al., 2002)113

Figure 31. Backscattered electron (BSE) and reflected polarized light microscopy images of pre-ore and ore stage sulfides from the studied deposits. **(A)** Framboids and spherules in association with pyrobitumen. **(B)** Framboids composed of randomly distributed euhedral microcrystals. **(C)** Framboidal pyrite being replaced by chalcopyrite from La Culebra deposit. **(D)** Aggregate of pyrite forming rosette-like textures with pyrobitumen in the center from Lorena deposit. **(E)** Representative euhedral pyrite. **(F)** Euhedral pyrite containing framboidal cores. This framboidal cores are also replaced by chalcopyrite.....114

Figure 32. Concentration boxplot for selected minor and trace elements in pyrite from Lorena, La Culebra and the El Soldado stratabound Cu-(Ag) deposits. LA-ICP-MS spot analysis data are included and shown as dotted lines and boxplots, respectively. Data are plotted in parts per million (ppm) on a vertical logarithmic scale. In each boxplot, minimum, median, and maximum concentrations are indicated.....115

Figure 33. Histogram of in-situ $\delta^{34}\text{S}$ values obtained by secondary ion mass spectrometry (SIMS) of pyrite minerals from Lorena, La Culebra and the El Soldado deposits. Range of previous published sulfur isotope signature are also show as horizontal bars.....116

Figure 34. Representative trace element concentrations and $\delta^{34}\text{S}$ compositions diagram from studied deposits. The horizontal axis represents the distance (μm) within pyrite grains where in-situ sulfur isotope analyses were performed. **(A)** and **(B)** Pyrite grains of MTCUL-2D sample from La Culebra deposit. **(C)** Representative diagram from Lorena deposit. **(D) – (F)** Pyrite grains from the El Soldado deposit (NW-167 sample).....117

Figure 35. Elemental concentration scatterplots for pyrite from the stratabound Cu-(Ag). **(A)** Tl vs As. **(B)** Mn vs As. **(C)** Cu vs As. **(D)** Pb vs As. **(E)** Mo vs As. **(F)** Mn vs Tl. **(G)** Ag vs Tl. Sulfur isotope range is also shown. All concentrations are reported in parts per million (ppm).....118

Figure 36. Summary figure showing key processes that led the sulfur fractionation of pyrite from bitumen-bearing stratabound Cu-(Ag) deposits119

Figure 37. Se/S and $\delta^{34}\text{S}$ plot used for evaluating fluid source. Higher $\delta^{34}\text{S}$ and lower Se/S correlate with basinal derived fluids, whereas lower $\delta^{34}\text{S}$ and higher Se/S correlate with magmatic-derived fluids. Source ranges were obtained by Fitzpatrick, 2008120

TABLES

Table 1. Trace element LA-ICP-MS analyses and SIMS sulfur isotope values of pyrite from Lorena, La Culebra and the El Soldado deposits, Chile. Concentrations are shown in parts per million (ppm) and sulfur isotope ratios are reported as $\delta^{34}\text{S}$ values (in per mil, ‰).121

Table 2. Statistical summary of LA-ICP-MS data for pyrite from Lorena, La Culebra and the El Soldado deposits, Chile. Trace elements with significant concentrations (in ppm) are shown124

CHAPTER 1

INTRODUCTION

1.1. OVERVIEW AND MOTIVATION

In the last decades, the empirical association between hydrocarbons and mineralization has been recognized for a wide variety of ore systems, including the Witwatersrand Au-U, sedimentary Cu, Carlin-type Au, and Mississippi Valley-type Pb-Zn deposits (Mossman et al., 1993; Robb and Meyer, 1995; Fuchs et al., 2016; Durieux and Brown, 2007; Anderson and Macqueen, 1982). The close spatial association between ore mineralization and liquid and/or residual petroleum (e.g., bitumen or pyrobitumen) has been commonly attributed to be either coincidental or to provide evidence for redox-driven ore precipitation. In the latter case, redox-sensitive elements such as Au, U or Cu would be reduced by interaction of metal-bearing aqueous fluids with organic matter during ore genesis (Parnell, 1988; Anderson, 1991; Spirakis, 1996; Sun and Püttmann, 2000; Cuney, 2009; Pfaff et al., 2010; Large et al., 2011; Szmihelsky et al., 2021). However, recent studies have provided evidence, based on the metal transport capacity of petroleum or oil (e.g., Hunt, 1996), that liquid hydrocarbons can play an active role during ore genesis by carrying dissolved metals and ligands, from its source to the site of ore deposition (Migdisov et al., 2017; Saintilan et al., 2019). High metal concentrations of V, Ni, Zn, Au, U, S, Cl, I among others have been reported in different organic phases derived from sediments during diagenesis (Colombo and Sironi, 1961; Colombo et al., 1964; Hitchon et al., 1975; Jones et al., 1975; Ellrich et al., 1985; Mastalerz and Glikson, 2000; Lo Mónaco et al., 2007; Fuchs et al., 2016). More importantly, recent experiments have determined that Zn, Au and U can be solubilized in crude oils (Migdisov et al., 2017), and studies in sediment-hosted Pb-Zn deposits suggest that crude oil could provide metals and reduced sulfur for metal sulfide precipitation (Saintilan et al., 2019).

On other hand, organic matter may play an important and active role during the process of bacterial or thermochemical sulfate reduction, where sulfide minerals can be precipitated by reaction of generated H₂S with metal cations (Leventhal, 1986; Leventhal and Giordano, 1998). This process is controlled by a combination of factors, including variable bacterial fractionation, the presence of specific microorganisms, variable sulfate reduction rates and limiting effects of sulfate, organic matter and reactive Fe concentrations (Strauss, 1997; Canfield et al., 2010). Pyrite is the most important sulfide derived from this process, in which framboidal textures are typical but not exclusive (Rickard, 1997; Rickard and Luther, 1997). For example, spheroidal and/or polygonal, subhedral and/or cubic pyrite grains forming aggregates can also be associated with organic matter (Wilson et al., 1998). The process of bacterial and thermochemical sulfate reduction is well known to produce significant fractionation of sulfur in sedimentary settings (Goldstein and Aizenshtat, 1994; Machel, 2001). Diagenetic sedimentary pyrite commonly exhibits a wide range in ³⁴S/³²S isotope ratios, expressed as δ³⁴S, from -60 to +60‰ (Strauss, 1997), in contrast to pyrite formed from magmatically-derived sulfur, which display δ³⁴S close to 0‰, with a narrow range and often <10‰ (Chaussidon et al., 1989).

Due to the above, some fundamental questions related to ore genesis in sedimentary settings remain unanswered. One of them relates to the timing of liquid hydrocarbon introduction into the ore system with respect to hydrothermal fluid circulation. This is critical to evaluate if the organic

phases act as a viable source of metals and ligands, most importantly sulfur, or if they play only a passive role as reducing agents. The second question relates to the amount of metals and ligands that are actually present in the liquid and solid hydrocarbon phases, when they occur in ore deposits. In general, the range of metal concentrations in natural organic phases remain mostly unconstrained (Fuchs et al., 2016). Another aspect that is not well understood is whether petroleum can effectively contribute with at least some metals and ligands during interaction with hydrothermal fluids or brines, or if metals and ligands are derived exclusively from hydrothermal fluids. This issue is relevant to determine, for example, the source reservoir for metals or sulfur compounds. Evidence is generally scarce and with the exception of a few studies (e.g., Jones, 1975; Ali et al., 1983; Wilson and Zentilli, 1999; Fuchs et al., 2016; Wu et al., 2020), the trace metal and sulfur isotopic signature in mineral-hydrocarbon assemblages remains mostly understudied in ore systems. Within this perspective, some ore-forming models may involve metal and ligands, such as sulfur, transported by hydrocarbons (Lewan, 1984; Watkinson, 2007; Khuhawar et al., 2012), which migrate through permeable rocks or favorable structural zones to shallow reservoirs. Alternatively, hydrocarbons could act as a geochemical trap, triggering metal precipitation during interaction with aqueous hydrothermal fluids of different origin (e.g., Parnell, 1988; Anderson, 1991; Cuney, 2009). Also, genetic models involving both endmembers may be feasible to explain the origin of specific deposits.

This research is largely motivated by these fundamental questions, and focus specifically on Cu deposits where sulfide assemblages are paragenetically related to migrated hydrocarbons. Stratabound or “Manto-type” Cu-(Ag) deposits in Chile provide an ideal setting to study the role and importance of organic matter during Cu metallogenesis. These Upper Jurassic to Lower Cretaceous deposits occur within the Coastal Range of northern and central Chile, and are characterized by the presence of residual petroleum, in the form of bitumen and pyrobitumen, in association with Cu mineralization. These deposits represent the third most important source of copper in Chile after porphyry Cu and iron oxide-copper-gold deposits (IOCG), and can also contain economic grades of Ag (Maksaev et al., 2007; Reich et al., 2010; 2013). Most importantly, several studies have recognized a casual relation between Cu-(Fe) sulfides, and bitumen/pyrobitumen in these deposits, which strongly suggests a genetic link (Mayer and Fontboté, 1990; Zentilli et al., 1997; Wilson and Zentilli, 1999; Wilson et al., 2003a, b; Cisternas and Hermosilla, 2006; Rieger et al., 2008; Carrillo-Rosúa et al., 2014). Also, these studies have shown that solid hydrocarbons, referred loosely as “organic matter”, “carbon” or “bitumen”, are morphologically and chemically complex phases.

Petroleum fluids are a mixture of organic molecules of different molar mass and structure that vary from a gaseous to liquid state. Figure 1 shows the main pathway of petroleum generation from different precursor materials. Kerogen is the main precursor in petroleum generation and is defined as insoluble (in organic solvents) sedimentary organic matter derived from plants and other biomass (e.g., bacteria, animals). During early stages of burial, kerogen is subject to microbial activity to form methane at temperature between 10°C up to 60-80°C. At greater depths and temperatures (usually >100°C), thermal dissociation (“cracking”) and disproportionation leads to the formation of liquid hydrocarbons (i.e., crude oil) and thermal gas. Another precursor is soluble organic matter (bitumen). Bitumen is mainly generated from kerogen and includes all oil, but also heavier, tar-like products. If this bitumen is thermally affected, it will crack into gas and a solid residue, ultimately methane and pyrobitumen (Gaupp et al., 2008). Hereafter, the term pyrobitumen is used to refer to these solid residues associated with Cu-bearing sulfides and which

are common in the Cretaceous stratabound Cu-(Ag) deposits. By focusing on the inorganic chemistry of pyrobitumen we intend to obtain information that is essential to understand the role of hydrocarbons and its potential role in the ore-forming process.

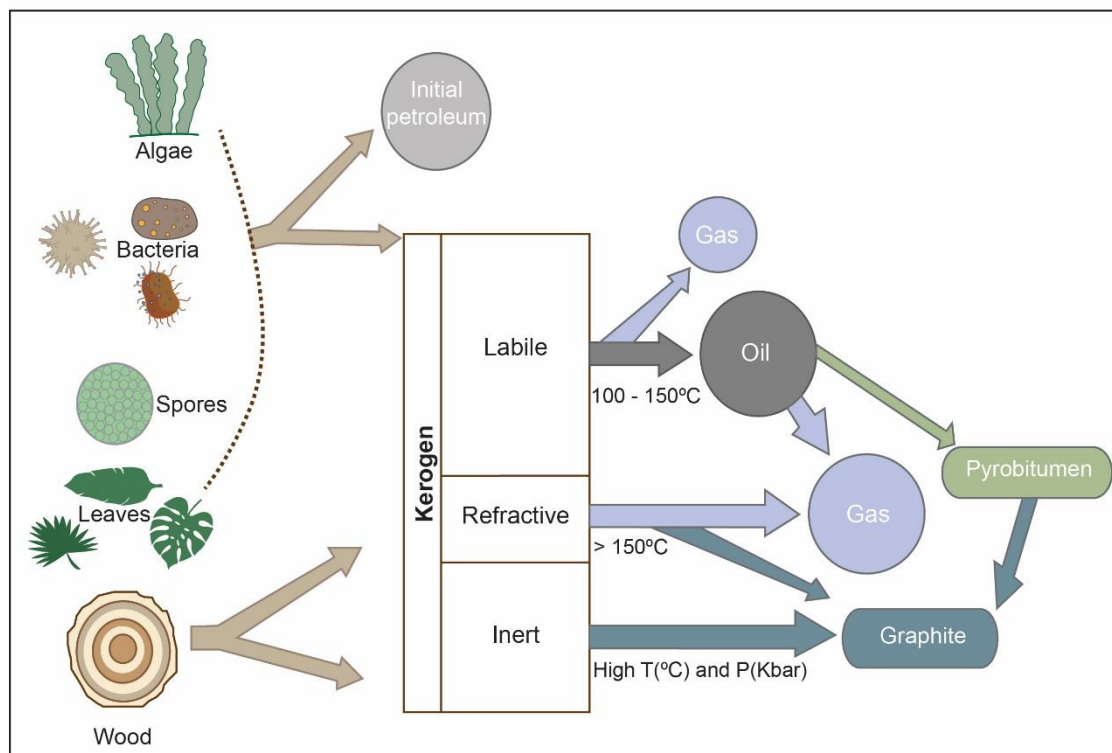


Figure 1. Schematic representation of the main pathways of petroleum and bitumen generation (modified from Gaupp et al., 2008).

To gain knowledge about the importance of residual hydrocarbons and their intimate association with Cu-(Ag) mineralization in Chilean stratabound or “Manto-type” deposits, this research focused on three main districts, from north to south, the Las Luces district near Taltal, the Copiapó district near the namesake city, and the El Soldado district north of Santiago (Fig. 2). The work presented here comprised detailed surface and drill core sample characterization, and petrographic observations, which were the basis for microanalysis and spectroscopic determinations in sulfide minerals and pyrobitumen. Detailed microtextural observations were performed using scanning electron microscopy (SEM), and major and minor element data and chemical maps of sulfides and pyrobitumen were obtained using electron microprobe analysis (EMPA). Desktop and synchrotron micro X-ray fluorescence (μ -XRF) techniques were used to image the distribution of trace elements in pyrobitumen. These data were complemented with synchrotron X-ray absorption near edge spectroscopy (XANES) to determine the sulfur speciation within pyrobitumen. Laser ablation inductively coupled mass spectrometry (LA-ICP-MS) analyses were carried out to quantify the trace element distribution in sulfides, with a particular focus on pyrite. Finally, in-situ sulfur isotope data of pyrite was obtained by secondary ionization mass spectrometry (SIMS) to fingerprint the source for sulfur in the deposits, and infer isotope fractionation processes.

In the next sections of this introductory chapter, a regional geological background of the belt is provided, followed by a general description of stratabound Cu-(Ag) deposits in Chile. Finally, the research objectives and working hypothesis are described, followed by a methodology section and a section summarizing the most relevant previous studies. The chapter ends with a list of publications and manuscripts that configure the main three chapters of this thesis. Organic (pyrobitumen) data are discussed in Chapter 2, while data collected for sulfides, mainly pyrite, are presented in Chapters 3 and 4. Chapter 5 summarizes the main conclusions of this research.

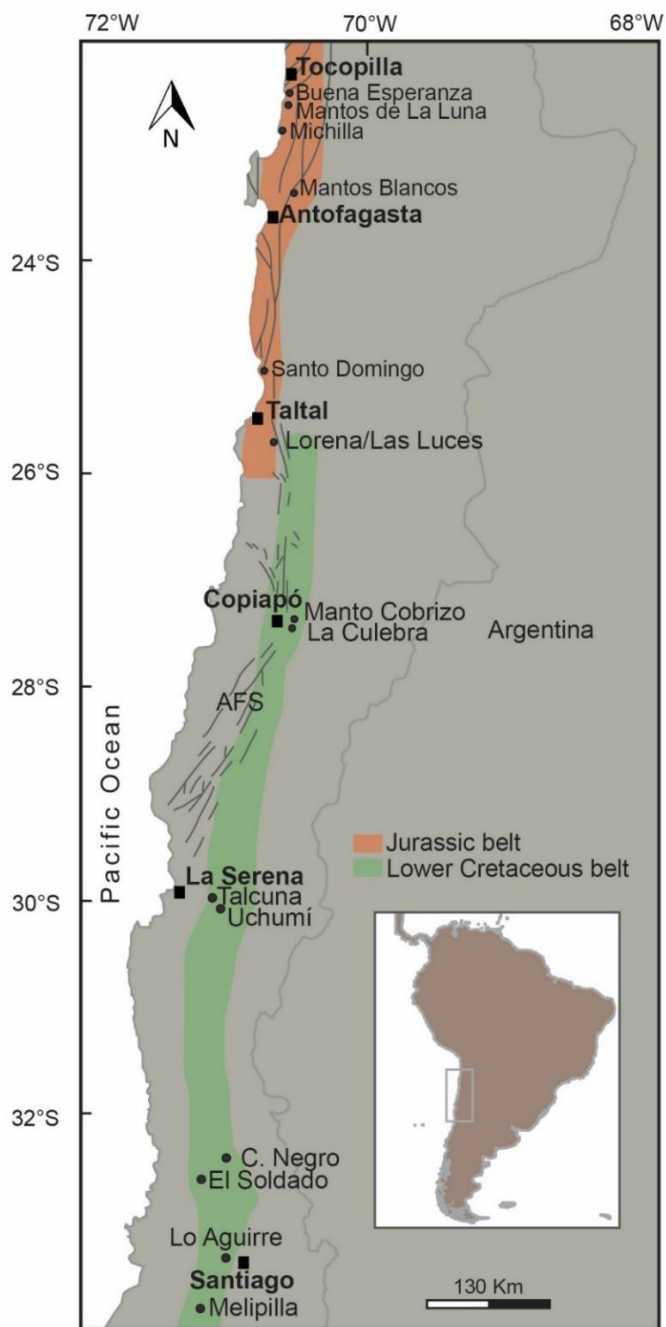


Figure 2. Location of stratabound Cu-(Ag) deposits in the Coastal Cordillera of northern-central Chile. AFS: Atacama Fault System.

1.2. GEOLOGICAL SETTING OF STRATABOUND Cu-(Ag) DEPOSITS

Two major stages are recognized in the geological evolution of the Andes in central-northern Chile: a Jurassic to Early Cretaceous extensional stage with a Mariana-type subduction, followed by a Late Cretaceous to Early Paleogene compressional stage configured by a Chilean-type subduction (Charrier et al., 2007; Jara et al., 2021 and references therein). The second stage, is not discussed here because it is not relevant for the purpose of this research.

The Jurassic to Early Cretaceous stage was controlled by a magmatic arc-system flanked to the east by a sedimentary marine back-arc basin developed within an extensional tectonic setting (Maksaev et al., 2002). Rapid subsidence of the magmatic arc and associated back-arc basin led to deposition of thick volcano-sedimentary sequences in arc position and of marine to continental sedimentary units interlayered with volcanic rocks in the back-arc region (Scheuber et al., 1994). This event is represented in northernmost Chile (21°- 26°S) by a thick basaltic to andesitic volcanic pile known as La Negra Formation. This thick (<7,000 m) unit has a calc-alkaline to K-rich calc-alkaline composition with initial stages of tholeiitic affinity (Rogers and Hawkesworth, 1989, Pichowiak, et al., 1990). La Negra was episodically intruded by several Jurassic and Lower Cretaceous calc-alkaline dioritic to granodioritic batholiths, stocks and conspicuous dike swarms (e.g., Marinovic et al., 1995, Dallmeyer et al., 1996, Maksaev, 2002). The main structural system developed during this period corresponds to the Atacama Fault System (AFS), which is a major margin-parallel sinistral strike-slip fault system that extends for more than 1,000 km along the Coastal Cordillera of northern Chile (Scheuber and Andriessen, 1990; Brown et al., 1993). Several authors describe sinistral followed by dextral arc-parallel strike-slip movements, caused by different configurations of oblique plate convergence (Scheuber et al., 1994; Scheuber and González, 1999; Grocott and Taylor, 2002). During the Early Cretaceous, transpression caused tectonic inversion of the former extensional back-arc basin (generating a foreland basin), and leading to essentially dextral and vertical displacements in pre-existing faults (Scheuber et al., 1994; Scheuber and González, 1999; Grocott and Taylor, 2002; Barra et al., 2017). This major structural system not only controlled magma ascent but also played a fundamental role in the emplacement of Cretaceous ore deposits (Barra et al., 2017).

Several types of mineral deposits were formed during the Upper Jurassic to Early Cretaceous in the Coastal Cordillera of northern Chile (between 21° and 33°S). These include stratabound Cu-(Ag), iron oxide-apatite (IOA), iron oxide-copper-gold (IOCG) deposits, and porphyry Cu deposits. Stratabound Cu-(Ag) deposits are hosted in dominantly Mesozoic volcano-sedimentary units in the western part of the Coastal Cordillera of north to north-central Chile. They have long been known as “Chilean Manto-type” or “Manto-type” deposits because of the broadly stratiform geometry of the Cu orebodies; however, veins and breccias are also common (Maksaev and Zentilli, 2002). These “Manto-type” deposits are divided into two main groups: those hosted by Jurassic volcanic-sedimentary sequences, i.e., La Negra Formation (Maksaev and Zentilli, 2002). Several deposits occur within this unit, among them Mantos Blancos, Mantos de la Luna, Santo Domingo, Buena Esperanza, Michilla, Las Luces and Mantos del Pacífico (Fig. 2). In these deposits, the Cu mineralization generally exhibits epigenetic features and occurs preferentially in permeable strata filling vesicles, disseminated and/or in veinlets and breccias (Kojima et al., 2003). In general, the hypogene sulfide paragenesis consists of chalcocite, digenite, bornite and

chalcopyrite that can contain “invisible” Ag (Kojima et al., 2003; Reich et al., 2009). Supergene mineralization consists of Ag-bearing chalcocite and covellite, and Cu oxide minerals such as atacamite, chrysocolla and Cu carbonates (Reich et al., 2009).

The second group is hosted by Lower Cretaceous volcanic and volcano-sedimentary rocks (Zentilli et al. 1997; Wilson and Zentilli 1999; Makshev et al., 2007; Kojima et al., 2009). A unique and unusual feature of these deposits is the intimate association of Cu sulfides with organic matter (migrated and/or residual petroleum) that is hosted in lavas, subvolcanic intrusive bodies and pyroclastic levels (Mayer and Fontboté, 1990; Zentilli et al., 1994; Zentilli et al., 1997; Wilson and Zentilli, 1999; Boric et al., 2002; Haggan et al., 2003; Wilson et al., 2003a,b; Wilson and Zentilli, 2006; Cucurella et al., 2005; Cisternas and Hermosilla, 2006; Rieger et al., 2008; Carrillo-Rosúa et al., 2014). The most important deposits of this group are the world-class El Soldado deposit north of Santiago, and the Melipilla-Naltahua and Lo Aguirre deposits, west of Santiago in Central Chile (Fig. 2). In northern Chile, deposits classified within this group occur near La Serena (e.g., Talcuna and Uchumí) and Copiapó (e.g., Manto Cobrizo, La Culebra) (Fig. 2). In general, sulfide mineral assemblages comprise a paragenesis of pyrite, chalcopyrite, bornite and chalcocite, where pyrite occasionally exhibits different textures including framboidal and rosette-like textures. Early mineralization (pyrite, chalcopyrite and bornite) can be partially replaced by Cu sulfides (Wilson et al., 1999). Bitumen and pyrobitumen are abundant in these deposits, and historically, organic matter has been reported to occur exclusively in the Lower Cretaceous deposits. However, and as a result of this research, pyrobitumen was reported for the first time in the Upper Jurassic deposit of Lorena in the Las Luces district (see Chapter 2).

Two main events of hypogene mineralization have been identified in bitumen-bearing stratabound Cu-(Ag) deposits in Chile, i.e., a pre-ore and a main Cu ore stage. These two stages were followed by a late supergene stage. The pre-ore stage is characterized by a pyrite-pyrobitumen assemblage with minor chalcopyrite and hematite (Wilson et al., 1999). The main Cu stage is characterized by a chalcopyrite-bornite-chalcocite assemblage with or without pyrobitumen (Wilson et al., 1999; Cisternas and Hermosilla, 2006). Late supergene minerals often include chrysocolla, covellite-djurleite aggregates with minor azurite and malachite. In general, a widespread but moderate Na-Ca metasomatism (chlorite, epidote and albite) is recognized, and calcite is present in late-stage veinlets. Low-grade metamorphic minerals (zeolite-prehnite-pumpellyite) are intimately associated with sulfides in amygdales, although their genetic relation is not clear (Cisternas and Hermosilla, 2006).

Several genetic models have been proposed to explain the formation of stratabound Cu-(Ag) deposits including syngenetic to epigenetic models (e.g., Ruiz et al., 1965, 1971; Kojima et al., 2003). Local discordant structures and geochronological data indicate that the Cu orebodies were emplaced after the deposition of host rocks, favoring epigenetic models (Oliveros et al., 2008). Models involving intrusion-derived hydrothermal fluids have also been proposed, based on dike intrusions closely associated with primary Cu mineralization in stratabound deposits of Jurassic age, such as Buena Esperanza, Santo Domingo and Mantos Blancos (Definis, 1985; Espinoza et al., 1996; Ramírez et al., 2006). However, a clear relationship between Cu orebodies and intrusions has not been observed in Cretaceous deposits (Camus, 1990). Kojima et al. (2009) reported that uniform Pb isotope data range between values for spatially associated igneous and sedimentary host rocks, suggesting that metals were derived from the volcano-sedimentary host rocks, favoring a model that involves hydrothermal circulation, leaching and later concentration. The involvement

of a sedimentary component is also strongly suggested by the extremely negative sulfur isotope values of hypogene sulfides and light carbon isotope signatures of hydrothermal calcite (Wilson et al., 1999; Carrillo-Rosúa et al., 2014). In addition, high $^{87}\text{Sr}/^{86}\text{Sr}$ initial ratios of hydrothermal calcite from deposits located in the Tocopilla-Taltal area, suggest an influx of seawater or addition of marine carbonate (Kojima et al., 2009). Therefore, models involving interaction between host rocks and magmatically-derived fluids, basinal brines, and/or meteoric fluids are likely to explain the genesis of stratabound Cu-(Ag) deposits. A heat source was needed to enhance circulation of hydrothermal fluids within the host rocks units, and therefore deep-seated plutonic complexes and stocks could be regarded as the most probable heat source (Kojima et al., 2009).

1.3. RESEARCH OBJECTIVES AND HYPOTHESIS

The aim of this study was to determine the role of organic matter, present as residual petroleum (bitumen and/or pyrobitumen), in the genesis of Chilean stratabound Cu-(Ag) deposits. In particular, the main goal was to assess the role of organic matter as source of metals and ligands in these deposits, and potentially, as a transport agent during ore genesis. Further, in order to constrain the chemical and physicochemical conditions of hydrothermal fluids involved in these deposits, the pyrite-bitumen assemblage was inquired. To achieve these objectives, several bitumen-bearing deposits were studied within the Coastal Cordillera of central-northern Chile, specifically, the Lorena deposit in the Las Luces district, the Manto Cobrizo and La Culebra deposits in the Copiapó district, and the El Soldado deposit near Santiago.

The working hypothesis involves testing whether hydrocarbons in the studied deposits played an active role as an ore fluid providing metals and ligands, or played a passive role as a redox barrier inducing sulfide precipitation, or a combination of both. To test this hypothesis, it necessary to evaluate if bitumen and pyrobitumen contain appreciable amounts of metals of economic interest (e.g., Cu, Ag, Au) and ligands (Cl, S). In addition, the speciation of those components in the organic phases needs to be determined to obtain information about the source of elements. In turn, detailed geochemical and isotopic data of the associated sulfides, particularly pyrite, is fundamental to test the mechanisms of ore precipitation, as well as the source of metals and sulfur. Overall, the data allow testing the hypothesis that a sedimentary component was involved in the genesis of stratabound Cu-(Ag) deposits.

1.4. METHODOLOGY

Samples were collected from stratabound Cu-(Ag) deposits in the Copiapó district (Manto Cobrizo and La Culebra) during two fields campaigns in the summer of 2017 and 2018. Samples from the Lorena deposit in the Las Luces district near Taltal were collected during a field trip in the spring of 2016. Sampling in all deposits was focused on the orebodies where bitumen was present. Representatives drill cores were selected and sampling strategy involved selecting samples where bitumen was present accompanied by Cu-Fe sulfides, also in sections where bitumen was not

related to sulfides. Additional samples were taken from mine workings in all deposits. Bitumen-bearing samples from El Soldado deposit were obtained from the personal collection of Professor Marcos Zentilli at Dalhousie University in Halifax, Canada.

All samples were photographed, scanned and inspected under a binocular microscope to select the most representative for thin section preparation. Over 80 polished thin sections were prepared for examination under transmitted and reflected light microscopy. Sulfides, pyrobitumen and alteration minerals were studied to construct a paragenetic sequence for the studied deposits.

Characterization of the pyrobitumen-sulfide assemblages in the studied deposits was achieved using a combination of different techniques. Imaging and micro-textural observations of pyrobitumen and sulfide samples were performed at the Andean Geothermal Center of Excellence (CEGA), Department of Geology, Universidad de Chile, Santiago using a FEI Quanta 250 scanning electron microscope (SEM). High resolution imaging of micro- to nano-scale particles in sulfides and pyrobitumen was achieved using field-emission scanning electron microscopy (FE-SEM) at the Center for Research in Nanotechnology and Advance Materials (CIEN), Pontificia Universidad Católica de Chile, Santiago. The chemical composition of major and minor elements in pyrite and pyrobitumen was determined in two analytical sessions. The first session was carried out using a JEOL JXA-8500F microprobe at the Peter Hooper GeoAnalytical Laboratory, Washington State University, Pullman, USA, and the second by using a JEOL JXA-8230 microprobe at the LAMARX Laboratory of the Universidad Nacional de Córdoba, Argentina.

Trace element concentrations in pyrite associated with pyrobitumen were determined by laser ablation inductively coupled mass spectrometry (LA-ICP-MS). LA-ICP-MS analyses were undertaken using a 193 nm ArF excimer laser (Teledyne-Photon Machines Analyte 193) coupled to a quadrupole ICP-MS (Thermo Fisher Scientific iCAP Q) at the Mass Spectrometry Laboratory of the Andean Geothermal Center of Excellence (CEGA), Department of Geology, Universidad de Chile. In-situ sulfur isotope analysis of pyrite were carried out by secondary-ion mass spectrometry (SIMS). These analyses were conducted using a CAMECA IMS1280 large-geometry ion microprobe at Centre for Microscopy, Characterisation and Analysis (CMCA) of The University of Western Australia, Perth.

Spectroscopic techniques were used to constrain the elemental distribution in pyrobitumen, as well as the speciation of sulfur within the same material. X-ray fluorescence microanalysis (μ -XRF) of bitumen-bearing samples was performed at CSIRO Mineral Resources, Perth, Australia using a Bruker Tornado XRF desktop instrument. Elemental maps obtained using this technique allowed visualization of chemical variations and relative abundances of major and few minor elements in the studied samples. Synchrotron X-ray fluorescence (S-XRF) analyses were performed at the XRF beamline of the Brazilian Synchrotron Light Laboratory (LNLS), Campinas, Brazil. These data allowed acquiring elemental maps of pyrobitumen at the micrometric scale. Finally, X-ray absorption near edge structure spectroscopy (XANES) was used to obtain chemical information of sulfur speciation in pyrobitumen samples.

1.5. PREVIOUS STUDIES

Chilean stratabound Cu-(Ag) deposits have been extensively studied over the years, with several authors proposing different models to explain the genesis of these deposits. For example, stratiform orebodies were first regarded as syngenetic volcanic exhalative (Ruiz et al., 1965). Sato (1984) described the general features of these Chilean stratabound Cu-(Ag) deposits indicating that the mineralization is hosted in amigdoidal lava flows and volcanoclastic sequences. In addition, he proposed that the mineralizing fluids could have been sourced from dehydration reactions related to burial metamorphism of the host rocks. Palacios (1990) supported an intimate relation between the hydrothermal and the extrusive magmatic activity at the Buena Esperanza stratabound deposit. Later, Vivallo and Henríquez (1998) studied some deposits from the Coastal Range in northern Chile, including Buena Esperanza, and concluded that their origin could be associated with magmatic-hydrothermal fluids sourced from mid-to-late Jurassic granitoids. Ramírez et al. (2006, 2008) proposed that the emplacement of dioritic and granodioritic porphyries during the early Cretaceous was related to the major hypogene copper sulfide mineralization at Mantos Blancos, supporting the hypothesis of hydrothermal activity related to magmatic intrusions. On the other hand, Makshev and Zentilli (2002) suggested that mineralization was produced by mixing of fluids of different origin. Kojima et al. (2009) provided a review summarizing the general aspects of these deposits, and suggested an epigenetic model with hydrothermal fluids dominating over basinal brines and meteoric waters. The interaction of mixed fluids with volcanic host rocks led to leaching of metals, and protracted hydrothermal fluid circulation was probably sustained by heat provided from deep plutonic complexes. Additional studies on stratabound Cu-(Ag) deposits have been conducted by Kojima et al. (2003), Tosdal and Munizaga (2003), Tristán-Aguilera et al. (2006), Oliveros et al. (2008), Reich et al. (2010, 2013) and Barra et al. (2017). Despite these advances, relatively few studies have focused on the role of organic matter in stratabound Cu-(Ag) deposits where pyrobitumen is present. A brief description of those studies are provided below.

Early studies by Zentilli et al. (1994, 1997) are considered seminal works because they are the first documentation of the textural relationship between pyrobitumen and Cu sulfides in the El Soldado deposit. These studies suggested that pyrobitumen represented liquid petroleum that present before and during the Cu mineralization event. Later, Wilson (1999) and Wilson and Zentilli (2003a, 2003b) carried out a detailed study of the organic matter at El Soldado, concluding that the formation of the deposit was the result of two main events, i.e., a Stage I or pre-ore event, and a Stage II or ore event. The pre-ore stage was dominated by biogenic pyrite framboids, spheroids and euhedral grains, which formed within and around semi-solid petroleum at low temperatures. Later, hydrothermal solutions introduced Cu into the system, replacing the earlier pyrite and the pyrobitumen, and forming the ore stage Cu sulfide paragenesis. The authors also concluded that pyrobitumen was an essential component in its formation, e.g., pyrobitumen acted as activated carbon, destabilizing CuCl complexes and thus precipitating Cu sulfides. Also, the sulfur isotope composition of pyrite revealed that pyrite from Stage I was formed by bacterial sulfate reduction. These authors also carried out studies in organic petrology, chemical composition and reflectance analysis of pyrobitumen. Boric (2002) suggested that pyrobitumen in El Soldado could promote the growth of pyrite grains and act as a reductant of oxidized Cu-rich solutions. The author also indicated that other paleo-petroleum reservoirs within the Early Cretaceous basin could be a locus for mineralization.

Cisternas (1999), Haggan et al. (2003) and Cisternas and Hermosilla (2006) studied different deposits in the Copiapó area where residual petroleum is associated with Cu-(Ag) mineralization. These studies indicate two distinct hydrothermal ore-forming events, similar to those described at El Soldado: (a) an early Fe-rich stage associated with the migration and emplacement of oil and the formation of pyrite, and (b) a late Cu-rich stage, where the organic matter induced reduction and Cu sulfide precipitation. This is in agreement with Wilson (1999) and Wilson and Zentilli (2003a, 2003b), although Cisternas and Hermosilla (2006) suggested a magmatic sulfur source for pyrite.

Rieger et al. (2008) performed hydrocarbon biomarkers in pyrobitumen from stratabound Cu-(Ag) deposits localized near the Copiapó area. Biomarker hydrocarbon analysis revealed a predominantly bacterial origin with minor contributions from phytoplankton and higher plants, which were deposited in a shallow marine environment. The authors also reported the presence of alkylated benzonaphthol- and dinaphthothiophenes suggesting that high sulfur concentrations in the hydrothermal fluids led to aromatization of the organic compounds.

Carrillo et al. (2014) presented a detailed stable isotope study in Fe-(Cu) sulfides for bitumen-bearing stratabound Cu-(Ag) deposits near Santiago and La Serena. These analyses revealed a wide range for $\delta^{34}\text{S}$ values, from -50 to $+14.3\%$, which were interpreted as a polygenic sulfur source for these deposits. Carrillo et al. (2014) also proposed a two-stage evolution model for the deposits, similar to the ones described above: 1) A pre-ore stage of framboidal pyrite growth, formed by bacterial sulfate reduction in an open system, and with diagenetic degradation of oil-related brines, followed by a Cu-bearing stage, where framboidal pyrite was replaced by Cu-sulfides.

1.6. PUBLICATIONS RESULTING FROM THIS RESEARCH

Publications

1. Herazo (2020) - Herazo, A.; Reich, M.; Barra, F.; Morata, D.; del Real, I.; Pages, A. Assessing the role of bitumen in the formation of stratabound Cu-(Ag) deposits: Insights from the Lorena deposit, Las Luces district, northern Chile". *Ore Geology Reviews*, 2020, 124, 103639. (Chapter 2)
2. Herazo (2021) - Herazo, A.; Reich, M.; Barra, F.; Morata, D.; del Real, I. Trace element geochemistry of pyrite from bitumen-bearing stratabound Cu-(Ag) deposits, northern Chile. *ACS Earth and Space Chemistry*. <https://dx.doi.org/10.1021/acsearthspacechem.0c00321>. (Chapter 3)
3. Herazo (2021) - (to be submitted). Sulfur isotope and trace element signature from bitumen-bearing stratabound Cu-(Ag) deposits, northern Chile: Implications for fluid source and mineralization processes. (Chapter 4)

Conference abstracts

1. Herazo, A., Reich, M., Barra, F., Morata, D., 2019. Bitumen as a source of sulfur in the Lorena stratabound Cu-(Ag) deposit, northern Chile. Society of Economic Geologists (SEG) Conference, Santiago, Chile, October 7–10, 2019.
2. Herazo, A., Reich, M., Barra, F., Morata, D., 2018. Bitumen-bearing stratabound Cu-(Ag) deposits in northern-central Chile: An active role for liquid hydrocarbons? Society of Economic Geologists (SEG) Conference, Keystone, Colorado, USA, September 22–25, 2018.
3. Herazo, A., Reich, M., Barra, F., Morata, D., 2018. Reassessing the role of organic matter in Chilean stratabound Cu-(Ag) deposits. Congreso Geológico Chileno, Concepción, Chile, November 18–23, 2018.
4. Herazo, A., Reich, M., Barra, F., Morata, D., 2017. Reassessing the role of organic matter on metal transport and deposition in Chilean stratabound Cu deposits. Goldschmidt Conference, Paris, France, August 13–18, 2017.

CHAPTER 2

Assessing the role of bitumen in the formation of stratabound Cu-(Ag) deposits: Insights from the Lorena deposit, Las Luces district, northern Chile

Andrea Herazo^{1,2*}, Martin Reich^{1,2}, Fernando Barra^{1,2}, Diego Morata^{1,2}, Irene del Real^{1,2}, Anais Pagès³

¹ Department of Geology and Andean Geothermal Center of Excellence (CEGA), FCFM, Universidad de Chile, Plaza Ercilla 803, Santiago, Chile

² Millennium Nucleus for Metal Tracing Along Subduction, FCFM, Universidad de Chile, Santiago, Chile.

³ Department of Water and Environmental regulation, Joondalup, Western Australia.

Published in: Ore Geology
Reviews

Corresponding author: Andrea Herazo
andrea.herazo@ug.uchile.cl

ABSTRACT

Stratabound Cu-(Ag) deposits located in north-central Chile have been grouped into two NS parallel belts according to the age of their volcanic and volcanoclastic host rocks. Deposits from the Cretaceous belt are characterized by an unusual assemblage of Cu sulfides with migrated hydrocarbons, whereas the presence of organic matter has not yet been recognized in deposits from the Jurassic belt. Here we report the first evidence of pyrobitumen in a Jurassic stratabound Cu-(Ag) deposit and evaluate its role in ore formation. We present a micro-analytical study of pyrobitumen associated with Cu-(Fe) sulfides in the Lorena deposit, located in northern Chile. Our approach involved a combination of surface and drill core sample characterization, (FE)-SEM observations, EMPA and μ -XRF mapping of pyrobitumen. In addition, we determined the speciation of sulfur in pyrobitumen by using synchrotron μ -XANES. Two main events of hypogene mineralization were identified at Lorena deposit, i.e., a pre-ore and a main Cu ore stage. The pre-ore stage is characterized by globularly-shaped pyrobitumen and minor pyrite, and a widespread albite alteration of the andesite host rock. Pre-ore pyrite was replaced by chalcopyrite, bornite and chalcocite, providing evidence for a late Cu inception. In the main Cu ore stage, chalcocite is often associated with sharp-edged, angular pyrobitumen, most likely indicating remobilization or a later pulse of hydrocarbons. EMPA data show that pyrobitumen at Lorena is enriched in Fe (0.02 – 1.74 wt.%), Cu (0.02 – 0.87 wt.%), S (0.01 – 0.43 wt.%) and Cl (0.01 – 0.4 wt.%). Other elements

detected include V, Co, Ni, Cr, Sb, As, Ag and Au. Both Ag and Au were only detected in a few spots, with Au reaching up to 600 ppm. Desktop and synchrotron μ -XRF mapping shows that S is homogeneously distributed within pyrobitumen, with lower S concentrations observed at grain rims. On the other hand, EMPA-WDS X-ray maps show that Cu precipitated on pyrobitumen grain surfaces, filling fractures and forming veinlets. In addition, textures showing the presence of micro- to nano-sized pyrobitumen inclusions within both pre-ore pyrite and main ore chalcocite grains point, unequivocally, to the interaction of hydrothermal fluids with hydrocarbons during the formation of this deposit. The high S concentrations measured in pyrobitumen and the presence of organosulfur compounds detected by μ -XANES can be attributed to an organic source. The pre-ore assemblage is interpreted as formed from a petroleum-aqueous fluid (connate waters?) mixture that migrated from the sedimentary source rock into the Jurassic host rocks where pyrite and pyrobitumen precipitated in the andesite. Late Cu-bearing hydrothermal fluids interacted with this pyrobitumen-pyrite assemblage to form Cu sulfides, either by replacement of pyrite or precipitation. We conclude that some of the S contained in pyrobitumen could have been released during interaction with the Cu-bearing hydrothermal fluid contributing, at least partially, to the S budget required for sulfide mineralization in the main ore stage. Our results provide evidence supporting pyrobitumen-fluid interaction as a key process in the formation of the Lorena deposit and possibly other stratabound Cu-(Ag) deposits in Chile.

Keywords: stratabound Cu-(Ag) deposits, Manto-type, pyrobitumen, hydrocarbons, Cu sulfides, Lorena deposit, Chile.

2.1. INTRODUCTION

Over the past decades, several studies have recognized that organic matter can have a crucial role in the formation of mineral deposits (Mossman et al., 1993; Rob and Meyer, 1995; Large et al., 2011). The close spatial association between ore mineralization and solid oil residues or bitumen has been commonly interpreted to be either coincidental or to provide evidence for redox-induced ore precipitation by interaction of metal-bearing fluids with organic matter (Parnell, 1988; Anderson, 1991; Spirakis, 1996; Sun and Püttmann, 2000; Cuney, 2009; Pfaff et al., 2010; Large et al., 2011). However, recent studies have provided evidence that liquid hydrocarbons or crude oil can play a more active role during ore genesis by transporting metals and ligands from its source to the site of ore deposition (Migdisov et al., 2017; Saintilan et al., 2019). It is well known that trace metals (V, Ni, Zn, Au, U) and ligands (S, Cl, I) can be concentrated in different organic materials derived from sediments during diagenesis. These include liquid and solid hydrocarbons such as crude oil and (pyro)bitumen, respectively, in which reported U, V, Ni, Fe, Zn and Au contents can reach economic concentrations (Colombo and Sironi, 1961; Colombo et al., 1964; Hitchon et al., 1975; Jones et al., 1975; Ellrich et al., 1985; Mastalerz and Glikson, 2000; Lo Mónaco et al., 2007; Fuchs et al., 2016). Furthermore, recent experimental data have shown that Zn, Au, U can be solubilized in crude oils under different temperature conditions (Migdisov et al., 2017), and studies in Pb-Zn sediment-hosted deposits suggest that crude oil or petroleum could not only provide metals but also supply reduced sulfur for metal sulfide precipitation (e.g., Laisvall deposit, Sweden, Saintilan et al., 2019). These investigations provided evidence of the potential role of liquid hydrocarbons in ore formation, highlighting that it could be more relevant than previously thought.

Despite these advances, two fundamental questions remain unanswered. The first relates to the relative timing of liquid hydrocarbon introduction into the ore system with respect to hydrothermal fluid circulation. This issue is critical in order to evaluate if the organic phase can act as a viable source of metals and ligands, or if it plays only a passive role as a reducing agent of dissolved species transported by the hydrothermal fluid. The second question deals with the absolute concentrations of trace metals that are present in liquid and solid hydrocarbons. Evidence is generally scarce and with the exception of a few studies (e.g., Jones, 1975; Ali et al., 1983; Wilson and Zentilli, 1999; Fuchs et al., 2016, Wu et al., 2020), the metal concentrations in organic phases remain mostly unconstrained. In addition, it is uncertain whether the organic phase retains its original metal load during interaction with hydrothermal ore fluids (Crede et al., 2019) or if hydrocarbons acquire metals as a result of this interaction. Within this perspective, hydrocarbons formed from a sedimentary rock could transport not only dissolved metals but also ligands such as sulfur (Lewan, 1984; Watkinson, 2007; Khuhawar et al., 2012), and later migrate through permeable rocks or favorable structural zones to shallower reservoir rocks where they can precipitate sulfide minerals. Alternatively, hydrocarbons could act as a geochemical trap for Cu-bearing aqueous hydrothermal fluids and Cu sulfides are precipitated as a result of changes in redox conditions.

The stratabound Cu-(Ag) deposits of northern and central Chile provide an ideal example to investigate some of the issues mentioned above. These deposits, also known as “Manto-type”, represent the third most important source of copper in Chile after porphyry Cu and iron oxide-copper-gold (IOCG) deposits, and can also contain economic levels of silver (Maksaev et al., 2007; Reich et al., 2010; 2013). Most importantly, several studies have recognized the association of Cu-(Fe) sulfides and sulfosalts with solid hydrocarbons or bitumen within “Manto-type” deposits of Cretaceous age in central Chile (Mayer and Fontboté, 1990; Zentilli et al., 1997; Wilson and Zentilli, 1999; Wilson et al., 2003a, b; Cisternas and Hermosilla, 2006; Rieger et al., 2008; Carrillo-Rosúa et al., 2014). These studies have shown that solid hydrocarbons, referred loosely as “organic matter”, “carbon” or “bitumen”, are morphologically and chemically complex structures.

Petroleum fluids are a mixture of organic molecules of different molar mass and structure that vary from a gaseous to liquid state. Kerogen is the main precursor in petroleum generation and is defined as insoluble (in organic solvents) sedimentary organic matter derived from plants and other biomass (e.g., bacteria, animals). During early stages of burial, kerogen is subject to microbial activity to form methane at temperature between 10°C up to 60 – 80°C. At greater depths and temperatures (usually >100°C), thermal dissociation (“cracking”) and disproportionation leads to the formation of liquid hydrocarbons (i.e., crude oil) and thermal gas. Another precursor is soluble organic matter (bitumen). Bitumen is mainly generated from kerogen and includes oil, but also heavier, tar-like products. If this bitumen is thermally affected, it transforms into gas and a solid residue, ultimately methane and pyrobitumen (Gaupp et al., 2008). By focusing on the inorganic chemistry of pyrobitumen, we intend to obtain information that is essential to understand the role of hydrocarbons in the ore-forming process.

In this study, we present the results of a mineralogical and geochemical study of pyrobitumen from the Jurassic Lorena stratabound Cu-(Ag) deposit, Las Luces district, northern Chile. The presence of pyrobitumen has not been previously recognized in the Jurassic belt. Hence, its specific role in processes leading to Cu mineralization remains unaccounted. We combined detailed surface and drill core sample characterization and micro-textural observations with elemental data and chemical mapping of pyrobitumen obtained using electron microprobe and microscopic X-ray

fluorescence analyses. In addition, we explored the speciation of sulfur in pyrobitumen using synchrotron-based spectroscopic techniques. The acquired data constrain the sources of metals and sulfur at Lorena and provide new insights into the role of hydrocarbons during the formation of stratabound Cu-(Ag) deposits in the Coastal Cordillera of northern Chile.

2.2. GEOLOGIC BACKGROUND

2.2.1. Upper Jurassic and Lower Cretaceous stratabound Cu-(Ag) deposits

Stratabound or “Manto-type” Cu-(Ag) deposits occur along the Coastal Cordillera of northern and central Chile (Fig. 3), and are hosted by Upper Jurassic or Lower Cretaceous volcanic and volcano-sedimentary rocks. In the Coastal Cordillera of northern Chile, the deposits are spatially associated with the NS-trending Atacama Fault System (AFS), which played a fundamental role in the formation of the Jurassic-Cretaceous metallogenic belt (Barra et al., 2017 and references therein). Two groups of stratabound Cu-(Ag) deposits occur along the Coastal Cordillera of northern-central Chile. The first group in northern Chile (e.g., Mantos Blancos, Michilla, Buena Esperanza, Las Luces) is hosted by the Jurassic La Negra Formation, a 7000 m thick volcanic and volcanoclastic sequence. The second group of deposits, located in central Chile (e.g., El Soldado, Talcuna, Uchumi), is hosted by Lower Cretaceous volcanic and volcano-sedimentary rocks (Zentilli et al. 1997; Wilson and Zentilli 1999; Makshev et al., 2007; Kojima et al., 2009).

Sulfide mineralization in stratabound Cu-(Ag) deposits comprise mainly bornite, chalcocite, chalcopyrite, and minor pyrite, covellite and djurlerite (Espinoza et al., 1996; Kojima et al., 2009; Barra et al., 2017). Orebodies are structurally and stratigraphically controlled and are dominated by breccias, veins and stratiform lenses or “mantos”. Hydrothermal alteration is represented by selective sodic alteration of plagioclase, weak calcium metasomatism and abundant hematite. A more detailed description of both the Jurassic and Cretaceous belt can be found in Makshev and Zentilli (2002), Makshev et al. (2007) and Kojima et al. (2009).

Deposits hosted by Lower Cretaceous volcanic rocks are unique due to their unusual association of Cu sulfides with migrated hydrocarbons hosted in lavas, subvolcanic intrusive bodies and pyroclastic units (Mayer and Fontboté, 1990; Zentilli et al., 1994; Zentilli et al., 1997; Wilson and Zentilli, 1999; Boric et al., 2002; Haggan et al., 2003; Wilson et al., 2003a,b; Wilson and Zentilli, 2006; Cucurella et al., 2005; Cisternas and Hermosilla, 2006; Rieger et al., 2008; Carrillo-Rosúa et al., 2014). In these deposits, hydrocarbons occur as pyrobitumen. The most notable example within this metallogenic belt is the El Soldado deposit in central Chile (Wilson and Zentilli, 1999; Wilson et al., 2003a, b), where pyrobitumen is found in close association with Cu minerals. Other pyrobitumen-bearing deposits of inferred Cretaceous age have been reported near the cities of Copiapó (e.g., Manto Cobrizo, La Culebra; Cisternas and Hermosilla, 2006), La Serena (e.g., Talcuna, Uchumi; Wilson and Zentilli, 2006), and Santiago (e.g., Melipilla-Naltahua; Carrillo-Rosúa et al., 2014, Lo Aguirre; Saric et al., 2003) (Fig. 3). The reconnaissance of an intimate spatial association of pyrobitumen and Cu mineralization has been considered by the cited authors as a key factor in the genesis of some of the Lower Cretaceous stratabound Cu-(Ag) deposits. In contrast, no pyrobitumen has been reported in the deposits hosted by the Jurassic La Negra Formation in the Coastal Cordillera of northern Chile.

2.2.2. The Lorena stratabound Cu-(Ag) deposit

The Lorena deposit (~200,000 metric tons @ ~1.5 % Cu sulfide; ~300,000 metric tons @ 0.9 % Cu oxide) forms part of the Las Luces district, near Taltal in the Antofagasta region of northern Chile (Fig. 4A). The Las Luces deposit, as a reference, has current resources estimated at 2.3 Mt with 1.11% Cu (Zamora, 2011). In the Las Luces district, the volcanic rocks of La Negra Formation are represented by basaltic andesite and andesite lava flows, volcanoclastic layers and minor volcanic breccias (Fig. 4B). The sequence forms a monocline fold with a NE trend and variable dip between 12° – 25° SE (Zamora, 2011). Jurassic volcanic rocks from the Posada de los Hidalgos Formation are present in the southwest part of the study area. Older Paleozoic metasedimentary rocks of the Las Tórtolas Formation and Early Jurassic (Hettangian to Sinemurian) marine sedimentary rocks from the Pan de Azúcar Formation (Naranjo, 1978; Ulriksen, 1979; Naranjo and Puig, 1984) outcrop in the western part of the district (Fig. 4B). La Negra Formation is intruded by several mafic to felsic stocks and dikes of Early Jurassic to Lower Cretaceous age that vary in composition from gabbro to diorite and granodiorite, with scarce tonalite and granites (e.g., Matancilla Plutonic Group, Naranjo and Puig, 1984). Geochronological data indicate that the emplacement of the plutonic bodies occurred mainly during two periods, i.e., 190 – 173 Ma and 160 – 142 Ma (Pichowiak et al., 1990; Boric et al., 1990; Scheuber and Gonzalez, 1999; Oliveros et al., 2006, 2008). La Negra Formation overlies marine sediments, continental deposits or metapelitic rocks of the Cifuncho Formation (Garcia, 1967; Pichowiak, 1990) (Fig. 4B). Overlying the volcanic rocks of La Negra is the Lower Cretaceous Aeropuerto Formation, which comprises porphyritic andesites intercalated with andesitic tuffs and breccias, conglomerates, sandstones and fossiliferous limestones (Naranjo and Puig, 1984; Boric et al., 1990). In the study area, the Aeropuerto Formation is completely covered by the unconsolidated Atacama Gravels of Oligocene to Miocene age (Fig. 3B).

The basaltic andesite to andesite rocks of the La Negra Formation, which host the Cu mineralization at Lorena, exhibit mainly a porphyritic texture with large plagioclase and pyroxene phenocrysts (~1 – 2 cm). Amygdaloidal and aphanitic textures are also recognized. The matrix is mostly intersectoral with plagioclase and pyroxene microliths, and disseminated magnetite. The deposit is both structurally and stratigraphically controlled, and the sulfide-pyrobitumen mineralization is mostly found in breccias and “mantos”. The main structural feature in the deposit is a NW-trending fault. Near this fault, the andesite is affected by pervasive albitization, with pyrobitumen within the albite-chlorite-hematite matrix. Additionally, post-mineralization mafic sills of diorite-gabbroic composition cross-cut the volcanic host rock sequence.

At Lorena, the Cu-(Fe) sulfide mineralization occurs in breccias, fractures, veins or vesicle-fillings (Fig. 5A-D). The ore mineral assemblage comprises chalcocite-bornite with minor chalcopyrite, pyrite and late digenite, covellite, chrysocolla and malachite. Pyrobitumen is observed filling mm- to cm-sized vesicles (Fig. 5A, B), and is intimately associated with Cu sulfides (Fig. 5B, C) and very low-grade metamorphic mineral assemblages (zeolite-prehnite-pumpellyite). Pyrobitumen also occurs as mm- to cm-sized granular aggregates and fracture fillings (Fig. 5C, D). Moderate calcic and sodic metasomatism (chlorite, epidote and albite) is also recognized and calcite is present in late-stage veinlets. A detailed description of the mineral paragenesis is presented in the Results section.

2.3. SAMPLES AND METHODS

One representative ~300 m long sub-vertical drill core from the Lorena deposit was selected for this study (drill core DDH15LO-05, 312 m; Fig. 4C). Thirty-four representative samples were obtained from this drill core, and twenty-six polished thin sections were selected for optical inspection using reflected and transmitted light microscopy. Sample selection was focused on the presence of pyrobitumen associated with sulfides. Characterization of the pyrobitumen-bearing sulfide assemblage at Lorena was achieved using a combination of imaging, microanalytical and spectroscopic techniques.

2.3.1. Scanning electron microscope (SEM)

Scanning electron microscopy (SEM) observations were performed at the Andean Geothermal Center of Excellence (CEGA), Universidad de Chile, Santiago, Chile using a FEI Quanta 250 SEM equipped with secondary electron (SE), backscattered electron (BSE) and X-ray energy-dispersive spectrometry (EDS) detectors. The analytical parameters were: accelerating voltage of 15 – 20 kV, filament current ~80 μ A, beam intensity of 1 nA, takeoff angle ~35°, a spot size of 4 – 5 μ m in diameter, and a working distance of ~10 mm. The INCA software was used for measurements and data processing. Semi-quantitative EDS analyses were used to constrain major elements in individual mineral phases and pyrobitumen. The EDS operating conditions were 20 keV, a spot size of 1 – 3 μ m and a working distance of 10 – 18 mm. High-resolution imaging of micro- to nano-sized inclusions in sulfides and pyrobitumen was achieved using field-emission scanning electron microscopy (FE-SEM). Observations were performed using a FEI Quanta 250 FEG instrument at the Center for Research in Nanotechnology and Advanced Materials (CIEN) at the Pontificia Universidad Católica de Chile, Santiago, Chile. The FE-SEM is equipped with in-column detector (ICD) for SE and BSE, and an EDS detector. Operating conditions included an accelerating voltage of 20 kV, the beam spot size was ~4 μ m in diameter, takeoff angle ~35 – 37°, live time was 45 s, and a working distance of ~10 mm.

The chemical composition of minor elements in pyrobitumen was determined in two analytical sessions performed at different electron microprobe laboratories. The first session was carried out using a JEOL JXA-8500F microprobe at the Peter Hooper GeoAnalytical Laboratory, Washington State University, Pullman, USA, and the second by using a JEOL JXA-8230 microprobe at the LAMARX Laboratory of the Universidad Nacional de Córdoba, Argentina. The same operating conditions were set in both instruments and included an accelerating voltage of 20 kV, a beam current of 10 nA and a 10 μ m beam. Evidence of beam damage of pyrobitumen grains was checked systematically between analyses. No pyrobitumen disturbance due to electron beam irradiation was noted. Calibration was achieved by using natural and synthetic standards and included YVO₄ (for V), FeCr₂O₄ (for Cr), FeS₂ (for Fe), Co⁰ (for Co), (Ni,Fe)₉S₈ for (Ni), FeAsS (for S and As), Sb₂S₃ (for Sb), AgI (for I), KCl (for Cl), Ag⁰ (for Ag), Au⁰ (for Au) and U₃O₈ (for U). Counting time (peak) was 10 s for Fe K α , Ni K α , Cu K α , S K α , Cl K α ; 15 s for V K α , Cr K α , Co K α , U K α 20 s for Ag L α , 25 s for I L α , 30 s for Sb L α , Au M α , and 60 s for Sb L α . The half (peak) counting time was used for total background readings. Mean detection limits ranged from 0.01 to 0.03 wt.% for most analyzed elements.

2.3.2. XRF elemental mapping

Micro X-ray fluorescence (μ -XRF) elemental mapping of pyrobitumen-bearing samples was performed at CSIRO Mineral Resources, Perth, Australia using a Bruker Tornado XRF desktop instrument equipped with a rhodium target X-ray tube operating at 50 kV and 500 nA without filters and an XFlash® silicon drift X-ray detector. Beam diameter and point spacing of 40 μm was used for optimal map resolution, with dwell times varying from 3 to 10 ms depending on sample size. The elemental maps allowed visualization of the spatial variations in relative abundances of major and a few minor elements (S, Fe, Cu and V).

Synchrotron X-ray fluorescence (S-XRF) mapping of selected pyrobitumen grains was performed at the XRF beamline of the Brazilian Synchrotron Light Laboratory (LNLS), Campinas, Brazil. The XRF source is a 1.67 T bending magnet. The beamline has a flux density of 2×10^8 photons/s/mm²/100 mA, and is equipped to cover an energy range of 5 to 20 keV, producing a highly focused microbeam of $22 \times 12 \mu\text{m}$. The excitation of the samples deposited on Si (111) layers was performed using synchrotron radiation of a beam operating at 16.5 keV. The fluorescence radiation was recorded by a Si(Li) detector with energy resolution of 165 eV at 5.9 keV, and the detector was placed at a 90° angle from the incident beam (Pérez et al., 1999). The irradiation time was 100 s. All measurements were performed in duplicate. Filters were used to attenuate effects of the matrix, atmosphere, detector and beam. Calibration was performed by using the NIST 612 reference material, which contains four major components (SiO₂, CaO, Na₂O, Al₂O₃) and twenty one elements (Co, Cu, Fe, Mn, Ni, Sr, Ti, K, Rb, Ba, Dy, Er, Nd, Ag, Ce, Eu, Gd, La, Pb, U, Yb). The standard was measured for 100 s. The obtained X-ray spectra were processed using the PyMca software in order to obtain the X-ray intensities for each element and the associated uncertainty.

2.3.3. Sulfur X-ray absorption near edge structure (XANES) spectroscopy

X-ray absorption near edge structure (XANES) was used to obtain chemical information of sulfur speciation in pyrobitumen (e.g., Pomerantz et al., 2014). Sulfur has six oxidation states that can be distinguished as peaks in the absorption spectrum within an X-ray energy window between 2470 and 2482 eV. In-situ XANES measurements of sulfur K-edge in pyrobitumen were recorded in fluorescence-yield mode at the SXS line of the Brazilian Synchrotron Light Laboratory (LNLS) in Campinas, Brazil. The beamline uses a high-flux beam ($\geq 4.5 \times 10^{11}$ photons/s/mm²/100 mA) that is equipped to achieve a focused 200 μm beam using toroidal mirrors, and can cover an energy range between 1 to 5 keV. Spectra were collected from 2430 to 2600 eV, with steps sizes of 0.2 eV at the S K-edge and 1 and 3 eV for the pre-and post-edge regions, using 1 s scan duration per energy step. The standard used for calibration was CaP (Bayovar). Chalcopyrite (CuFeS₂), sodium sulfite (Na₂SO₃) and gypsum (CaSO₄) powders were used as inorganic standards. These were diluted in boron nitrate at approximately <1 wt.% to minimize self-absorption. The diluted standards were transferred into a cup and sealed with 7.5 μm thick Kapton film before analysis in the X-ray source. XANES measurements were performed on thin sections with large pyrobitumen grains (mm-cm). Only isolated pyrobitumen grains were analyzed to avoid contamination by sulfide minerals. The spectra acquisition was carried out with the Amptek DPPMCA software. The data were analyzed by fitting the measured spectra to a linear combination of the model compounds and compared to sulfur K-edge XANES spectra for sulfur standards (Bolin et al., 2016; Annex A.1).

2.4. RESULTS

2.4.1. Variations with depth

Mineralization at the Lorena deposit comprises stratiform lenses (“mantos”), breccias, veins and disseminations hosted in basaltic andesite to andesitic rocks of the La Negra Formation (Fig. 5, 6).

Drill core DDH15LO-05 shows that the orebodies are mineralized layers or “mantos” interspersed with unaltered or “fresh” rock (Fig. 6). Based on lithological and mineralogical characteristics, the investigated drill core was divided into three main sections, i.e., shallow (0 – 98.6 m), intermediate (~98.6 – 167 m), and deep (167 – 312 m), where different pyrobitumens were identified: globular or rounded pyrobitumen (OM1), pyrobitumen inclusions (OM2) and angular pyrobitumen (OM3). The shallow or upper section is dominated by aphanitic andesite and hydrothermal breccias (Fig. 6A-B) with minor chrysocolla. No pyrobitumen or hypogene sulfide mineralization were observed in this section.

The middle section (~98.6 – 167 m) is characterized by a transition from the shallow aphanitic andesite to a vesicular and porphyritic andesite texture with sulfide mineralization. Mineralization is spread along this section and comprises pyrite, chalcopyrite as well as bornite with abundant chalcocite and minor covellite-digenite. The section is cross-cut by a barren microdiorite dike composed of abundant pyroxene and plagioclase. Pyrobitumen grains, which occur throughout this section (starting at ~98.6 m), range in size from a few tens of micrometers to a few centimeters. It is observed within the calcite/metamorphic minerals matrix, filling vesicles and fractures (Fig. 6C). Pyrobitumen in this section displays two distinct textures: globular (or rounded), and angular (or sharp-edged grains). Globular pyrobitumen (OM1) is dominant and occurs as disseminated, drop-shaped vesicle fillings of approximately 1 – 5 mm in size (Fig. 6D), although in some cases pyrobitumen fillings can reach cm-sizes (e.g., Fig. 5A). Globular pyrobitumen (OM1) is related to albite, calcite and minor chlorite in vesicles. Angular pyrobitumen (OM3), on the other hand, is mostly restricted to fractures where it is intimately associated with sulfides (pyrite, chalcopyrite and chalcocite) and magnetite (Fig. 6E, F).

The deep or lower section (~167 – 312 m) corresponds to the main part of the deposit. The host rock is a vesicular andesite with a porphyritic texture comprising >15% of plagioclase and minor pyroxenes. Sulfide minerals include pyrite, chalcopyrite and abundant chalcocite, which occur filling fractures, veins or vesicles. The highest Cu grades are found in breccias or near structures (mainly faults or fractures). Sulfides are associated with pyrobitumen, and usually form mineralized “mantos” up to ~15 m thick. Angular pyrobitumen (OM3) is the dominant textural type of pyrobitumen in this section and is often observed filling the center and/or coating the walls of large vesicles (Fig. 6E, F). Globular pyrobitumen (OM1) is also present as mm- to cm-sized aggregates, filling vesicles or fractures. Iron and Fe-Cu-bearing mineral inclusions occur within pyrobitumen, particularly at grain rims or filling both fractures and vesicles. Pyrobitumen (OM1 - OM3) is cross-cut by calcite and sulfides veinlets.

2.4.2. Hydrothermal alteration and mineralization

The dominant hydrothermal alteration type in the deposit is albitization with minor epidote, sericite, chlorite and abundant calcite (Fig. 7). Albitization is observed as a widespread pre-ore alteration event that affected the andesite host rock and locally, the breccia matrix. Albite occurs replacing primary plagioclase laths (Fig. 7A, B, E). Albitized plagioclase can be further altered to sericite (Fig. 7B). Chlorite was recognized replacing pyroxene phenocrysts. It was also observed associated with prehnite-pumpellyite-pyrobitumen and calcite, filling vesicles, fractures and veinlets (Fig. 7C, D). Zeolites, prehnite-pumpellyite, chlorite, calcite and minor chalcedony, as well as pyrobitumen, are found filling vesicles and in the breccia matrix. Calcite is dominant over chlorite and two forms were identified, i.e., small calcite crystals with chlorite in veinlets and large calcite grains filling vesicles (Fig. 7E, F).

Pyrite is widespread and occurs mostly as small grains intimately associated with pyrobitumen (OM1) in zones with no Cu mineralization. Pyrite grains occur mainly as isolated or aggregates of euhedral crystals and rosette-like spherules (Fig. 8A-E). Pyrobitumen occurs mainly as isolated aggregates, filling vesicles and often with globular shape (OM1) (Fig. 6C, D). The most distinctive feature of the pre-ore mineralization is the abundant presence of pyrobitumen and euhedral pyrite (Fig. 8A).

In the upper section of the drill core, pyrite is scarce, occurring mostly in the intermediate to deep zones (>98.6 m depth). As mentioned previously, pyrite is intimately associated with pyrobitumen (OM1), and occurs as disseminated euhedral to anhedral grains in the host rocks or filling vesicles (Fig. 9A, B). A sharp increase in pyrite abundance was recognized at ~289.05 m in the drill core. Overall, two main textural types of pyrite were identified: 1) Euhedral to subhedral grains (Pyrite I) with occasional cubic and pyritohedral shapes ranging in size between 80 and 900 μm , but occasionally reaching up to 1.5 mm (Fig. 9A). These crystals display abundant fractures and minor magnetite inclusions. Aggregates of pyrite grains can form rosette-spherules (Pyrite II) textures (e.g., Fig. 9B). These aggregate grains display sharp, irregular rims with some pyrobitumen in the center of the crystals. In addition, abundant fractures have affected some of these grains resulting in a puzzle-like texture. Pyrobitumen (OM3) can be observed in some of these fractures.

The main Cu-(Fe) sulfide minerals consist of chalcocite, bornite and chalcopyrite (Fig. 8F). Chalcocite is the dominant Cu sulfide, and occurs as disseminated aggregates and filling fractures and is also intimately associated with pyrobitumen (Fig. 5B, C; Fig. 8G, H). Chalcocite also occurs filling veinlets and within amygdales of the volcanic host rock, which are elongated and rounded, with sinuous, sharp edges, forming aggregates reaching up to 1.5 mm in diameter. Disseminated grains of chalcocite reach up to 250 μm , and to a lesser extent as a replacement mineral of bornite. In the analyzed samples, chalcocite was observed in association with pyrobitumen, calcite, and prehnite-pumpellyite at depth (>105 m). Chalcocite grains usually occur with angular fragments of pyrobitumen (OM3) (Fig. 5C). Hematite is associated with chalcocite and can also replace magnetite in the upper part of the deposit. Late-stage (supergene) assemblages include covellite, digenite, djurleite, chrysocolla and malachite, generally replacing chalcopyrite and chalcocite (e.g., Figs. 5D, 8F, G).

2.4.3. Pyrobitumen inclusions in pyrite and chalcocite

Petrographic observations at Lorena show the occurrence of drop-like pyrobitumen inclusions within pyrite and chalcocite (OM2). For example, a distinct feature of pyrite grains from the deep section of the drill core is the ubiquitous presence of micrometer- and nanometer-sized pyrobitumen inclusions. These inclusions consist mainly of droplet-shaped pyrobitumen grains (Fig. 10). They occur in pyrite grains as randomly oriented inclusions (Fig. 10A-C), following crystallographic planes and growth zones (Fig. 10B-D), and also near the grain rims (Fig. 10A). Detailed observations using a high-resolution FE-SEM show that the pyrobitumen inclusions (OM2) are up to 600 nm in size (Fig. 11). In addition to the linear alignment of pyrobitumen inclusions (Fig. 10), isolated pyrobitumen micro-inclusions were observed in the cores of pyrite grains (Fig. 11D-E). FE-SEM-EDS revealed the presence of Al and Si rich nanoparticles within these pyrobitumen micro-inclusions (Fig. 11F). These nanoparticles were usually observed in the center or at the rims of pyrobitumen droplets.

Most importantly, droplet-shaped inclusions of pyrobitumen of variable size (~700 nm to 20 μm) were also recognized randomly distributed within chalcocite grains (Figs. 8H; 12). These bitumen inclusion-bearing chalcocite crystals, when present, are commonly associated with larger pyrobitumen grains.

2.4.4. Elemental composition and pyrobitumen textures

Electron microprobe analyses of pyrobitumen from the Lorena deposit are reported in [Annex A.2](#). Analyses were performed on clean pyrobitumen areas with no visible mineral inclusions. Iron, Cu, S, Cl, Ag, Au, U, V, Co, As, Cr, Ni and Sb were measured. It is important to note that only globular (OM1) and angular (OM3) bitumen grains were analyzed. The smaller bitumen inclusions in the sulfides (OM2) could not be analyzed due to their small size (< 1 μm), usually below the spatial resolution of the electron probe (and the other micro-analytical techniques used here, i.e., XRF and XANES) (see Methods section).

A statistical summary of elements with concentrations above the detection limit is presented in [Figure 13](#). All elemental data are displayed in [Annex A.3](#), including below detection values. No significant chemical differences were observed between globular (OM1) and angular (OM3) pyrobitumens. Hence, and for the sake of simplicity, EMPA data are plotted as a whole in [Figure 13](#). Pyrobitumen at Lorena display high concentrations in Fe, Cu, S and Cl, reaching maximum concentrations in the 1000 ppm range. Concentrations of the aforementioned elements are variable, spanning from 100's to 1000's of ppm. Sulfur was detected in almost all analyses revealing some of the highest concentrations (up to 0.43 wt.%), and also showing the lowest variability. Vanadium, Co and As were detected in about 25% of the analyses with mean concentrations of 200, 290 and 230 ppm, respectively. Chromium, Ni, Sb, Ag were detected only in a few pyrobitumen grains with concentrations <400 ppm and U was only reported in one spot with a concentration of 200 ppm ([Annex A.2](#)). Silver was detected in only two spots with a concentration of 300 ppm and Au was detected in 15 spots reaching up to 600 ppm with a median concentration of 400 ppm ([Fig. 13](#)).

Figure 14 depicts the above-detection EMPA data of pyrobitumen, plotted as a function of depth (all elemental data are included in Annex A.4). Pyrobitumen at Lorena show some chemical variations with depth. In particular, Fe, Cu and Cl concentrations increase progressively as a function of depth, whereas S shows moderate variation, ranging from an average of 0.35 wt% in the shallow-intermediate section to 0.28 wt% in the deep zone (Fig. 14). In the intermediate section, average concentrations of Cu, Fe and Cl are 0.13, 0.09 and 0.01 wt%, respectively. Pyrobitumen grains located at depth, when compared to those in the upper section, display a larger compositional variability with average Fe, Cu and Cl concentrations of 0.14, 0.24 and 0.17 wt%, respectively.

2.4.5. Pyrobitumen XRF maps

Elemental maps at the mm-scale of selected pyrobitumen grains (OM1 - OM3) from Lorena are presented in Figure 15. Desktop μ -XRF (Fig. 15B-J) and synchrotron XRF (Fig. 15L-R) maps were obtained for pyrobitumen from the shallow, intermediate and deep sections of the studied drill core.

Elemental maps of globular-rounded (OM1) and angular pyrobitumen (OM3) from the shallow section reveal that sulfur is homogeneously distributed within the grains (Fig. 15B, G). Copper concentrations were detected in fractures around pyrobitumen, and only sparse copper pixels were observed within pyrobitumen (e.g., Fig. 15H). Vanadium was also recognized in pyrobitumen although the highest signal intensity was observed in the host rock (Fig. 15D, I).

Synchrotron XRF (S-XRF) maps show that sulfur is distributed within pyrobitumen grains in moderate to highly mineralized samples from the intermediate section, in good agreement with desktop μ -XRF maps. Furthermore, and due to the higher resolution of the technique, S-XRF maps show lower S concentrations towards pyrobitumen grain rims in samples from deep section (Fig. 15M). On most maps, higher Ca concentration zones around pyrobitumen grains reflect the presence of calcite (Fig. 15C, L). Other elements, such as As, Cr, Ag and Cu, were only randomly observed in maps (Fig. 15N-Q) and are usually detected along fractures (e.g., Cu, Fig. 15H, J). EMPA-WDS X-ray maps provide additional spatial information about the Cu distribution in pyrobitumen at the grain scale. These images show that the highest Cu concentrations are observed in the host rock matrix surrounding pyrobitumen grains (Fig. 16).

2.4.6. Sulfur XANES data

Sulfur XANES measurements in pyrobitumen were performed in two samples from the deep section. These pyrobitumen-bearing samples were selected considering the size (mm to cm) of the pyrobitumen grains and also the absence of Cu-(Fe) sulfides. Several spots were analyzed and merged to achieve average oxidation states for sulfur within each sample (see Evans et al., 2014; Konecke et al., 2017). Two different spectral types were identified (Fig. 17). Globular pyrobitumen (OM1) in sample LO-24-SP1 shows peaks at 2470 eV and 2482 eV that correspond to elemental sulfur (S^0) and sulfate (S^{6+}) species, respectively. Pyrobitumen in brecciated areas (OM3) in sample LO-24-SP4 exhibits an average sulfur K-edge sharp peak of S^{2-} (2471 eV) with a minor peak at 2473 eV, and a S^{2+} broad peak (2478 eV) (Fig. 17). These peaks correspond primarily to two sulfur species, i.e., thiophene (2471 eV) and sulfone (2478 eV).

2.5. DISCUSSION

2.5.1. Paragenetic sequence and ore-forming processes

Sulfide mineralization at Lorena is similar to that described at the Las Luces deposit, where main hypogene and late supergene assemblages are identified (Maureira, 2018). The hypogene stage comprises two sub-stages, i.e., a pre-ore and a main-ore stage. At Las Luces, the pre-ore stage is characterized by the presence of magnetite and pyrite, with minor chalcopyrite and hematite. In this event, pyrite is replaced by chalcopyrite in fractures. The main ore (Cu) stage is characterized by bornite-chalcocite assemblages with myrmekitic textures. The (late) supergene stage, on the other hand, is characterized by the formation of fine aggregates of digenite/covellite replacing hypogene chalcocite, and minor quantities of azurite and malachite are recognized (Maureira, 2018). Our petrographic observations at the Lorena deposit (Fig. 18) are thus in agreement with those described for Las Luces. At Lorena, the pre-ore stage is characterized by the presence of pyrite grains that are intimately associated with globular pyrobitumen (OM1). This assemblage is common, for example, in the drill core segments (98.6 – 167 m, Fig. 6C, D). The main Cu ore stage, as described, consists of chalcocite, bornite and chalcopyrite, where chalcocite occurs as disseminated aggregates filling fractures, and is also intimately associated with angular pyrobitumen (OM3) (167 – 312 m, Fig. 6E, F). Pyrobitumen inclusions in pyrite and chalcocite (OM2) are present mostly in the deeper part of the drillcore (167–312 m, Fig. 6E, F; Figs. 10, 11, 12). Although the precise paragenetic position of the micro- to nanosized pyrobitumen inclusions is difficult to constrain, they are interpreted here to have formed during both the pre-ore stage (i.e., pyrobitumen inclusions in pyrite) and the ore stage (i.e., pyrobitumen inclusions in chalcocite).

The paragenetic sequence (Fig. 18) and the occurrence of sulfide-pyrobitumen assemblages at Lorena is similar to those previously described for the pyrobitumen-bearing, Lower Cretaceous stratabound Cu deposits in central Chile (e.g., El Soldado: Zentilli et al., 1997; Wilson and Zentilli, 1999; Wilson et al., 2003a, b, Talcuna-Uchumi: Wilson and Zentilli, 2006; Carrillo-Rosúa et al., 2014 and deposits near Copiapó: Cisternas et al., 1999; Hagan et al., 2003; Cisternas and Hermosilla, 2006). In these deposits, the intimate association of pyrobitumen with Cu mineralization has been considered a key factor in the genesis of the stratabound orebodies, and two genetic stages have been recognized, i.e., a pre-ore stage involving thermal degradation of oil-bearing brines resulting in the accumulation of pyrobitumen, followed by an ore stage where previously formed pyrite was replaced by Cu sulfides (Carrillo-Rosúa et al., 2014). The most accepted model for these deposits involves, therefore, the introduction of externally derived Cu-rich hydrothermal fluids. The hydrothermal fluids, independently of their proposed origin (e.g., magmatic-hydrothermal, basinal, meteorically-derived or mixed), interacted with the pyrobitumen-bearing pre-ore assemblages to form Cu sulfides, either by replacement or direct precipitation. Since the occurrence of pyrobitumen is distinctive and has not been previously reported in the Jurassic Las Luces district (or any other Jurassic stratabound Cu deposit in northern Chile), it is important to highlight that the Lorena deposit shares common attributes with the pyrobitumen-bearing deposits of the central Chile Lower Cretaceous belt (Fig. 3).

At Lorena, the pre-ore stage assemblage is characterized by the presence of pyrobitumen and pyrite and widespread albite alteration that affected the andesite host rock. Chlorite, zeolites,

prehnite-pumpellyite, calcite and minor chalcedony, as well as pyrobitumen, are found filling vesicles and in the breccia matrix (Fig. 7). This assemblage has been recognized in other stratabound deposits that some authors have interpreted as formed by regional low-grade metamorphism prior to the hydrothermal event (Losert 1973; Boric et al. 2002; Cisternas and Hermosilla 2006; Carrillo-Rosúa et al. 2014).

Our observations suggest that the pre-ore assemblage formed when petroleum was mobilized from the source rock into the La Negra andesites by aqueous (connate?) fluids, precipitating pyrite as early phase. This resulted in the incorporation of pyrobitumen droplets into pyrite during sulfide growth from the solution, pointing to coexistence between aqueous fluids and hydrocarbons during the first stages of the deposit. Pyrobitumen inclusions (OM2) within pyrite crystal suggests that petroleum was widespread and is significant in terms of abundance during introduction into the host rock of the deposit. These observations are in agreement with data reported by Wilson et al. (2003) for the El Soldado deposit in central Chile. Considering the coexistence of pyrobitumen, pyrite and low-grade alteration minerals in vesicles, it is likely that petroleum migration was probably synchronous with regional alteration related to low-grade (burial) metamorphism (Wilson and Zentilli, 1999; Wilson et al., 2003a, b; Cisternas and Hermosilla 2006; Rieger et al., 2008; Carrillo-Rosúa et al., 2014).

As described above, two textural types of pyrite were found associated with pyrobitumen in Lorena, i.e., euhedral-subhedral pyrite grains (Pyrite I; Figs. 8A, 9A) and rosette-shaped spherules of pyrite (Pyrite II) which suggest apparent growth from early pyrite cores (Fig. 10C, D). These two types are indicative of at least two events of pyrite formation. The rosette-like aggregates are interpreted as continuous growth from a pyrite core/seed into subhedral aggregates. On the other hand, the euhedral-subhedral pyrite type shows distinctive micro- to nano-sized pyrobitumen inclusions (OM2) (Fig. 11). These pyrobitumen inclusions (OM2) are arranged following a concentric pattern from the pyrite core, where pyrobitumen inclusions are randomly distributed, to the outer sections of the pyrite grain where inclusions are arranged following crystallographic planes (Fig. 10). The textural occurrence of pyrobitumen inclusions within pyrite crystals strongly suggests that pyrite grew in the presence of petroleum, as it happens in detrital grains (quartz and feldspars) along migration pathways or in reservoirs where petroleum inclusions are trapped (Munz, 2001).

The main ore (Cu) stage is characterized by minor chalcopyrite, bornite and chalcocite. Hypogene chalcocite was also precipitated directly, filling vesicles and fractures (Fig. 8G, H). In both cases, chalcocite can be observed accompanied by pyrobitumen (OM1 - OM3), however, textural observations show that chalcocite filling vesicles is mainly in contact with globular pyrobitumen (OM1) or replacing it, indicating that Cu sulfide precipitation was redox-induced by the presence of organic matter. On the other hand, chalcocite in fractures is associated with the more angular type of pyrobitumen (OM3) (e.g. Fig. 5C), most likely representing a later pulse of pyrobitumen or a (globular) pyrobitumen remobilization event (Fig. 5A). In addition, the presence of micro- to nano-sized pyrobitumen inclusions within chalcocite grains (Fig. 8H; Fig. 12) indicate that (liquid) hydrocarbon phases were not restricted to the pre-ore stage, but were also present during the ore stage. During the main Cu event, pyrobitumen could have been in a semi-solid state induced by fluid mixing, water-washing and/or an increase in temperature (Wilson et al., 1998).

Covellite, digenite-djurleite and Cu oxide minerals (mainly chrysocolla and malachite) are only minor phases in Lorena and are indicative of a late supergene event. This mineral assemblage was formed by in-situ replacement/oxidation of primary (hypogene) Cu sulfides and occurs in vesicles and isolated masses (Fig. 5D). The lack of a relevant supergene, secondary sulfide blanket is possibly related to the minor presence of pyrite and hence, sulfuric acid production by sulfide weathering.

2.5.2. Evidence for hydrocarbon-hydrothermal fluid emulsions

The timing of pyrobitumen introduction in stratabound Cu-(Ag) deposits has been considered to pre-date the Cu mineralization event (Wilson and Zentilli, 1999; Cisternas and Hermosilla, 2006; Rieger et al., 2008; Carrillo-Rosúa et al., 2014). Observations at the Lorena deposit reveal the presence of pyrobitumen in both stages, i.e., in the pre-ore stage and the main Cu event. A first (initial) pulse is represented by globular pyrobitumen (OM1) and pyrite mainly, filling vesicles in the intermediate zone of the deposit (Fig. 6), whereas a later pulse is associated with angular pyrobitumen (OM3) chalcocite and hematite in the deeper section of the deposit. Globular pyrobitumen (OM1) is partially replaced by Cu-(Fe) sulfides (chalcocite and bornite) (Fig. 8G). This indicates that the metal-bearing hydrothermal fluid could have interacted with pre-existing organic matter, which is capable of reducing complexed metals in solution to form sulfides (Dissanayake, 1993). In addition, a later pulse of hydrocarbons is represented by angular pyrobitumen (OM3) intergrown with Cu sulfides and calcite. This assemblage suggests that during the ore stage hydrocarbons were introduced either as a new, fresh pulse or remobilized from pre-existing (globular) pyrobitumen.

Most importantly, the presence of micro to nano-sized pyrobitumen inclusions within pyrite and chalcocite (Figs. 8H, 10, 12) points, unequivocally, to coexistence between hydrothermal fluids and hydrocarbons during the evolution of the deposit. Droplet-like pyrobitumen inclusions (OM2) within sulfides indicate the presence of liquid hydrocarbons during crystal growth as fine, immiscible oil droplets (petroleum) in a water emulsion. Water in the hydrothermal fluid could act as the dispersion medium (continuous phase) of micron-sized oil droplets (Sjöblom, 2001, Bibette et al., 2002). Individual droplets could have formed larger aggregates and/or rearranged at the water/oil interface (Langevin et al., 2004). Water-oil emulsions stability is dependent on several factors including viscosity, which is influenced by temperature and water content among other factors (Chen and Tao, 2005). The occurrence of small size (~500 nm) pyrobitumen inclusions within pyrite (Figs. 10, 11) could be indicative of aqueous emulsion stability, where solution properties such as pH and temperature would have prevented the coalescence of smaller droplets into larger particles (e.g., 1 – 10 µm or larger). In addition, Si- and Al-bearing particles found within the pyrobitumen inclusions (Fig. 11F) could have increased the stability of the emulsion, as documented for particles in crude oil or in seawater suspended sediments (Lee., 1999). Energy and mixing time are other important factors for emulsifications, where the latter makes the emulsifier more effective (Chen and Tao, 2005). Water-oil emulsions have been proposed to play a role in the formation of stratabound Cu deposits in central Chile. Wilson and Zentilli (1999) and Wilson et al. (2003a, b) interpreted that pyrobitumen globules associated with framboidal pyrite at the El Soldado deposit may represent original droplets of semi-liquid petroleum. Droplets of oil were probably generated in the source rocks, coalesced and migrated with connate waters as an emulsion following a hydraulic gradient (Wilson, 1998). Spheres and globules of pyrobitumen identical to those observed at El Soldado and Lorena, have also been described in Mississippi Valley-type Pb-

Zn deposits (Marikos et al., 1986; Gregg and Shelton, 2012) and Californian Hg deposits (Peabody, 1993). These studies have proposed that mineralization is associated with the generation and migration of hydrocarbons, which often mix with waters of various origins to form water-oil emulsions.

At Lorena, the formation and stabilization of a water-oil emulsion could have occurred as a result of convection and fluid mixing in the volcano-sedimentary sequences, triggered by temperature changes induced by either regional low-grade (burial) metamorphism, the intrusion of dikes, and/or thermal effects related to deep-seated intrusions (e.g., Kojima et al., 2009). There are no fluid inclusions data from Lorena but microthermometric studies of Jurassic and Lower Cretaceous deposits have reported homogenization temperatures mostly within the 150 – 360°C range (Maksaev et al., 2007; Kojima et al., 2009). Experimental studies have shown that heating to ~93°C can result in an emulsified crude oil-water mixture (Cartmill and Dickey, 1970). Other experiments have shown that crude oil affected by temperatures close to 200°C behave as low temperature liquid phases, although temperature degradation processes are likely to start at 250°C (Migdisov et al., 2017). Potentially, the Lorena pyrobitumen was exposed to temperatures ranging from ~100 to 300°C, coeval to pyrite crystallization during the pre-ore stage, which resulted in the incorporation of pyrobitumen droplets during sulfide growth from the aqueous fluid. Observations at Lorena also show pyrobitumen inclusions in chalcocite from the main Cu mineralization stage. These inclusions are scarcer than those in pyrite, and have a random distribution within the sulfide crystals and show rounded and sigmoid shapes (Figs. 8F, 12B-D). This suggests that pyrobitumen was probably in lower concentrations in a water-oil emulsion destabilized and/or in a semi-liquid state when hypogene chalcocite crystallized from hydrothermal Cu-rich fluids, precipitating at temperature >150°C (Mathur et al., 2018).

2.5.3. Key metals in bitumen

Although limited data of trace and minor element on pyrobitumen are available, the role of hydrocarbons during metallogenesis has been explored in several mineralized systems (e.g., Manning and Gize, 1993; Wilson and Zentilli, 1999, 2006; Fuchs et al., 2016). These studies have suggested that organic matter may have acted as a source or carrier of metals including Au (e.g., Carlin-type deposits in Nevada, Emsbo and Koenig, 2007), U and Ti (e.g., Witwatersrand Au deposits, Fuchs et al., 2015), Pb (e.g., Laisvall Pb-Zn deposit, Saintilan et al., 2019), and V (e.g., Western Cordillera, Central Perú, Hagan and Parnell, 2000). Furthermore, Manning and Gize (1993) suggested that petroleum liquids are potentially capable of transporting Cu. In fact, earlier investigations have reported high Cu concentrations in crude oil (0.01 – 28 ppm Cu; Colombo and Sironi, 1961; Colombo et al., 1964; Jones, 1975; Ali et al., 1983; Ellrich et al., 1985; Duyck et al., 2008), suggesting that Cu can substitute Ni and V in porphyrin-like structures in petroleum, which are abundant in natural oils (Manning and Gize, 1993). The chemical composition of pyrobitumen obtained in this study reveals significant concentrations of base metals at Lorena, e.g., high Cu and Fe concentrations (average of 0.16 and 0.1 wt.%, respectively). Precious metals such as Au (and some Ag) were also detected. Ligands (Cl and S) also exhibit high concentrations, with average values of 0.09 and 0.34 wt.% for Cl and S, respectively (Fig. 13).

Since Cu and other metals such as Fe are particularly high in pyrobitumen at Lorena, one further aspect to evaluate is whether these elements were originally enriched in the hydrocarbon

phase or if the high concentrations are the result of the interaction of Cu-rich hydrothermal fluids with the pre-existing hydrocarbons. The main limitation to address this issue relates to the fact that published trace element data of pyrobitumen or liquid hydrocarbons is generally, very sparse. Also, as for the present study case at Lorena, available data corresponds to pyrobitumen in ore deposits and not the organic material from the source rocks or the original and unmodified migrated hydrocarbons. Available pyrobitumen EMPA data reported by [Wilson and Zentilli \(1999\)](#) for the El Soldado deposit are in agreement with microanalytical data presented here ([Fig. 12](#)). Microprobe analyses of isotropic cores of pyrobitumen grains show Cu~0.7 wt.%, Pb~2.8 wt.% and Cl of up to 2.25 wt.%, while the anisotropic, hydrothermally disturbed domains contain more Cu (>1 wt.%), some Fe (~0.5 wt.%), S (>1 wt.%), less Pb (0.7-1 wt.%), and generally less Cl (<1 wt.%) ([Wilson and Zentilli, 1999](#)). This is interpreted by those authors as evidence that components of the hydrothermal fluid (Cu, S and Cl) were incorporated into pyrobitumen as a result of metasomatic processes during the Cu mineralization stage.

It is well documented that hydrocarbons and organic matter can contain significant amounts of metals, although evaluating the contribution of petroleum-derived metals to mineralization remains challenging. Recent experiments to determine the isothermal bulk solubility of selected metals in crude oil have demonstrated that metals such as Au, Zn and U can be efficiently transported and re-deposited by hydrocarbons. For example, at temperatures <250°C, solubility of Zn in crude oil is ~28 ppm ([Migdisov et al., 2017](#)), which is considered sufficient for the formation of a Mississippi Valley-type deposit ([Leach et al., 2006](#)). Pyrobitumen extracted from shale rocks, on the other hand, can have high concentrations of Zn (from 41 to 24,125 ppm) and Pb (between 3 and 400 ppm), suggesting that petroleum-derived Pb could make large contributions to ore formation ([Saintilan et al., 2019](#)). For the particular case of Cu, no experiments have been conducted to determine the solubility of this metal in liquid hydrocarbons and only traditional theoretical considerations have been proposed ([Manning and Gize, 1993](#)). Calculated stability indices of metal-organic compound (metalloporphyrins) for Cu²⁺ and other metals ions (e.g., VO²⁺, Pd²⁺, Ni²⁺, Co²⁺, Fe²⁺, Zn²⁺, Pb²⁺) predict the empirical potential capacity of liquid petroleum to transport metals. These stability indices were determined based on ionic charge, electronegativity and ionic radius ([Buchler, 1978](#); [Manning and Gize, 1993](#)) with VO²⁺, Ni²⁺ and Zn²⁺ exhibiting values of 11.05, 6.8 and 4.1, respectively, indicating a high solubility for these cations. The calculated stability index for Cu²⁺ metal-organic compounds is 6.1, indicating that Cu could be potentially transported by liquid petroleum. However, this should be demonstrated experimentally and evaluated thoroughly in future studies.

At the Lorena deposit, mineralogical observations and WDS elemental maps show that the highest concentrations of Cu in pyrobitumen occur surrounding globular grains and within fractures ([Fig. 16](#)). Therefore, the evidence presented here strongly suggests that Cu detected in bitumen was most likely sourced from an external aqueous fluid that migrated through the pre-ore assemblage rather than from the hydrocarbon phase. We conclude that most of the Cu in Lorena was introduced to the system from external Cu-rich hydrothermal fluids during the main ore stage in agreement with previous studies ([Wilson and Zentilli, 1999](#); [Cisternas and Hermosilla, 2006](#) and [Carrillo-Rosúa et al., 2014](#)). However, the possibility that pyrobitumen may have provided at least a small fraction of Cu and other components at Lorena cannot be ruled out. FE-SEM observations reveal angular Cu-Fe sulfide nanocrystals ~500 nm in size that are immersed within pyrobitumen grains ([Fig. 19](#)). Although the origin of these Cu-Fe nanocrystals cannot be fully assessed, recent studies have provided mineralogical and geochemical evidence that the presence of individual and complex

nanocrystals could also reflect time-dependent growth of metals within a hydrocarbon phase (Fuchs et al., 2015).

2.5.4. Pyrobitumen as a source of organic sulfur

XANES data of pyrobitumen in the Lorena deposit show different species of sulfur including thiophene, elemental, sulfone and sulfate (Fig. 17). These sulfur species are dominant in kerogen, pyrobitumen, asphaltene and coals (Gobarty et al., 1990; Kelemen et al., 2007; Lewan et al., 2007; Le Doan et al., 2013; Pomerantz et al., 2014; Bolin et al., 2016). Although the XANES data reported here are the first synchrotron measurements in bitumen in Chilean deposits, organic geochemistry data by Rieger et al. (2008) for bitumen-bearing Lower Cretaceous deposits in the Copiapó area (~200 km south of Lorena) allow for some comparisons. Analyses of the molecular composition of aliphatic and aromatic compounds performed in pyrobitumen samples by Rieger et al. (2008) showed that total aromatic hydrocarbon fraction in this location exhibits an unusually high percentage of sulfur-bearing components (thioaromatics) with dibenzothiophenes, naphthobenzothiophenes and dinaphthobenzothiophenes; the latter being most abundant. These results indicate that a potentially significant fraction of sulfur in the pyrobitumen has thioaromatic components such as thiophene, i.e., sulfur in an aromatic ring. This is one of the most common forms of sulfur reported in pyrobitumen (Birdwell et al., 2018) and the most thermally stable form of organic sulfur in petroleum (Huffman et al., 1991). Hence, thiophene is expected to occur as a large fraction of the total sulfur present in pyrobitumen associated with petroleum source rocks (Bolin et al., 2016). Elemental sulfur, on the other hand, typically occurs in natural crude oil (Eccleston et al., 1952; Pomerantz et al., 2014, Greenfield et al., 2015), while sulfone can be derived from the oxidation of organic sulfur compounds under elevated temperature (Gorbaty et al., 1992), including the oxidation of pyrobitumen. Oxidation of organic matter during the formation of sulfide ores has been documented in sedimentary hosted Pb-Zn deposits (Pratt and Warner 1998) and at the El Soldado deposit. Wilson and Zentilli (1999) proposed that CO₂ resulting from bitumen oxidation formed calcite. Our exploratory XANES data of sulfur speciation in pyrobitumen suggest that thiophene and elemental compounds are dominant sulfur species at Lorena, and results are indicative of the presence of organosulfur compounds that can be attributed to an organic source for this element in pyrobitumen. The formation of sulfone and sulfate species, on the other hand, may have resulted from modification (probably oxidation) of the organic compounds at higher temperature, during the main ore stage, when externally derived Cu-rich hydrothermal fluids circulated through pyrobitumen, as suggested by Wilson and Zentilli (1999) for the El Soldado deposit.

Although the organic origin of sulfur in the pyrobitumen at Lorena is unknown, a possible source could be the same sedimentary rocks that probably generated the hydrocarbons, e.g., the Pan de Azúcar or the Las Tórtolas formations (Fig. 4). Even though the Lower Jurassic is not a particularly hydrocarbon source rock worldwide, the Hettangian-Sinemurian shows evidence of inhospitable, sulphurous seas along many coasts (e.g. Richez et al. 2012). In the ancestral Chilean Coast the end Triassic was a low-stand with deep erosion, but the early Jurassic deposited fossil-rich beds when sealevel rose during transgression. If petroleum was an important element helping to concentrate pyrite (and hence sulfur) during liquid oil maturation, migration and concentration, it probably had the same potential in many areas where the Pan de Azucar Fm. is preserved under the volcanics. This should be taken into account in future studies assessing prospectivity surveys in the district.

In sedimentary rocks, the largest fraction of the organic sulfur is in the high-molecular-weight form, which can be inherited in the residual products like pyrobitumen formed after diagenesis and generation processes of hydrocarbons. Sulfur concentrations in organic-rich sedimentary rocks, such as black shales, can be higher than 6 wt.% (Wedepohl, 1978). Diagenetic processes of these rocks can form different types of light, moderate and heavy hydrocarbons, and asphaltenes. These organic phases can incorporate a large amount of the sulfur available in the source rock and are rich in asphaltenes (high molecular weight compounds with significant N, S and O heteroatoms) (Parnell, 1993), which when accompanied by heavy aromatics, can accommodate most of the sulfur compounds in hydrocarbons (Speight, 1991), with concentrations ranging from 0.07 to 10 wt.% (Rospondek, 1994; Riazi et al., 1999).

Pyrobitumen (OM1 - OM3) from the Lorena deposit hosts significant concentrations of sulfur (Figs. 13, 14). Small variations were found along the drill core with slightly higher sulfur concentrations in the intermediate section with respect to the lower section (average of 0.35 to 0.28 wt.%, respectively). These variations most likely reflect the depletion and/or enrichment of sulfur in pyrobitumen as a result of interaction with hydrothermal fluids. X-ray elemental maps of sulfur in this pyrobitumen show that sulfur is homogeneously distributed within grains (Fig. 15B, G), and probably reflect the primary sulfur content. In contrast, elemental sulfur maps in pyrobitumen from deeper levels (~289 m) display lower concentrations towards the grain rims (Fig. 15M), suggesting that sulfur decrease was probably caused by the chemical interaction with hydrothermal fluids. During this interaction, pyrobitumen was likely exposed to higher temperatures (>100 – ~300°C) under which geochemical changes, such as isomerization to lower steric energy and aromatization, can occur. Consequently, carbon bonds are broken, increasing electron unpairing (Gize et al., 1999) and sulfur release from the organic phase into the hydrothermal fluid.

Experimental evidence suggested that the solubility peak of some cations in pyrobitumen is achieved at temperatures above the oil window (Migdisov et al., 2017), where the upper limit is typically between 120 – 170°C (Philippi, 1965). It is also known that the solidification of liquid petroleum and subsequent thermal cracking is associated with bond breakage (Landais and Gize, 1997), and at temperatures above 150°C dehydrogenization reactions can be induced with emission of hydrogen sulfide (De Filippis et al., 1998; Masegosa et al., 2012). At Lorena, lower sulfur concentrations are observed in pyrobitumen grain rims (Fig. 15M), indicating that these grains were likely in contact with a high temperature hydrothermal fluid. This interaction would have caused chemical bond breakage and trigger the loss of external heteroatoms including thiols compounds from pyrobitumen and hence, sulfur from heteroatoms could have been incorporated into the hydrothermal fluid. Hydrogen sulfide (H₂S) loss from such reactions could have contributed, at least partially, to the sulfur budget available for sulfide mineralization during the ore stage, when hydrothermal fluids mixed with pyrobitumen. The interaction of pyrobitumen with Cu-bearing aqueous solutions would have triggered Cu sulfide precipitation assuming that Cu was transported as CuCl₂⁻ (Akinfiyev and Zotov; 2001, 2010). The pyrobitumen phase would in turn be oxidized during the interaction to form CO₂, which can also be incorporated in the fluid. This could explain the common association of chalcocite with pyrobitumen and calcite. Textural evidence for this hydrocarbon-triggered precipitation of Cu from hydrothermal fluids is provided by the occurrence of microscopic, angular particles that precipitate around and between pyrobitumen fractures (Figs. 7D, 12C-D). The bitumen-fluid interaction resulted in loss and addition of components from pyrobitumen as revealed by μ-XRF and EMPA data (Figs. 14, 15), where high concentrations of chlorine and the lowest concentrations of sulfur were determined in angular

pyrobitumen (OM3) from the deep zone. The evidence presented here suggests that at least a part of the sulfur in pyrobitumen could have been released slowly and gradually over time as pyrobitumen aromatizes. This aromatization would allow the loss of the outer rings, i.e., the thioaromatic components, releasing sulfur (i.e., H₂S) which is then incorporated in the hydrothermal fluids during the Cu ore stage.

2.6. GENETIC MODEL AND CONCLUDING REMARKS

Mineralogical observations and geochemical data show evidence that Cu-(Fe) sulfides and pyrobitumen are intimately associated in the Lorena stratabound Cu-(Ag) deposit. Based on textural observations, two main events of hypogene mineralization were identified at Lorena: a pre-ore stage, characterized by the presence of pyrobitumen (OM1), minor pyrite and widespread albite alteration followed by an ore stage with abundant chalcocite, and minor chalcopyrite and bornite. The study of pyrobitumen at Lorena is essential in understanding the processes involved in the formation of the deposit from the evolution of the organic phase to the pre-ore and ore stages (Fig. 20). The early stages involved hydrocarbon (petroleum) generation in the sedimentary source rocks (Fig. 20A, B), which was mobilized as immiscible droplets by aqueous (connate?) waters. Some micro- to nano-sized pyrite crystals were most likely formed and transported within the organic phase during this early pre-ore stage. Later, the migrated hydrocarbons (OM1) were injected into the volcanic host rocks, filling vesicles and fractures (globular pyrobitumen, OM1) (Fig. 20C, D). At Lorena, the formation and stabilization of the water-oil emulsion could have occurred as a result of convection and fluid mixing in the volcano-sedimentary sequence, temperature changes induced by regional low-grade (burial) metamorphism, the intrusion of dikes, and/or thermal effects related to deep-seated intrusions. Pyrite II was formed around early pyrite cores (Pyrite I) in the presence of hydrocarbons with micro- to nano-sized pyrobitumen inclusions (OM2, Fig. 20D). During the ore stage, an externally derived Cu-rich hydrothermal fluid was introduced into the system and interacted with organic matter (pyrobitumen). The pyrobitumen/fluid interaction triggered Cu sulfide precipitation by redox process, (Fig. 20E, F). Evidence of a second event of hydrocarbon introduction or remobilization of the pre-existing pyrobitumen, OM1, during the Cu ore stage, is represented by the angular pyrobitumen (OM3). This close association between chalcocite and organic matter is also evidenced by the presence of pyrobitumen inclusions in chalcocite (OM2) (Fig. 20F). At the same time, metasomatic processes may have resulted in thermal cracking of the organic phase, resulting in chemical bond breakage and loss of sulfur, which was incorporated into the hydrothermal fluid.

Results presented here are in agreement with previous studies on Cretaceous stratabound Cu-(Ag) deposits in central Chile supporting the notion that pyrobitumen played a key role during ore formation as a redox trap for Cu sulfide precipitation. In addition, our data indicate that at least some of the sulfur – and eventually some metals, such as Cu and Au – may have been sourced from pyrobitumen.

This is the first report of the occurrence of pyrobitumen in the Jurassic stratabound Cu-(Ag) deposit in northern Chile. It is uncertain at this point if this constitutes a unique case due to the presence of sedimentary rocks in the Las Luces district. Further studies are required not only to investigate the presence of bitumen in other Jurassic deposits and to constrain the role of bitumen in ore formation in Chilean stratabound Cu-(Ag) deposits.

2.7. ACKNOWLEDGEMENTS

Funding for this study was provided by Millennium Science Initiative (MSI) through “Millennium Nucleus for Metal Tracing Along Subduction” grant, and by FONDECYT project #1140780. The authors acknowledge support from FONDAP project #15090013 “Centro de Excelencia en Geotermia de los Andes, CEGA”. Research supported by the LNLS - Brazilian Synchrotron Light Laboratory, CNPEM/MCTIC is acknowledged, as well as travel funding by CNPEM. We thank technical assistance of Carlos Pérez, Dalton Abdala and Santiago Tassara during synchrotron analyses. We also thank technical assistance by Owen Neil during EMPA analyses at Washington State University. The FE-SEM instrument used in this study was funded by FONDEQUIP project EQM150101. We thank Compañía Minera Las Cenizas for providing access to drill core samples. Andrea Paola Herazo thanks financial support provided by a Doctoral scholarship from CONICYT (21171385) and the Hugh McKinstry grant from the Society of Economic Geologists Foundation (SEGF). We thank chief editor Franco Pirajno, associate editor Si-yu Hu and three reviewers (Dr. Yafei Wu and two anonymous reviewers) for helpful comments and suggestions.

2.8. REFERENCES

- Akinfiyev, N.N., and Zotov, A.V., 2001. Thermodynamic description of chloride, hydrosulphide, and hydroxide complexes of Ag(I), Cu(I), and Au(I) at temperatures of 25–500°C and pressures of 1–2000 bar. *Geochem. Int.* 39, 990–1006.
- Akinfiyev, N.N., and Zotov, A.V., 2010. Thermodynamic description of aqueous species in the system Cu- Ag-Au-S-O-H at temperatures of 0–600°C and pressures of 1–3000 bar. *Geochem. Int.* 48, 714-720.
- Ali, M.F., Bukhari, A., Saleem, M., 1983. Trace metals in crude oils from Saudi Arabia. *Ind. Eng. Chem. Prod. Res. Dev.* 22, 691-694.
- Anderson, G.M., 1991. Organic maturation and ore precipitation in Southeast Missouri. *Econ. Geol.* 86, 909-926.
- Barra, F., Reich, M., Selby, D., Rojas, P., Simon, A., Salazar, E., Palma, G., 2017. Unraveling the origin of the Andean IOCG clan: A Re-Os isotope approach. *Ore Geol. Rev.* 81, 62-78.
- Bibette, J., Leal-Calderon, F., Schmitt, V., Poulin, P., 2002. Introduction, in: *Emulsion science - Basic principles*, Springer.
- Birdwell, J.E., Lewan, M.D., Bake, K.D., Bolin, T.B., Craddock, P.R., Forsythe, J.C., Pomerantz, A.E., 2018. Evolution of sulfur speciation in bitumen through hydrous pyrolysis induced thermal maturation of Jordanian Ghareb Formation oil shale. *Fuel* 219, 214-222.

Bolin, T., Birdwell, M., Lewan, D., Hill, R., Grayson, M., Mitra-Kirtley S., Bake K., Craddock, P., Abdallah, W., Pomerantz A., 2016. Sulfur Species in Source before and after Hydrous Pyrolysis Determined by X-ray Absorption Near-Edge Structure. *Energ. Fuel.* 30, 8, 6264-6270.

Boric, R., Díaz, F., Maksaev, V., 1990. Geología y Yacimientos Metalíferos de la Región de Antofagasta. SERNAGEOMIN, Santiago, Chile, Boletín 40, 246 (in Spanish).

Boric, R., Holmgren, C., Wilson, N.S.F., Zentilli, M., 2002. The Geology of the El Soldado Manto Type Cu (Ag) Deposit, Central Chile; in Porter, T.M. (Ed.), *Hydrothermal Iron Oxide Copper-Gold & Related Deposits: A Global Perspective, Volume 2*; PGC Publishing, Adelaide, 163-184.

Buchler, J.W., 1978. Synthesis and properties of metalloporphyrins; in: Smith K.M. (Ed.), *Porphyrins and Metalloporphyrins*, Elsevier, 157-231.

Carrillo-Rosúa, J., Boyce A., Morales-Ruano, S., Morata, D., Roberts, S., Munizaga, F., Moreno-Rodríguez, V., 2014. Extremely negative and inhomogeneous sulfur isotope signatures in Cretaceous Chilean manto-type Cu-(Ag) deposits, Coastal Range of central Chile. *Ore Geol. Rev.* 56, 3-24.

Cartmill, J.C. and Dickey, P.A., 1970. Flow of a disperse emulsion of crude oil in water through porous media. *Am. Assoc. Pet. Geol. Bull.* 54, 2438-2447.

Chen, C., Tao, D., (2005). An experimental study of stability of oil-water emulsion. *Fuel Process. Technol.* 55, 143-151.

Cisternas, M.E., Frutos, J., Galindo, E., Spiro, B., 1999 Lavas con pyrobitumen en el Cretácico Inferior de Copiapó: petroquímica importancia metalogénica. *Revista Geologica de Chile* 26, 205-226 (in Spanish).

Cisternas, E., Hermosilla, J., 2006. The role of bitumen in strata-bound copper deposit formation in the Copiapó area, Northern Chile. *Miner. Depos.* 41, 339-355.

Colombo, U., Sironi, G., 1961. Geochemical analysis of Italian oils and asphalts, *Geochim. Cosmochim. Acta* 25, 24-51.

Colombo, U., Sironi, G., Fasolo, G.B., Malvano, R., 1964. Systematic neutron activation technique for the determination of trace metals in petroleum. *Anal. Chem.* 36, 802-807.

Crede, L.S., Liu, W., Evans, K., Rempel, K., Testemale, D., Brugger, J., 2019. Crude oils as ore fluids: An experimental in-situ XAS study of gold partitioning between brine and organic fluid from 25 to 250°C. *Geochim. Cosmochim. Acta* 244, 352-365.

Cucurella, J., Canut de Bon, C., Cisternas, M.E., 2005. Pyrobitumen related to silver-copper deposits in a Cretaceous volcanic-sedimentary sequence: Talcuna district, Coquimbo, Chile. *Mineral. Polonica* 36, 1, 21-29.

Cuney, M., 2009. The extreme diversity of uranium deposits. *Miner. Depos.* 44, 3-9.

- Detlef, K., 2002. Geologisch-tektonische Karte der Küstenkordillere südlich von Taltas (Nordchile). Maßstab 1:150.000.
- De Filippis, P., Giavarini, C. Santarelli, M.L., 1998 Sulphur-extended Asphalt: Reaction Kinetics of H₂S evolution. *Fuel* 77, 5, 463.
- Dissanayake, C.B., 1993. Gold and other metals in graphite; in: Parnell, J., Kucha, H., Landais, P., (Eds.), *Bitumen in ore deposits*. Society for Geology Applied to Mineral Deposits, Sp 9, 138-152.
- Duyck, C., Miekeley, N., Fonseca, T.C.O., Szatmari, P., Vaz dos Santos Neto, E., 2008. Trace Element Distributions in Biodegraded Crude Oils and Fractions from the Potiguar Basin, Brazil. *J. Braz. Chem. Soc.*, 19, 5, 978-986.
- Eccleston, B.H., Morrison, M. Smith, H.M., 1952. Elemental Sulfur in Crude Oil. Petroleum Experiment Station, Bureau of Mines, Bartlesville, Okla.
- Ellrich, J., Hirner, A., Stark, H., 1985. Distribution of trace elements in crude oils from southern Germany. *Chem. Geol.* 48, 313-323.
- Emsbo, P., Koenig, A.E., 2007. Transport of Au in petroleum: evidence from the northern Carlin trend, Nevada; in: Andrew, C.J., Borg, G. (Eds.), *Digging Deeper*, Proceedings of the Ninth Biennial SGA Meeting. Irish Association for Economic Geology, Dublin, 695-698.
- Espinoza, S., Véliz, H., Esquivel, J., Arias, J., Moraga, A., 1996. The cupriferous province of the Coastal Range, northern Chile; in: Camus, F., Sillitoe, R.H., Petersen, R. (Eds.), *Andean Copper Deposits: New Discoveries, Mineralization, Styles and Metallogeny*. Society of Economic Geologist Sp Pub 5, pp. 19-32.
- Evans, K.A., Dyar, M.D., Reddy, S.M., Lanzirrotti, A., Adams, D.T., and Tailby, N., 2014. Variation in XANES in biotite as a function of orientation, crystal composition, and metamorphic history. *Amer. Miner.* 99, 443-457.
- Fuchs, S., Schumann, D., Williams-Jones, A.E., Vali, H., 2015. The growth and concentration of uranium and titanium minerals in hydrocarbons of the Carbon Leader Reef, Witwatersrand Supergroup, South Africa. *Chem. Geo.* 393-394, 55-66.
- Fuchs, S., Williams-Jones, A.E., Przybylowicz, W.J., 2016. The origin of the gold and uranium ores of the Black Reef Formation, Transvaal Supergroup, South Africa. *Ore Geol. Rev.* 72, 149-164.
- Gaupp, R., Moller, P., Lüders, V., di Primio, R., Littke, R., 2008. Fluids in sedimentary basin: an overview. *Dynamics of Complex Sedimentary Basins - The Example of the Central European Basin System*. 347-365.
- García, F. (1967) *Geología del Norte Grande de Chile*, Simposio, Geosinclinal Andino, Sociedad Geológica de Chile. Publicaciones 3, 138 (in Spanish).
- Gize, A.P., 1999. Organic Alteration in Hydrothermal Sulfide Ore Deposits. *Econ. Geol.* 94, 967-980.

Gorbaty, M. L.; George, G. N.; Kelemen, S. R., 1990. Chemistry of organically bound sulphur forms during the mild oxidation. *Fuel* 69, 945-949.

Gorbaty, M.L., Kelemen, S.R., George, G.N., Kwiatek, P.J., 1992. Characterization and thermal reactivity of oxidized organic sulfur forms in coals. *Fuel* 71, 1255-1264.

Greenfield, M.L., Byrne, M., Mitra-Kirtley, S., Kercher, E.M., Bolin, T.B., Wu, T., Craddock, P.R., Bake, K.D., Pomerantz A.E., 2015. XANES measurements of sulfur chemistry during asphalt oxidation. *Fuel* 162, 179-85.

Gregg, Jay M., and Kevin L. Shelton., 2012. Mississippi Valley-type mineralization and ore deposits in the Cambrian-Ordovician great American carbonate bank; in: J. R. Derby, R. D. Fritz, S. A. Longacre, W. A. Morgan, and C. A. Sternbach (Eds), *The great American carbonate bank: The geology and economic resources of the Cambrian–Ordovician Sauk megasequence of Laurentia: AAPG Memoir 98*, p. 161-185.

Haggan, T., Parnell, J., 2000. Hydrocarbon-metal associations in the Western Cordillera, Central Peru. *J. Geochem. Explor.* 69-70, 229-234.

Haggan, T., Parnell, J., Cisterna, M.E., 2003. Fluid history of andesite-hosted CuS-bitumen mineralization, Copiapó district, north central Chile. *J. Geochem. Explor.* 78-79, 631-633.

Hitchon, B., Filby, R.H., Shah, K.R., 1975. Geochemistry of trace elements in crude oils, Alberta, Canada; in Yen, T.F (Ed.), *The Role of Trace Metals in Petroleum*, Ann Arbor Science Publisher 111-112.

Huffman, G.P., Mitra-Kirtley, S., Huggins, F.E., Shah, N., Vaidya, S., Lu, F., 1991. Quantitative analysis of all major forms of sulfur in coal by X-ray absorption fine structure spectroscopy. *Energ. Fuel.* 5, 574-581.

Jones, P., 1975. Trace Elements and Other Elements in Crude Oil- A Literature Review. Report of British Petroleum Research Centre, Sunburry.

Kelemen, S.R., Afeworki, M., Gorbaty, M.L., Sansone, M., Kwiatek, P.J., Walters, C.C., Freund, H., Siskin, M., Bence, A.E., Curry, D.J., Solum, M.S., Pugmire, R.J., Vandenbroucke, M., Leblond, M., Behar, F., 2007. Direct characterization of kerogen by X-ray and solid-state ¹³C nuclear magnetic resonance methods. *Energ. Fuel.* 21, 1548-1561.

Khuhawar, M.Y., Mirza, M.A., Jahangir, T.M., 2012. Determination of Metal Ions in Crude Oils; in: Abdul-Raouf, M.E.-S. (Ed.), *Crude Oil Emulsions - Composition Stability and Characterization*. InTech, Croatia, 1-25, doi: 10.5772/36945.

Kojima, S., Tristá-Aguilera, D., Hayashi, K. (2009) Genetic aspects of the manto-type copper deposits based on geochemical studies of North Chilean deposits. *Resour. Geol.* 59, 1, 87-98.

Konecke, B., Fiege, A., Simon, A., Parat, F., Stechern, A., 2017. Co-variability of S₆₊, S₄₊, and S₂₋ in apatite as a function of oxidation state: Implications for a new oxybarometer. *Amer. Miner.* 102, 3, 548-557.

Landais and Gize., 1997. Organic matter in hydrothermal ore deposits; in Barnes, H.E. (Ed.), *Geochemistry of Hydrothermal Ore Deposits*, John Wiley & Sons, New York.

Langevin, D. Poteau, S., Hénaut I., Argillier, J.F., 2004. Crude Oil Emulsion Properties and their Application to Heavy Oil Transportation. *Oil Gas Sci. Technol. Rev. IFP*, 59 (5), 511-521.

Large, R.R., Bull, S.W., Maslennikov, V.V., 2011. A carbonaceous sedimentary source-rock model for carlin-type and orogenic gold deposits. *Econ. Geol.* 106, 331–358.

Leach, D., Macquar, J.C., Lagneau, V., Leventhal, J., Emsbo, P., Premo, W., 2006. Precipitation of lead–zinc ores in the Mississippi Valley-type deposit at Trèves, Cévennes region of southern France. *Geofluids* 6, 24-44.

Le Doan, T.V., Bostrom, N.W., Burnham, A.K., Kleinberg, R.L., Pomerantz, A.E., Allix, P., 2013. Green River oil shale pyrolysis: semi-open conditions. *Energ. Fuel.* 27, 6447-59.

Lee, R.F., 1999. Agents which Promote and Stabilize Water-in- Oil Emulsions. *Spill Sci. Technol. Bull.*, 5, 117-126.

Lewan, M., 1984. Factors controlling the proportionality of vanadium to nickel in crude oils. *Geochim. Cosmochim. Acta* 48, 2231-2238.

Lewan, M.D., Hill, R.J.; in: Boak, J. (Ed.), *Proceedings of the 27th Oil Shale Symposium*, Colorado School of Mines: Golden, CO, 2007.

Losert, J., 1973. Genesis of copper mineralizations and associated alterations in the Jurassic volcanic rocks of the Buena Esperanza mining area, Departamento de Geología, Universidad. de Chile, 40, 64.

Lo Mónaco, S., López, L., Rojas, H., Lugo, P., García, D., Gastiel, J., 2007. Applications of electron microprobe analysis (EPMA) in the study of Venezuelan source rocks: La Luna and Querecual Formations. *Fuel* 86, 641-648.

Maksaev, V., Zentilli, M., 2002. Chilean strata-bound Cu–(Ag) deposits: an overview. In: Porter, T.M. (Ed.), *Hydrothermal Iron Oxide Copper–Gold & Related Deposits. A Global Perspective*. PGC Publishing, Adelaide, 185-205.

Maksaev, V., Townley, B., Palacios, C., Camus, F., 2007. Metallic ore deposits; in Moreno, T., Gibbons, W. (Eds.), *The Geology of Chile*. The Geological Society, London: 179-199. London.

Manning, D.A.C. and Gize, A.P., 1993. The Role of Organic Matter in Ore Transport Processes; in Engel, M.H, and Macko, S.A. (Eds.), *Organic Geochemistry, Principles and Applications*, Chapter 5, 547-563.

Marikos, M. A., Laudon, R. C., and Leventhal, J. S., 1986. Solid insoluble pyrobitumen in the Magmont West Orebody, Southeast Missouri, *Econ. Geol.*, 81, 1983-1988.

Maureira, I., 2018. Estudio comparativo entre los depósitos Altamira y Las Luces, Cordillera de la Costa, Región de Antofagasta: Implicancias para el origen de los depósitos estratoligados de Cu – (Ag). Tesis de Magister, Universidad de Chile. (In Spanish, <http://repositorio.uchile.cl/handle/2250/151836>).

Masegosa R.M., Cañamero, P., Sánchez Cabezudo, M., Viñas, T., Salom, C., Prolongo, M.G., Páez, A., Ayala, M., 2012. Thermal behavior of bitumen modified by sulphur addition. 5th Eurasphalt & Eurobitumen Congress, Istanbul.

Mastalerz, M., Glikson, M., 2000. In-situ analysis of solid bitumen in coal: Examples from the Bowen Basin and the Illinois Basin. *Int. J. Coal Geol.* 42, 207-220.

Mathur, R., Falck, H., Belogub, E., Milton, J., Wilson, M., Rose, A., Powell W., 2018. Origins of Chalcocite Defined by Copper Isotope Values. *Geofluids*, 9 pp.

Mayer, C.K., Fontboté, L., 1990. The stratiform Ag-Cu deposit El Jardín, Northern Chile; in: Fontboté, L., Amstutz, G.C., Cardozo, M., Cedillo, E. & Frutos, J. (Eds.), *Stratabound ore deposits in the Andes*. Berlin, Springer, 637-646.

Migdisov, A.A., Guo, X., Williams-Jones, A.E., Sun, C.J., Vasyukova, O., Sugiyama, I., Fuchs, S., Pearce, K., Roback, R., 2017. Hydrocarbons as ore fluids. *Geochem. Perspect. Let.* 5, 47-52.

Mossman, D., Nagy, B., Davis, D., 1993. Hydrothermal alteration of organic matter in uranium ores, Elliot Lake, Canada: Implications for selected organic-rich deposits. *Geochim. Cosmochim. Acta* 57, 3251-3259.

Munz, I.A., 2001. Petroleum inclusions in sedimentary basins: systematics, analytical methods and applications. *Lithos* 55, 195-212.

Naranjo, J., 1978. Geología de la zona interior de la Cordillera de la Costa entre los 26°20' Sur, Región de Atacama. *Carta Geológica de Chile*, escala 1:100.000. Instituto de Investigaciones Geológicas 34, 48 (in Spanish).

Naranjo, J., Puig, A., 1984. Hojas Taltal y Chañaral, Regiones de Antofagasta y Atacama, escala 1: 250.000, *Carta Geológica de Chile* N° 62-63 (in Spanish).

Oliveros, V., Féraud, G., Aguirre, L., Fornari, M., Morata, D., 2006. The early Andean magmatic province (EAMP): ⁴⁰Ar/³⁹Ar dating on Mesozoic volcanic and plutonic rocks from the Coastal Cordillera, Northern Chile. *J. Volcanol. Geotherm. Res.* 157, 4, 311-330.

Oliveros, V., Féraud, G., Aguirre, L., Ramírez, L., Fornari, M., Palacios, C., Parada, M., 2008. Detailed ⁴⁰Ar/³⁹Ar dating of geologic events associated with the Mantos Blancos copper deposit, northern Chile. *Miner. Depos.* 43, 3, 281-293.

Pfaff, K., Hildebrandt, L.H., Leach, D.L., Jacob, D.E., Markl, G., 2010. Formation of the Wiesloch Mississippi Valley-type Zn-Pb-Ag deposit in the extensional setting of the Upper Rhinegraben, SW Germany. *Miner. Depos.* 45, 7, 647-666.

Parnell, J., 1988. Metal enrichments in solid bitumens: a review. *Miner. Depos.* 23, 191-199.

Parnell, J. 1993. Bitumens in ore deposits. Special Publication No. 9 of the Society for Geology Applied to Mineral Deposits, Springer-Verlag, p. 1-6.

Peabody, C. E., 1993. The association of Cinnabar and Pyrobitumen in Mercury Deposits of the California Coast Range; in Parnell, J., Kucha, H., and Landais, P. (Eds.), *Pyrobitumens in Ore Deposits*, Special Publication No.9 of the Society of Geology Applied to Mineral Deposits, Springer-Verlag, Berlin, p.178-209.

Philippi, G.T., 1965. On the depth, time and mechanism of petroleum generation. *Geochim. Cosmochim. Acta* 29, 1021-1049.

Pérez C.A., Radtke, M., Sanchez, H.J., Tolentino, H., Neuenschwander, R.T., Barg, W., Rubio, M., Bueno, M.I.S., Raimundo, I., Rohwedder, J.J.R., 1999. Synchrotron radiation X-ray fluorescence at the LNLS: beamline instrumentation and experiments. *X-ray Spectrom.* 28, 320-326.

Pichowiak, S., Buchelt, M., Damm, K.W., 1990. Magmatic activity and tectonic setting of the early stages of the Andean cycle in northern Chile. *Geol. Soc. Am., Sp Pub* 241, 127-144.

Pomerantz, A.E., Bake, K.D., Craddock, P.R., Kurzenhauser, K.W., Kodalen, B.G., Mitra-Kirtley, S., Bolin, T.B., 2014. Sulfur speciation in kerogen and bitumen from gas and oil shales. *Org. Geochem.* 68, 5-12.

Pratt, L.M. and Warner, M., 1998. Roles of organic matter in shales and carbonate hosted base metal deposits; in Kettler, R.M., Giordano, T.H., and Wood, S.Z. (Eds.), *Ore genesis and Exploration: The roles of Organic Matter*, SEG Short Course.

Reich, M., Chryssoulis, S.L., Deditius, A., Palacios, C., Zuñiga, A., Weldt, M., Alvear, M., 2010. "Invisible" silver and gold in supergene digenite. *Geochim. Cosmochim. Acta* 74, 6157-6173.

Reich, M., Palacios, C., Barra, F., Chryssoulis, S.L., 2013. "Invisible" silver in chalcopyrite and bornite from the Mantos Blancos Cu deposit, northern Chile. *Eur. J. Mineral.* 25, 453-460.

Riazi, M.R., Nasimi, N., Roomi Y.A., 1999. Estimation of Sulfur Content of Petroleum Products and Crude Oils. *Ind. Eng. Chem. Res.* 38, 11, 4507-4512.

Richoz, S., van de Schootbrugge, B., Pross, J., Püttmann, W., Heunisch, C., Fiebig, J., Schouten, S., P.B. Wignall., 2012. Hydrogen sulphide poisoning of shallow seas following the end-Triassic extinction. *Nat. Geosci.* 5, 662-667.

Rieger, A., Schwark, L., Cisternas, M.E., Miller, H., 2008. Society of Economic Geologists, Inc. *Econ. Geol.* 103, 387-404.

- Robb, L.J., Meyer, F.M., 1995. The Witwatersrand Basin, South Africa: Geological framework and mineralization processes. *Ore Geol. Rev.* 10, 67-94.
- Rospondek, M., Leeuw, J., Baas, M., Bergen, P., Leereveld, H., 1994. The role of organically bound sulphur in stratiform ore sulphide deposits. *Org. Geochem.* 21, 12, 1181-1191.
- Saintilan, N.J., Spangenberg, J.E., Chiaradia, M., Chelle-Michou, C., Stephens, M.B., Fontboté, L., 2019. Petroleum as source and carrier of metals in epigenetic sediment-hosted mineralization. *Sci. Rep.* 9, 8283.
- Saric, N., Kreft, C., Huete, C., 2003. Geología del yacimiento Lo Aguirre. *Rev. Geol. Chile* 30, 2 (in Spanish).
- Scheuber, E., Gonzalez, G., 1999. Tectonics of the Jurassic-Early Cretaceous magmatic arc of the north Chilean Coastal Cordillera (22°–26°S): a story of crustal deformation along a convergent plate boundary. *Tectonics* 18, 895-910.
- Sjöblom, J., 2001. *Encyclopedic Handbook of Emulsion Technology*, Marcel Dekker, New York.
- Speight J.G., 1991. *The chemistry and technology of petroleum*, Inc.
- Spirakis C.S., 1996. The roles of organic matter in the formation of uranium deposits in sedimentary rocks. *Ore Geol. Rev.* 11, 53-69.
- Sun, Y.Z., Püttmann, W., 2000. The role of organic matter during copper enrichment in Kupferschiefer from the Sangerhausen basin, Germany. *Org. Geochem.* 31, 11, 1143-1161.
- Ulriksen, C., 1979. Regional geology, geochronology, and metallogeny of the Coastal Cordillera between 23°30' and 26°S [Thesis]: Halifax, Nova Scotia, Dalhousie University, 180.
- Watkinson, P., 2007. Deposition from Crude Oils in Heat Exchangers. *Heat Transfer Eng.* 28, 177-184.
- Wedepohl, K.H., 1978. *Handbook of Geochemistry* 11, Sections 73, B-G. Springer-Verlag.
- Wilson, N.S.F., 1998. The role of petroleum in the formation of the Soldado copper deposit, Chile: Hydrothermal replacement of a biodegraded petroleum reservoir. Unpublished Ph.D. thesis, Halifax, Canada, Dalhousie University, 418 p.
- Wilson, N., Zentilli, M., 1999. The Role of Organic Matter in the Genesis of the El Soldado Volcanic-Hosted Manto-Type Cu Deposit, Chile. *Econ. Geol.* 94, 1115-1136.
- Wilson, N., Zentilli, M., Reynolds, P.H., Boric, R., 2003a. A age of mineralization by basinal fluids at the El Soldado manto-type copper deposit, Chile ⁴⁰Ar/³⁹Ar geochronology of K-feldspar. *Chem. Geol.* 197, 161-176.

Wilson, N., Zentilli, M., Spiro, B., 2003b. A sulfur, carbon, oxygen, and strontium isotope study of the volcanic-hosted El Soldado manto type copper deposit, Chile: The essential role of bacteria and petroleum. *Econ. Geol.* 98, 163-174.

Wilson, N., Zentilli, M., 2006. Association of pyrobitumen with copper mineralization from the Uchumi and Talcuna districts, central Chile. *Int. J. Coal Geol.* 65, 1, 158-169.

Wu, Y., Evans, K., Fisher, L.A., Zhou, M., Hu, S., Fougereuse, D., Large, R., Li, J. Distribution of trace elements between carbonaceous matter and sulfides in a sediment-hosted orogenic gold system. *Geochim. Cosmochim. Acta* 276, 345-362.

Zamora, A., 2011. Geología Proyecto Las Luces. Internal report. Compañía Minera Las Cenizas.

Zentilli, M., Boric, R., Munizaga, F. and Graves, M.C., 1994. Petroleum involvement in the genesis of some strata-bound copper deposits of Chile. *Proceedings, 7th Chilean Geological Congress, Concepcion, Chile, II*, 1542-1546.

Zentilli, M., Munizaga, F., Graves, M.C., Boric, R., Wilson, N.S.F., Mukhopadhyay, P.K., Snowden, L.T., 1997. Hydrocarbon involvement in the genesis of ore deposits: an example in Cretaceous strata-bound (manto-type) copper deposits of central Chile. *Int. Geol. Rev.* 39, 1-21.

2.9. FIGURES

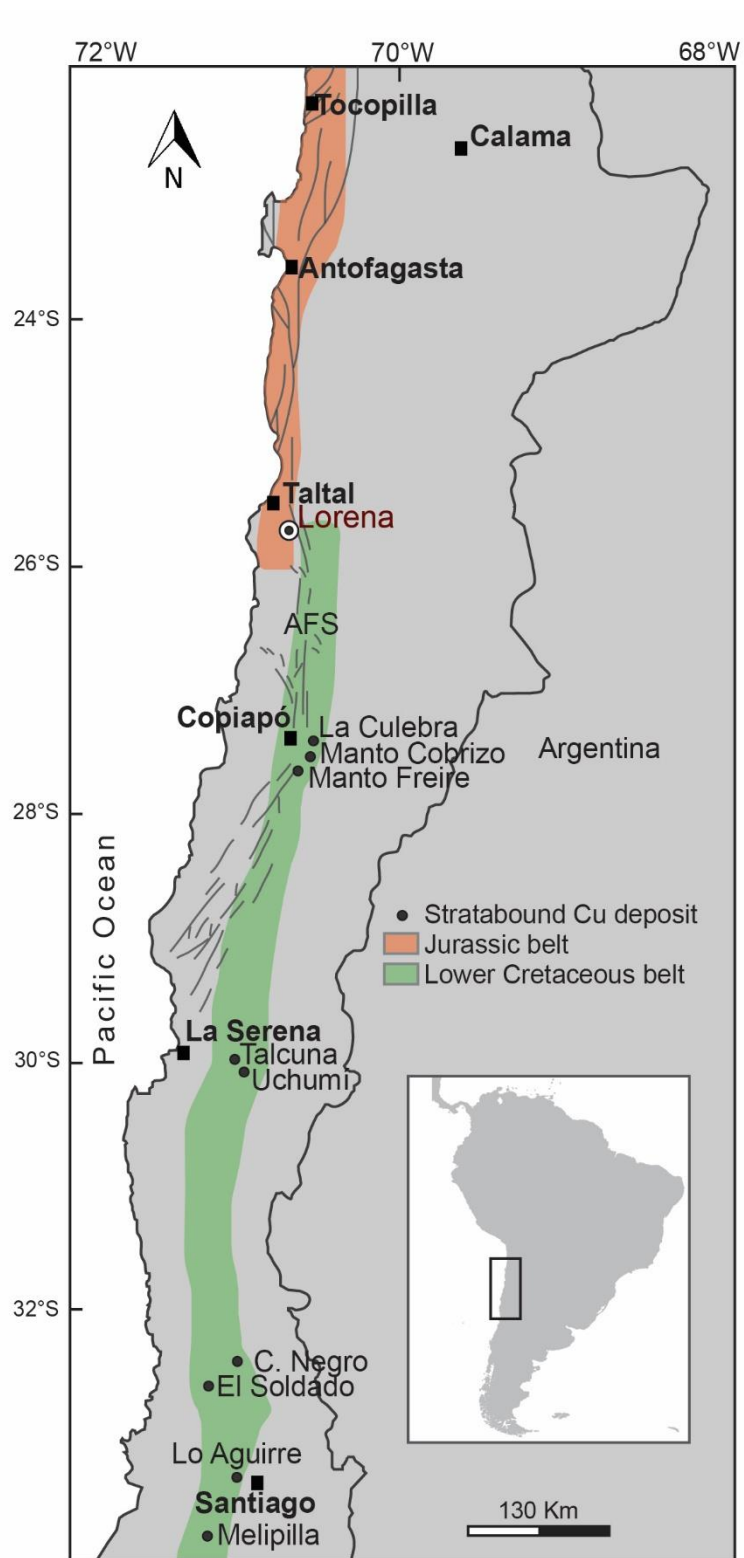


Figure 3. Location of representative Jurassic and Cretaceous stratabound Cu-(Ag) deposits of the Coastal Cordillera of northern-central Chile. The extension of Jurassic and Lower Cretaceous belts and the NS-trending Atacama Fault System (AFS) are also shown.

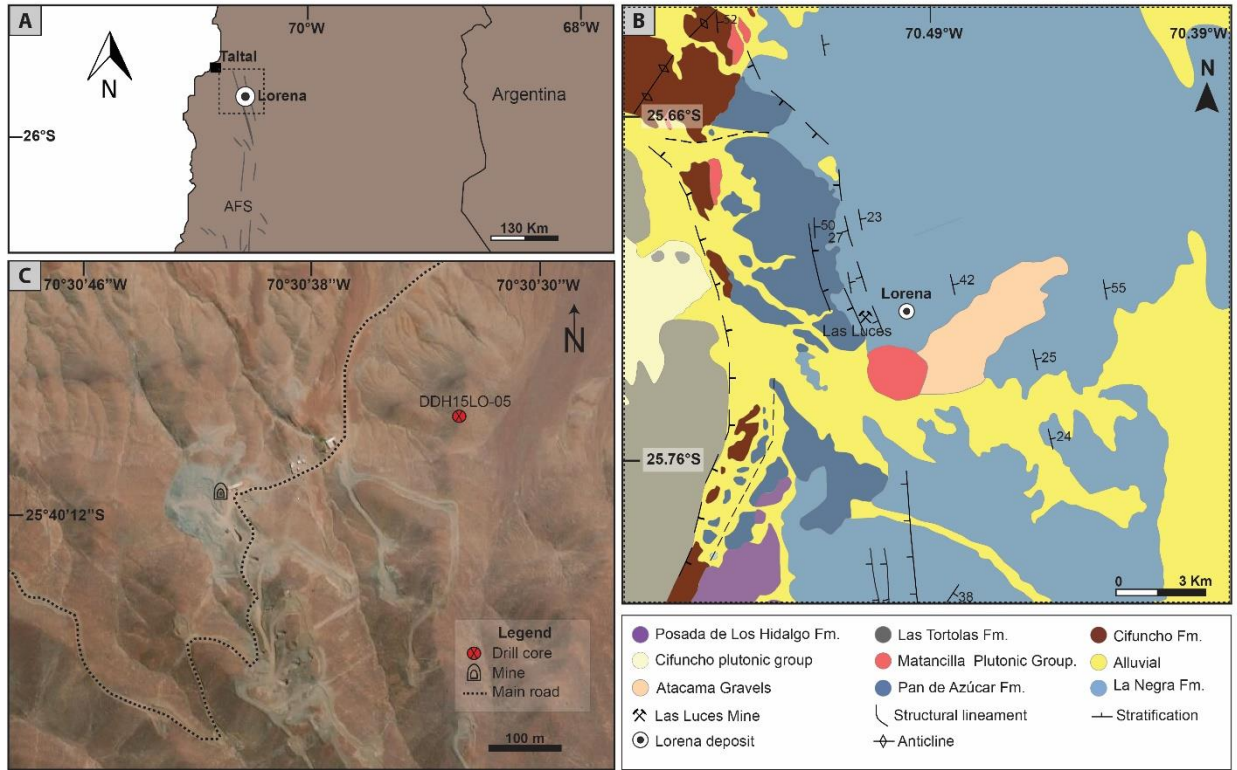


Figure 4. **A)** Location of the Lorena deposit, Las Luces district. **B)** Geologic map of the Las Luces district (modified from Detlef, 2002). **C)** Satellite image of the Lorena (underground) mine showing the location of the sub-vertical DDH15LO-05 drill hole collar.

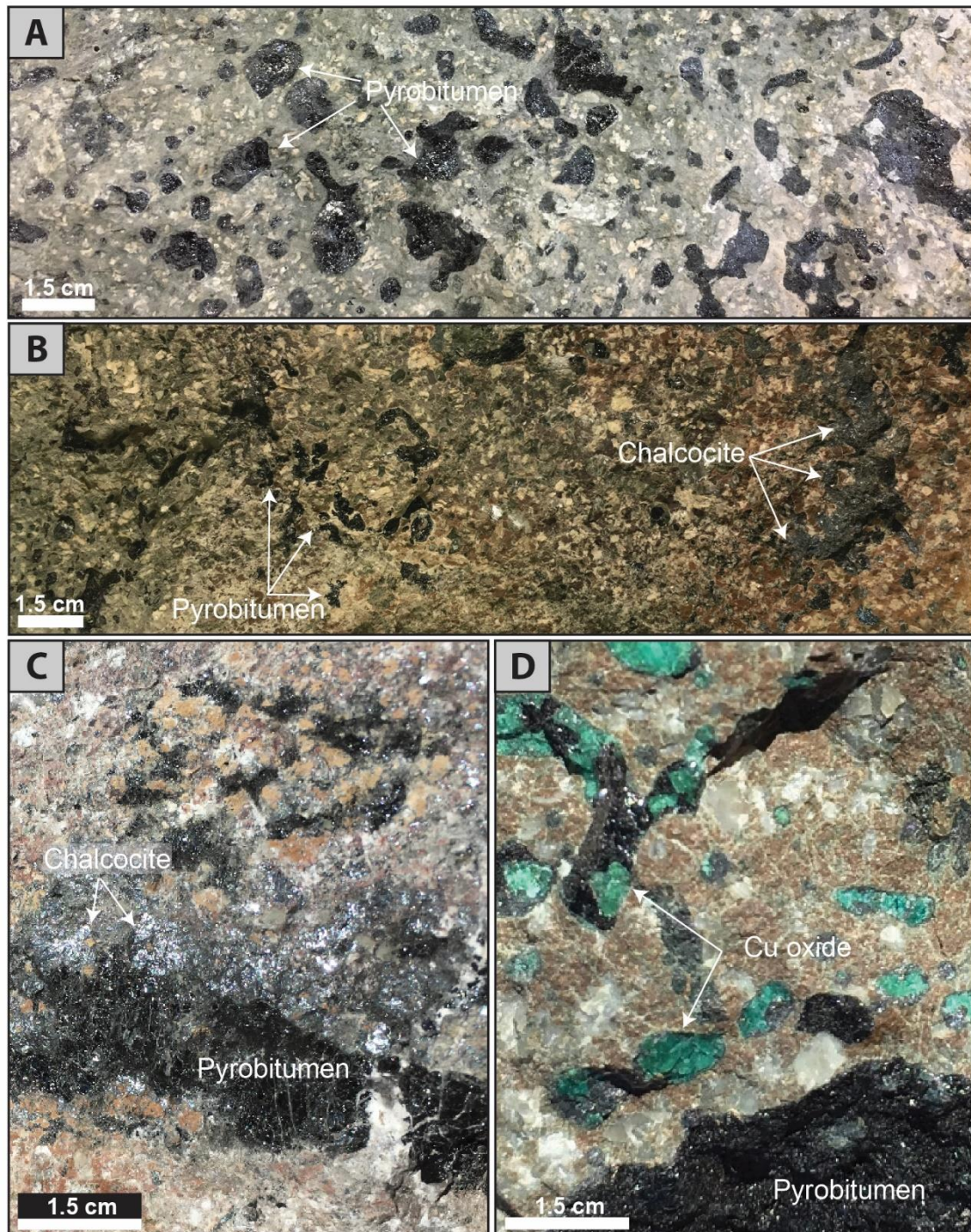


Figure 5. Representative pyrobitumen-bearing andesitic host rock samples from the Lorena deposit. **A)** and **B)** Pyrobitumen filling vesicles has a black color, glassy luster and conchoidal fracture. **C)** Pyrobitumen associated with hypogene chalcocite. **D)** Pyrobitumen in contact with Cu oxides formed by in-situ oxidation of hypogene sulfides.

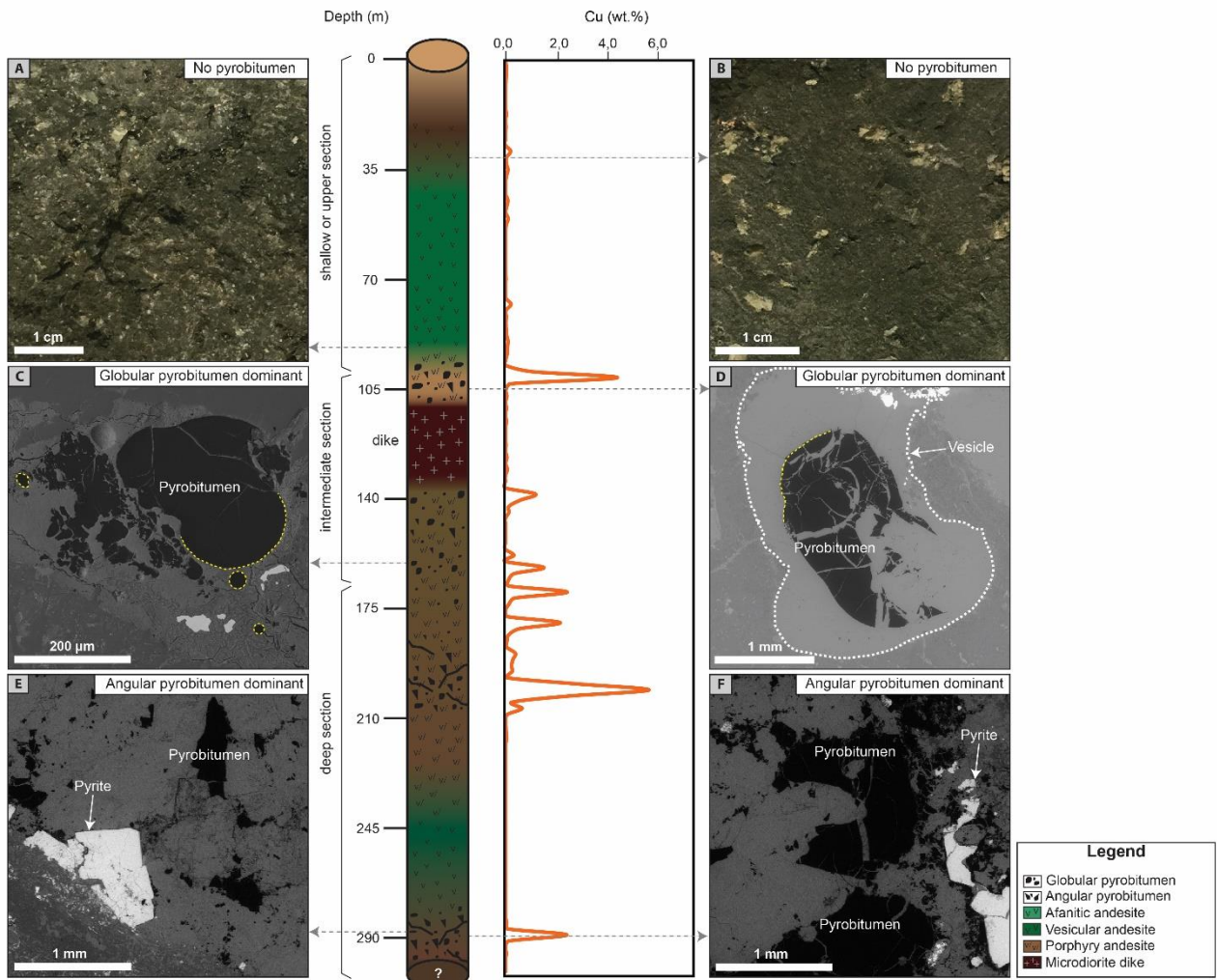


Figure 6. Schematic illustration of drill core DDH15LO-05 from the Lorena deposit showing lithological variations (center) and images of representative samples along the drill core. The orange line indicates the average Cu grade from the top to the bottom of the drill core. **A)** Andesite with ~5-30 modal percentage of plagioclase phenocrysts. **B)** Afanitic andesite with scarce plagioclase phenocrysts (<5 modal percentage). **C-D)** Backscattered electron (BSE) images of globular pyrobitumen filling a vesicle in a sample from the intermediate section. **E-F)** Backscattered electron (BSE) images of angular pyrobitumen. This textural type is dominant in the deep zone. Angular pyrobitumen grains vary in size and is commonly observed in brecciated zones.

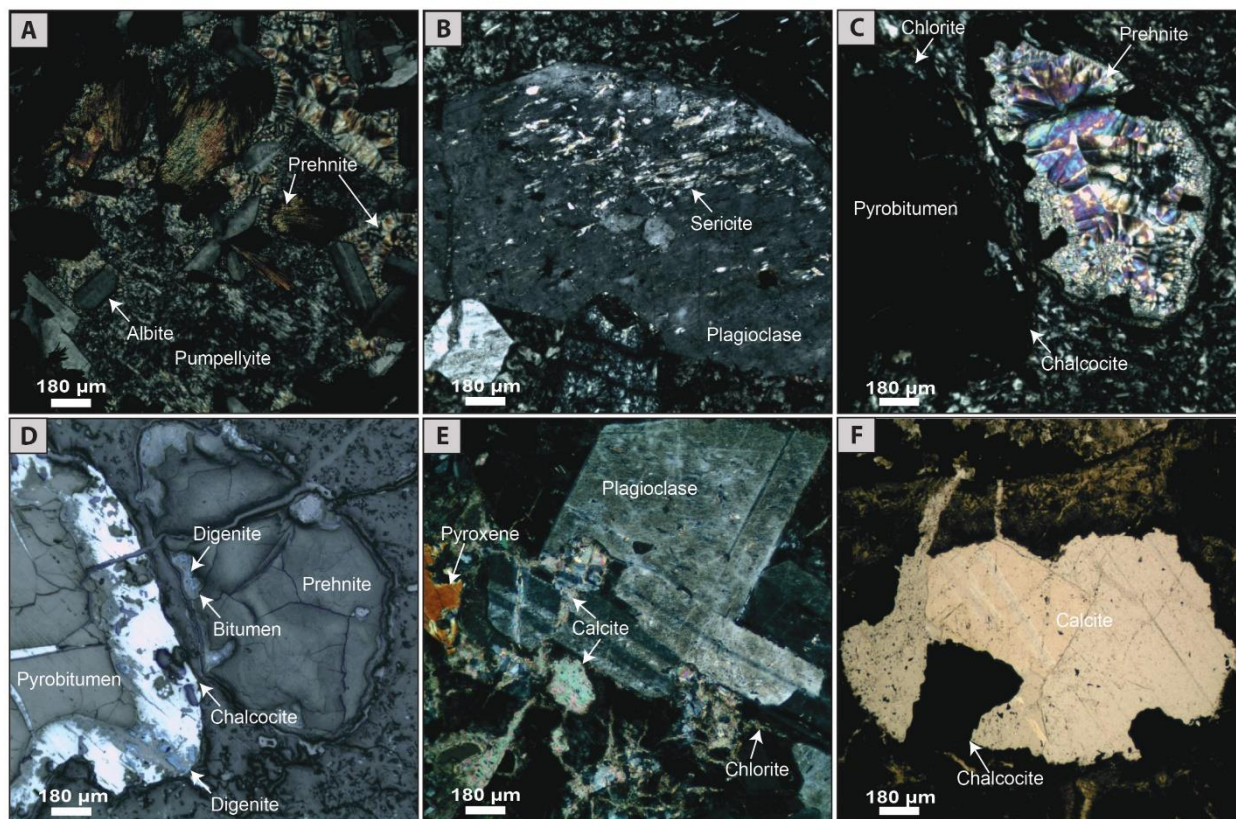


Figure 7. Transmitted and reflected polarized light microscopy photomicrographs of representative alteration minerals at Lorena. **A)** Prehnite and pumpellyite in vesicles with albite microcrysts. **B)** Albitized plagioclase with minor sericite. **C)** Vesicle infilled with prehnite with minor pyrobitumen at the edges. **D)** Reflected light image of (C) where copper sulfides (chalcocite and digenite) are observed in close association with pyrobitumen. **E)** Albitized plagioclase phenocrysts cross-cut by thin calcite veinlets. **F)** Calcite and chalcocite amygdale in volcanic host rock.

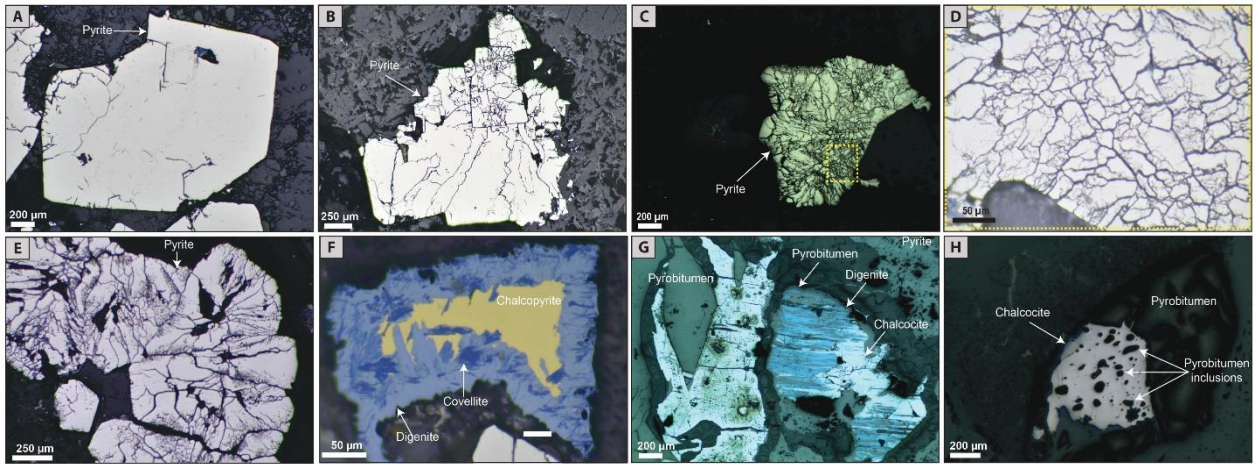


Figure 8. Reflected polarized light microscopy images of pre-ore and ore stage assemblages from the Lorena deposit. **A)** Euhedral pyrite (Pyrite I) from the pre-ore stage, **B)** Pyrite overgrowths from on pre-existing euhedral pyrite core, forming elongated and sub-rounded clusters. **C)** Rosette-shaped pyrite aggregates (Pyrite II). **D)** shows the magnified image of the yellow rectangle in (C), highlighting the finer structures of the pyrite aggregates. **E)** Set of rosette-shaped pyrite aggregates. **F)** Chalcopyrite grain replaced by digenite and covellite. **G)** Pyrobitumen/chalcocite association replaced by late digenite. **H)** Droplet-shaped, micrometer-sized pyrobitumen inclusions within chalcocite.

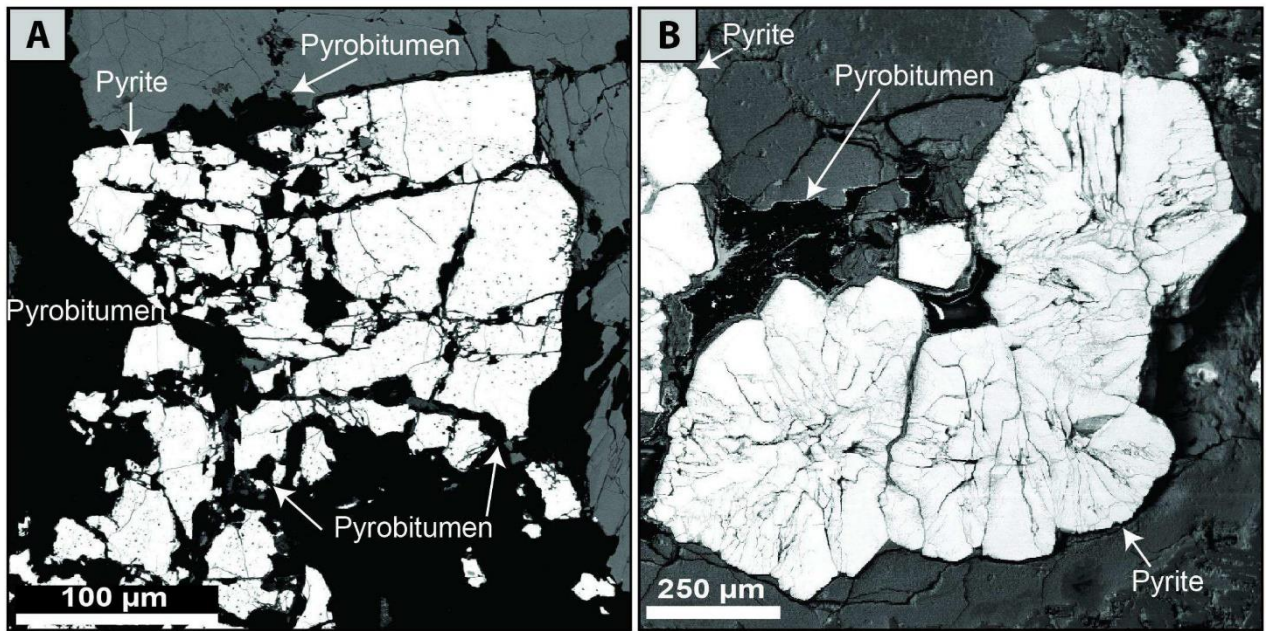


Figure 9. Backscattered electron (BSE) images showing pyrobitumen in association with pyrite. **A)** Subhedral pyrite grains with pyrobitumen interspersed or filling fractures. **B)** Rosette-shaped pyrite, showing pyrobitumen inclusions and in simple contact with pyrobitumen grains.

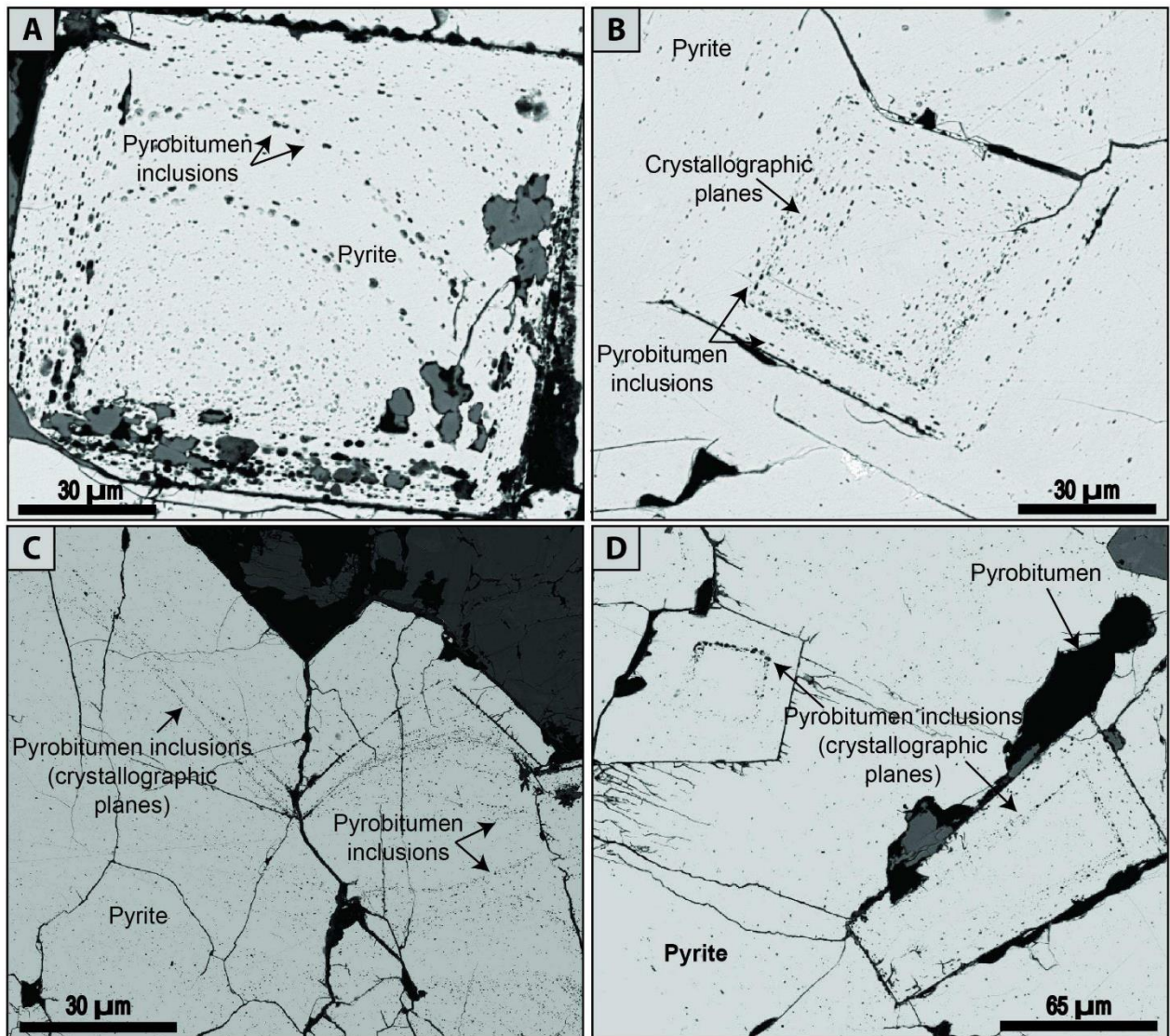


Figure 10. A-D) Field emission scanning electron microscopy (FE-SEM) images revealing the presence of micro- to nano-sized pyrobitumen inclusions within Pyrite I. Pyrobitumen inclusions usually have droplet-like shapes and show a regular distribution following crystallographic planes. Pyrobitumen grains are also observed in fractures or near crystal rims.

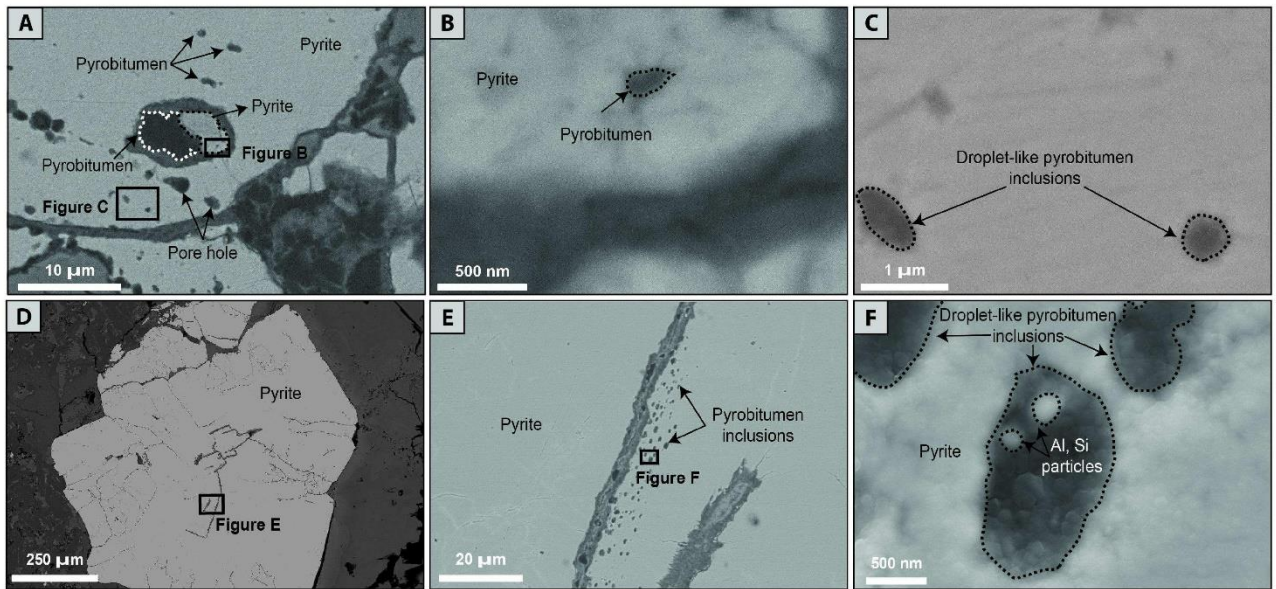


Figure 11. Detailed FE-SEM images of micro- to nano-sized pyrobitumen inclusions in Pyrite I. **A)** Elongated, sub-rounded pyrobitumen inclusions within a pyrite grain. Pores are also observed. **B)** Detail view of nano-sized pyrobitumen droplet in pyrite inclusion observed in image (A). **C)** Rounded and elongated pyrobitumen nano-inclusions from image (A). **D)** Pyrobitumen inclusions bordering a fracture in the center of a pyrite grain. **E)** Detail view of pyrobitumen inclusions observed in (D). **F)** Al- and Si-bearing nanoparticles within a pyrobitumen droplet.

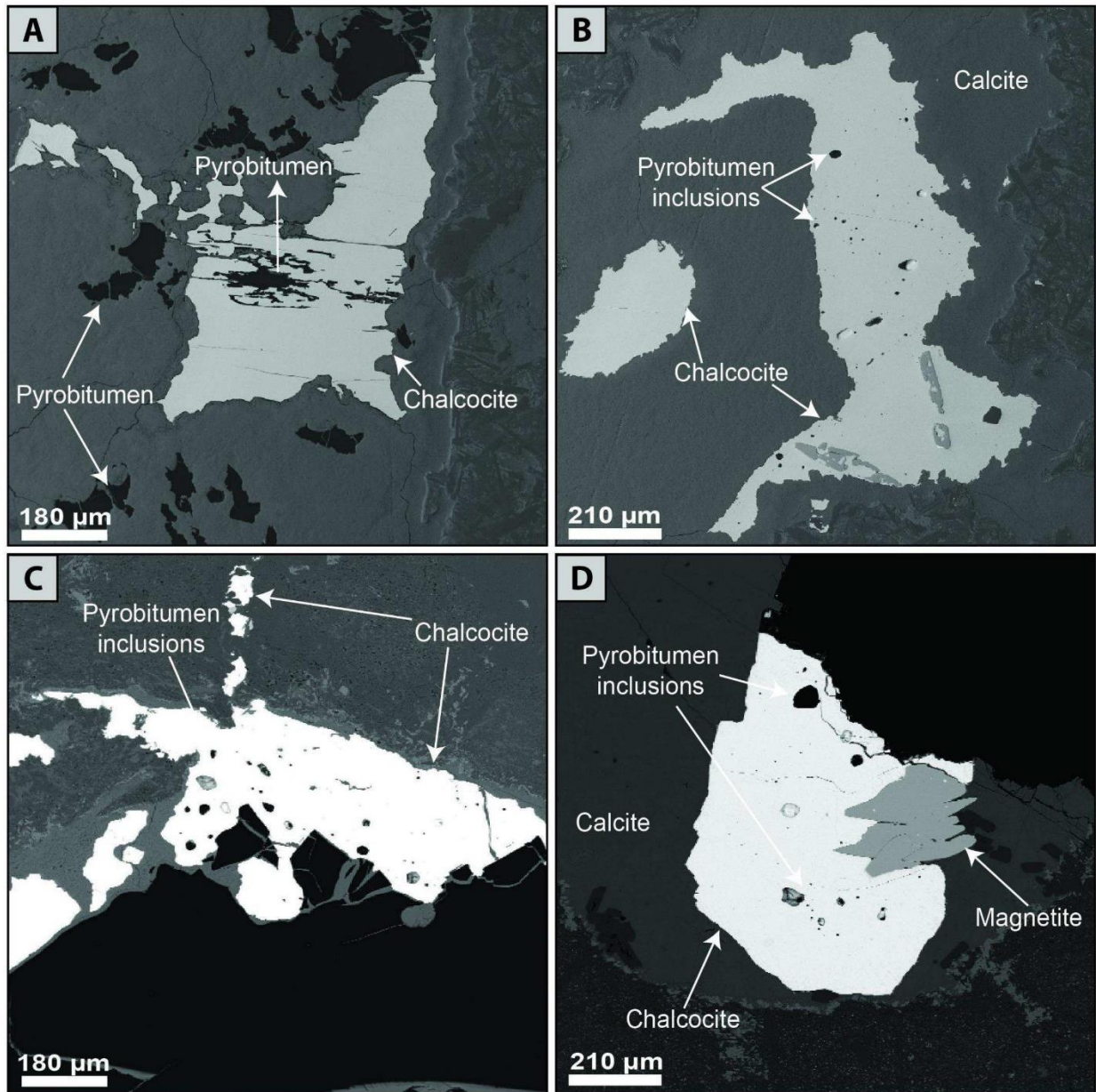


Figure 12. Backscattered electron (BSE) images showing pyrobitumen in association with chalcocite. **A)** Angular pyrobitumen in close proximity to anhedral chalcocite grains. Also observed is pyrobitumen filling fractures in chalcocite. **B)** Rounded and randomly oriented inclusions of pyrobitumen within chalcocite. **C)** Angular pyrobitumen is observed in contact with and partially surrounded by chalcocite. Rounded pyrobitumen inclusions in chalcocite are also present. **D)** Chalcocite grain in contact with pyrobitumen and magnetite in a calcite amygdale. Pyrobitumen droplets within chalcocite are also observed.

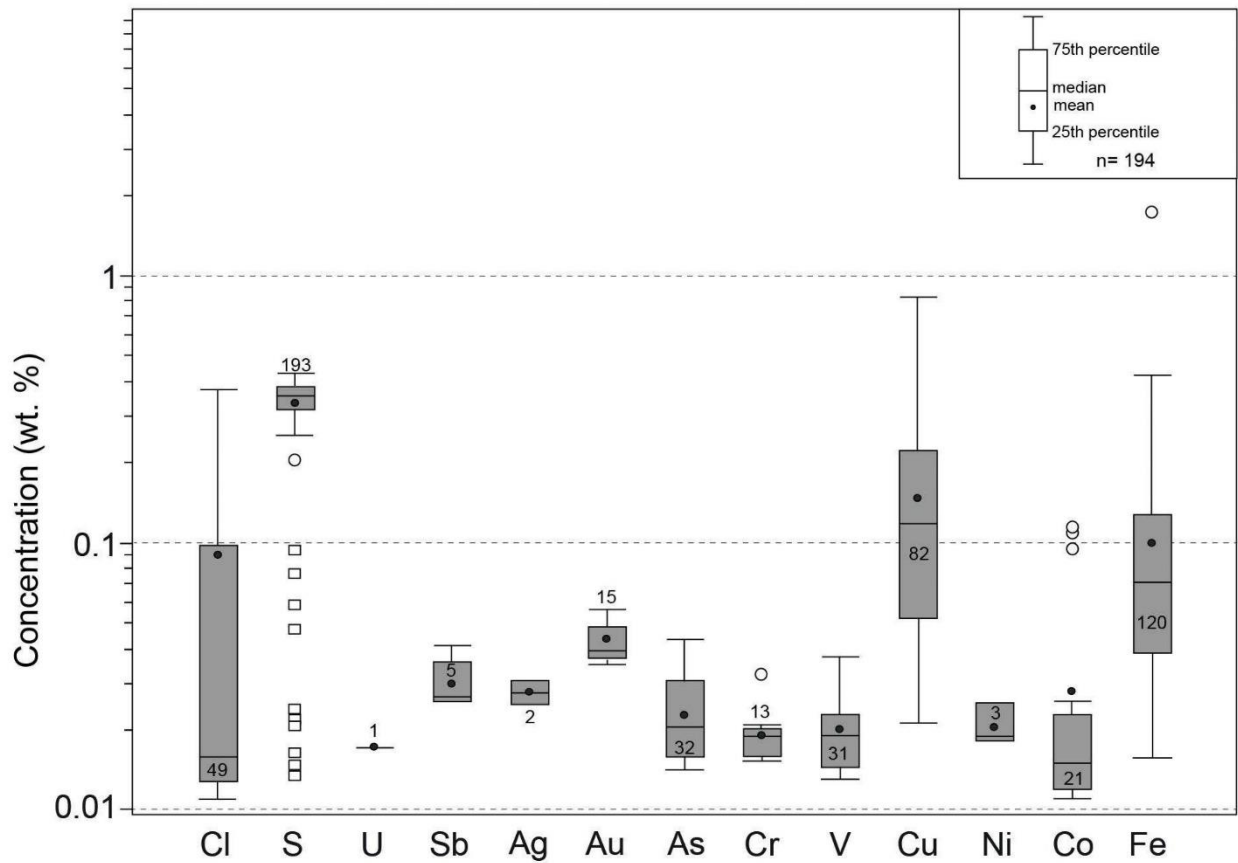


Figure 13. Concentration boxplot for selected minor elements in pyrobitumen from Lorena. Electron microprobe analyses (EMPA) are plotted in weight percent (wt.%) on a vertical logarithmic scale. In the boxplot, mean and median concentrations are shown, as well as the number of analyses above detection limit for each element (displayed in or outside of each box). A circle outlier is a data point above $1.5 \times (75\text{th percentile} - 25\text{th percentile})$.

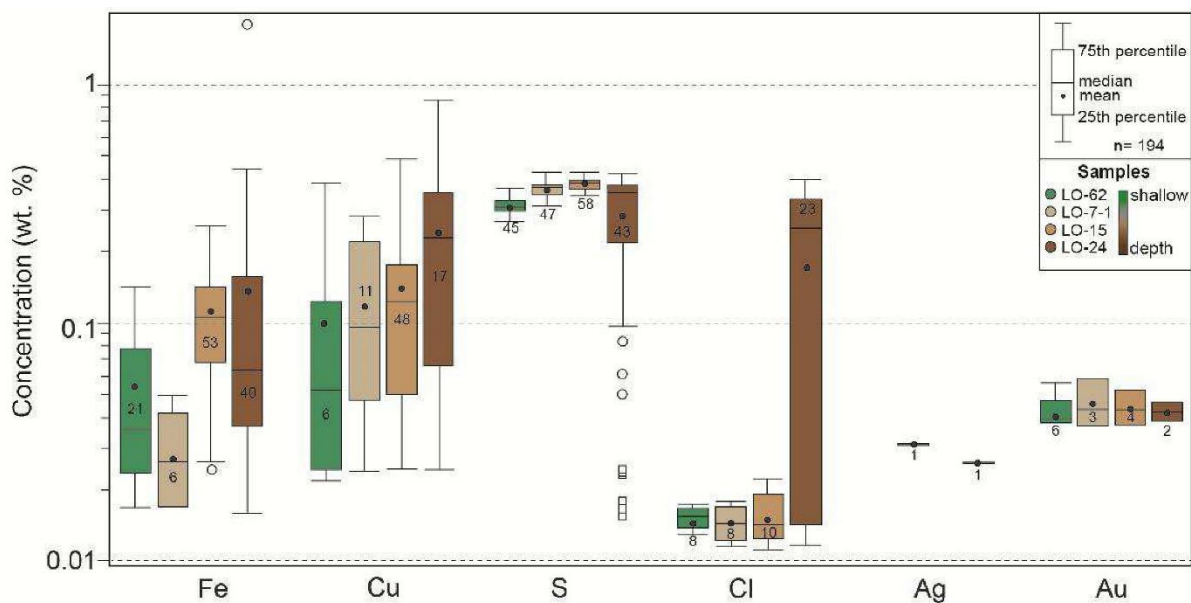


Figure 14. Boxplot showing the concentration of Fe, Cu, S, Cl, Ag and Au in pyrobitumen plotted as a function of sample depth (LO-62, LO-7-1 and LO-15: intermediate-shallow samples, LO-24: deep sample). EMPA data are plotted in weight percent (wt.%) on a vertical logarithmic scale. In each boxplot, mean concentrations are marked and the number of analyses above detection limit for each element is displayed inside/out of each box. A circle outlier is above $1.5 \times$ (quartile 3- quartile 1) while a square outlier is above $3.0 \times$ (75th percentile - 25th percentile).

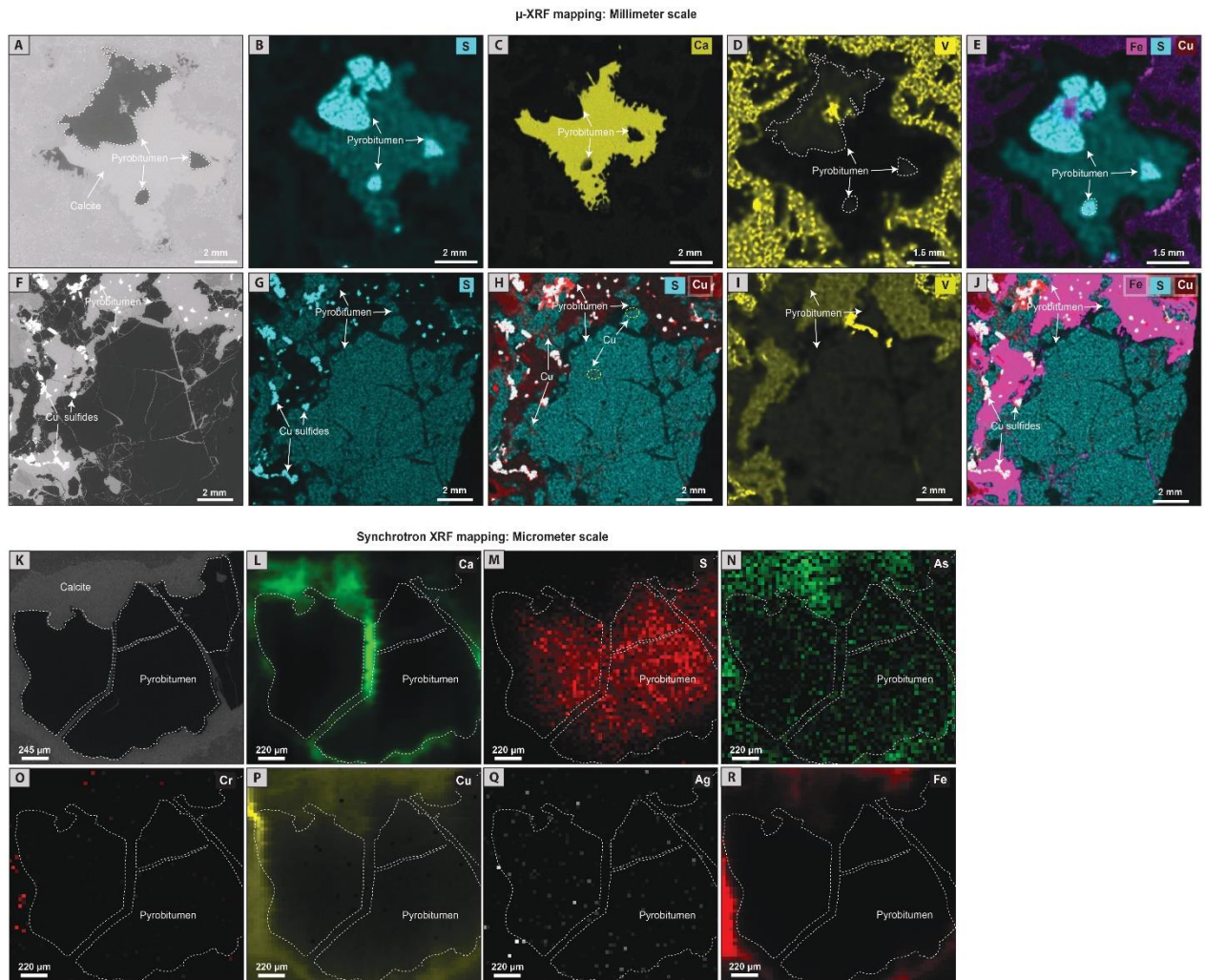


Figure 15. XRF elemental maps of pyrobitumen grains from Lorena obtained by desktop (B-J) and synchrotron (L-R) μ -XRF. A, F, K) Backscattered electron (BSE) images of the analyzed pyrobitumen grains. See text for discussion.

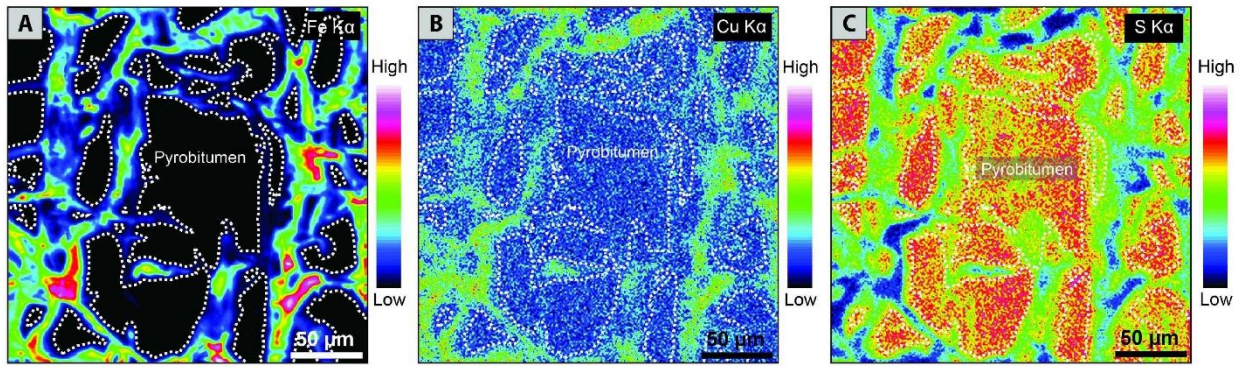


Figure 16. Wavelength dispersive spectrometry (WDS) EMPA X-ray maps (Fe, Cu, S) of pyrobitumen grains within andesite host rock. The WDS maps show a high concentration of S and a low concentration of Cu in pyrobitumen. Slight variations in the S concentration are observed in the pyrobitumen grains, whereas Cu appears more homogeneous. No Fe was detected in the analyzed grains.

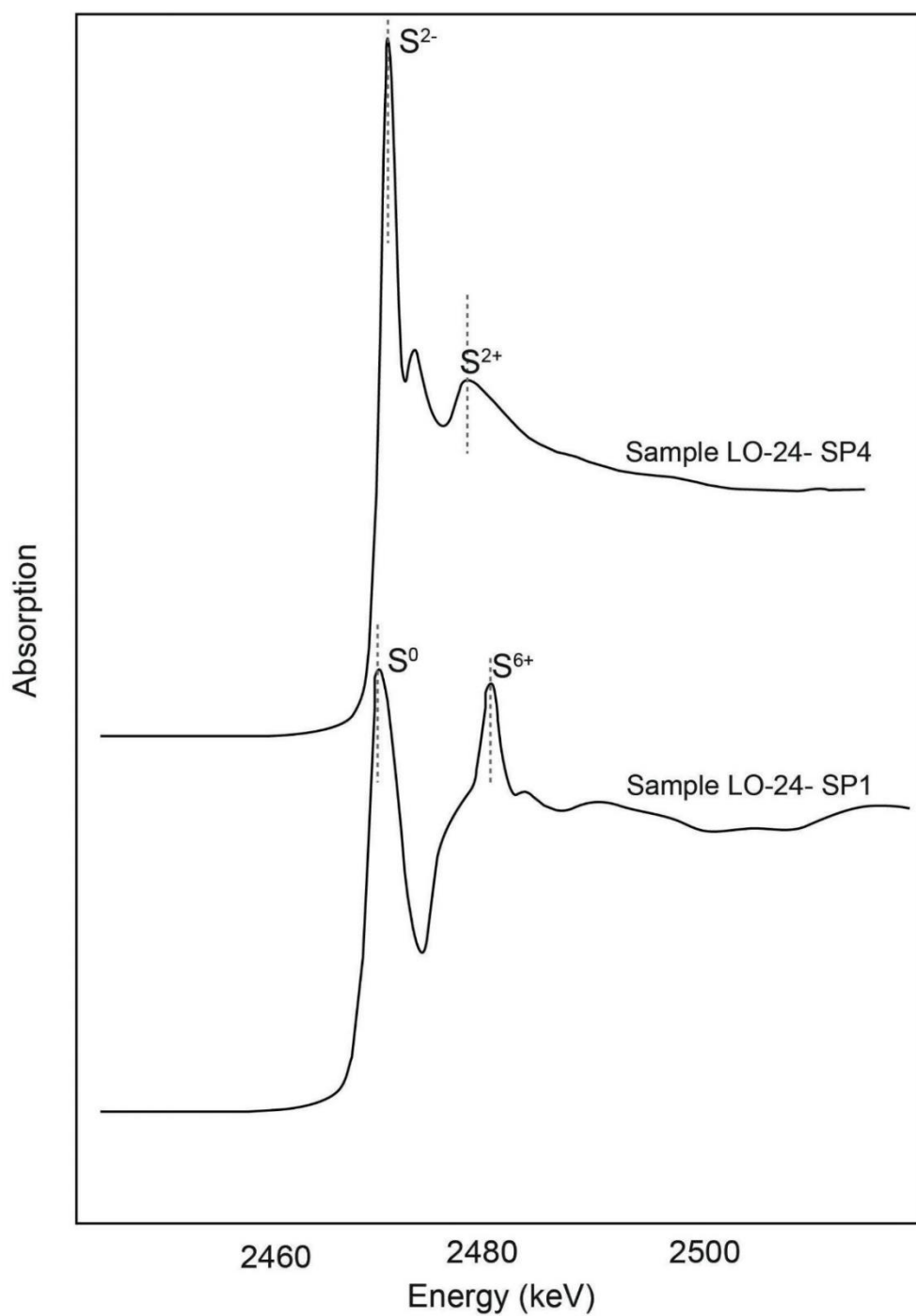


Figure 17. Sulfur speciation in pyrobitumen obtained using synchrotron XANES. Several analyses were performed and merged to achieve each spectrum. XANES data of pyrobitumen from the Lorena deposit indicate the presence of thiophene and sulfone species (LO-24-SP4). Sample LO-24-SP1, on the other hand, shows peaks associated with elemental sulfur and sulfate.

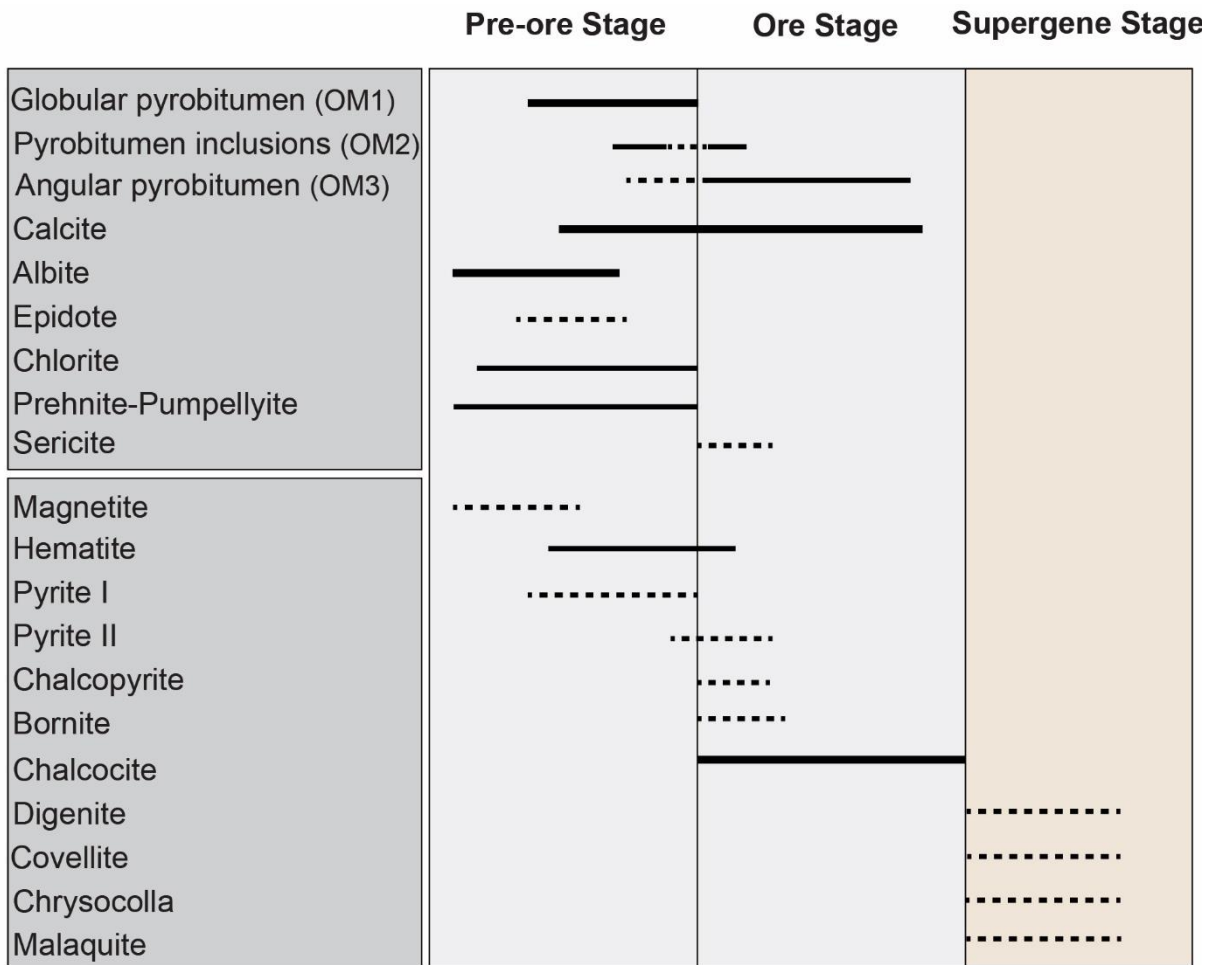


Figure 18. Paragenetic sequence for the Las Luces deposit. The thick bars represent more abundant phases (dashed line, thin line and thick bar indicate low, moderate and abundant, respectively).

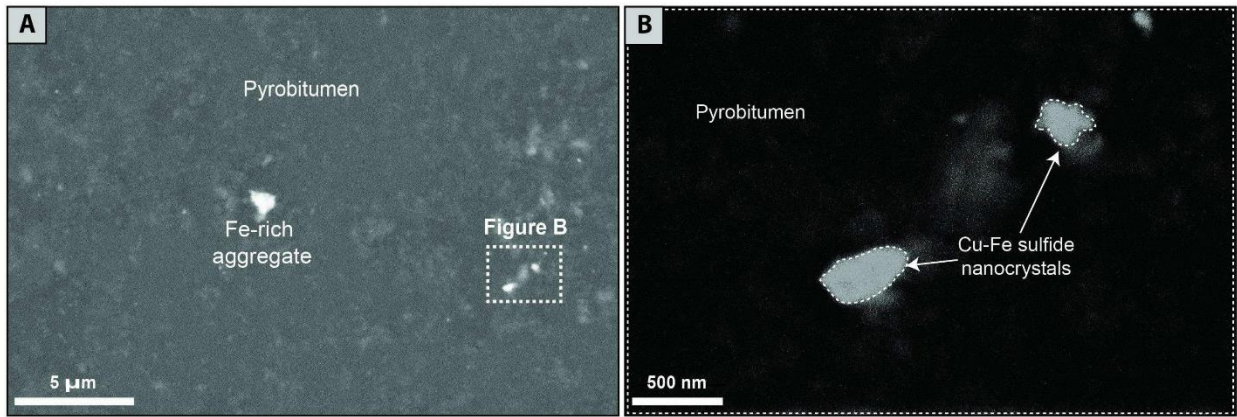


Figure 19. FE-SEM BSE images showing micro- to nano-sized Cu-Fe sulfide inclusions within pyrobitumen. The BSE image on the right (**B**) shows a magnified view of the ~250-500 nm Cu-Fe sulfide nanocrystals.

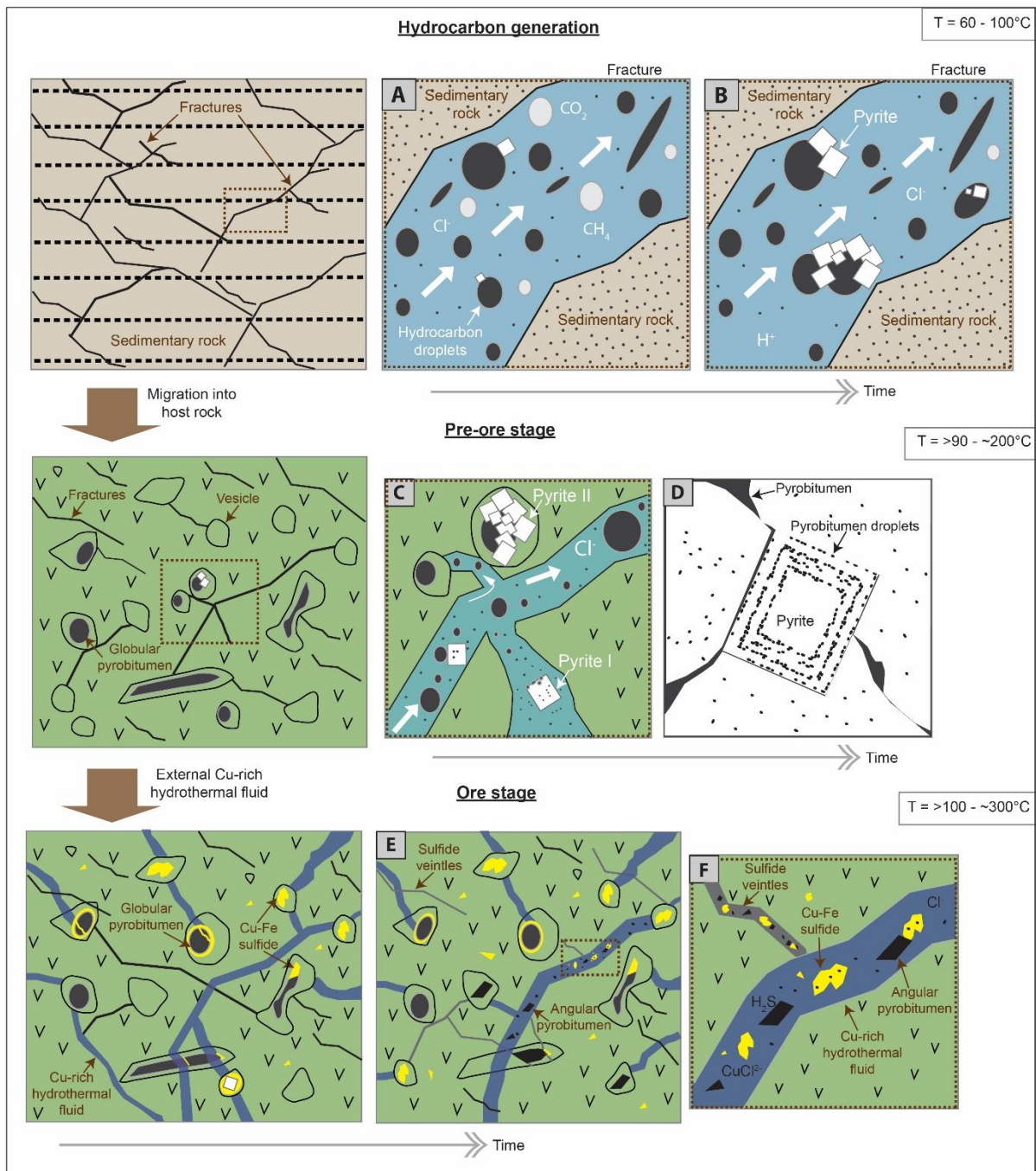


Figure 20. Summary figure showing key processes that led to the formation of the bitumen-bearing Lorena stratabound Cu-(Ag) deposit. **A) and B)** The first stage involves hydrocarbon generation from a sedimentary rock source. Petroleum was mobilized as immiscible droplets in an aqueous fluid through permeability zones. At the same time, hydrocarbon gases were emitted (e.g., CH_4 and CO_2) and pyrite grains are bound by coalescence into the petroleum phase. **C) and D)** Migrated hydrocarbons were injected into the andesite rocks filling vesicles (OM1) and pyrite crystals grew in the presence of hydrocarbons (e.g., OM2). **E) and F)** External Cu-rich fluids circulated through the andesite host rock. The pyrobitumen-fluid interaction triggered Cu sulfide precipitation and a second pulse of hydrocarbon or remobilization event is evidenced by the presence of angular pyrobitumen (OM3) in close association with chalcocite (which can also show bitumen inclusions, OM2). At the same time, the organic phase is affected by thermal cracking, resulting in chemical bond breakage and leading to a slow, gradual released of sulfur as pyrobitumen becomes more aromatized. See text for details.

CHAPTER 3

Trace element geochemistry of pyrite from bitumen-bearing stratabound Cu-(Ag) deposits, northern Chile

Andrea Herazo^{1,2*}, Martin Reich^{1,2}, Fernando Barra^{1,2}, Diego Morata^{1,2}, Irene del Real^{1,2}

¹Department of Geology and Andean Geothermal Center of Excellence (CEGA), FCFM, Universidad de Chile, Plaza Ercilla 803, Santiago, Chile

²Millennium Nucleus for Metal Tracing Along Subduction, FCFM, Universidad de Chile, Santiago, Chile

Published in:

ACS Earth and Space Chemistry

Corresponding author: Andrea Herazo
andrea.herazo@ug.uchile.cl

ABSTRACT

The Coastal Cordillera metallogenic province of northern Chile comprises several styles of mineralization, including stratabound Cu-(Ag), iron oxide-copper-gold (IOCG), iron oxide-apatite (IOA) and porphyry Cu deposits. Stratabound Cu-(Ag) or “Manto-type” deposits from the Coastal Cordillera of northern Chile formed during two main periods, i.e., the Late Jurassic and Late Cretaceous. These deposits are hosted in volcanic and volcano sedimentary rocks and some of them are characterized by the presence of solid hydrocarbons (bitumen), which are closely associated with pyrite and Cu-(Fe) sulfides. Although pyrite is ubiquitous and in some cases abundant in this deposit type, its trace element content and mineralogical form of incorporation, i.e., nanoscale inclusions or solid solution, remains largely unknown. In this study, we focus on pyrite from bitumen-bearing stratabound Cu-(Ag) deposits from northern Chile to assess the formation conditions of these deposits by using a combination of EPMA and LA-ICP-MS. Our results show that pyrite from stratabound Cu-(Ag) deposits hosts significant concentrations of Cu, As, Mn, Pb, Tl, Co, Ni, V and Mo that range from a few parts per million (ppm) to wt.% levels. Among all elements analyzed, Cu, As, Mn and Tl are the most abundant, reaching concentrations up to ~2.8 wt.% (Cu), ~0.25 wt.% (As) ~2.4 wt.% (Mn), and ~0.09 wt.% (Tl). These elements occur dominantly in solid solution, although LA-ICP-MS depth profiles suggest the presence of micro- to nano-sized mineral inclusions. Pyrite from stratabound Cu-(Ag) deposits is characterized by distinctively lower Co/Ni (~0.1 to 10) and Co/Cu ratios (~0.0001 to 10) and higher Ag/Co values (~0.001 to 10) than pyrite from Cretaceous iron oxide-apatite (IOA) and IOCG deposits from the Coastal Cordillera metallogenic province. We interpret these variations as resulting from differences in physico-chemical parameters of the pyrite-forming fluid, i.e., temperature, redox

conditions, and source of metals/sulfur. Based on our data we conclude that pyrite from the studied stratabound Cu-(Ag) deposits formed at relatively low temperatures (100 to ~300°C), reducing conditions, and with a strong sedimentary component as reflected in its trace element geochemistry. Therefore, our data supports the use of the trace element content of pyrite to fingerprint the formation conditions of ore mineralization in different deposit types with possible applications as a vectoring tool within the Coastal Cordillera metallogenic province and elsewhere.

Keywords: pyrite, trace elements, stratabound Cu-(Ag) deposits, Manto-type, Chile.

3.1. INTRODUCTION

The Coastal Cordillera of central-northern Chile hosts a variety of magmatic-hydrothermal mineral systems, including porphyry copper, iron oxide-apatite (IOA), iron oxide-copper-gold (IOCG) and stratabound Cu-(Ag) deposits. Stratabound or “Manto-type” Cu-(Ag) deposits, in particular, are currently the third largest source of copper in Chile after porphyry and IOCG deposits, and are hosted within volcanic and volcano-sedimentary rocks of Jurassic to Cretaceous age located between Santiago and Antofagasta (Fig. 21). These deposits are divided into two groups, the first being hosted by volcanic rocks of Jurassic age in northern Chile (e.g., Mantos Blancos, Michilla, Las Luces) (Orrego et al., 2006; Reich et al., 2013a; Herazo et al., 2020), second is hosted by volcanic and volcano-sedimentary rocks of Lower Cretaceous age in north-central Chile (e.g., El Soldado, Talcuna, Uchumí, La Culebra, Manto Cobrizo) (Herazo et al., 2020; Zentilli et al., 1997; Wilson and Zentilli, 1999; Maeksaev et al., 2007; Cisternas and Hermosilla, 2006; Kojima et al., 2009).

Hypogene mineralization in stratabound Cu-(Ag) deposits comprises bornite, chalcocite and chalcopyrite, with minor pyrite, covellite and digenite/djurlerite (Espinoza et al., 1996; Kojima et al., 2003; Barra et al., 2017). In addition, variable amounts of “invisible” silver are contained in the Cu-bearing sulfides, and in some deposits Ag is recovered as a by-product from Cu mining (Reich et al., 2013a; Reich et al., 2010). One of the most intriguing characteristics of Lower Cretaceous stratabound Cu-(Ag) deposits is the occurrence of variable amounts of solid hydrocarbons (bitumen) in close association with sulfide minerals (Mayer and Fontboté, 1990; Zentilli et al., 1994; Zentilli et al., 1997; Wilson and Zentilli, 1999; Boric et al., 2002; Haggan et al., 2003; Wilson et al., 2003a,b; Cucarella et al., 2005; Cisternas and Hermosilla, 2006; Wilson and Zentilli, 2006; Maeksaev et al., 2007; Rieger et al., 2008; Carrillo-Rosúa et al., 2014). More recently, Herazo et al.5 reported for the first time the presence of bitumen in the Lorena deposit, in Las Luces district, and provided insights on the role of solid hydrocarbons in the ore forming processes. In this study we focus on the geochemistry of pyrite from bitumen-bearing stratabound Cu-(Ag) deposits, northern Chile, in order to further constrain the conditions responsible for the early, pyrite-bearing pre-ore mineralization stage and evaluate the use of specific trace elements than could serve as an exploration tool for these deposits.

Pyrite (FeS₂) is an ubiquitous and sometimes locally abundant phase in stratabound Cu-(Ag) deposits of the Coastal Cordillera of central-northern Chile. Previous studies show that bitumen-bearing deposits are characterized by two main events of hypogene mineralization, i.e., a pre-ore stage where (pyro)bitumen occurs with pyrite, followed by a late Cu-ore stage where pre-ore pyrite can be replaced by chalcopyrite, bornite and hypogene chalcocite (Wilson and Zentilli,

1999; Cisternas and Hermosilla, 2006). Despite being the dominant sulfide in the pre-ore mineralization stage, very few studies have reported information regarding the chemical composition of pyrite and most of them focused on textural descriptions and bulk sulfur isotope ($\delta^{34}\text{S}$) data, e.g., El Soldado (Wilson and Zentilli, 1999); Copiapó district (Cisternas and Hermosilla, 2006); La Serena and Melipilla-Naltahua (Carrillo-Rosúa et al., 2014). Major, minor and trace element data for pyrite are not currently available, but are crucial to better understand the early stages of ore genesis in bitumen-bearing stratabound Cu-(Ag) deposits and to fingerprint the source of metals.

Since the early 1990's, a significant number of microanalytical studies have focused on determining the trace element geochemistry of pyrite in several types of ore deposits (Cook and Chryssoulis, 1990; Fleet et al., 1993; Huston et al., 1995; Large et al., 1999, 2009; Palenik et al., 2004; Vaughan and Kyin, 2004; Reich et al., 2005, 2006, 2013b; Cook et al., 2009; Deditius et al., 2009a, 2011, 2014; Gregory et al., 2015a; Fontboté et al., 2017; Tardani et al., 2017; Keith et al., 2018; Román et al., 2019; Kusebauch et al., 2019; del Real et al., 2020; Crespo et al., 2020). These studies have shown that pyrite chemistry not only allows the fingerprinting of different ore-forming environments, but also can provide information on the chemical and physico-chemical evolution of hydrothermal fluids. Pyrite samples from the Lorena deposit within the Jurassic Las Luces district near Taltal, and from the Lower Cretaceous Manto Cobrizo and La Culebra deposits near Copiapó were selected for this study. Major, minor and trace element data were obtained by using a combination of electron probe microanalysis (EPMA) and laser ablation inductively coupled plasma mass spectrometry (LA-ICP-MS) techniques. The data obtained here are compared to published information on pyrite chemistry from Cretaceous IOA and IOCG deposits located in the Chilean Coastal Cordillera to determine specific chemical signatures in pyrite that could be used to fingerprint and/or as a vectoring tool for stratabound Cu-(Ag) deposits.

3.2. GEOLOGICAL BACKGROUND

During Mesozoic to Cenozoic times, the evolution of the Andean margin was controlled by the subduction of the Farallon oceanic plate under the South American continent, configuring a north-south oriented magmatic arc-backarc setting (Coira, 1982; Mpodozis and Kay, 1992; Buchelt, 1998; Charrier et al., 2007; Coloma et al., 2017; Zentilli et al., 2018). Extensional tectonic conditions characterized the Jurassic-Early Cretaceous period, with intense magmatic activity along the arc and abundant sedimentation in extensional basins in the back-arc region. This extensional setting was generated by the decoupling of an old and cold oceanic plate from the continental plate during renewed subduction (Jaillard et al., 1990). This decoupling induced a slab roll-back resulting in a steep subduction (Barra et al., 2017). In contrast, during the Late Cretaceous to Early Paleogene a compressional tectonic regime resulted in less steep subduction (Coira, 1982; Charrier et al., 2007). During the extensional cycle, several types of mineral deposits were formed in the Coastal Cordillera of northern Chile (between 21° and 33°S) including stratabound Cu-(Ag), iron oxide apatite (IOA) and iron oxide-copper-gold (IOCG) deposits (Maeksaev et al., 2007; Barra et al., 2017).

Las Luces district

The Las Luces district host rocks are dominantly represented by basaltic andesite and andesite lava flows of La Negra and Posada de Los Hidalgos formations of Jurassic age (Fig. 21B). Metasedimentary rocks from the Las Tórtolas (Ordovician to Devonian) and Pan de Azúcar (Hettangian to Sinemurian) formations also outcrop in the area (Naranjo, 1978; Ulriksen, 1979; Bell, 1982; Naranjo and Puig, 1984) (Fig. 20B). Several plutonic bodies of Early Jurassic to Lower Cretaceous age (e.g., Matancilla Plutonic Group; Naranjo and Puig, 1984) intruded the rocks from the La Negra, Las Tórtolas and Pan de Azúcar formations. Marine sediments or metapelitic rocks of the Cifuncho Formation (Upper Triassic) underlie the La Negra Formation (García, 1967; Pichowiak, 1990), whereas volcanic and volcano-sedimentary rocks from the Aeropuerto Formation (Lower Cretaceous) overlie the volcanic rocks of La Negra. The Aeropuerto Formation is completely covered by the unconsolidated Atacama Gravels of Oligocene to Miocene age (Figure. 21B).

The Lorena stratabound deposit has estimated reserves of ~200,000 metric tons @ 1.5% Cu sulfide and ~300,000 metric tons @ 0.9% Cu oxide (Rojo, 2016). The deposit is hosted in volcanic rocks from the La Negra Formation and the Cu mineralization is both structurally and stratigraphically controlled, i.e., associated with breccias bodies spatially related to faults and in amygdaloids from vesicular lavas forming the ore “mantos”. The main structural feature in the deposit is a NW-trending fault where the highest Cu grades are found. At Lorena, the dominant hydrothermal alteration type is albitization with minor epidote, sericite, chlorite and abundant late calcite. Zeolites, prehnite-pumpellyite and minor chalcedony, as well as pyro(bitumen) are also found filling vesicles and in the breccia matrix (Herazo et al., 2020).

Copiapó district

The stratabound deposits in the Copiapó district are hosted within the Lower Cretaceous Pabellón Formation (Fig. 21C). This unit is composed of calcareous sandstone rocks with minor bioextraclastic calcilutites and laminated mudstones, capped by porphyritic lavas and small, irregular lenses of lithic tuffs (Cisternas and Hermosilla, 2006). The Pabellón Formation represents the top of the Chañarcillo group and overlies the shallow marine sedimentary sequences of the Chañarcillo group (e.g., Nantoco Formation, Early Hauterivian), which in turn overlie the volcanic rocks from the Berriasian Punta del Cobre Formation (Marschik and Fontboté, 2001). The Cerrillos Formation (Aptian) is above unconformity with the Pabellón Formation. Calc-alkaline diorite to monzodiorite stocks outcrop in the central part of the district, intruding the Chañarcillo group (Marschik et al., 2003). Finally, unconsolidated sediments (Atacama Gravels) and alluvial deposits are recognized in the area (Fig. 21C).

The Manto Cobrizo deposit (~400,000 metric tons @ 2.0% Cu sulfide) (Gonzalez, 2016), and La Culebra deposit (monthly production of 250 metric tons @ 2.4% Cu sulfide) (Oetiker, 2016) are hosted in the andesitic volcanic unit of the Pabellón Formation. These deposits are stratigraphically controlled and Cu mineralization occurs as veins, veinlets, disseminated grains and filling vesicles. Sulfides are associated with pyrobitumen, and usually form ore “mantos” of up to 10 m thick. Hydrothermal alteration in these deposits includes a moderate to strong Ca-Na metasomatism, silicification and carbonate minerals. Pervasive alteration with potassic feldspar, albite and epidote is also common. Zeolites and chlorite usually are intergrown with Cu sulfides (Cisternas and Hermosilla).

Mineralization in the Las Luces and Copiapó deposits

Regardless of the age the volcanic host rocks, sulfide mineralization in the studied stratabound Cu-(Ag) deposits comprises an assemblage dominated by pyrite-chalcopyrite-bornite-chalcocite with (pyro)bitumen (Cisternas and Hermosilla, 2006; Herazo et al., 2020) (Fig. 22). In the Las Luces and Copiapó districts, the sulfide mineralization has been attributed to two main consecutive stages, i.e., a pre-ore event followed by the main Cu ore stage. Pre-ore mineralization is characterized by a paragenesis of pyrite with magnetite, hematite and minor chalcopyrite, in close association with bitumen (Cisternas and Hermosilla, 2006; Herazo et al., 2020) (Fig. 22A-C). The main Cu mineralization episode, on the other hand, consists mainly of chalcopyrite, bornite, chalcocite and minor sulfosalts (Fig. 22D-F). In Lorena, chalcocite is the dominant Cu sulfide and occurs as disseminated grains, aggregates and filling fractures and amygdales (Fig. 22D). Bitumen is often spatially associated with sulfides from both stages (Herazo et al., 2020). In the Copiapó deposits, chalcopyrite and bornite replaced early pyrite, and comprise the main Cu sulfide assemblage in Manto Cobrizo and La Culebra (Fig. 22E,F). Cu-(Fe) sulfides are intimately associated with solid hydrocarbons filling vesicles and fractures in the host rock forming an interconnected network (Cisternas and Hermosilla, 2006). In both districts, a poorly developed late supergene stage is characterized by the formation of covellite-djurleite aggregates with minor azurite and malachite.

3.3. SAMPLES AND METHODS

A total of nine representative samples from the pre-ore stage in the Lorena, La Culebra and Manto Cobrizo deposits were selected for this study. The samples are characterized by abundant pyrite observed in close association with (pyro)bitumen. Each sample was studied using polarized light microscopy and then analyzed using a FEI Quanta 250 scanning electron microscope (SEM) at the Andean Geothermal Center of Excellence (CEGA), Universidad de Chile. The SEM is equipped with secondary electron (SE), backscattered electron (BSE) and X-ray energy-dispersive spectrometry (X-Act EDS) detectors. Analytical conditions were: accelerating voltage of 15-20 kV, beam current of 1 nA, takeoff angle $\sim 35^\circ$, a spot size of 4-5 μm in diameter, and a working distance of ~ 10 mm.

The concentration of major and minor elements in pyrite was determined by using electron probe microanalysis (EPMA) in two analytical sessions. The first session was carried out at the Peter Hooper GeoAnalytical Laboratory, Washington State University, Pullman, USA, using a JEOL JXA-8500F microprobe, whereas for the second session we used a JEOL JXA-8230 microprobe at the LAMARX Laboratory of the Universidad Nacional de Córdoba, Argentina. The same operating conditions were used in both sessions and included an accelerating voltage of 20 kV, a beam current of 50 nA and a 1 μm beam. No evidence of beam damage on pyrite grains was observed. Elements were acquired using the following analyzing crystals: LiFH for Zn K α , Fe K α , Co K α , Ni K α and Cu K α ; PETJ for Hg K α , Pb M α , S K α , Sb L α , Te L α , Ag L α , Au M α and Bi M β ; TAP for As L α and Se L α . The standards used for calibration included natural and synthetic metals, sulfides and arsenides, including ZnS (for Zn), HgS (for Hg), PbS (for Pb), FeS₂ (for Fe and S), Co⁰ (for Co), (Ni,Fe)₉S₈ (for Ni), Cu₂O (for Cu), FeAsS (for As), ZnSe (for Se), Sb₂S₃ (for Sb), Sb₂Te₃ (for Te), Ag⁰ (for Ag), Au⁰ (for Au) and Bi₁₂GeO₂₀ (for Bi). Counting time (peak) was 10 s for Fe K α , Cu K α , S K α ; 30 s for Zn K α , Ni K α ; Hg K α ; 50 s for Pb M α , Co K α , Ag L α , Bi M β ; 75 s for As L α , Se L α , Sb L α , Te L α and 100 s for Au M α . The same (peak) counting time was used for total background readings. Mean detection limits ranged from 0.01 to 0.04 wt.% for most analyzed elements: S (0.01 wt.%), Fe (0.01 wt.%), Co (0.04 wt.%), Ni (0.01 wt.%), Cu (0.02

wt.%), Au (0.02 wt.%), Ag (0.02 wt.%), Zn (0.02 wt.%), As (0.02 wt.%), Sb (0.02 wt.%), Se (0.02 wt.%), Te (0.02 wt.%), Hg (0.03 wt.%), Pb (0.03 wt.%) and Bi (0.03 wt.%).

Laser ablation inductively coupled plasma mass spectrometry (LA-ICP-MS) spot analyses were performed on selected pyrite grains in order to determine minor and trace element concentrations. LA-ICP-MS analyses were undertaken using a 193 nm ArF excimer laser (Teledyne-Photon Machines Analyte 193) coupled to a quadrupole ICP-MS (Thermo Fisher Scientific iCAP Q) at the Mass Spectrometry Laboratory of the Andean Geothermal Center of Excellence (CEGA), Universidad de Chile. Analyses were performed following the protocol described by Román et al., 2019. The ICP-MS calibration was initiated by ablating a NIST SRM 610 glass reference material, to ensure acceptable levels of plasma robustness (i.e., $^{238}\text{U}^+ / ^{232}\text{Th}^+$ between 0.95 and 1.05), oxide production ($\text{ThO}^+ / \text{Th}^+ < 0.5\%$) and double charged production ($^{22}\text{M}^+ / ^{44}\text{Ca}^{++} < 0.01\%$). Spot analysis was carried out using a laser pulse frequency of 4 Hz, an energy density of 2.5 J/cm², and a laser diameter of 40 μm in most cases. The laser spot size was reduced to 20 μm when analyzing small grains, or to avoid ablating visible mineral inclusions. Pure He was used as carrier gas. Each spot was ablated for 52 s following 30 s of gas background collection. The analyses were bracketed by calibration using the MASS-1 synthetic sulfide reference material (Wilson, 2002), as the primary standard and GSE-1 glass reference material (Jochum et al., 2005), as a secondary standard for quality control. Iron concentrations obtained previously by EPMA were used as an internal standard. External standard measurements were performed at the beginning and at the end of each analysis round of 20 analyses. Data integration and reduction was carried out using the Iolite™ (v. 3.63) data reduction software (Paton et al., 2011). The following isotopes were monitored: ^{34}S , ^{51}V , ^{52}Cr , ^{53}Cr , ^{55}Mn , ^{57}Fe , ^{59}Co , ^{60}Ni , ^{63}Cu , ^{65}Cu , ^{66}Zn , ^{69}Ga , ^{72}Ge , ^{73}Ge , ^{75}As , ^{77}Se , ^{82}Se , ^{95}Mo , ^{97}Mo , ^{107}Ag , ^{109}Ag , ^{111}Cd , ^{115}In , ^{118}Sn , ^{120}Sn , ^{121}Sb , ^{123}Sb , ^{125}Te , ^{182}W , ^{197}Au , ^{202}Hg , ^{205}Tl , ^{206}Pb , ^{207}Pb , ^{208}Pb and ^{209}Bi . Detection limits for the most analyzed elements are: ^{51}V (1.10 ppm), ^{52}Cr (2.70 ppm), ^{55}Mn (1.20 ppm), ^{59}Co (0.27 ppm), ^{60}Ni (0.98 ppm), ^{63}Cu (1.20 ppm), ^{66}Zn (2.90 ppm), ^{72}Ge (1.20 ppm), ^{75}As (2.10 ppm), ^{82}Se (14 ppm), ^{95}Mo (0.40 ppm), ^{107}Ag (0.12 ppm), ^{111}Cd (0.39 ppm), ^{115}In (0.02 ppm), ^{120}Sn (0.15 ppm), ^{121}Sb (0.15 ppm), ^{125}Te (0.54 ppm), ^{197}Au (0.12 ppm), ^{202}Hg (0.30 ppm), ^{205}Tl (0.02 ppm), ^{208}Pb (0.06 ppm) and ^{209}Bi (0.05 ppm).

3.4. RESULTS

3.4.1. Micro-Textural Observations

In the studied samples, pyrite occurs in amygdales, fractures and as disseminated grains within the volcanic host rocks (Fig. 23). Pyrite in all studied samples has euhedral to subhedral shapes, ranging in size between 80 and 900 μm, but occasionally reaching up to 1.5 mm (Fig. 23A,B). Also, aggregates of fine, (sub)-euhedral pyrite crystals can form elongated or rosette-shaped spherules ranging in size between 200 and 1000 μm (Fig. 23C-E). Some of these aggregates display abundant fractures filled with chalcopyrite or gangue minerals (e.g., calcite, hematite and prehnite-pumpellyite) (Fig. 23A,B,D-F). In addition, pyrite is intimately associated with bitumen, where the

latter is observed as inclusions, surrounding or in close contact with pyrite grains (Fig. 23A-F). (Pyro)bitumen was observed in thin sections and detected by EDS analysis. Also, pyrite can be partially replaced by chalcopyrite, bornite, chalcocite and minor covellite (Figs. 22B,E; 23D).

3.4.2. Chemical Composition of Pyrite

All EPMA and LA-ICP-MS data of pyrite are reported in the Appendix and are summarized in Figure 24. A boxplot showing the pyrite data disaggregated per deposit is shown in Figure 25.

Electron microprobe data show that Fe and S range from 44.60 to 47.11 wt.% and 49.61 to 54.92 wt.%, respectively (Annex B.1). Arsenic values above 1 wt.% usually correlate with low S. Copper and As were detected in most analyses (>50%), revealing some of the highest concentrations in the dataset (up to 2.87 wt.% for Cu and 5.22 wt.% for As; Fig. 24). Cobalt, Zn and Au were detected in about 20% of the EPMA data points, with median concentrations of 500, 200 and 400 ppm, respectively. Nickel, Pb, Sb, Se, Te, Bi, Ag and Hg were detected only in a few spots (<12% of the analyses), usually with concentrations <900 ppm (Fig. 24). Silver was detected in six spots, and Pb and Bi in only three.

Minor elements concentrations determined by LA-ICP-MS are broadly consistent with EPMA results, but the former allows us to measure concentrations at the sub-ppm level (Figures. 24 and 25 and Annex B.2), providing a better characterization of minor and trace elements in pyrite. Besides the relatively high Cu, Mn and As contents, which span from a few ppm to wt.% levels (median of ~130, ~80 and ~35 ppm, respectively), Co, Ni, Pb, Se, V, Mo and Tl display concentrations >100 ppm, i.e., Co (0.31 to 460 ppm), Ni (1.28 to 297 ppm), Pb (0.16 to 750 ppm), Se (27 to 1400 ppm), V (1.67 to 299 ppm), Mo (0.75 to 422 ppm) and Tl (0.06 to 904 ppm). All other elements such as Zn, Sb, Te, Bi, Au, Ag, Ge, Sn, Cd, Hg, In are present in concentrations below 100 ppm. Among these, only Sb, Ag, and Ge were frequently detected during LA-ICP-MS analysis (Fig. 24). In general, the concentration range of the analyzed trace elements is similar among the studied deposits; however, some variability is recognized for Cu, Pb, Ag, Mn, Mo and Tl (Fig. 25). For instance, median concentrations of Cu, Pb, Ag and Mn are higher at Manto Cobrizo (Copiapó). On the other hand, Mo concentrations are higher at Lorena, while Tl is relatively enriched at La Culebra (Copiapó) with respect to the two other deposits.

3.5. DISCUSSION

3.5.1. Trace element incorporation in pyrite from stratabound Cu-(Ag) deposits

It is well documented that pyrite can incorporate trace elements in two different mineralogical forms, i.e., as solid solution within the crystal structure and as mineral nanoparticles, nanominerals or nanoscale metal clusters (Simon et al., 1999; Reich et al., 2005; Deditius et al., 2008; Hochella et al., 2008; Deditius et al., 2009b; 2011; Ciobanu et al., 2012; Reich et al., 2013b; Sykora et al., 2018; Gopon et al., 2019; Wu et al., 2019). Those studies have shown that a correct understanding of the mechanism(s) of trace element incorporation into pyrite is fundamental because it provides key evidence of large-scale mineralizing phenomena. Geochemical data presented here show that pyrite from the Lorena, Manto Cobrizo and La

Culebra stratabound Cu-(Ag) deposits had incorporated high amount of Cu, As, Mn, Pb, Tl, Co, Ni, V and Mo (Fig. 24). These elements were detected systematically using EPMA and LA-ICP-MS methods and their concentration can vary from sub-ppm levels up to thousands of ppm.

In particular, Cu shows a large concentration range spanning up to five orders of magnitude (ppm to wt.% levels; Fig. 24). As discussed by Reich et al., 2013b, it is likely that most Cu present in concentrations below ~3 wt.% occurs in solid solution with a substantial fraction accommodated within the pyrite structure through $\text{Cu}^{2+} \leftrightarrow \text{Fe}^{2+}$ substitution (e.g., Einaudi, 1968; Clark, 1970; Radcliffe and McSween, 1969; Pacevski et al., 2008). The relatively flat ^{63}Cu signal in the time-resolved LA-ICP-MS depth profile in Figure 26A is representative of this structural incorporation form. In contrast, analyses with Cu concentrations higher than ~3 wt.%—including some outliers reaching up to ~31 wt.%—strongly suggest the presence of micro- to nano-sized Cu-bearing sulfides that were not visible during petrographic inspection. Cu-bearing inclusions show up in the transient LA-ICP-MS profile as spiky ^{63}Cu signals, in some cases consistent with other profiles as ^{107}Ag (Fig. 26B). On the other hand, Co and Ni most likely occur in solid solution considering their generally lower concentrations (0.31 to 460 ppm and 1.28 to 297 ppm, respectively), and high affinity for isovalent substitution with Fe within the pyrite structure (Reich et al., 2016; Tardani et al., 2017; Román et al., 2019).

Silver concentrations in pyrite are also variable but generally low (0.26 to 300 ppm), and are positively correlated with the Cu content (Annex B.2). It is possible that some Ag contained in solid solution in pyrite was incorporated by replacement in structural sites (Deditius et al., 2014). However, recent studies show that Ag is preferentially incorporated as inclusions in pyrite (Crespo et al., 2020). Our LA-ICP-MS profiles support the notion that most Ag in pyrite is present as submicron-sized inclusions (spiky ^{107}Ag signals in Fig. 26). Such inclusions apparently also contain Cu and possibly Pb (Fig. 25B); therefore, they may correspond to Cu-Ag-Pb-bearing sulfide phases such as chalcopyrite/bornite and galena, or other phases like native Ag, electrum and/or Cu-Ag sulfosalts (Huston et al., 1995; Abraitis et al., 2004; Deditius et al., 2011; Crespo et al., 2020, in press).

Another metal frequently occurring in pyrite in the studied deposits is Pb. Lead concentrations are relatively homogeneous, varying from ~1 to 100s of ppm (up to 900 ppm; Fig. 24). As with Ag, Pb is likely present as mineral inclusions, although isovalent substitution of Fe^{2+} with Pb^{2+} is also possible (Deditius et al., 2008). The presence of Pb submicron-sized inclusions (probably galena) is suggested in LA-ICP-MS profiles (Fig. 26B), where spiky ^{208}Pb signals are observed, in some cases associated with Ag.

Figure 24 shows that pyrite also contains a high concentration of Mn, reaching up to ~2 wt.%. Unlike previously discussed elements—which did not show variations between different textural types of pyrite—Mn concentrations vary distinctly with texture. Pyrite aggregates forming rounded and rosette-like textures (Fig. 23D) show a higher Mn content (mean: 2206 ppm; median: 261 ppm) than (sub)ehedral pyrite grains (Fig. 23F) (mean: 365 ppm; median: 47 ppm). These variations point to a textural control and possibly crystal growth effects on the incorporation of Mn. Euhedral and subhedral pyrite in the studied deposits are usually coarse-grained, sometimes reaching mm sizes, implying slow growth kinetic conditions possibly controlled by diffusional transport of Fe from a hydrothermal fluid. In contrast, pyrite with rosette-like textures may indicate more rapid growth kinetics, enhancing Mn adsorption from local iron oxide sources (Huerta-Díaz, 1992). LA-ICP-MS depth profiles indicate that Mn occurs in both solid solution and as micro-inclusions in pyrite (Fig. 26). The relatively flat ^{55}Mn signal suggests structural incorporation,

while the ^{55}Mn spikes point to the presence of Mn-bearing inclusions (oxi-hydroxide particles?). A high Mn content has been related to pyrite formation with a sedimentary contribution, which is absorbed from seawater and local pore waters in seafloor and/or sedimentary basins (Huerta-Diaz and Morse, 1992; Shikazono et al., 1994; Large et al., 2007, 2009, 2014; Gregory et al., 2015a). The studied stratabound deposits are hosted in volcano-sedimentary sequences where bitumen is intimately associated with both pyrite and Cu sulfides (Cisternas and Hermosilla, 2006; Herazo et al., 2020). Accordingly, the high Mn concentrations can be derived from the sedimentary sources underlying the volcanic host rocks (e.g., Pan de Azúcar Formation for Lorena and Nantoco Formation for the Copiapó district deposits; Fig. 25).

On the other hand, the presence of V in pyrite (1.67 to 299 ppm, Fig. 24)—hydrothermal pyrite range from 0.01 to <60 ppm V, while diagenetic pyrite vary from 3 to <10,000 ppm V (Large et al., 2009)—could point to (pyro)bitumen as a possible source of both Mn and V, which have also been reported as abundant in bitumen (Herazo et al., 2020). Furthermore, the relatively high concentrations of Mo detected in pyrite (0.75 to 422 ppm) also supports a sedimentary or bitumen contribution, as evidenced from pyrite studies in euxinic environments (e.g., Helz et al., 1996; Morse and Luther, 1999; Sundby et al., 2004; Gregory et al., 2015a). Additionally, recent studies have shown that Mo is more likely to be held within organic matter, i.e., fixation and possible reduction of Mo by natural organic matter could be one pathway to explain Mo enrichments (Chappaz et al., 2014), in particular in the Lorena deposit where concentrations of this element is higher. A sedimentary contribution is further supported by the presence of Tl (0.02 to 904 ppm, Fig. 24), based on pyrite geochemistry data from sediment-hosted deposits, such as Carlin-type gold, sedimentary-exhalative (SEDEX) and barite–pyrite (Pb-Zn-Ag) vein deposits (Radtke, 1985; Ikramuddin et al., 1986; Hosfra and Cline, 2000; Reich et al., 2005; Large et al., 2014; Gregory et al., 2015b; Mukherjee and Large, 2017; D’Orazio et al., 2017). The incorporation of Tl and heavy metals such as Au, Hg and Tl is favored by the structural distortion and surface modification caused by the presence of As in pyrite (Lehner et al., 2006, 2012; Deditius et al., 2014; Deditius and Reich, 2016). In stratabound Cu-(Ag) deposits, Tl could have been incorporated into pyrite as both solid solution and sub-micrometer sized mineral inclusions. Although the solubility curve for Tl-As relations has not been determined, Deditius and Reich, 2016 suggested that the upper limit ratio $\text{Tl/As} = 1$ may represent the solid solubility limit in arsenian pyrite (Fig. 27A). Tl-As analyses of the studied pyrite grains, suggest that Tl occurs dominantly as a structurally bound element (plot below the 1:1 line in Fig. 27A), which is corroborated by the generally flat ^{205}Tl signals observed in LA-ICP-MS depth-profiles (Fig. 26A). However, analyses plotting above the 1:1 line are most likely related to the presence of Tl-bearing nanoinclusions (Fig. 27A), which may be represented by ^{205}Tl spikes in LA-ICP-MS depth profiles (Figure. 26B). This seems to be the case, in particular, for the La Culebra deposit, where Tl concentrations are the highest (Fig. 25 and Fig. 27A).

Gold was detected in some spots only and hence, it is only of marginal importance in stratabound Cu-(Ag) deposits. The solubility curve defined by Reich et al., 2005 explains the strong affinity of As with this element, and shows that Au can occur as either a structurally bound element (Au^{1+}) (Merkulova et al., 2019) or forming native Au (Au^0) nanoparticles. Data plotted in the Au-As solubility diagram (Fig. 27B) show that analyses with lower Au/As ratios are related to Au in solid solution, while those with a high Au/As ratio are probably related to the presence of Au-nano- to micro-inclusions. Arsenic concentration in pyrite varies from 4 ppm to ~5 wt.% (Fig. 24), and may occur in solid solution as As^{-1} within the structure, although incorporation as As^{+3} (Deditius et al., 2008; Savage et al., 2000; Manceau et al., 2020) or even as FeAsS nanoclusters and amorphous As-Fe-S nanoscale inclusions (Deditius et al., 2009b), cannot be ruled out (Fig. 27C).

3.5.2. Comparisons with IOA and IOCG deposits within the Coastal Cordillera

In the Coastal Cordillera of northern Chile, stratabound Cu-(Ag) deposits are spatially associated with IOA and IOCG deposits (Maksaev et al., 2007; Barra et al., 2017). Hence, genetic connections between them have been proposed, with some authors suggesting that stratabound or Manto-type deposits are Fe-poor end-members of the IOCG clan or shallow/distal manifestations of IOCG mineralization style (Vivallo and Henríquez 1998; Williams 1999; Pollard 2000; Orrego et al. 2000; Maksaev et al., 2007), while others argue that there is no clear evidence to support a genetic connection to IOCGs (Sillitoe, 2003). Although deposits from the Andean IOCG clan have distinctive characteristics, some common features have been recognized between stratabound Cu-(Ag), IOA and IOCG deposits, such as the abundant presence of iron oxides (hematite and/or magnetite), a conspicuous Ca-Na alteration and a spatial association with upper Jurassic to Lower Cretaceous intrusions (Maksaev and Zentilli, 2002; Maksaev et al., 2007; Sillitoe, 2003; Barton et al., 2014; Barra et al., 2017). As described here, pyrite is ubiquitous in the pre-ore stage of the studied stratabound Cu-(Ag) deposits, and is also present in IOA and IOCG mineralization assemblages. Here, we compare our pyrite trace element data for Lorena, La Culebra and Manto Cobrizo with published information on two large IOA and IOCG deposits within the Coastal Cordillera metallogenic province, i.e., Los Colorados (Reich et al., 2016) and Candelaria (del Real et al., 2020), in order to identify possible chemical similarities or differences. Figure 28A shows a distinct Co-Ni relation for the three deposit types. Pyrite from stratabound Cu-(Ag) deposits is characterized by lower Co and Ni concentrations and a narrower range in Co/Ni ratios (~0.1 to 10) than IOA and IOCG deposits (Co/Ni ~0.01 to >100). Low Co/Ni ratios are generally attributed to low temperature sedimentary environments, while high Co/Ni ratios (usually >1) are associated with high-temperature or magmatic-hydrothermal systems related to mafic sources (Bralia et al., 1979; Mookherjee and Philip, 1979; Bajwah et al., 1987; Large et al., 2009; Koglin et al., 2010; Large et al., 2014; Gregory et al., 2015a; Reich et al., 2016; Román et al., 2019). Hence, we interpret the Co-Ni data as evidence for a high temperature magmatic-hydrothermal fluid in the formation of pyrite from IOA and IOCG systems, whereas pyrite in stratabound deposits is probably related to low temperature hydrothermal fluids of basinal/sedimentary origin, as also supported by the high Mn, Tl and Mo concentrations reported here (Mn: 2 ppm to ~2.4 wt.%; Tl: 0.02 ppm to 0.09 wt.%; Mo: ~1 to 422 ppm; Fig. 24). The low Co and Ni concentrations in pyrite from stratabound Cu-(Ag) deposits are also related to low As concentrations, which are generally higher in pyrite from IOA and IOCG deposits (Fig. 28B,C). In addition, some other chemical trends can be recognized among Cu, Ag and As. The concentration of Cu and Ag are usually higher in stratabound Cu-(Ag) deposits but show significant dispersion in IOA and IOCG deposits (Fig. 28D-F). Further, the pyrite trace metal signature from the Candelaria IOCG deposit suggests the contribution of two competing sources: a magmatic vs. basin-derived components (del Real et al., 2020).

In the Ag/Co versus Co/Cu plot, the three deposit types form distinct clusters that configure an inverse array (Fig. 29). Notably, stratabound Cu-(Ag) deposits are characterized by the highest Ag/Co ratios (~0.001 to 10) and the lowest Co/Cu ratios (~0.0001 to 10). In contrast, pyrite from Candelaria shows the lowest Ag/Co ratios (~0.1 to 10⁻⁶) and the highest Co/Cu ratios (~0.1 to 105). Pyrite in Los Colorados IOA deposit displays intermediate Ag/Co and Co/Cu values, i.e., ~0.01 to 1, and 1 to 10,000, respectively.

Although no experimental partitioning data are available for Cu, Co and Ag in pyrite, it is probable that the characteristic trace element trends observed in [Figure 29](#) are controlled by physico-chemical parameters such as temperature, pH and redox conditions. A similar trend was reported by [Rivas-Romero et al. \(under review\)](#) for pyrite from the Chuquicamata porphyry Cu-Mo deposit, where higher Ag and Cu concentrations are related to the high temperature (600–450°C) potassic alteration, while higher Co contents are associated with low temperature alterations, i.e., quartz-sericite (400–300°C) and chloritic (300–200°C) alterations, suggesting that the Ag/Co and Co/Cu ratios in pyrite could be used as a vectoring tool towards the higher-temperature ore zone in porphyry Cu deposits ([Rivas-Romero et al., under review](#)). The specific controls on the Ag/Co and Co/Cu ratios and the resulting trend observed here are yet to be determined, as more data are needed to evaluate the particular effects of temperature, pH and/or fO_2 on the pyrite composition in each deposit type.

Fluid inclusion data on late quartz and calcite reported by [Kojima et al., 2009](#) show that stratabound Cu-(Ag) deposits formed by hydrothermal fluids of moderate to low temperatures (360–150°C) and variable salinity (~1.5–30 wt.% equiv. NaCl). In contrast, pyrite from the Candelaria IOCG deposit formed under higher temperature conditions (600–394°C) as determined by using the sulfur isotope geothermometer ([del Real et al., 2020](#)). The latter values are consistent with temperatures estimated for the Fe mineralization in the IOCG deposits in the Candelaria district (600–400°C; [Hopf, 1987](#); [Marschick and Fontboté, 2001](#)). In addition, fluid inclusions analyses from quartz and anhydrite in the Candelaria deposit yielded homogenization temperatures between 330 and >470°C ([Ulrich et al., 2001](#); [Marschik and Chiaradia, 2000](#)). On the other hand, recent works estimated temperatures between ~600 up to 850°C for the magnetite-pyrite assemblage in Los Colorados IOA deposit ([Knipping et al., 2015](#); [Bilenker et al., 2016](#); [Reich et al., 2016](#)). Therefore, we argue that temperature exerts a first-order control on the Ag/Co and Co/Cu ratios in pyrite; however, it is likely that pH and fO_2 of the pyrite-forming fluid(s) also play a significant role in the incorporation of trace elements within the pyrite structure (e.g., [Peterson and Mavrogenes, 2014](#); [Tanner et al., 2016](#); [Sanchez-Alfaro et al., 2016](#); [Tardani et al., 2017](#); [Román et al., 2019](#)). In particular, the potential redox effects related to biodegradation of bitumen in stratabound Cu-(Ag) deposits ([Wilson et al., 2003b](#); [Herazo et al., 2020](#)) may also have a critical control on the incorporation of metals into pyrite. All these effects, including possible partitioning related to co-crystallizing sulfide phases, need to be investigated in more detail in future studies.

3.6. CONCLUDING REMARKS

Electron probe and LA-ICP-MS data reveal that pyrite from bitumen-bearing stratabound Cu-(Ag) deposits in northern Chile hosts several trace elements, most notably Cu, As, Mn, Pb, Tl, Co, Ni, V and Mo. Other elements, such as Ag, Au, Bi, Hg, Zn, Te, Sb, Ge, Cd, In Sn and Cr are commonly detected, but are present in low concentrations. The former elements occur dominantly in solid solution, although spikes in depth-concentration LA-ICP-MS profiles also suggest submicron-sized inclusions. In particular, the high concentration of Mn, Mo, V and Tl in pyrite points to a sedimentary/basinal source or could have been derived directly from (pyro)bitumen, which is usually observed in close association with pyrite in the studied deposits ([Cisternas and Hermosilla, 2006](#); [Herazo et al., 2020](#)). The incorporation of trace metals in pyrite is strongly dependent on the main physico-chemical conditions, with temperature evidently being one of the main controls on metal partitioning and possibly the redox effects related to bitumen biodegradation. It is relevant to note that, in spite of differences in their location, host rocks and age

of mineralization, pyrite in both districts (Las Luces and Copiapó) share a similar trace element geochemical signature.

A comparison among Andean IOCG, IOA and stratabound Cu-(Ag) deposits show that pyrite from the latter formed under lower temperature conditions probably with a strong sedimentary contribution. In contrast, a main magmatic-hydrothermal component is inferred for IOA and IOCG deposits based on higher Co/Ni ratios in pyrite. In addition, pyrite from stratabound deposits has a geochemical signature characterized by a high Ag/Co and low Co/Cu ratios, and low Co-Ni concentrations in comparison with Andean IOA and IOCG pyrite. Future studies should further evaluate the potential applications of the Ag/Co and Co/Cu ratios in pyrite as a complementary tool for exploration of stratabound Cu-(Ag), IOCG and IOA deposits within the Coastal Cordillera of central-northern Chile, and possibly elsewhere.

3.7. ACKNOWLEDGMENTS

Funding for this study was provided by ANID through Millennium Science Initiative Program (NCN13_065) “Millennium Nucleus for Metal Tracing Along Subduction, and FONDECYT grants #1140780 and #1190105. The authors acknowledge additionally support from ANID-FONDAP project 15090013 “Centro de Excelencia en Geotermia de Los Andes, CEGA. The LA-ICP-MS analytical work was funded by ANID-FONDEQUIP instrumentation grant EQM120098. We thank technical assistance of Rurik Romero during LA-ICP-MS analyses. Compañía Minera Las Cenizas and Compañía Minera Carmen Bajo are acknowledged for providing access to the deposits. Andrea Paola Herazo thanks financial support provided by a Doctoral scholarship from ANID (21171385) and the Hugh McKinstry grant from the Society of Economic Geologists Foundation (SEGF). We thank associate editor Sumit Chakraborty for handling the manuscript. Three anonymous reviewers are acknowledged for their helpful comments and suggestions.

3.8. REFERENCES

- Abraitis, P. K.; Patrick, R. A. D.; Vaughan, D. J., 2004. Variations in the compositional, textural and electrical properties of natural pyrite: a review. *Int. J. Miner. Process.* 74, 41–59.
- Arévalo, C.; Pérez, Y.; Espinoza, M., 2009. Geología de la Cuenca del Río Copiapó: Carta Copiapó, Región de Atacama, escala 1:100.000. Servicio Nacional de Geología y Minería, 4 (in Spanish).
- Bell, C.M., 1982. The Lower Paleozoic metasedimentary basement of the Coastal Range of Chile between 25°30' and 27°S. *Revista Geológica de Chile*, 17, 21–29 (in Spanish).
- Bajwah, Z. U.; Seccombe, P. K.; Offler, R., 1987. Trace element distribution, Co:Ni ratios and genesis of the big cadia iron-copper deposit, new south wales, Australia. *Miner. Depos.* 22, 292–300.
- Barra, F.; Reich, M.; Selby, D.; Rojas, P.; Simon, A.; Salazar, E.; Palma, G., 2017. Unraveling the origin of the Andean IOCG clan: A Re-Os isotope approach. *Ore Geol. Rev.* 81, 62–78.

- Barton, M.D., 2014 Iron oxide(-Cu-Au-REE-P-Ag-U-Co) systems. *Treatise Geochem.* 13, 515–541.
- Bilenker, L.D.; Simon, A.C.; Reich, M.; Lundstrom, C.C.; Gajos, N.; Bindeman, I.; Barra, F.; Munizaga, R., 2016. Fe–O stable isotope pairs elucidate a high-temperature origin of Chilean iron oxide-apatite deposits. *Geochim. Cosmochim. Acta*, 177, 94–104.
- Boric, R.; Holmgren, C.; Wilson, N.S.F.; Zentilli, M., 2002. The Geology of the El Soldado Manto Type Cu (Ag) Deposit, Central Chile; in Porter, T.M. (Ed.), *Hydrothermal Iron Oxide Copper-Gold & Related Deposits: A Global Perspective, Volume 2*; PGC Publishing, Adelaide, 163–184.
- Bralia, A.; Sabatini, G.; Troja, F., 1979. A revaluation of the Co/Ni ratio in pyrite as geochemical tool in ore genesis problems. *Miner. Depos.* 14, 353–374.
- Buchelt, M., Téllez, C., 1998. The Jurassic La Negra Formation in the area of Antofagasta, northern Chile (lithology, petrography, geochemistry). In: Bahlburg, H., Brektrouz, C., Giese, P. (Eds.). *The Southern Central Andes Lecture Notes in Earth Sciences 17*. Springer, Heidelberg, 171–182.
- Carrillo-Rosúa, J.; Boyce A.; Morales-Ruano, S.; Morata, D.; Roberts, S.; Munizaga, F.; Moreno-Rodríguez, V., 2014. Extremely negative and inhomogeneous sulfur isotope signatures in Cretaceous Chilean manto-type Cu-(Ag) deposits, Coastal Range of central Chile. *Ore Geol. Rev.* 56, 3–24.
- Cisternas, E.; Hermosilla, J., 2006. The role of bitumen in strata-bound copper deposit formation in the Copiapó area, Northern Chile. *Miner. Depos.* 41, 339–355.
- Ciobanu, C.L.; Cook, N.J.; Utsunomiya, S.; Kogagwa, M.; Green, L.; Gilbert, S.; Wade, B., 2012. Gold-telluride nanoparticles revealed in arsenic-free pyrite. *Am. Mineral.* 97, 1515–1518.
- Charrier, R., Pinto, L., Rodríguez, M.P., 2007. Tectonostratigraphic evolution of the Andean Orogen in Chile. In: Moreno, T., Gibbons, W. (Eds) *The geology of Chile*. The Geological Society, London, 21–114.
- Chappaz, A.; Lyons, T.W.; Gregory, D.D.; Reinhard, C.T.; Gill, B.C.; Li, C.; Large, R.R., 2014. Does pyrite act as an important host for molybdenum in modern and ancient euxinic sediments?. *Geochim. Cosmochim. Acta*, 126, 112–122.
- Clark, A.H., 1970. Copper zoning in pyrite from Cerro de Pasco, Perú: further discussion. *Am. Mineral.* 55, 525–527.
- Coira, B., Davidson, C., Mpodozis, C., Ramos, V., 1982. Tectonic and magmatic evolution of the Andes of northern Argentina and Chile. *Earth Sci. Rev. Issue 18*, 303–332.
- Coloma, F., Valin, X., Oliveros, V., Vásquez, P., Creixell, C., Salazar, E., Ducea, M., 2017. Geochemistry of Permian to Triassic igneous rocks from northern Chile (28°–30°15'S): implications on the dynamics of the proto-Andean margin. *Andean Geol.* 44, 147–178.
- Cook, N.J. and Chryssoulis, S.L., 1990. Concentrations of invisible gold in the common sulfides. *Can. Mineral.* 28, 1–16.
- Cook, N.J.; Ciobanu, C.L.; Mao, J., 2009. Textural control on gold distribution in As-free pyrite from the Dongping, Huangtuliang and Hougou gold deposits, North China Craton (Hebei Province, China). *Chem. Geol.* 264, 101–121.

Crespo, J.; Reich, M.; Barra, F.; Verdugo, J.J.; Martínez, C.; Leisen, M.; Romero, R.; Morata, D.; Marquardt, C., 2020. Occurrence and distribution of silver in the world-class Río Blanco porphyry Cu-Mo deposit, Central Chile. *Econ. Geol.* 115, 8, 1619–1644.

Cucurella, J.; Canut de Bon, C.; Cisternas, M.E., 2005. Pyrobitumen related to silver-copper deposits in a Cretaceous volcanic-sedimentary sequence: Talcuna district, Coquimbo, Chile. *Mineral. Polonica* 36, 1, 21–29.

Detlef, K., 2002. Geologisch-tektonische Karte der Küstenkordillere südlich von Taltas (Nordchile). Maßstab 1:150.000.

Deditius, A.P.; Utsunomiya, S.; Renock, D.; Ewing, R.C.; Ramana, C.V.; Becker, U.; Kesler, S.E., 2008. A proposed new type of arsenian pyrite: composition, nanostructure and geological significance. *Geochim. Cosmochim. Acta* 72, 2919–2933.

Deditius, A.P.; Utsunomiya, S.; Ewing, R.C.; Chryssoulis, S. L.; Venter, D.; Kesler, S.E., 2009. Decoupled geochemical behavior of As and Cu in hydrothermal systems. *Geology* 37, 707–710.

Deditius, A.P.; Utsunomiya, S.; Ewing, R.C.; Kesler, S.E., 2009. Nanoscale “liquid” inclusions of As-Fe-S in arsenian pyrite. *Am. Mineral.* 94, 391–394.

Deditius, A.P.; Utsunomiya, S.; Reich, M.; Kesler, S.E.; Ewing, R.C.; Hough, R.; Walshe, J., 2011. Trace metal nanoparticles in pyrite. *Ore Geol. Rev.* 42, 32–46.

Deditius, A.P.; Reich, M.; Kesler, S.E.; Utsunomiya, S.; Chryssoulis, S.L.; Walshe, J.; Ewing, R.C., 2014. The coupled geochemistry of Au and As in pyrite from hydrothermal ore deposits. *Geochim. Cosmochim. Acta* 140, 644–670.

Deditius, A.P.; Reich, M., 2016. Constraints on the solid solubility of Hg, Tl, and Cd in arsenian pyrite. *Am. Mineral.* 101, 1451–1459.

D’Orazio, M.; Biagioni, C.; Dini, A.; Vezzoni, S., 2017. Thallium-rich pyrite ores from the Apuan Alps, Tuscany, Italy: constraints for their origin and environmental concerns. *Miner. Depos.* 52, 687–707.

Einaudi, M.T., 1968. Copper zoning in pyrite from Cerro de Pasco, Perú. *Am. Mineral.* 53, 1748–1752.

Espinoza, S.; Véliz, H.; Esquivel, J.; Arias, J.; Moraga, A., 1996. The cupriferous province of the Coastal Range, northern Chile; in: Camus, F.; Sillitoe, R.H.; Petersen, R. (Eds.), *Andean Copper Deposits: New Discoveries, Mineralization, Styles and Metallogeny*. Society of Economic Geologist Sp Pub, 5, 19–32.

Fleet, M.E.; Chryssoulis, S.L.; MacLean, P.J.; Davidson, R.; Weisener, C.G., 1993. Arsenian pyrite from gold deposits; Au and As distribution investigated by SIMS and EMP, and color staining and surface oxidation by XPS and LIMS. *Can. Miner.* 31, 1–17.

Fontboté, L.; Kouzmanov, K.; Chiaradia, M.; Pokrovski, G.S., 2017. Sulfide minerals in hydrothermal deposits. *Elements*, 13, 97–103.

García, F., 1967. Geología del Norte Grande de Chile, Simposio, Geosinclinal Andino, Sociedad Geológica de Chile. *Publicaciones* 3, 138 (in Spanish).

Gregory, D.D.; Large, R.R.; Halpin, J.A.; Baturina, E.L.; Lyons, T.W.; Wu, S.; Danyushevsky, L.; Sack, P.J.; Chappaz, A.; Maslennikov, V.V.; Bull, S.W., 2015a. Trace element content of sedimentary pyrite in black shales. *Econ. Geol.* 110, 1389–1410.

Gregory, D.D.; Large, R.R.; Halpin, J.A.; Steadman, J.A.; Hickman, A.H.; Ireland, T.R.; Holden, P., 2015b. The chemical conditions of the late Archean Hamersley basin inferred from whole rock and pyrite geochemistry with $D^{33}S$ and $\delta^{34}S$ isotope analyses. *Geochim. Cosmochim. Acta* 149, 223–250.

Gonzalez, C., 2016. Manto Cobrizo Staff. Personal Communication.

Gopon, P.; Douglas, J.O.; Auger, M.A.; Hansen, L.; Wade, J.; Cline, J.S.; Robb, L.J.; Moody, M.P., 2019. A Nanoscale Investigation of Carlin-Type Gold Deposits: An Atom-Scale Elemental and Isotopic Perspective. *Econ Geol.* 114, 1123–1133.

Haggan, T.; Parnell, J.; Cisterna, M.E., 2003. Fluid history of andesite-hosted CuS-bitumen mineralization, Copiapó district, north central Chile. *J. Geochem. Explor.* 78–79, 631–633.

Helz, G.R.; Miller, C.V.; Charnock, J.M.; Mosselmans, J.F.W.; Patrick, R.A.D.; Garner, C.D.; Vaughan, D.J., 1996. Mechanism of molybdenum removal from the sea and its concentration in black shales. EXAFS evidence. *Geochim. Cosmochim. Acta* 60, 3631–3642.

Herazo, A.; Reich, M.; Barra, F.; Morata, D.; del Real, I.; Pagès, A., 2020 Assessing the role of bitumen in the formation of stratabound Cu-(Ag) deposits: Insights from the Lorena deposit, Las Luces district, northern Chile. *Ore Geol. Rev.* 124, 103639.

Hermosilla, J., 2001. Rol de la materia orgánica en la formación de los depósitos minerales del Metalotecto Ocoita-Pabellón. Copiapó, III Región de Atacama. Undergraduate Thesis, Departamento de Ciencias de la Tierra, Universidad de Concepción, 213 (in Spanish).

Hochella, M.F.; Lower, S.K.; Maurice, P.A.; Penn, R.L.; Sahai, N.; Sparks, D.L.; Twining, B.S., 2008. Nanominerals, Mineral Nanoparticles, and Earth Systems. *Science* 319, 1631–1635.

Hofstra, A.H.; Cline, J.S., 2000. Characteristics and Models for Carlin-Type Gold Deposits. *Reviews in Econ. Geol.* 13.

Hopf, S., 1987. Petrographische, Mineralogische und Geochemische Beobachtungen an der Cu-Lagerstätte Agustina/Distrikt Punta del Cobre/Chile: Unpublished Diplomarbeit, Heidelberg, Universität Heidelberg, 144.

Huerta-Díaz, M.; Morse, J., 1992. Pyritization of trace metals in anoxic marine sediments. *Geochim. Cosmochim Acta* 56, 2681–2702.

Huston, D. L.; Sie, S.H.; Suter, G.F.; Cooke, D.R.; Both, R.A., 1995. Trace elements in sulfide minerals from eastern Australian volcanic-hosted massive sulfide deposits; Part I, proton microprobe analyses of pyrite, chalcopyrite, and sphalerite, and Part II, selenium levels in pyrite; comparison with $\delta^{34}S$ values and implications for the source of sulfur in volcanogenic hydrothermal systems. *Econ. Geol.* 90, 1167–1196.

Ikramuddin, M.; Besse, L.; Nordstrom, M., 1986 Thallium in the Carlin-type gold deposits. *Appl. Geochem.* 1, 493–502.

Jaillard, E.; Soler, P.; Carrier, G.; Mourier, T., 1990. Geodynamic evolution of the northern and central Andes during early to middle Mesozoic times: a Tethyan model. *J. Geol. Soc. Lond.* 147, 1009–1022.

Jochum, K.P.; Willbold, M.; Raczek, I.; Stoll, B.; Herwig, K., 2005. Chemical characterisation of the USGS reference glasses GSA-1G, GSC-1G, GSD-1G, GSE-1G, BCR-2G, BHVO-2G and BIR-1G using EPMA, ID-TIMS, ID-ICP-MS and LAICP-MS. *Geostand. Geoanal. Res.* 29, 285–302.

Keith, M.; Smith, D.; Jenkin, G.; Holwell, D.; Dye, M., 2018. A review of Te and Se systematics in hydrothermal pyrite from precious metal deposits: Insights into ore-forming processes. *Ore Geol. Rev.* 96, 269–282.

Koglin, N.; Frimmel, H.E.; Minter, W.E.L.; Brätz, H., 2010. Trace-element characteristics of different pyrite types in Mesoarchaeon to Palaeoproterozoic placer deposits. *Miner. Depos.* 45, 259–280.

Kojima, S.; Astudillo, J.; Rojo, J.; Tristá, D.; Hayashi, K., 2003. Ore mineralogy, fluid inclusion, and stable isotopic characteristics of stratiform copper deposits in the coastal Cordillera of northern Chile. *Miner. Depos.* 38, 208–216.

Kojima, S.; Tristá-Aguilera, D.; Hayashi, K., 2009. Genetic aspects of the manto-type copper deposits based on geochemical studies of North Chilean deposits. *Resour. Geol.* 59, 1, 87–98.

Knipping, J.L.; Bilenker, L.D.; Simon, A.C.; Reich, M.; Barra, F.; Deditius, A.P.; Wälle, M.; Heinrich, C.A.; Holtz, F.; Munizaga, R., 2015. Trace elements in magnetite from massive iron oxide-apatite deposits indicate a combined formation by igneous and magmatic-hydrothermal processes. *Geochim. Cosmochim. Acta* 171, 15–38.

Kusebauch, C.; Gleeson, S.A.; Oelze, M., 2019. Coupled partitioning of Au and As into pyrite controls formation of giant Au deposits. *Sci. Adv.* 5, eaav5891.

Large, D.J.; Sawlowocz, Z.; Spratt, J.A., 1999. Cobaltite-framboidal pyrite association from the Kupferschiefer; possible implications for trace element behaviour during the earliest stages of diagenesis. *Mineral. Mag.* 63, 353–361.

Large, R.R.; Maslennikov, V.V.; Robert, F.; Danyushevsky, L.V.; Chang, Z., 2007. Multistage sedimentary and metamorphic origin of pyrite and gold in the Giant Sukhoi log deposit, Lena Gold Province, Russia. *Econ. Geol.* 102, 1233–1267.

Large, R.R.; Danyushevsky, L.; Hollit, C.; Maslennikov, V.; Meffre, S.; Gilbert, S.; Bull, S.; Scott, R.; Emsbo, P.; Thomas, H.; Singh, B.; Foster, J., 2009. Gold and trace element zonation in pyrite using a laser imaging technique: Implications for the timing of gold in orogenic and carlin-style sediment-hosted deposits. *Econ. Geol.* 104, 635–668.

Large, R.R.; Halpin, J.A.; Danyushevsky, L.V.; Maslennikov, V.V.; Bull, S.W.; Long, J.A.; Gregory, D.D.; Lounejeva, E.; Lyons, T.W.; Sack, P.J.; McGoldrick, P.J.; Calver, C.R., 2014. Trace element content of sedimentary pyrite as a new proxy for deep-time ocean-atmosphere evolution. *Earth Planet. Sci. Lett.* 389, 209–220.

Lehner, S.W.; Savage, K.; Ayers, J.C., 2006. Vapour growth and characterization of pyrite (FeS₂) doped with Ni, Co, and As: Variations in semiconducting properties, 2006. *J. Cryst. Growth* 286, 306–317.

- Lehner, S.W.; Newman, N.; van Schilfgaarde, M.; Bandyopadhyay, S.; Savage, K.; Buseck, P., 2012. Defect energy levels and electronic behaviour of Ni-, Co-, and As-doped synthetic pyrite (FeS₂) J. Appl. Phys. 111, 083717.
- Maksaev, V.; Zentilli, M., 2002. Chilean strata-bound Cu–(Ag) deposits: an overview. In: Porter, T.M. (Ed.), Hydrothermal Iron Oxide Copper–Gold & Related Deposits. A Global Perspective. PGC Publishing, Adelaide, 85-205.
- Maksaev, V.; Townley, B.; Palacios, C.; Camus, F., 2007. Metallic ore deposits; in: Moreno, T.; Gibbons, W. (Eds.), The Geology of Chile. The Geological Society, London, 179–199.
- Manceau, A.; Merkulova, M.; Mathon, O.; Glatzel, P.; Murdzek, M.; Batanova, V.; Simionovici, Al.; Steinmann, S.N.; Paktunc, D., 2020. The Mode of Incorporation of As^(-I) and Se^(-I) in Natural Pyrite Revisited. ACS Earth Space Chem. 4, 3, 379–390.
- Marschik, R. and Chiaradia, 2000. Lead isotope signatures of ore, volcanic, and batholith rocks of the Candelaria-Punta del Cobre area. 31st International Geological Congress. Rio de Janeiro, Brazil.
- Marschik, R. and Fontboté, L., 2001. The Punta del Cobre Formation, Punta del Cobre-Candelaria area, northern Chile. J. South Am. Earth Sci. 14, 401–433.
- Marschik, R.; Fontignie, D.; Chiaradia, M.; Voldet, P., 2003. Geochemical and Sr–Nd–O isotope composition of granitoids of the Early Cretaceous Copiapó plutonic complex (27°30' S), Chile. J. South. Am. Earth Sci. 16, 381–398.
- Mayer, C.K.; Fontboté, L., 1990. The stratiform Ag-Cu deposit El Jardín, Northern Chile; in: Fontboté, L.; Amstutz, G.C.; Cardozo, M.; Cedillo, E.; Frutos, J. (Eds.), Stratabound ore deposits in the Andes. Berlin, Springer, 637–646.
- Merkulova, M.; Mathon, O.; Glatzel, P.; Rovezzi, M.; Batanova, V.; Marion, P.; Boiron, M.C.; Manceau, A., 2019. Revealing the Chemical Form of “Invisible” Gold in Natural Arsenian Pyrite and Arsenopyrite with High Energy-Resolution X-ray Absorption Spectroscopy. ACS Earth Space Chem. 3, 9, 1905–1914.
- Morse, J.W. and Luther, G.W.I.I.I., 1999. Chemical influences on trace metal-sulfide interactions in anoxic sediments. Geochim. Cosmochim. Acta 63, 3373–3378.
- Mukherjee, I.; Large, R., 2017. Application of pyrite trace element chemistry to exploration for SEDEX style Zn-Pb deposits McArthur basin, northern territory, Australia. Ore Geol. Rev. 81, 4, 1249–1270.
- Mookherjee, A. and Philip, R., 1979 Distribution of copper, cobalt and nickel in ores and host-rocks, Inghadhah, Karnataka, India. Miner Depos. 14, 33–55.
- Mpodosis, C., Kay, S.M., 1992. Late Paleozoic to Triassic evolution of the Gondwana margin: Evidence from Chilean Frontal Cordilleran batholiths (28°S to 31°S). Geological Society of America Bulletin, 04, 999–1014.
- Naranjo, J., 1978. Geología de la zona interior de la Cordillera de la Costa entre los 26°20' Sur, Región de Atacama. Carta Geológica de Chile, escala 1:100.000. Instituto de Investigaciones Geológicas, 34, 48 (in Spanish).

- Naranjo, J. and Puig, A., 1984 Hojas Taltal y Chañaral, Regiones de Antofagasta y Atacama, escala 1: 250.000, Carta Geológica de Chile, N° 62–63 (in Spanish).
- Oetiker, R., 2016. Modelo Metalogénico y Potencial Económico de Mina La Culebra, Región de Atacama, Chile. Tesis de Pregrado, Universidad de Atacama. (in Spanish).
- Orrego, M.; Robles, W.; Sanhueza, A.; Zamora, R.; Infanta J., 2006. Mantos Blancos y Manto Verde: depositos del tipo Fe-Cu-Au? Una comparación con implicancias en la exploración. Actas 9° Congreso Geológico Chileno, 2, 145–149 (in Spanish).
- Pacevski, A.; Libowitzky, E.; Zivkovic, P.; Dimitrijevic, R.; Cvetkovic, L., 2008. Copper-bearing pyrite from the Coka Marin polymetallic deposit, Serbia: mineral inclusions or true solid-solution?. *Can. Mineral.* 46, 249–261.
- Palenik, C.S.; Utsunomiya, S.; Reich, M.; Kesler, S.E.; Wang, L.; Ewing, R.C., 2004. “Invisible” gold revealed: direct imaging of gold nanoparticles in a Carlin-type deposit. *Am. Mineral.* 89, 1359–1366.
- Paton, C.; Hellstrom, J.; Paul, B.; Woodhead, J.; Hergt, J., 2011. Iolite: freeware for the visualisation and processing of mass spectrometric data. *J. Anal. At. Spectrom.* 26, 2508–2518.
- Peterson E.C. and Mavrogenes J.A., 2014. Linking high-grade gold mineralization to earthquake-induced fault-valve processes in the Porgera gold deposit, Papua New Guinea. *Geology* 42, 383–386.
- Pichowiak, S.; Buchelt, M.; Damm, K.W., 1990. Magmatic activity and tectonic setting of the early stages of the Andean cycle in northern Chile. *Geol. Soc. Am. Sp Pub* 241, 127–144.
- Pollard, P.J., 2000. Evidence of a magmatic fluid and metal source for Fe-oxide Cu-Au mineralization. In: Porter, T.M. (Ed.). *Hydrothermal Iron Oxide Copper-Gold and Related Deposits: A Global Perspective*. Australian Mineral Foundation, Adelaide, 27–46.
- Radtke, A., 1985. *Geology of the Carlin Gold Deposit, Nevada*. U.S. Geological Survey Professional Paper, 1267.
- Radcliffe, D. and McSween, H.Y., 1969. Copper zoning in pyrite from Cerro de Pasco, Perú: a discussion. *Am. Mineral.* 1216–1217.
- del Real, I.; Thompson, J.F.H.; Simon, A.C.; Reich, M., 2020. Geochemical and isotopic signature of pyrite as a proxy for fluid source and evolution in the Candelaria-Punta del Cobre IOCG district, Chile. *Econ. Geol.* 115, 7, 1493–1518.
- Reich, M.; Kesler, S.E.; Utsunomiya, S.; Palenik, C.S.; Chryssoulis, S.L.; Ewing, R.C., 2005. Solubility of gold in arsenian pyrite. *Geochim. Cosmochim. Acta* 69, 2781–2796.
- Reich, M.; Utsunomiya, S.; Kesler, S.E.; Wang, L.; Ewing, R.C.; Becker, U., 2006. Thermal behavior of metal nanoparticles in geologic materials. *Geology* 34, 1033–1036.
- Reich, M.; Chryssoulis, S.; Deditius, A.; Palacios, C.; Zuniga, A.; Weldt, M.; Alvear, M., 2010. “Invisible” silver and gold in supergene digenite (CuS). *Geochem. Cosmochim. Acta* 74, 6157–6173.
- Reich, M.; Palacios, C.; Barra, F.; Chryssoulis, S., 2013a. “Invisible” silver in chalcopyrite and bornite from the Mantos Blancos copper deposit. *Eur. J. Mineral.* 25, 453–460.

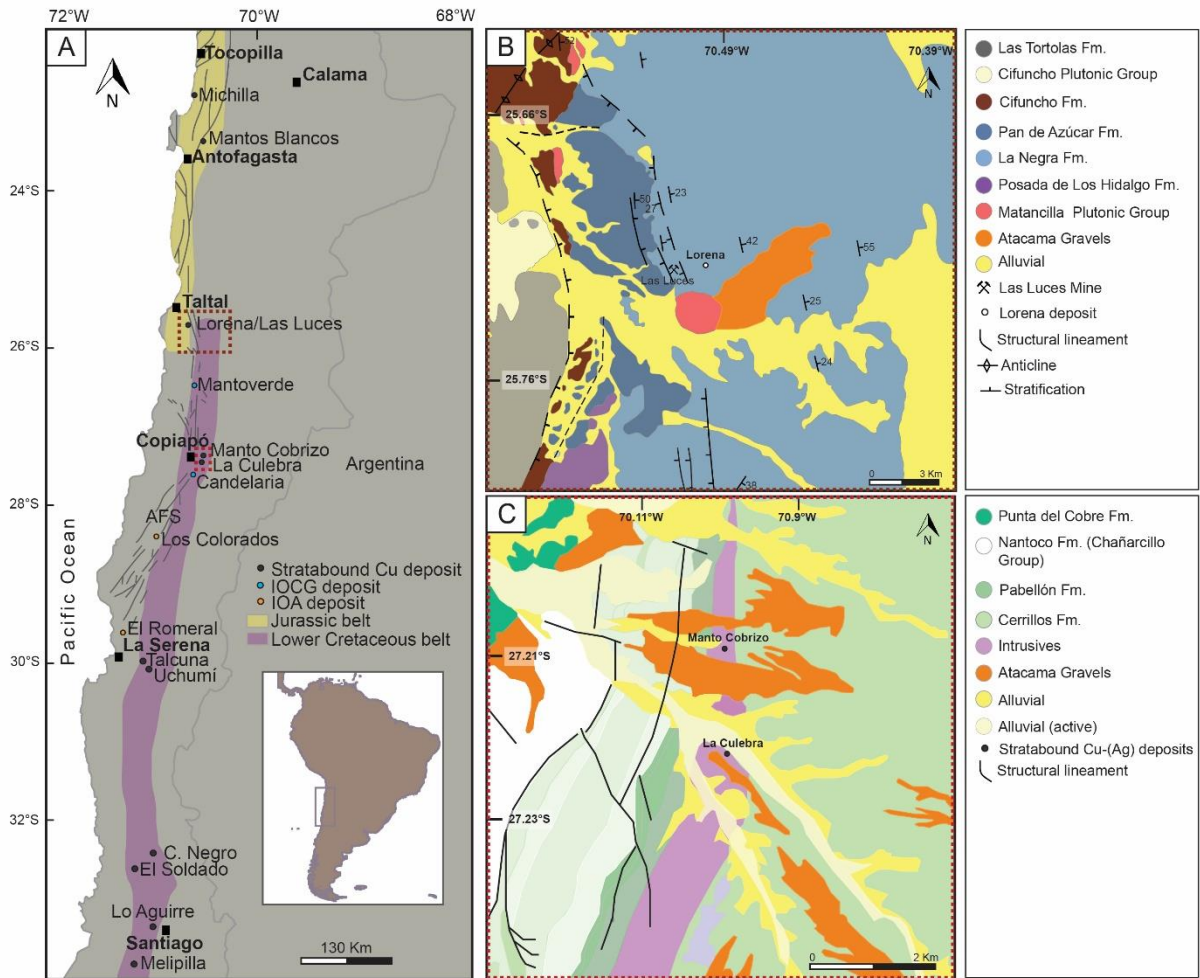
- Reich, M.; Deditius, A.; Chryssoulis, S.; Li, J.W.; Ma, C.Q.; Parada, M.A.; Barra, F.; Mittermayr, F., 2013b. Pyrite as a record of hydrothermal fluid evolution in a porphyry copper system: a SIMS/EMPA trace element study. *Geochim. Cosmochim. Acta* 104, 42–62.
- Reich, M.; Simon, A.C.; Deditius, A.; Barra, F.; Chryssoulis, S.; Lagas, G.; Tardani, D.; Knipping, J.; Bilenker, L.; Sánchez-Alfaro, P.; Roberts, M.P.; Munizaga, R., 2016. Trace element signature of pyrite from the Los Colorados Iron Oxide-Apatite (IOA) deposit, Chile: a missing link between Andean IOA and Iron Oxide Copper-Gold systems?. *Econ. Geol.* 111, 743–761.
- Rieger, A.; Schwark, L.; Cisternas, M.E.; Miller, H., 2008. Genesis and Evolution of Bitumen in Lower Cretaceous Lavas and Implications for Strata-bound Copper Deposits, North Chile. Society of Economic Geologists, Inc. *Econ. Geol.* 103, 387–404.
- Rivas-Romero, C.; Reich, M.; Barra, F.; Gregogy, D.; Pichott, S., 2020. The relation between trace element composition of Cu-(Fe) sulfides and hydrothermal alteration in a porphyry copper deposit: insights from the Chuquicamata Underground mine, Chile. *Miner. Depos.* (under review).
- Royo, M.; Knabe, J., 2016. Lorena Staff. Personal Communication.
- Román, N.; Reich, M.; Leisen, M.; Morata, D.; Barra, F., 2019. Geochemical and micro-textural fingerprints of boiling in pyrite. *Geochim. Cosmochim. Acta*, 246, 60–85.
- Sánchez-Alfaro, P.; Reich, M.; Driesner, T.; Cembrano, J.; Arancibia, G.; Pérez-Flores, P.; Heinrich, C.A.; Rowland, J.; Tardani, D.; Lange, D.; Campos, E., 2016. The optimal windows for seismically-enhanced gold precipitation in the epithermal environment. *Ore Geol. Rev.* 79, 463–473.
- Savage, K.S.; Tingle, T.N.; O'Day, P.A.; Waychunas, G.A.; Bird, D.K., 2000. Arsenic speciation in pyrite and secondary weathering phases, Mother Lode Gold District, Tuolumne County, California. *Appl. Geochem.* 15, 1219–1244.
- Shikazono, N.; Nakata, M.; Tokuyama, E., 1994. Pyrite with high Mn content from the Nankai Trough formed from subduction-induced cold seepage. *Mar. Geol.* 118, 303–313.
- Sillitoe, R.H., 2003. Iron oxide-copper-gold deposits: an Andean view. *Miner. Depos.* 38, 787–812.
- Simon, G.; Huang, H.; Penner-Hahn, J.E.; Kesler, S.E.; Kao, L.S., 1999. Oxidation state of gold and arsenic in gold-bearing arsenian pyrite. *Am. Mineral.* 84, 1071–1079.
- Steadman, J.; Large, R.; Olin, P.; Danyushevsky, L.; Meffre, S.; Huston, D.; Fabris, A.; Lisitsin, V.; Wells, T., 2021. Pyrite trace element behavior in magmatic-hydrothermal environments: An LA-ICPMS imaging study. *Ore Geol. Rev.* 128, 103878.
- Sundby, B.; Martinez, P.; Gobeil, C., 2004. Comparative geochemistry of cadmium, rhenium, uranium, and molybdenum in continental margin sediments. *Geochim. Cosmochim. Acta* 68, 2485–2493.
- Sykora, S.; Cooke, D.R.; Meffre, S.; Stephanov, A.S.; Gardner, K.; Scott, R.; Selley, D.; Harris, A.C., 2018. Evolution of Pyrite Trace Element Compositions from Porphyry-Style and Epithermal Conditions at the Lihir Gold Deposit: Implications for Ore Genesis and Mineral Processing. *Econ. Geol.* 113, 193–208.

- Tanner, D.; Henley, R.W.; Mavrogenes, J.A.; Holden, P., 2016. Sulfur isotope and trace element systematics of zoned pyrite crystals from the El Indio Au–Cu–Ag deposit, Chile. *Contrib. Mineral. Petrol.* 171, 4, 1–17.
- Tardani, D.; Reich, M.; Deditius, A.P.; Chryssoulis, S.; Sánchez- Alfaro, P.; Wrage, J.; Roberts, M.P., 2017. Copper–arsenic decoupling in an active geothermal system: a link between pyrite and fluid composition. *Geochim. Cosmochim. Acta* 204, 179–204.
- Ulrich, T.; Clark, A.; Kyser, K., 2001. The Candelaria Cu-Au deposit, III region, Chile: Product of long-term mixing of magmatic-hydrothermal and evaporite-sourced fluids. GSA Annual Meeting.
- Ulriksen, C., 1979. Regional geology, geochronology, and metallogeny of the Coastal Cordillera between 23°30' and 26°S. [Thesis], Halifax, Nova Scotia, Dalhousie University, 180.
- Vaughan, J.P.; Kyin, A., 2004. Refractory gold ores in Archean greenstones, Western Australia: mineralogy, gold paragenesis, metallurgical characterization and classification. *Mineral. Mag.* 68, 255–277.
- Vivallo, W.; Henríquez, F., 1998. Génesis común de los yacimientos estratoligados y vetiformes de cobre del Jurásico Medio a Superior en la Cordillera de la Costa, Región de Antofagasta, Chile. *Rev. Geol. Chile* 25, 199–228 (in Spanish).
- Wilson, N.; Zentilli, M., 1999. The Role of Organic Matter in the Genesis of the El Soldado Volcanic-Hosted Manto-Type Cu Deposit, Chile. *Econ. Geol.* 94, 1115–1136.
- Wilson, N.; Zentilli, M., 2006. Association of pyrobitumen with copper mineralization from the Uchumi and Talcuna districts, central Chile. *Int. J. Coal Geol.* 65, 1, 158–169.
- Wilson, S.A.; Ridley, W.I.; Koenig A.E., 2002. Development of sulfide calibration standards for the laser ablation inductively- coupled plasma mass spectrometry technique. *J. Anal. At. Spectrom.* 17, 406–409.
- Wilson, N.; Zentilli, M.; Reynolds, P.H.; Boric, R., 2003a. Age of mineralization by basinal fluids at the El Soldado manto-type copper deposit, Chile $^{40}\text{Ar}/^{39}\text{Ar}$ geochronology of K-feldspar. *Chem. Geol.* 197, 161–176.
- Wilson, N.; Zentilli, M.; Spiro, B. A., 2003b. Sulfur, carbon, oxygen, and strontium isotope study of the volcanic-hosted El Soldado manto type copper deposit, Chile: The essential role of bacteria and petroleum. *Econ. Geol.* 98, 163-174.
- Williams, P.J., 1999. Fe-oxide-Cu-Au deposits of the Olympic Dam/Ernest Henry-type. In: New developments in the understanding of some major ore types and environments, with implications for exploration. In: Proc Prospectors and Developers Association of Canada Short Course, Toronto, 2-43.
- Wu, Y.F.; Fougereuse, D.; Evans, K.; Reddy, S.M.; Saxey, D.W.; Guagliardo, P.; Li, J.W., 2019. Gold, arsenic, and copper zoning in pyrite: a record of fluid chemistry and growth kinetics. *Geology*, 47, 7, 641–644.
- Zentilli, M.; Boric, R.; Munizaga, F.; Graves, M.C., 1994. Petroleum involvement in the genesis of some strata-bound copper deposits of Chile. Proceedings, 7th Chilean Geological Congress, Concepcion, Chile, II, 1542–1546.

Zentilli, M.; Munizaga, F.; Graves, M.C.; Boric, R.; Wilson, N.S.F.; Mukhopadhyay, P.K.; Snowdon, L.T., 1997. Hydrocarbon involvement in the genesis of ore deposits: an example in Cretaceous strata-bound (manto-type) copper deposits of central Chile. *Int. Geol. Rev.* 39, 1–21.

Zentilli, M.; Makshev, V.; Boric, R.; Wilson, J., 2018. Spatial coincidence and similar geochemistry of Late Triassic and Eocene-Oligocene magmatism in the Andes of northern Chile: evidence from the MMH porphyry type Cu-Mo deposit, Chuquicamata District. *Int. J. Earth Sci.* 107, 3, 1097–1126.

3.9. FIGURES



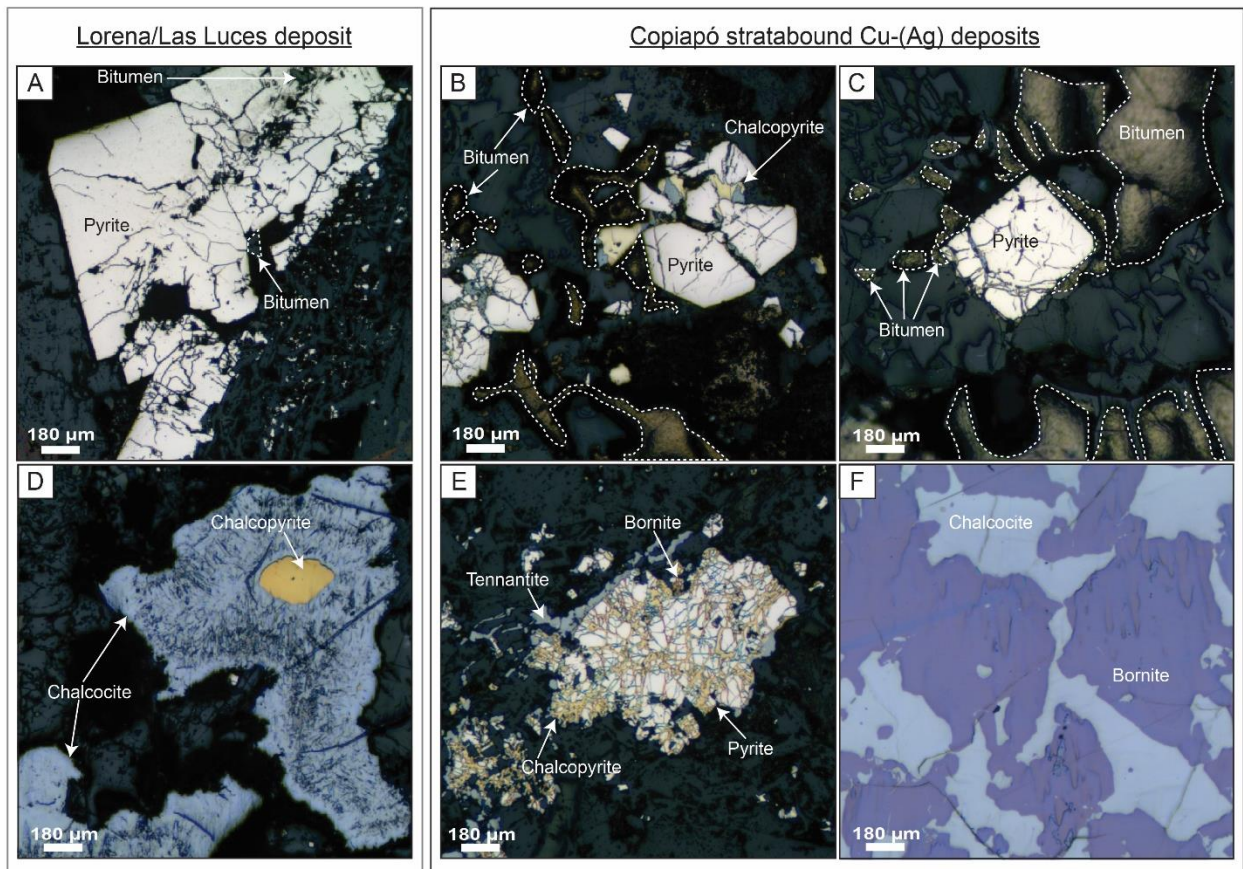


Figure 22. Reflected polarized light microscopy photomicrographs of representative sulfide ore assemblages from the Lorena and Copiapó stratabound Cu-(Ag) deposits. **A)** Subhedral pyrite grains associated with bitumen. **B)** (Sub-)euhedral pyrite grains in contact with bitumen. Late Cu sulfides are also observed. **C)** Euhedral pyrite grain associated with bitumen **D)** Chalcopyrite grain replaced by chalcocite. **E)** Pyrite grains replaced along fractures by chalcopyrite, bornite and chalcocite/digenite. Late tennantite is also observed. **F)** Cu-(Fe) sulfides (chalcocite-bornite).

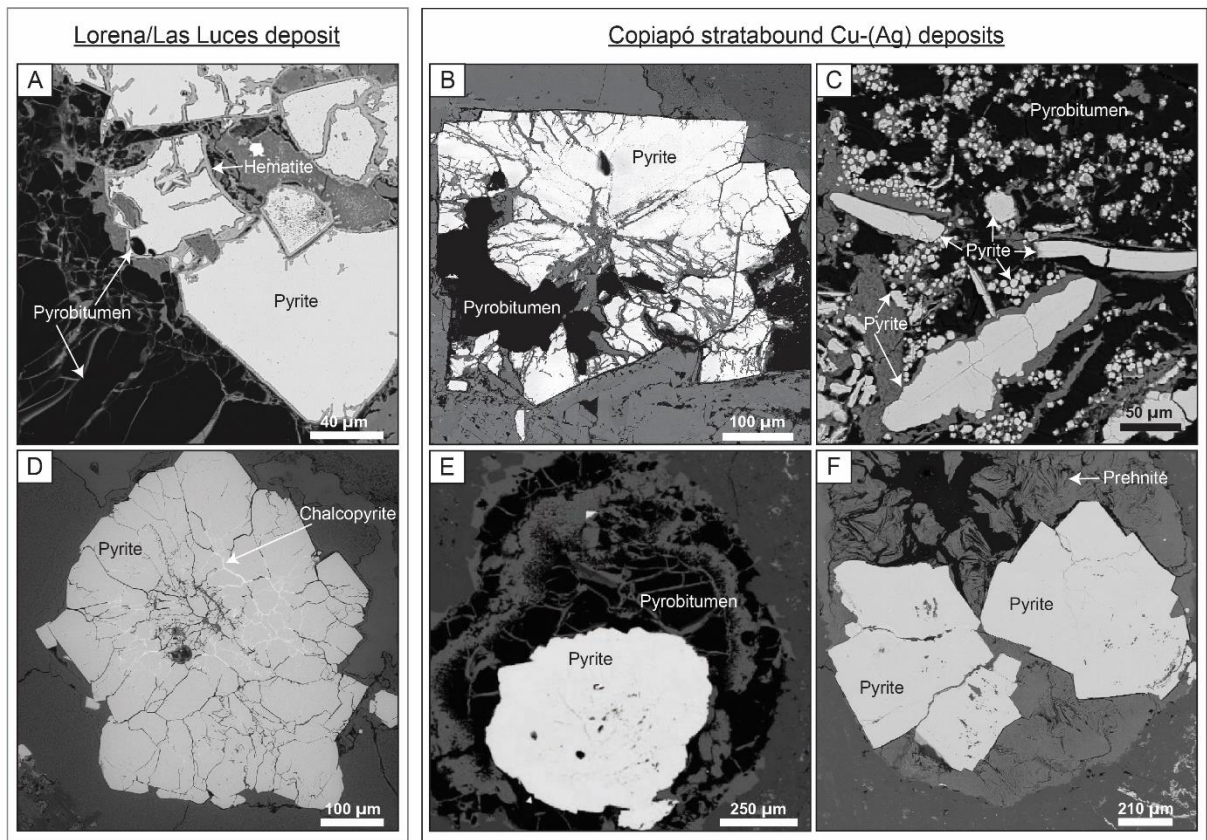


Figure 23. Backscattered electron (BSE) images showing pyrite in association with bitumen (pre-ore stage). **A)** Sub-euhedral pyrite grains with droplet-shaped micrometer-sized inclusions of bitumen. **B)** Pyrite in close association with bitumen. **C)** Elongated pyrite grains in association with bitumen. Aggregates of fine euhedral pyrite crystals are also observed. **D)** Pyrite fractures filled with chalcopyrite. **E)** Rounded pyrite grains in close contact with bitumen. **F)** Euhedral to subhedral pyrite grain in contact with bitumen.

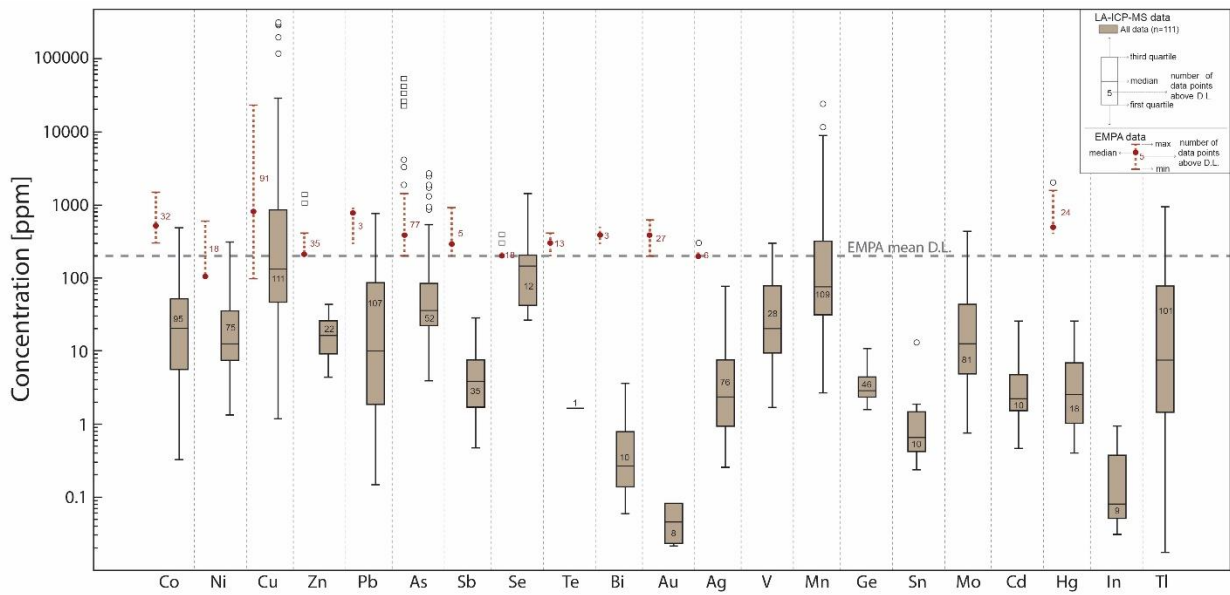


Figure 24. Concentration boxplot for selected minor and trace elements in pyrite from Lorena and the Copiapó stratabound Cu-(Ag) deposits. EMPA and LA-ICP-MS spot analysis data are included and shown as dotted lines and boxplots, respectively. Data are plotted in parts per million (ppm) on a vertical logarithmic scale. In each boxplot, minimum, median and maximum concentrations are indicated. The horizontal dashed line marks the mean detection limit (mdl) of EPMA analyses for all elements. A circle outlier in EPMA and LA-ICP-MS analysis is above $1.5 \times$ (quartile 3- quartile 1) while a square outlier is above $3.0 \times$ (75th percentile - 25th percentile).

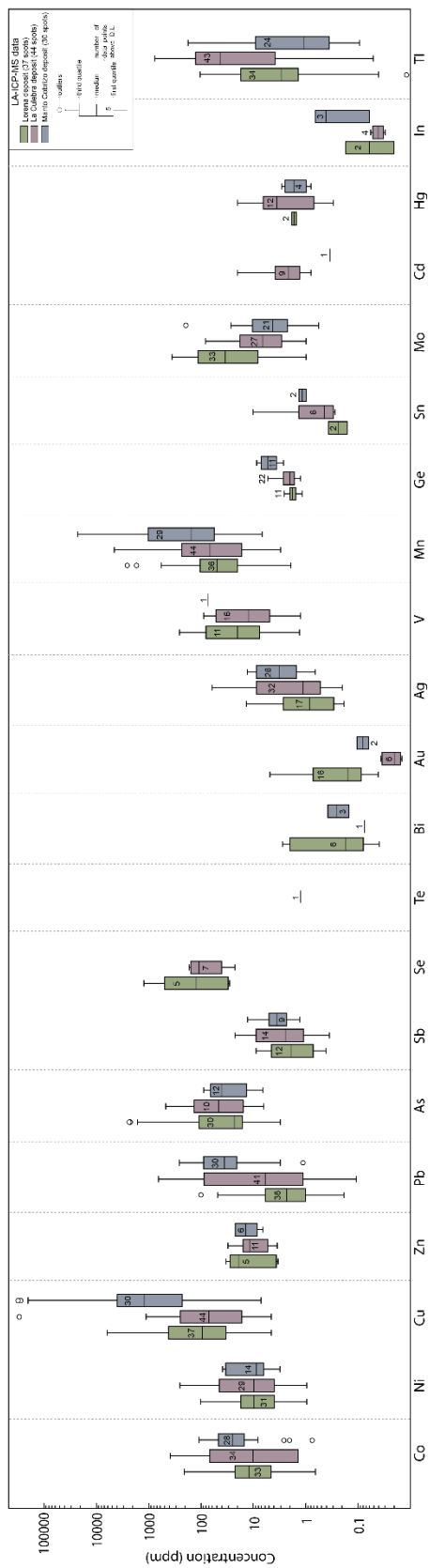


Figure 25. Concentration boxplot for selected minor and trace elements in pyrite from stratabound Cu-(Ag) deposits (Lorena, La Culebra and Manto Cobrizo). Only LA-ICP-MS spots data are included. Data are plotted in parts per million (ppm) on a vertical logarithmic scale. In each boxplot, minimum, median and maximum concentrations are marked.

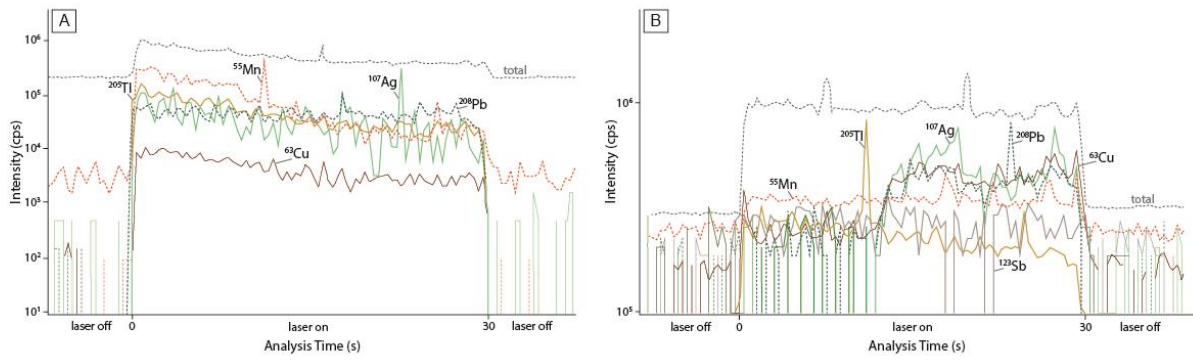


Figure 26. Representative LA-ICP-MS depth-concentrations profiles (time vs. intensity) for Sselected isotopes (^{55}Mn , ^{63}Cu , ^{107}Ag , ^{123}Sb , ^{205}Tl and ^{208}Pb) in pyrite from stratabound Cu-(Ag) deposits. See text for discussion.

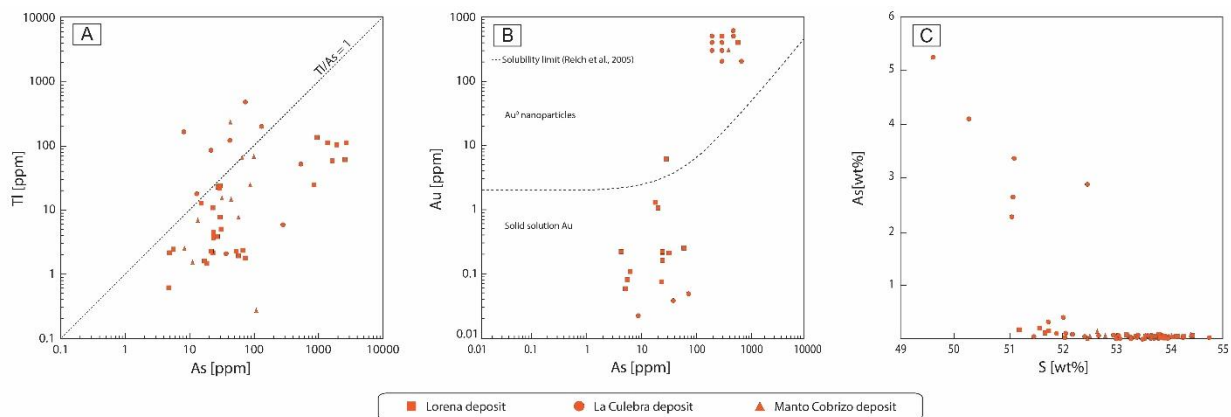


Figure 27. Elemental concentration scatterplots for pyrite from stratabound Cu-(Ag) deposits. **A)** Tl vs As. **B)** Au vs As. **C)** As vs S. In **(A)** the dotted line corresponds to a Tl/As = 1.0. The dashed curve in **(B)** represents the solubility limit of Au as a function of As concentrations, as determined by Reich et al., 2005. Concentrations are reported in parts per million (ppm) in **(A)** and **(B)**, while in **(C)** they are in weight percent (wt. %).

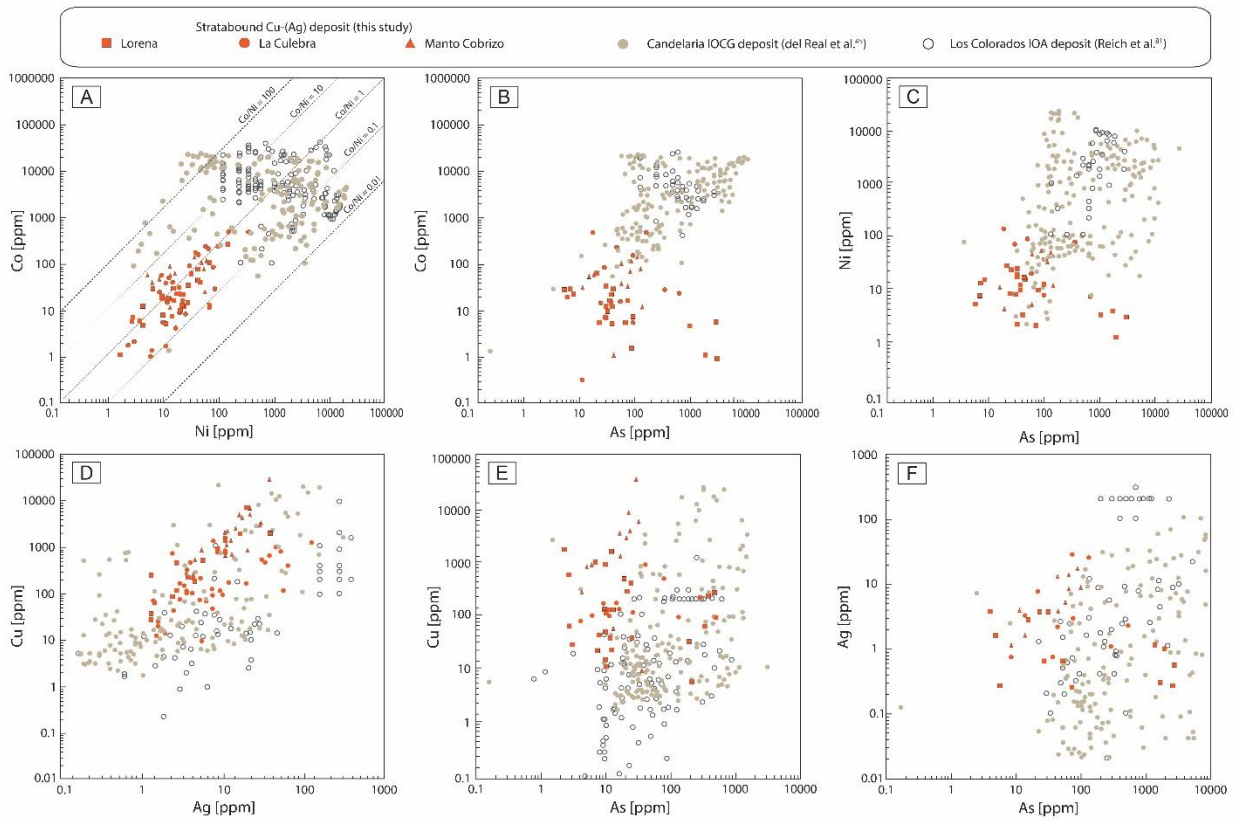


Figure 28. Elemental concentration scatterplots for pyrite from the stratabound Cu–(Ag), IOA, and IOCG deposits. **A)** Co vs Ni. **B)** Co vs As. **C)** Ni vs As. **D)** Cu vs Ag. **E)** Cu vs As. **F)** Ag vs As. All concentrations are reported in parts per million (ppm).

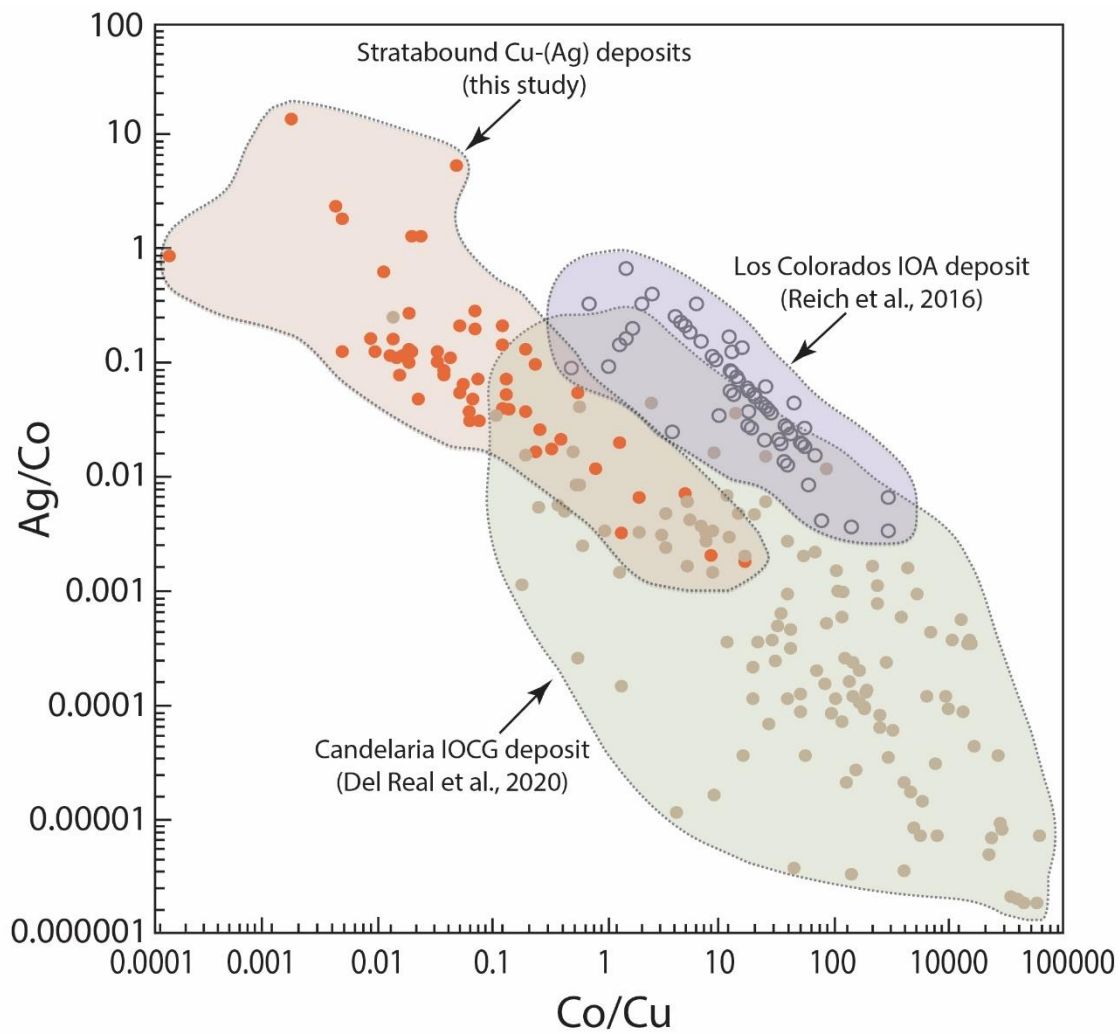


Figure 29. Ag/Co vs Co/Cu scatterplot diagram for pyrite from stratabound Cu-(Ag), iron oxide-apatite (IOA) and iron oxide-copper-gold (IOCG) deposits from northern Chile. Data are plotted on a logarithmic scale. Data (SIMS and LA-ICP-MS) for the Los Colorados IOA and Candelaria IOCG deposit were obtained by Reich et al., 2016 and del Real et al., 2020, respectively.

CHAPTER 4

Sulfur isotope and trace element signatures of pyrite from bitumen-bearing stratabound Cu-(Ag) deposits, northern Chile: Implications for fluid sources and ore-forming processes

Andrea Herazo^{1,2*}, Martin Reich^{1,2}, Fernando Barra^{1,2}, Diego Morata^{1,2}, Irene del Real^{1,2}, Laure Martin³

¹ Department of Geology and Andean Geothermal Center of Excellence (CEGA), FCFM, Universidad de Chile, Plaza Ercilla 803, Santiago, Chile

² Millennium Nucleus for Metal Tracing Along Subduction, FCFM, Universidad de Chile, Santiago, Chile.

³ Centre for Microscopy, Characterisation, and Analysis, University of Western Australia, Australia.

Corresponding author: Andrea Herazo
andrea.herazo@ug.uchile.cl

ABSTRACT

Stratabound Cu-(Ag) deposits in north-central Chile have been grouped in two NS-trending belts according to the age of the volcanic and volcano-sedimentary host rocks, i.e., the Upper Jurassic and Lower Cretaceous belt. Cretaceous deposits are characterized by an unusual assemblage of Cu-(Fe) sulfides with migrated hydrocarbons (bitumen and pyrobitumen). Despite the fact that several genetic models have been proposed for the origin of these deposits, few geochemical and isotopic data are available for the metallic mineralization and pyrobitumen. Here, we report in-situ secondary ion mass spectrometry (SIMS) sulfur isotope data ($\delta^{34}\text{S}$) of pyrite, which is an abundant phase in the pre-ore stage and occurs intimately associated with pyrobitumen in stratabound Cu-(Ag) deposits. Pyrite was also analyzed by using laser ablation inductively coupled plasma mass spectrometry (LA-ICP-MS) to better constrain the source of metals in the Lorena (Las Luces district), La Culebra (Copiapó) and El Soldado deposits. Our data reveal a wide range of $\delta^{34}\text{S}$ values for pyrite (-30 to $+60\text{‰}$), which are interpreted as a result of different sulfur sources and fractionation processes during the genesis of these stratabound Cu-(Ag) deposits. $\delta^{34}\text{S}_{\text{pyrite}}$ values from -30 to $+10\text{‰}$ most likely reflect incomplete sulfate reduction in a partially closed system dominated by connate seawater sulfate. In contrast, the heaviest $\delta^{34}\text{S}_{\text{pyrite}}$ values, up to $+60\text{‰}$, are close to the maximum fractionation recorded for single organic sulfate reduction in natural settings, and may indicate alternative processes as anaerobic methane oxidation. LA-ICP-MS trace element data of pyrite reveals significant concentrations of Cu, As, Mn, Pb, Tl, Co, Ni, and Mo that range from a few ppm to wt.% levels. Among all elements analyzed, Cu, As, Mn, and Tl are the most abundant with maximum values of 0.84 wt.% (Cu), 0.67 wt.% (As), 0.36 wt.% (Mn), and 0.14 wt.% (Tl). These high concentrations are correlated with the heaviest $\delta^{34}\text{S}_{\text{pyrite}}$

values determined by SIMS and their incorporation is controlled by different processes including ionic substitution, metal availability, elemental solubility in the hydrothermal-hydrocarbon mixture and the geological environment of formation. Our geochemical data indicate that sulfur and metals were most likely derived from different sources, including a relevant sedimentary component.

4.1. INTRODUCTION

Stratabound Cu-(Ag) deposits occur forming a NS trending belt along the Coastal Cordillera of north-central Chile. The deposits range in age from Upper Jurassic to Lower Cretaceous and are hosted in volcanic rocks of intermediate composition interbedded with sedimentary units. Historically, these deposits have been an important source of Cu in Chile due to their high grades (>1 wt.% Cu). Regardless of their economic importance, their origin has been debated for decades due to sparse geologic information. Stratabound Cu-(Ag) deposits are also known as “Manto-type” because of the stratiform and lenticular morphology of the ore bodies, although irregularly-shaped mineralized zones are commonly recognized (e.g., veins, breccias and pipes, among others) (Maksaev and Zentilli, 2002).

These deposits have been grouped in two belts of different age. The first belt comprises deposits hosted by a Jurassic volcano-sedimentary sequence known as La Negra Formation. Several deposits have been identified in this belt including Mantos Blancos, Mantos de la Luna, Buena Esperanza, Mantos del Pacífico, Michilla and Las Luces, but only a few are currently in operation (Fig. 30A). Copper mineralization in these deposits mostly occurs in amygdaloidal basalt-andesites as disseminated grains, veinlets and minor breccias (Kojima et al., 2003). The hypogene sulfide paragenesis consists of chalcocite, bornite and chalcopyrite, which can contain up to 100's ppm Ag (Kojima et al., 2003; Reich et al., 2013a). Supergene mineralization comprises Ag-bearing chalcocite, digenite and covellite and Cu-oxide minerals such as atacamite and chrysocolla (Reich et al., 2009, 2010). Recently, Herazo et al. (2020) reported the first occurrence of organic matter (pyrobitumen) associated with Cu-(Fe) sulfides in the Jurassic Lorena deposit, Las Luces district.

The second group of deposits is hosted by Lower Cretaceous volcanic and volcano-sedimentary rocks (Zentilli et al. 1997; Wilson and Zentilli 1999; Maksaev et al., 2007; Kojima et al., 2009). A unique and unusual feature of these deposits is the intimate association of Cu sulfides with pyrobitumen hosted in lavas, subvolcanic intrusive bodies and pyroclastic units (Mayer and Fontboté, 1990; Zentilli et al., 1994; Zentilli et al., 1997; Wilson and Zentilli, 1999; Boric et al., 2002; Haggan et al., 2003; Wilson et al., 2003a,b; Wilson and Zentilli, 2006; Cucurella et al., 2005; Cisternas and Hermosilla, 2006; Rieger et al., 2008; Carrillo-Rosúa et al., 2014). The most studied bitumen-bearing stratabound Cu-(Ag) deposits of Lower Cretaceous age is the world-class El Soldado deposit, located north of Santiago (Fig. 30). Other minor deposits in central Chile include the Melipilla-Naltahua and Lo Aguirre deposits, and in northern Chile Talcuna and Uchumí near La Serena and Manto Cobrizo, La Culebra close to Copiapó (Fig. 30A). Regardless of the age of the host rocks, the mineral paragenesis comprises pyrite-chalcopyrite-bornite-chalcocite with pyrobitumen (Wilson and Zentilli, 1999; Cisternas and Hermosilla, 2006; Herazo et al., 2020, 2021).

Multiple interpretations and models have been proposed to explain the formation of stratabound Cu-(Ag) deposits. Some authors have proposed a syngenetic-magmatic origin (Ruiz et al., 1965, 1970), whereas others support an epigenetic model (Kojima et al., 2003, 2009; Oliveros et al., 2008). The latter is based on field observations and geochronological data. Currently the two prevailing epigenetic models are: 1) A magmatic-hydrothermal origin where fluids and metals are derived from a magmatic source at depth (e.g., Palacios 1990; Vivallo and Henríquez 1998; Makshev and Zentilli 2002), and 2) A hydrothermal origin with fluids of mixed origin that are heated and mobilized by cooling intrusions (Makshev and Zentilli, 2002). In the latter, the fluids can be either of metamorphic, magmatic or sedimentary/meteoritic origin, or a mix of them (Barra et al., 2017). In addition, Kojima et al. (2009) proposed a host rock-derived model, arguing that the volcano-sedimentary host units are the source of the ore-forming fluids. An important feature of Lower Cretaceous deposits is a strong “sedimentary” signature, which is evidenced by the presence of organic sulfur in the pyrobitumen (e.g., Herazo et al., 2020) and the bulk sulfur isotope values (e.g., Carrillo-Rosúa et al., 2014). Unlike the Upper Jurassic deposits that have a narrow and more magmatic $\delta^{34}\text{S}$ signature (-6.6 to 0 ‰; Sasaki et al., 1984; Vivallo and Henríquez, 1998; Kojima et al., 2003), the Lower Cretaceous deposits are characterized by a wide range of $\delta^{34}\text{S}$ values ranging from -50 to $+28$ ‰ (Carrillo-Rosúa et al., 2014, and references therein).

In the Lower Cretaceous stratabound Cu-(Ag) deposits, pyrite is an ubiquitous and abundant phase that is intimately associated with pyrobitumen (Wilson et al., 1999; Cisternas and Hermosilla, 2006; Herazo et al., 2021). Pyrite, which predates the Cu mineralization, is host to several trace elements that can be used to obtain information on the source of metals and fluids. Trace elements in pyrite have been successfully used to unravel the evolution of hydrothermal fluids in a large variety of mineral deposits, including Carlin-type Au, volcanogenic massive sulfide (VMS), sedimentary-hosted Cu/U, Archean to Mesozoic lode Au, iron oxide-copper-gold (IOCG) and porphyry Cu and epithermal Au deposits, among many others (Cook and Chryssoulis, 1990; Hannington et al., 1999; Reich et al., 2005; Large et al., 2009; Cook et al., 2009; Reich et al., 2013b; Gregory et al., 2015; Keith et al., 2016;; Román et al., 2019). Furthermore, when trace element data of pyrite is coupled with in-situ sulfur isotope ($\delta^{34}\text{S}$) data, ore-forming processes can be precisely fingerprinted at the grain scale, providing key information on both the source and physico-chemical evolution of mineralizing fluids (Barker et al., 2009; Peterson and Mavrogenes, 2014; Tanner et al., 2016; Gregory et al., 2019; Holley et al., 2019; del Real et al., 2020; Li et al., 2020).

In this study, we present the results of a geochemical and isotopic study of pyrite from bitumen-bearing stratabound Cu-(Ag) deposits in central-northern Chile. The studied deposits, i.e., Lorena, La Culebra and El Soldado, contain abundant pyrite that is intimately associated with pyrobitumen in the early, pre-ore assemblages. We combined micro-textural observations with trace element data obtained using laser ablation inductively coupled mass spectroscopy (LA-ICP-MS). In addition, we explored the in-situ sulfur isotope signature ($\delta^{34}\text{S}$) of pyrite determined by secondary ion mass spectrometry (SIMS) analysis. Since only bulk sulfur isotope analyses are currently available for pyrite (or any other sulfide) in stratabound Cu-(Ag) deposits in Chile, the new data presented here provide an unprecedented view of the trace element composition and $\delta^{34}\text{S}$ signature of pyrite at the grain scale. In particular, the acquired data provide constraints on the source of sulfur and metals and the key ore-forming processes involved during the early stages of bitumen-bearing stratabound Cu-(Ag) deposits, where pyrite is the dominant sulfide.

4.2. GEOLOGICAL BACKGROUND

The Andean tectonic cycle comprises two major stages: an early stage during the Jurassic to Lower Cretaceous, characterized by the formation of a magmatic arc-system flanked to the east by a sedimentary marine back-arc basin within an extensional tectonic setting, followed by a later stage from the Late Cretaceous to present, with the consolidation of the cordilleran arc on a continental environment under a compressive tectonic setting (Mpodozis and Ramos, 1990; Charrier et al., 2007; Horton et al., 2018; Jara et al., 2021, and references therein). Within this context, the Chilean stratabound Cu-(Ag) deposits studied here were formed during the first stage of the Andean cycle (Maksaev and Zentilli, 2002; Maksaev et al., 2007). Figure 30A shows the location of the three studied deposits, from north to south, Lorena in the Las Luces district near Taltal, La Culebra near Copiapó, and El Soldado north of Santiago. These deposits occur within the Jurassic to Lower Cretaceous belt in the Coastal Cordillera of north-central Chile.

4.2.1. Las Luces district

Figure 30B shows the location of the Lorena deposit and the main geologic units in the Las Luces district. The oldest rocks recognized in the area correspond to metasediments from the Las Tórtolas Formation (Ordovician – Devonian). The Cifuncho Plutonic Group intruded the Las Tórtolas Formation and is covered by marine sedimentary/metapelitic rocks from the Upper Triassic Cifuncho Formation (Naranjo, 1978; Ulriksen, 1979; Naranjo and Puig, 1984). The latter unconformably overlies the Las Tórtolas metasedimentary rocks and conformably underlies the Early Jurassic sedimentary rocks of the Pan de Azúcar Formation (Maksaev, 1990; Boric et al., 1990). The Jurassic sequence is represented by volcanic rocks from the La Negra and Posada de Los Hidalgos formations (Fig. 30B). The Early Jurassic to Lower Cretaceous Matancilla Plutonic Group intruded the La Negra volcanic rocks. Overlying La Negra is the Lower Cretaceous Aeropuerto Formation (Naranjo and Puig 1984; Boric et al. 1990). Sediments from the Atacama Gravels (Oligocene to Miocene) and modern alluvial deposits are the youngest units in the area.

The Lorena stratabound Cu-(Ag) deposit is hosted in volcanic rocks from the La Negra Formation. Copper reserves are estimated at ~200,000 tons with a ~1.5% Cu sulfide and ~300,000 tons @ 0.9% Cu oxides. At Lorena, the Cu-(Fe) sulfide mineralization occurs in breccias, fractures, veins or vesicle-fillings. The sulfide mineralization includes chalcocite-bornite with minor chalcopyrite, pyrite and late digenite and covellite. Cu-oxides comprises chrysocolla and malachite. The metallic mineralization is intimately associated with pyrobitumen. Lorena is both structurally and stratigraphically controlled, but the sulfide-pyrobitumen mineralization is mostly present forming stratabound “mantos” (Herazo et al., 2020). A NW-trending fault is the main structural feature in the deposit. The dominant hydrothermal alteration type is albitization with minor epidote, sericite, chlorite, and abundant late calcite. Low-grade metamorphic mineral assemblages (zeolites, prehnite-pumpellyite, and minor chalcedony), as well as pyrobitumen, are also found filling vesicles and in the breccia matrix (Herazo et al., 2020).

4.2.2. Copiapó district

The La Culebra stratabound Cu-(Ag) deposit in the Copiapó district is hosted in the Lower Cretaceous Pabellón Formation, which is composed of carbonate sedimentary rocks, capped by

porphyritic lavas flows (Cisternas and Hermosilla, 2006) (Fig. 30C). The Pabellón Formation represents the top of the Chañarcillo Group and overlies the shallow marine sedimentary sequences of the same group (e.g., Nantoco Formation, Early Hauterivian), which in turn overlays volcanic rocks from the Berriasian Punta del Cobre Formation (Marschik and Fontboté, 2001). Calc-alkaline diorites and monzodiorites intruded the Chañarcillo Group (Marschik et al., 2003). The Cerrillos Formation (Aptian) overlies by erosional discordance the Pabellón Formation. Unconsolidated sediments (Atacama Gravels) and alluvial deposits are the more recent units identified in the area (Fig. 30C).

The La Culebra deposit is hosted in the andesitic volcanic unit of the Pabellón Formation and monthly production is 250 t at 2.4% Cu sulfide. Copper sulfides (chalcopyrite-bornite-chalcocite) are associated with pyrobitumen, and usually form ore “mantos” of up to 10 m thick. Mineralization occurs filling vesicles, in veins and veinlets as fine disseminations. A poorly developed late supergene stage is evidenced by secondary covellite, azurite and chrysocolla. These constitute the main Cu assemblage, with Cu-(Fe) sulfides replacing the early pyrite-pyrobitumen association (Cisternas and Hermosilla, 2006; Herazo et al., 2021). Hydrothermal alteration in La Culebra includes a moderate to strong Ca–Na metasomatism, silicification and carbonate alteration. Pervasive alteration with potassic feldspar, albite, and epidote is also common (Hermosilla, 2001).

4.2.3. El Soldado district

In the El Soldado area, Lower Cretaceous rocks are represented by the Lo Prado Formation (Berriasian–Hauterivian); a bi-modal volcanic suite with marine and continental sedimentary intercalations (Fig. 30D). The Lo Prado Formation is overlain by basaltic andesites, tuffs, volcanic epiclastic breccias, redbeds and lacustrine sediments from the Veta Negra Formation (Barremian–Albian), which in turn is overlain by the Lower-Upper Cretaceous Las Chilcas Formation (Rivano et al., 1993; Boric et al., 2002). The El Soldado stratabound Cu-(Ag) deposit is hosted within the (upper) basaltic-rhyodacite member of the Lo Prado Formation, which also contains marine carbonaceous shales and volcanoclastic sandstones. These strata are underlain by the lower member of Lo Prado Formation, a thick (~1500 m) marine, organic-rich calcareous shale-siltstone-sandstone unit (Boric et al., 2002). Underlying conformably the Lo Prado Formation is the volcanic Upper Jurassic Horqueta Formation (Boric et al., 2002) (Fig. 30D). More detailed descriptions of the geology and stratigraphy of the El Soldado district can be found in Wilson and Zentilli (1999) and Boric et al. (2002).

The El Soldado deposit is one of the largest stratabound Cu-(Ag) deposit in Chile with an estimated historical production of ~1.15 Mt Cu (Comisión Chilena del Cobre, 2016). The Cu mineralization is structurally and lithologically controlled forming orebodies within a general NS to NNW regional fracture system (Wilson and Zentilli, 1999). Two main mineralization stages are recognized, a pre-ore and main Cu ore stage (Wilson and Zentilli, 1999; Boric et al., 2002; Wilson et al., 2003a,b). Framboidal pyrite is the most distinctive feature of the pre-ore stage. Euhedral and spheroidal pyrite grains are also present in association with pyrobitumen, and minor arsenopyrite and sphalerite. The main Cu ore stage is represented by a chalcopyrite-bornite and chalcocite paragenesis with early pyrite being replaced by the Cu-(Fe) sulfides (Wilson et al., 1999). Hydrothermal alteration minerals include abundant calcite, chlorite, albite, K feldspar, epidote, silica, titanite and minor sericite and clay minerals (Holmgren, 1987; Boric, 1997).

4.3. SAMPLES AND METHODS

A total of eleven samples from the bitumen-bearing stratabound Cu-(Ag) deposits described above were selected for study. Samples of the pre-ore stage were collected from drill cores. After a detailed petrographic inspection, a total of five pyrite-bearing samples representative of the pre-ore stage in the three deposits were selected for further study. Coupled trace element and in-situ sulfur isotope data were obtained for pyrite in samples from Lorena (LO-24), La Culebra (MTCUL-2D) and El Soldado (NW-165, NW-167). In the studied samples pyrite is abundant and occurs in close association with pyrobitumen.

Pyrite textures vary within and between deposits (Fig. 31). Framboidal pyrite is the most relevant texture observed in El Soldado, and occurs as isolated or in clusters composed of numerous uniform, loosely-aggregated microcrystals (Fig. 31A,B). Framboidal pyrite grains are less frequent in the La Culebra deposit and are mostly replaced by Cu sulfides minerals (Fig. 31C), whereas at Lorena, framboids were not observed. Euhedral to subhedral grains with occasional cubic and pyritohedron forms are common in the three studied deposits (Fig. 31E,F), as well as aggregates of euhedral pyrite that form rosette-like spherules grains (Fig. 31D). These aggregates can develop from a euhedral and/or framboidal pyrite core, and usually occur within or adjacent to amygdales and to lesser extent in veinlets.

4.3.1. LA-ICP-MS

The pyrite grains were first inspected using a FEI Quanta 250 scanning electron microscope (SEM) at the Andean Geothermal Center of Excellence (CEGA), Universidad de Chile in Santiago. The SEM is equipped with secondary electron (SE), backscattered electron (BSE) and X-ray energy-dispersive spectrometry (EDS) detectors. Analytical conditions were: accelerating voltage of 15-20 kV, beam current of 1 nA, takeoff angle $\sim 35^\circ$, a spot size of 4-5 μm in diameter, and a working distance of ~ 10 mm.

The concentration of minor and trace elements in pyrite was determined by using laser ablation inductively coupled plasma mass spectrometry (LA-ICP-MS). The analyses were undertaken at the Mass Spectrometry Laboratory of the Andean Geothermal Center of Excellence (CEGA), Universidad de Chile. Analyses were performed using a 193 nm ArF excimer laser (Teledyne-Photon Machines Analyte 193) coupled to a quadrupole ICP-MS (Thermo Fisher Scientific iCAP-Q). To ensure acceptable levels of plasma robustness (i.e., $^{238}\text{U}^+ / ^{232}\text{Th}^+$ between 0.95-1.05), oxide production ($\text{ThO}^+ / \text{Th}^+ < 0.5\%$) and double charged production ($^{22}\text{M}^+ / ^{44}\text{Ca}^{++} < 0.01\%$), the ICP-MS calibration was carried out by ablating a glass reference material (NIST SRM 610). Spot data was obtained using a laser pulse frequency of 4 Hz and an energy density of 2.5 J/cm^2 . A laser spot size of 40 μm was used, but a 20 μm size was preferred to avoid ablating visible mineral inclusions and/or when analyzing small grains. Each spot was ablated for 52 s following 30 s of gas background collection (carrier gas used was pure He). Sample analysis was performed using the sample -bracketing method using the synthetic sulfide MASS-1 reference material (Wilson et al., 2002) as the primary standard. The GSE-1 glass reference material was employed as secondary standard for quality control (Jochum et al., 2005). The Fe concentration in pyrite obtained previously by EPMA (Herazo et al., 2021) was used as an internal standard. External standard measurements were performed at the beginning and at the end of each analysis round of 20 spot analyses. The IoliteTM v. 3.63 software was used for data integration and

reduction (Paton et al., 2011). The following isotopes were analyzed: ^{34}S , ^{51}V , ^{52}Cr , ^{53}Cr , ^{55}Mn , ^{57}Fe , ^{59}Co , ^{60}Ni , ^{63}Cu , ^{65}Cu , ^{66}Zn , ^{69}Ga , ^{72}Ge , ^{73}Ge , ^{75}As , ^{77}Se , ^{82}Se , ^{95}Mo , ^{97}Mo , ^{107}Ag , ^{109}Ag , ^{111}Cd , ^{115}In , ^{118}Sn , ^{120}Sn , ^{121}Sb , ^{123}Sb , ^{125}Te , ^{182}W , ^{197}Au , ^{202}Hg , ^{205}Tl , ^{206}Pb , ^{207}Pb , ^{208}Pb and ^{209}Bi . Detection limits for most analyzed elements are: ^{51}V (1.10 ppm), ^{55}Mn (1.20 ppm), ^{59}Co (0.27 ppm), ^{60}Ni (0.98 ppm), ^{63}Cu (1.20 ppm), ^{66}Zn (2.90 ppm), ^{72}Ge (1.20 ppm), ^{75}As (2.10 ppm), ^{82}Se (14 ppm), ^{95}Mo (0.40 ppm), ^{107}Ag (0.12 ppm), ^{111}Cd (0.39 ppm), ^{121}Sb (0.15 ppm), ^{125}Te (0.54 ppm), ^{197}Au (0.12 ppm), ^{202}Hg (0.30 ppm), ^{205}Tl (0.02 ppm), ^{208}Pb (0.06 ppm) and ^{209}Bi (0.05 ppm)

4.3.2. In-situ sulfur isotope analysis - Secondary-ion mass spectrometry (SIMS)

In-situ sulfur isotope measurements of pyrite were conducted using a CAMECA IMS1280 large-geometry ion microprobe at the Centre for Microscopy, Characterisation and Analysis (CMCA) of The University of Western Australia, Perth. Pyrite crystals were separated from rock fragments by handpicking, and then embedded in 1-inch-diameter circular resin mounts. All the crystals were distributed within 6 mm from the center of the mount, where the standard reference material was placed. The resin mounts were then coated with 30 nm layer of gold. Analytical procedures were performed following the protocol described by LaFlamme et al. (2016), which is summarized here. The SIMS was operated in multicollection mode with a Cs^+ primary beam of intensity $\sim 1\text{--}4\text{ nA}$ in Gaussian mode that interacted with the sample at 20 keV. Secondary sulfur ions from the analyzed sample were extracted at -10 kV following a 30 s pre-sputter. The ions were admitted to the mass spectrometer with a field magnification of $133\times$, with automated centering of the secondary beam in the field/aperture (both x and y; aperture size $4000\text{ }\mu\text{m}$) and entrance slit (x direction only; slit width $60\text{ }\mu\text{m}$ or $90\text{ }\mu\text{m}$ in some cases) (LaFlamme et al., 2016). At the beginning of each session, the NMR magnetic field controller locked the axial mass. The mass spectrometer operated at a mass resolution ($M/\Delta M$) of about 2500 (exit slit width of $500\text{ }\mu\text{m}$ on the multicollector). Under these conditions, the hydrite interference $^{32}\text{S}^1\text{H}$ on the ^{33}S peak was avoided by offsetting the ^{33}S peak centre to the low mass side (LaFlamme et al., 2016).

Triple sulfur isotope (^{32}S , ^{33}S and ^{34}S) measurements were carried out using a $15\text{ }\mu\text{m}$ raster. Sulfur isotopes were detected simultaneously by three Faraday cups, and signals were collected over 123 s of acquisition time in 20 integration cycles (LaFlamme et al., 2016). Count rates on ^{32}S varied from 1×10^9 to 3.5×10^9 cps on pyrite, depending on the intensity of the primary beam but is typically $2.2\text{--}2.4\times 10^9$ cps with a 2.5 nA primary beam (LaFlamme et al., 2016). The Sierra pyrite reference material (LaFlamme et al., 2016) was used as a bracketing standard to monitor instrument stability and analytical spot-to-spot reproducibility. Grains of Sierra pyrite, embedded in the center of each sample mount, were measured 2-5 times before and after, every five unknowns. Data were corrected using the standard analyses versus time and the instrumental mass fractionation, corrected using the alpha SIMS (calculated as the ratio between the averaged standard value measured during the session and the laser fluorination value of the standard). Measured ratios of $^{34}\text{S}/^{32}\text{S}$ were reported in delta notation ($\delta^{34}\text{S}$) relative to the Vienna Canyon Diablo Troilite (VCDT) according to the equation: $\delta^{34}\text{S} = [({}^{34}\text{S}/^{32}\text{S})_{\text{sample}} / ({}^{34}\text{S}/^{32}\text{S})_{\text{standard}} - 1] \times 1000$ (‰).

The precision of each measured point, considers the internal error and the precision on alpha SIMS. Absolute standard deviation (σ abs) varies between $0.15\text{--}0.33\text{ }‰$.

4.4. RESULTS

4.4.1. Chemical composition of pyrite

All LA-ICP-MS analyses of pyrite from the Lorena, La Culebra and El Soldado deposits are reported in [Table 1](#) and a statistical summary is presented in [Table 2](#). Analyses were performed on clean pyrite surfaces with no visible mineral inclusions. A total of 71 spots were analyzed for 21 elements, i.e., V, Mn, Cu, Co, Ni, Zn, Ge, As, Se, Mo, Ag, Cd, In, Sn, Sb, Te, Au, Hg, Tl, Pb and Bi. Au LA-ICP-MS data were discarded because of possible contamination caused by the Au coating of mounts.

LA-ICP-MS results reveal that pyrite from the studied deposits is enriched in minor and trace elements ([Table 2](#)). Cu, Mn, As and Tl were detected in almost all spots with highly variable concentrations, spanning from sub-ppm to weight percent levels. Maximum concentration values are 0.84 wt% for Cu, 0.36 wt% for Mn, 0.67 wt% for As and 0.14 wt% for Tl ([Table 2](#)). Other elements such as Co, Ni, Zn, Pb, Ag, Ge and Mo were also systematically detected. Ni, Zn, Ag and Ge show concentrations lower than 50 ppm, while Co, Pb and Mo reach up to ~300 ppm. Antimony, Bi, Se, Te, V and Cd were detected in a few grains, with concentrations <10,000 ppm for Se, <150 ppm for V, <10 ppm for Sb and Cd, <1 ppm for Te and Bi ([Table 1](#)).

In all deposits, significant concentrations of minor and trace elements were detected in pyrite. The concentration range of the analyzed elements, i.e., minimum and maximum values, is similar in the three deposits, however, major compositional differences were identified. Pyrite from El Soldado displays the highest median concentration for Cu, Zn, Pb, As, Mn, Mo and Tl, and the lowest median concentrations for Se ([Fig. 32](#)). In contrast, pyrite from Lorena shows the lowest median Cu, Zn, Pb and Tl concentrations ([Fig. 32](#)). Median concentrations of Co, Ni, Sb and Ag are similar in all three deposits. In particular, As displays a similar median concentration in Lorena and La Culebra (~20 ppm), while at El Soldado As is anomalously high (~1500 ppm). Median concentrations of Cu are similar in El Soldado and La Culebra (~330 ppm), and relatively lower at Lorena (110 ppm) ([Fig. 32](#)).

4.4.2. Sulfur isotope composition

In situ sulfur isotope data are reported in [Table 1](#) and displayed in [Figure 33](#). SIMS analyses were carried out using a 15 μm beam along ~200–450 μm transects on large pyrite grains (>200 μm). These grains were also analyzed by LA-ICP-MS. The results reveal a wide range of $\delta^{34}\text{S}$ values from -29.56 to +59.44‰, i.e., a total variability of ~89‰ ([Fig. 33](#)). In particular, pyrite from the Lorena deposit displays $\delta^{34}\text{S}$ values from -29.56 to +5.84‰ and La Culebra between -27.19 and +9.65‰. In contrast, the heaviest sulfur isotope values were measured in pyrite from El Soldado, covering a range from +17.58 to +59.44‰ ([Fig. 33](#)).

Analyzed pyrite grains from Lorena show significant inter-grain variability in $\delta^{34}\text{S}$ values, with some grains showing heavier $\delta^{34}\text{S}$ values while others show lighter values (variability of 3.26 to 17.88‰) ([Annex Figure C.1](#)). In contrast, pyrite from La Culebra exhibits significant intra-grain variability, with $\delta^{34}\text{S}$ values ranging from heavy to light values within the same grain, e.g., values of -27.19 to +4.45‰ and -17.35 to +15.05‰ ([Annex Figure C.2](#)). In the El Soldado deposit, inter-grain variability in $\delta^{34}\text{S}$ values range between +0.94 and +36.37‰ ([Annex Figure C.3](#)).

4.4.3. LA-ICP-MS and SIMS transects

Figure 34 shows transects where LA-ICP-MS trace element data are plotted along respective $\delta^{34}\text{S}$ values. Despite some significant inter-grain variability, these data allow visualization of combined chemical and isotopic information within pyrite, in the three deposits. For La Culebra and Lorena, $\delta^{34}\text{S}$ values of pyrite grains are lighter ($<+5\text{‰}$) and vary significantly along the transects, showing isotopic shifts of up to $\sim 30\text{‰}$ between spots, usually showing very negative excursions (Fig. 34A-C). $\delta^{34}\text{S}$ values for El Soldado are heavier ($>+20\text{‰}$) and also show significant inter-grain variability, with shifts of up to $\sim 30\text{-}40\text{‰}$ between consecutive spots (Fig. 34D-F). In general, a broad trend between Cu and $\delta^{34}\text{S}$ can be recognized. At La Culebra and Lorena, high Cu concentrations are broadly correlated with high $\delta^{34}\text{S}$ values, and the highest Cu concentrations ($>800\text{-}1000$ ppm) are observed when $\delta^{34}\text{S}$ values seem to oscillate between ~ -5 and $+5\text{‰}$ (Fig. 34A-C). At El Soldado, trends in elemental concentrations vs. $\delta^{34}\text{S}$ values are not evident.

4.5. DISCUSSION

4.5.1. Pyrite textures and geochemical variations

Pyrite textures, trace element geochemistry and sulfur isotope data provide relevant information to better assess the source of metals and sulfur in stratabound Cu-(Ag) deposits, and evaluate genetic models of ore formation. Framboidal pyrite, rosette-shaped pyrite grains and euhedral/sub-euhedral are common pyrite textures in the studied deposits. Pyrite in the sulfide-bitumen, pre-ore stage are of interest because their formation is driven by decomposition of organic matter, and represents reducing conditions. Framboids and micro-sized euhedral pyrite crystals are related to early diagenetic processes. These spherical and polycrystalline aggregates are important sinks for metals and sulfur and are formed within the water column and sediments (Gregory et al., 2014). A paragenetic association of pyrite and pyrobitumen has been recognized in the El Soldado deposit, where framboidal pyrite texture is ubiquitous and constitute the early (or pre-ore) stage of mineralization (Wilson et al., 1999; 2003a). Framboids at El Soldado are composed of euhedral pyrite microcrystals, whose aggregates vary from loosely to densely packed (Fig. 31A,B). Most framboids are surrounded by pyrobitumen, and this fills the space between framboids, implying that pyrite grew preferably in the presence of organic matter, being compatible with a bacterial origin by biodegradation of petroleum (Fig. 31A; Wilson et al., 1999; Wilson et al., 2003a). At the El Soldado deposit there is also clear evidence that Cu sulfide framboids (chalcopyrite, bornite and chalcocite) were also formed by replacement of pre-existing pyrite (Fig. 31F). Textures showing the growth stages from individual framboids to spherules to larger grains are comparable to textures reported from the Kupferschiefer sedimentary Cu deposits in Poland and Germany (Sawlowicz, 1990; Borg et al., 2012), where a transition between framboids and spherules as a homogenization of Cu sulfide framboids was defined. This was probably due to a continuous supply of metals permitting the growth of individual microcrystals leading to their amalgamation (Wilson et al., 1998). Scarce pyrite framboids were observed in La Culebra, where they are replaced by chalcopyrite and bornite during the main Cu ore stage (Fig. 31C). Therefore, and as reported for El Soldado, it is likely that at least part of the pyrite in the pre-ore assemblages at La Culebra grew in the presence of organic matter.

Trace element data of pyrite show the highest concentrations of Cu, As, Mn and Tl in the El Soldado deposit (median concentrations of 370 ppm for Cu, 1560 ppm for As, 1231 ppm for Mn, and 318 ppm for Tl) (Fig. 32). Lower concentrations of the aforementioned elements were measured in the Lorena (median concentrations of 110 ppm for Cu, 23 ppm for As, 65 ppm for Mn and 3 ppm for Tl) and La Culebra deposits (329 ppm for Cu, 20 ppm for As, 214 for Mn and 25 ppm for Tl) (Fig. 32). These elements belong to the suite elements that are typically concentrated by organic processes during sedimentation and diagenesis of organic-rich sediments in euxinic environments (Coveney and Martin, 1983; Wood, 1996; Coveney, 2000; Algeo and Maynard, 2004; Rimmer, 2004; Gregory et al., 2015; 2019; Herazo et al., 2021). These elements form strong organometallic bonds, which lead to their capture from seawater onto organic matter, on and immediately below the sea floor (Large et al., 2009). Despite the fact that Chilean stratabound Cu-(Ag) deposits are not considered sedimentary deposits per se (Maksaev et al., 2007; Barra et al., 2017), the presence of pyrobitumen-sulfides assemblage filling vesicles in volcanic rocks suggest a strong sedimentary contribution and a key role of organic matter in ore formation (Wilson et al., 1999, Cisternas and Hermosilla, 2006, Carrillo-Rosúa et al., 2014; Herazo et al., 2020; 2021). Within this context, it is likely that the significantly higher concentrations of As, Mn and Tl at El Soldado, reflect a strong sedimentary contribution (Fig. 32). Pyrite from La Culebra, contain more Mn and Tl than Lorena, which also suggests a sedimentary input.

The geological environment of formation of the three deposits allows exploring potential contributions from sedimentary rocks that may have conditions the geochemical signature of pyrite. El Soldado deposit is hosted in Cretaceous sedimentary rocks formed in a marine back-arc basin. This sedimentary sequence contains more than 3% of organic matter, and has been proposed as the most likely source of bitumen in El Soldado (Zentilli et al., 1997; Wilson et al., 1998). Therefore, the strong sedimentary signature of pyrite is probably related to the degradation of petroleum. On the other hand, the source of hydrocarbons in La Culebra, is possibly associated with marine bituminous algal-mat facies formed in a deep subtidal environment (Hosffsteffer et al., 1957; Cisternas and Díaz, 1990; Arevalo, 2005; Cisternas and Hermosilla, 2006). In Lorena, a possible source of hydrocarbons could be spatially related sedimentary formations (Herazo et al., 2020). The geochemical differences observed in pyrite from the three deposits may be related to source characteristics and variable sedimentary contributions. It is well known that sedimentary rocks can contain a wide diversity of organic matter of different origin (Powell, 1986), among others also define the Crude oil (pyrobitumen) composition and the trace metal content of hydrocarbons is the result of burial history, geothermal gradient, saline and anoxic conditions (Powell and Snowdon, 1983; Powell, 1984). The geochemical signature of the organic matter would be later reflected in the pyrite composition; however, extrinsic factors such as the intensity and extent of hydrothermal processes during mineralization may also play a fundamental role.

4.5.2. Sources(s) of sulfur and fractionation processes

It is well recognized that sulfur plays a crucial role in the formation of ore deposits (Candela and Piccoli, 2005; Seedorff et al., 2005; Williams-Jones and Heinrich, 2005; Seo et al., 2009; Simon and Ripley, 2011). However, the total sulfur content in a deposit can be derived from different sources (Simon and Ripley, 2011). Sulfur isotopes can be used to determine the source and processes involved in the formation of sulfides. Variations in $\delta^{34}\text{S}$ values can be related to formation temperature, redox reactions and pH of hydrothermal fluids (Ohmoto, 1972; Rye and Ohmoto, 1974; Ohmoto and Goldhaber, 1997; Seal, 2006).

Pyrite sulfur isotope data for Lorena and La Culebra are relatively lighter than values for El Soldado, i.e., $\delta^{34}\text{S}$ ranges of ~ -30 to $+10\text{‰}$ and $+18$ to $+60\text{‰}$, respectively (Fig. 33).

Sulfate in oil field waters and marine evaporate sequences would have a $\delta^{34}\text{S} > 10\text{‰}$ or similar to dissolved sulfate in modern oceans ($\delta^{34}\text{S} = +21\text{‰}$; Rees et al., 1978; Claypool et al., 1980; Böttcher et al., 2007; Tostevin et al., 2014). In contrast, the $\delta^{34}\text{S}$ of modern sedimentary pyrite formed in deep sea to shallow marine environments, is quite variable ranging between -50 and $+20\text{‰}$, although with mostly negative values (Chambers 1982; Sælen et al. 1993; Strauss 1997). Pyrite crystallization in these anoxic to oxic environments can be affected by microbial processes, such as organoclastic sulfate reduction, sulfur disproportionation, and sulfate-driven anaerobic methane oxidation (e.g., Goldhaber and Kaplan, 1980; Borowski et al., 2013), resulting in a potentially complex diagenetic/crystallization history (Lin et al., 2016).

The $\delta^{34}\text{S}$ data of pyrite from Lorena and La Culebra, may reflect incomplete sulfate reduction in a partially closed system dominated by connate seawater sulfate (e.g., Carrillo-Rosúa et al., 2014), that is, sulfate replenishment from the overlying water column exceeded sulfate consumption (Jørgensen, 1979; Canfield, 2001a,b; Habicht and Canfield, 2001). However, $\delta^{34}\text{S}$ data values close to 0‰ and $+10\text{‰}$ could also indicate that pyrite formed from magmatically-derived sulfur (Chaussidon et al., 1989). Heavier $\delta^{34}\text{S}$ values for El Soldado, on the other hand, are close to the maximum fractionation values reported for single organic sulfate reduction in natural settings (e.g., Canfield et al., 2010; Wortmann et al., 2001; Sim et al., 2011). A cumulative isotope effect resulting from sulfate reduction and disproportionation of intermediate sulfur species (e.g., Canfield and Teske, 1996) is not required to achieve this extreme isotopic fractionation, but it cannot be ruled out (Lin et al., 2016). Therefore, it is plausible that the isotopic enrichment in heavy sulfur at El Soldado is related to sulfate reduction, although it is likely that additional fractionation processes as sulfate-driven anaerobic methane oxidation were involved.

Figure 35 integrates LA-ICP-MS and SIMS data of pyrite in the studied deposits, which allow further exploring possible fractionation pathways. Concentrations of key elements are plotted as bivariate plots for each deposit, and for each data point the $\delta^{34}\text{S}$ value was classified into the three categories: 1) light sulfur ($\delta^{34}\text{S} < -5\text{‰}$), 2) near-zero sulfur ($-5\text{‰} < \delta^{34}\text{S} < +5\text{‰}$), and 3) heavy sulfur ($\delta^{34}\text{S} > +5\text{‰}$). Heavy $\delta^{34}\text{S}$ values broadly correlate with higher concentrations of trace elements, particularly those elements that are typically concentrated by organic processes in sedimentary settings, e.g., Mn, Mo, Tl, As (Fig. 35). Therefore, trace element data support the notion that heavy $\delta^{34}\text{S}$ values are related to an increased organic contribution, which is most evident at El Soldado. In this deposit, Wilson et al. (1999) documented the occurrence of irregular vesicles in pyrobitumen that represent fossilized degassing structures of the solidified petroleum. Methane gas (CH_4) dissolved in liquid oil under pressure may exsolve on decompression and buoyantly rise to the upper surface of the oil accumulation (Wilson et al., 1999). The presence of CH_4 suggests that sulfate in connate seawater was consumed via sulfate-driven anaerobic methane oxidation at a rapid rate, although this process is energetically less favorable than organoclastic sulfate reduction (Niewöhner et al., 1998; Kasten and Jørgensen, 2000; Sivan et al., 2007; Antler et al., 2014). Sulfate-driven anaerobic methane oxidation consumes most of the marine sulfate in volcanic-sedimentary sequence (e.g., Aharon and Fu, 2000; Jørgensen et al., 2004; Antler et al., 2014; Deusner et al., 2014). $\delta^{34}\text{S}$ values of dissolved sulfide progressively increase in the resultant pyrite, which is significantly heavier at El Soldado than the other two deposits (Fig. 36). It follows that complex sulfur fractionation mechanisms were involved during pyrite crystallization, leading to significant variations in $\delta^{34}\text{S}$ values. Further, $\delta^{34}\text{S}$ values vary significantly within pyrite grains from all three deposits, but no systematic variability in the trace element content was observed. The data point to either different sulfur source(s) and/or complex fractionation processes at the

microscale during pyrite growth. For example, $\delta^{34}\text{S}$ values close to 0‰ and higher concentrations for Cu in pyrite (Fig. 34A and C) could indicate an influx of Cu-rich magmatic-hydrothermal fluids (Wilson et al., 2003; Cisternas and Hermosilla, 2006; Carrillo-Rosúa et al., 2014; Herazo 2020). However, these grains also show sporadic lighter $\delta^{34}\text{S}$ values (up to -27‰) and high variability in As, Tl and Mn. We interpret these differences as related to changes in the physicochemical conditions of the pyrite-forming fluid and probably the result of sulfur addition from several sources. Several studies have recognized that sedimentary processes are involved in the formation of Chilean stratabound Cu-(Ag) deposits. The presence of bitumen in association with pyrite, including framboidal textures suggests that biogenic mechanisms drive sulfur isotope fractionation through thermochemical sulfate reduction or by biodegradation of petroleum. In fact, high concentrations of sulfur were reported in pyrobitumen from the Lorena deposit, where XANES sulfur speciation data indicate that thiophene and elemental sulfur are the dominant sulfur species. These organosulfur compounds can be attributed to an organic source for sulfur (Herazo et al., 2020).

Thermochemical sulfate reduction or petroleum biodegradation to sulfide coupled with oxidation of hydrocarbons, yield CO_2 , H_2S and highly refractory sulfur-rich solid bitumen (Goldstein and Aizenshtat, 1994). In-situ thermal cracking of S-rich pyrobitumen could add H_2S and other sulfur compounds to the pyrite-forming fluid. $\delta^{34}\text{S}$ data for pyrite inclusions in bitumen from the Carboniferous of Ireland show values around -25‰ (Parnell, 1993). However, heavy $\delta^{34}\text{S}$ values, between $+15\text{‰}$ and $+25\text{‰}$, have also been reported within pyrobitumen grains in carbonate-hosted-sphalerite-galena-pyrite veins in north Greenland (Jakobsen and Ohmoto, 1993; King et al., 2014). This suggests that the pyrobitumen $\delta^{34}\text{S}$ signature is influenced by organosulfur species present in the migrated petroleum (King et al., 2014), which results in an isotopic composition that is close to its parent oil (Orr, 1986; Idiz et al., 1990; Amrani et al., 2005). Although the $\delta^{34}\text{S}$ values of pyrobitumen in Chilean stratabound Cu-(Ag) deposits remain unconstrained, it is likely that it will vary according to the characteristics of the source rock. Also, these values would also be influenced by thermochemical sulfate reduction reactions, which is one of the most important organic-inorganic interactions (Orr, 1974; Worden and Smalley, 1996; Nöth, 1997; Machel, 2001; Cai et al., 2003; Seewald, 2003). Therefore, S isotope studies of pyrobitumen are necessary to understand the basic mechanisms of sulfur fractionation, and to better assess the potential source(s) of sulfur in the studied deposits.

4.5.3. Implications for ore mineralization processes

Several genetic models have been proposed for the genesis of the stratabound Cu-(Ag) deposits including epigenetic (Holmgren, 1987) or syngenetic models (Sato, 1984; Westra, 1988). The epigenetic origin is currently favored, based on field evidence of unconformable orebodies (Maksaev and Zentilli, 2002), and geochronological data indicating that these were emplaced after the deposition of the host rocks (Oliveros et al., 2008). In addition, the ubiquitous hydrothermal alteration (albitization, chloritization and sericitization) associated with the orebodies support an epigenetic model (Palacios and Definis, 1981; Espinoza et al., 1996; Maksaev and Zentilli, 2002). Despite this agreement, there is no consensus about the origin of the ore-forming fluids and the source of metals and sulfur. Magmatic-derived hydrothermal fluids have been proposed as a source of metals and sulfur for the Upper Jurassic stratabound Cu-(Ag) deposits (e.g., Buena Esperanza, Santo Domingo, Michilla, Mantos Blancos), evidenced by dike intrusions and stocks spatially associated with the Cu orebodies (Definis, 1985; Espinoza et al., 1996; Ramírez et al., 2006; Tristán-Aguilera, 2007). However, a clear genetic relationship between Cu mineralization and intrusions in

the Lower Cretaceous deposits has not been proven (Camus, 1990). Hydrothermal leaching models have also been proposed, which point to andesitic host rocks as the source of the ore-forming components (Kojima et al., 2009). Hydrothermal fluids of different origin, e.g., magmatic-hydrothermal, meteoric, connate, metamorphic, basin-related or seawater (Kojima et al., 2003; Tosdal and Munizaga, 2003) could be responsible for extracting metals and sulfur for the host units (Losert, 1973, 1974; Sato, 1984). In this scenario, cooling, deep plutons and/or dikes generate thermal convection of these non-magmatic waters (Tosdal and Munizaga, 2003; Kojima et al., 2003, 2009).

Bulk $\delta^{34}\text{S}$ data ranging between 0 and +7‰ support a magmatic source for sulfur in the Upper Jurassic stratabound Cu-(Ag) deposits (Sasaki et al., 1984; Vivallo and Henríquez, 1998; Saric et al., 2003; Ramirez et al., 2006; Tristá-Aguilera, 2007) (Fig. 33, horizontal bar). In contrast, bulk of $\delta^{34}\text{S}$ values showing a wide variability (-50.4 to +12‰) in the Lower Cretaceous deposits indicate that the sulfur isotopic signature was the result of bacteriogenic sulfate reduction (Wilson et al., 2003b; Carrillo-Rosúa et al., 2014). However, recent studies have also suggested that at least some sulfur can be derived from hydrocarbon (pyrobitumen) compounds, i.e., organic sulfur released during pyrobitumen aromatization (Herazo et al., 2020). Similarly, trace element data in pyrite in stratabound Cu-(Ag) deposits show high concentrations of Mn, Mo and Tl, pointing to a sedimentary/basinal source, or even partly derived from pyrobitumen (Herazo et al., 2021). These data are consistent with a strong sedimentary contribution in the formation of bitumen-bearing stratabound Cu-(Ag) deposits. The wide range of $\delta^{34}\text{S}$ data (-29.56 to +59.44‰) are interpreted as the result of sulfate reduction mediated by bacteria and sulfate-driven anaerobic oxidation of methane.

The nature of the hydrothermal fluids can be assessed using trace elements and sulfur isotopes. It is well documented that basinal water and magmatic-hydrothermal fluids have distinct Se/S ratios (e.g., Huston et al., 1995; Rowins et al., 1997; Fitzpatrick, 2008; Li et al., 2018). Basinal water has an average $\delta^{34}\text{S}$ value of around +21‰ and a mass $\sum\text{Se}/\sum\text{S}$ ratio of $5\text{--}25 \times 10^{-8}$, whereas magmatic-hydrothermal fluids have a $\delta^{34}\text{S}$ value of 0 ± 5 ‰ and a mass $\sum\text{Se}/\sum\text{S}$ ratio of $1.2\text{--}5 \times 10^{-8}$ (e.g., Huston et al., 1995; Rowins et al., 1997; Seal, 2006 and references therein; Fitzpatrick, 2008; Li et al., 2018, del Real et al., 2020). Although Se concentrations were measured only sporadically in pyrite from the studied stratabound Cu-(Ag) (Table 1), our data show that the Se/S broadly vary as a function of $\delta^{34}\text{S}$ (Fig. 37). Higher Se/S ratios of pyrite (~0.0001-0.1) at Lorena and La Culebra are related to lower $\delta^{34}\text{S}$ values (-10 to +5‰), while lower Se/S ratios (<0.0001) at El Soldado correlate with heavier $\delta^{34}\text{S}$ values (+20 to +40‰). Several pyrite samples from the Lorena deposit fall within the range of magmatic-hydrothermal fluids (Fitzpatrick, 2008). However, the significant variability of Se/S ratios and the lighter $\delta^{34}\text{S}$ (<-10‰) values suggest the involvement of a fluid possibly of sedimentary origin (Herazo et al., 2020). In the El Soldado deposit, most pyrite data show similar Se/S ratios, with a wider range of $\delta^{34}\text{S}$ values, consistent with a more prominent sedimentary influence, with fluids sourced from sedimentary rocks (connate waters), seawater, or a mixture of hydrocarbon-rich fluids.

In addition, High Re and radiogenic Os concentrations (i.e., 15 ppm Re and 65 ppb Os), and an extremely high $^{187}\text{Os}/^{188}\text{Os}$ ratio (3.94977) reported for El Soldado support a strong crustal contribution reflecting a radiogenic source (Ruiz et al., 1997). These data are consistent with a model where oxidized saline brines leached metals (and sulfur?) from the host rocks with a partial contribution from magmatic-derived fluids (Barra et al., 2017).

4.6. FINALS REMARKS

The LA-ICP-MS and SIMS data presented in this study provide some insights on the source of metals and sulfur in bitumen-bearing stratabound Cu-(Ag) deposits from the Coastal Cordillera in central-northern Chile. Our LA-ICP-MS and SIMS data, coupled with previously published bulk sulfur isotope data for these deposits (e.g., Wilson et al., 1999; Carrillo-Rosúa et al., 2014), indicate that the source of sulfur and by interference metals contained in these deposits was derived from different sources with a strong (but highly variable) sedimentary component.

The trace element content in pyrite is similar to those reported for sedimentary pyrite (Large et al., 2009). Furthermore, the high concentrations of Mn, As, and Tl support a sedimentary/basinal contribution, which is more prominent at El Soldado. Sulfur isotope data of pyrite display a wide range of $\delta^{34}\text{S}$ values (−30 to +60‰), consistent with sulfur derived from various sources including basinal brines, seawater, and magmatic-hydrothermal. The lighter to intermediate $\delta^{34}\text{S}$ values (−30 to +10‰), typical of the Lorena and La Culebra deposits, are interpreted to reflect incomplete sulfate reduction in a partially closed system of connate seawater sulfate. The significantly heavier $\delta^{34}\text{S}$ values (up to +60‰) measured at El Soldado are close to the maximum fractionation recorded for single organic sulfate reduction in nature, although it is highly likely that other fractionation processes as anaerobic methane oxidation were involved.

Results presented here support a leaching of basement rocks model and where oxidized saline brines played a fundamental role in the formation of bitumen-bearing stratabound Cu-(Ag) deposits in northern-central Chile.

4.7. ACKNOWLEDGMENTS

Funding for this study was provided by Iniciativa Científica Milenio through “Millennium Nucleus for Metal Tracing Along Subduction” grant, and by FONDECYT grants #1140780 and #1190105. The authors acknowledge additionally support from FONDAP project #15090013 “Centro de Excelencia en Geotermia de los Andes, CEGA”. The LA-ICP-MS analytical work was funded by CONICYT-FONDEQUIP instrumentation grant EQM120098. We thank technical assistance of Rurik Romero during LA-ICP-MS analyses. We thank Marcos Zentilli for providing access to samples from the El Soldado deposit. Compañía Minera Las Cenizas and Compañía Minera Carmen Bajo are acknowledged for providing access to the deposits. Andrea Paola Herazo thanks financial support provided by a Doctoral scholarship from ANID (21171385) and the Hugh McKinstry grant from the Society of Economic Geologists Foundation (SEGF).

4.8. REFERENCES

Aharon, P., Fu, B.S., 2000. Microbial sulfate reduction rates and sulfur and oxygen isotope fractionations at oil and gas seeps in deepwater Gulf of Mexico. *Geochim. Cosmochim. Acta* 64, 233–246.

Algeo, T.J., and Maynard, J.B., 2004, Trace-element behaviour and redox facies in core shales of Upper Pennsylvanian Kansas-type cyclothems. *Chem. Geol.* 206, 289–318.

- Amrani, A., Lewan, M., Aizenshtat, Z., 2005. Stable sulfur isotope partitioning during simulated petroleum formation as determined by hydrous pyrolysis of Ghareb Limestone, Israel. *Geochim. Cosmochim. Acta* 69, 22, 5317.
- Antler, G., Turchyn, A.V., Herut, B., Davies, A., Rennie, V., Sivan, O., 2014. Sulfur and oxygen isotope tracing of sulfate driven anaerobic methane oxidation in estuarine sediments. *Estuar. Coast. Shelf Sci.* 142, 4–11.
- Arévalo, C., 2005. Carta Copiapó, Región de Atacama. Servicio Nacional de Geología y Minería. Carta Geológica de Chile, Serie Geología Básica, 91, scale 1:100.000.
- Barker, S. L. L., Hickey, K. A., Cline, J. S., Dipple, G. M., Kilburn, M. R., Vaughan, J. R., Longo, A. A., 2009. Uncloaking invisible gold: use of nanosims to evaluate gold, trace elements, and sulfur isotopes in pyrite from Carlin-type gold deposits: *Econ. Geol.* 104, 897–904.
- Barra, F., Reich, M., Selby, D., Rojas, P., Simon, A., Salazar, E., Palma, G., 2017. Unraveling the origin of the Andean IOCG clan: a Re-Os isotope approach. *Ore Geol. Rev.* 81, 62–78.
- Boric, R., Díaz, F., Maksaev, V., 1990. Geología y yacimientos metalíferos de la Región de Antofagasta. Servicio Nacional de Geología y Minería, Boletín No 40 (in Spanish).
- Boric, R., 1997. Nuevos antecedentes sobre el modelo geológico del yacimiento de cobre, El Soldado, Chile Central. Congreso Geológico Chileno, Antofagasta, Chile, p 862–866 (in Spanish).
- Boric, R., Holmgren, C., Wilson, N.S.F., Zentilli, M., 2002. The Geology of the El Soldado Manto Type Cu (Ag) Deposit, Central Chile; in Porter, T.M. (Ed.), *Hydrothermal Iron Oxide Copper-Gold & Related Deposits: A Global Perspective, Volume 2*; PGC Publishing, Adelaide, 163–184.
- Borowski, W.S., Rodriguez, N.M., Paull, C.K., Ussler III, W., 2013. Are 34S-enriched authigenic sulfide minerals a proxy for elevated methane flux and gas hydrates in the geologic record?. *Mar. Pet. Geol.* 43, 381–395.
- Böttcher, M.E., Brumsack, H.J., Dürselen, C.D., 2007. The isotopic composition of modern seawater sulfate: I. Coastal waters with special regard to the North Sea. *J. Mar. Syst.* 67, 73–82.
- Cai, C.F., Worden, R.H., Bottrell, S.H., Wang, L.S., Yang C.C., 2003. Thermochemical sulphate reduction and the generation of hydrogen sulphide and thiols (mercaptans) in Triassic carbonate reservoirs from the Sichuan Basin, China. *Chem. Geol.* 202, 1–2, 39.
- Camus, F., 1990. Geological characteristics of Strata-bound Deposits Associated with Lacustrine Sediments, Central Chile; in: Fontboté, et al. (Eds.) *Stratabound Ore Deposits in the Andes*. Berlin, Springer-Verlag, p. 449–462.
- Candela, P.A., Piccoli, P.M., 2005. Magmatic Processes in the Development of Porphyry Type Ore Systems; in: Hedenquist, J.W., Thompson, J.F.H., Goldfarb, R.J., Richards, J.P. (Eds.), *Economic Geology 100th Anniversary Volume*, 25–38.
- Canfield, D.E., Teske, A., 1996. Late Proterozoic rise in atmospheric oxygen concentration inferred from phylogenetic and sulphur-isotope studies. *Nature* 382, 127–132.

- Canfield, D.E., 2001a. Isotope fractionation by natural populations of sulfate-reducing bacteria. *Geochim. Cosmochim. Acta* 65, 1117–1124.
- Canfield, D.E., 2001b. Biogeochemistry of sulfur isotopes. *Rev. Mineral. Geochem.* 43, 607–636.
- Canfield, D.E., Farquhar, J., Zerkle, A.L., 2010. High isotope fractionations during sulfate reduction in a low-sulfate euxinic ocean analog. *Geology* 38, 415–418.
- Carrillo-Rosúa, J., Boyce A., Morales-Ruano, S., Morata, D., Roberts, S., Munizaga, F., Moreno-Rodríguez, V., 2014. Extremely negative and inhomogeneous sulfur isotope signatures in Cretaceous Chilean manto-type Cu-(Ag) deposits, Coastal Range of central Chile. *Ore Geol. Rev.* 56, 3–24.
- Chambers, L. A., 1982, Sulfur isotope study of a modern intertidal environment, and the interpretation of ancient sulfides: *Geochim. Cosmochim. Acta* 46, 721–728.
- Charrier, R., Pinto, L., Rodríguez, M.P., 2007. Tectonostratigraphic evolution of the Andean Orogen in Chile in Moreno, T., Gibbons, W. (Eds.), *The Geology of Chile*. The Geological Society, London.
- Cisternas, M.E., Diaz, L., 1990. Geologic evolution of the Atacama basin during the Lower Cretaceous; in: Fontboté L, Amstutz CG, Cardozo M, Cedillo E, Frutos J (Eds.), *Stratabound ore deposits in the Andes*. Springer, Berlin Heidelberg New York, pp 496–504.
- Cisternas, E., Hermosilla, J., 2006. The role of bitumen in strata-bound copper deposit formation in the Copiapó area, Northern Chile. *Miner. Depos.* 41, 339–355.
- Claypool, G.E., Holser, W.T., Kaplan, I.R., Sakai, H., Zak, I., 1980. The age curves of sulfur and oxygen isotopes in marine sulfate and their mutual interpretation. *Chem. Geol.* 28, 199–260.
- Coleman ML, Moore, M.P., 1978. Direct reduction of sulfates to sulfur dioxide for isotopic analysis. *Anal. Chem.* 50, 1594–1598.
- Comisión Chilena del Cobre (Cochilco), Ministerio de Minería, Gobierno de Chile, 2016. *Franjas metalogénicas de los Andes Centrales: blancos clave para la exploración minera* (in Spanish).
- Cook, N., and Chryssoulis, S. L., 1990. Concentrations of “Invisible Gold” in the common sulfides: *Canad. Mineral.* 28, 1–16.
- Cook, N. J., Ciobanu, C. L., and Mao, J., 2009. Textural control on gold distribution in As-free pyrite from the Dongping, Huangtuliang and Hougou gold deposits, North China Craton (Hebei Province, China): *Chem. Geol.* 264, 101–121.
- Coveney, R.M., and Martin, S.P., 1983. Molybdenum and other heavy metals of the Mecca Quarry and Logan Quarry shales. *Econ. Geol.* 78, 132–149.
- Coveney, R.M., 2000. Metaliferous shales and the role of organic matter, with examples from China, Poland, and the United States: A review: *Econ. Geol.* 95, 251–280.

Cucurella, J., Canut de Bon, C., Cisternas, M.E., 2005. Pyrobitumen related to silver-copper deposits in a Cretaceous volcanic-sedimentary sequence: Talcuna district, Coquimbo, Chile. *Mineral. Polonica* 36, 1, 21–29.

Definis, A. 1985. Antecedentes geológicos del yacimiento de cobre Santo Domingo, Taltal y discusión acerca de su relación con un sistema de filones gabrodioríticos. *Congreso Geológico Chileno, IV, Antofagasta, Chile, Vol. 2, 3–204, 3–215 (in Spanish).*

Detlef, K., 2002. Geologisch-tektonische Karte der Küstenkordillere südlich von Taltas (Nordchile). Maßstab 1:150.000.

Deusner, C., Holler, T., Arnold, G.L., Bernasconi, S.M., Formolo, M.J., Brunner, B., 2014. Sulfur and oxygen isotope fractionation during sulfate reduction coupled to anaerobic oxidation of methane is dependent on methane concentration. *Earth Planet. Sci. Lett.* 399, 61–73.

Espinoza, S., Véliz, H., Esquivel, J., Arias, J., y Moraga, A., 1996. The Cupriferous Province of the Coastal Range, Northern Chile; in: Camus, F., Sillitoe, R.H., and Petersen, R. (Eds.), *Andean Copper Deposits: New Discoveries, Mineralization, Styles and Metallogeny*. Society of Economic Geologists, Special Publication Number 5, pp. 19–32.

Fitzpatrick, A.J., 2008. The measurement of the Se/S ratios in sulphide minerals and their application to ore deposit studies. Doctoral thesis, Queens University, Canada.

García, F., 1967. Geología del Norte Grande de Chile, Simposio, Geosinclinal Andino, Sociedad Geológica de Chile. *Publicaciones* 3, 138 (in Spanish).

Goldhaber, M.B. and Kaplan, I.R., 1980. Mechanisms of sulfur incorporation and isotope fractionation during early diagenesis in sediments of the Gulf of California. *Mar. Chem.* 9, 95–143.

Goldstein, T. and Aizenshtat, Z., 1994. Thermochemical sulfate reduction – a review. *J. Therm. Anal.* 42, 1, 241–290.

Gregor, B., Piestrzyński, A., Bachmann, G.H., Püttmann, W., Walther, S., Fiedler, M., 2012. An overview of the European Kupferschiefer deposits. *Geology and genesis of major copper deposits and districts of the world: a tribute to Richard H. Sillitoe, Jeffrey, W. Hedenquist, Michael Harris, Francisco Camus*. Special Publication No. 16 of the Society of Economic Geologists.

Gregory, D., Meffre, S., Large, R., 2014. Comparison of metal enrichment in pyrite framboids from a metal-enriched and metal-poor estuary. *Am. Mineral.* 99, 4, 633–644.

Gregory, D.D., Large, R.R., Halpin, J.A., Baturina, E.L., Lyons, T.W., Wu, S., Danyushevsky, L., Sack, P.J., Chappaz, A., Maslennikov, V.V., Bull, S.W., 2015. Trace element content of sedimentary pyrite in black shales. *Econ. Geol.* 110, 1389–1410.

Gregory, D., Mukherjee, I., Olson, S., Large, R., Danyushevsky, L., Stepanov, A., Avila, J., Cliff, J., Ireland, T., Raiswell, R., Olin, P., Maslennikov, V., Lyons, T., 2019. The formation mechanisms of sedimentary pyrite nodules determined by trace element and sulfur isotope microanalysis. *Geochem. Cosmochim. Acta* 259, 53–68.

- Habicht, K.S., Canfield, D.E., 2001. Isotope fractionation by sulfate-reducing natural populations and the isotopic composition of sulfide in marine sediments. *Geology* 29, 555–558.
- Hagan, T., Parnell, J., Cisterna, M.E., 2003. Fluid history of andesite-hosted CuS-bitumen mineralization, Copiapó district, north central Chile. *J. Geochem. Explor.* 78–79, 631–633.
- Hannington, M.D., Poulsen, K.H., Thompson, J.F.H., Sillitoe, R.H., 1999. Volcanogenic Gold in the Massive Sulfide Environment, in *Volcanic-associated massive sulfide deposits; processes and examples in modern and ancient settings: Society of Economic Geologists*, p. 325–356.
- Herazo, A., Reich, M., Barra, F., Morata, D., del Real, I., Pagès, A., 2020. Assessing the role of bitumen in the formation of stratabound Cu-(Ag) deposits: Insights from the Lorena deposit, Las Luces district, northern Chile. *Ore Geol. Rev.* 124, 103639.
- Herazo, A.; Reich, M., Barra, F., Morata, D., del Real, I., 2021. Trace element geochemistry of pyrite from bitumen-bearing stratabound Cu-(Ag) deposits, northern Chile. *ACS Earth and Space Chem.* <https://dx.doi.org/10.1021/acsearthspacechem.0c00321>.
- Hermosilla, J., 2001. Rol de la materia orgánica en la formación de los depósitos minerales del Metalotecto Ocoita-Pabellón. Copiapó, III Región de Atacama. Undergraduate Thesis, Departamento de Ciencias de la Tierra, Universidad de Concepción, p 213 (in Spanish).
- Hoffstetter, R., Fuenzalida, H., Cecioni, G., 1957. *Lexique Stratigraphique International*, 5, 444, Amérique Latine, Chile.
- Holgrem, C., 1987. Antecedentes para un modelo genético del yacimiento El Soldado, V Región de Valparaíso, Chile. *Revista Geológica de Chile*, N° 30, pp. 3–18 (in Spanish).
- Holley, E., Lowe, J., Johnson, C., Pribil, M., 2019. Magmatic-hydrothermal gold mineralization at the Lone Tree Mine, Battle Mountain District, Nevada. *Econ. Geol.* 114, 5, 811–856.
- Horton, B.K., 2018. Tectonic regimes of the central and southern Andes: Responses to variations in plate coupling during subduction. *Tectonics* 37, 402–429.
- Huston, D.L., Sie, S.H., Suter, G.F., Cooke, D.R., Both, R.A., 1995. Trace elements in sulfide minerals from eastern Australian volcanic-hosted massive sulfide deposits: part I. Proton microprobe analyses of pyrite, chalcopyrite, and sphalerite, and part II. Selenium levels in pyrite: comparison with $\delta^{34}\text{S}$ values and implications. *Econ. Geol.* 90, 1167–1196.
- Idiz, E., Tannenbaum, E., Kaplan, I., 1990. Pyrolysis of high-sulfur Monterrey kerogen; in: Orr, W. and White, C. (Eds), *Geochemistry of sulfur in Fossil Fuels*, 429, ACS Symposium Series. Am. Chem. Soc. 575–591.
- Jakobsen, U. and Ohmoto, H., 1993. Bitumen associated with precipitation of sulphides in carbonate-hosted vein mineralization, North Greenland. *Bitumens in ore deposits. Special Publication No. 9 of the Society for Geology Applied to Mineral Deposits*, Springer-Verlag, 1–6.
- Jara, J.J., Barra, F., Reich, M., Morata, D., Leisen, M., Romero, R., 2021. Geochronology and petrogenesis of intrusive rocks in the Coastal Cordillera of northern Chile: Insights from zircon U-Pb dating and trace element geochemistry. *Gondwana Res.* 93, 48–72.

- Jochum, K.P., Willbold, M., Raczek, I., Stoll, B., Herwig, K., 2005. Chemical characterisation of the USGS reference glasses GSA-1G, GSC-1G, GSD-1G, GSE-1G, BCR-2G, BHVO-2G and BIR-1G using EPMA, ID-TIMS, ID-ICP-MS and LAICP-MS. *Geostand. Geoanal. Res.* 29, 285–302.
- Jørgensen, B.B., 1979. A theoretical model of the stable sulfur isotope distribution in marine sediments. *Geochim. Cosmochim. Acta* 43, 363–374.
- Jørgensen, B.B., Böttcher, M.E., Lüschen, H., Neretin, L.N., Volkov, I.I., 2004. Anaerobic methane oxidation and a deep H₂S sink generate isotopically heavy sulfides in Black Sea sediments. *Geochim. Cosmochim. Acta* 68, 2095–2118.
- Kasten, S., Jørgensen, B.B., 2000. Sulfate reduction in marine sediments; in: Schulz, H.D., Zabel, M. (Eds.), *Marine Geochemistry*. Springer, Berlin, Heidelberg, 263–281.
- Keith, M., Haase, K.M., Klemd, R., Krumm, S., Strauss, H., 2016. Systematic variations of trace element and sulfur isotope compositions in pyrite with stratigraphic depth in the Skouriotissa volcanic-hosted massive sulfide deposit, Troodos ophiolite, Cyprus. *Chem. Geol.* 423, 7–18.
- Kojima, S., Astudillo, J., Rojo, J., Tristá-Aguilera, D., Hayashi, K., 2003. Ore mineralogy, fluid inclusion, and stable isotopic characteristics of stratiform copper deposits in the Coastal Cordillera of Northern Chile. *Miner Depos* 38, 208–216.
- Kojima, S., Tristá-Aguilera, D., Hayashi, K., 2009. Genetic aspects of the manto-type copper deposits based on geochemical studies of North Chilean deposits. *Resour. Geol.* 59, 1, 87–98.
- LaFlamme, C., Martin, L., Jeon, H., Reddy, S.M., Selvaraja, V., Caruso, S., Bui, T.H., Roberts, M.P., Voute, F., Hagemann, S., Wacey, D., Littman, S., Wing, B., Fiorentini, M., Kilburn, M.R., 2016. In situ multiple sulfur isotope analysis by SIMS of pyrite, chalcopyrite, pyrrhotite, and pentlandite to refine magmatic ore genetic models. *Chem. Geol.* 444, 1–15.
- Large, R.R., Danyushevsky, L., Hollit, C., Maslennikov, V., Meffre, S., Gilbert, S., Bull, S., Scott, R., Emsbo, P., Thomas, H., Singh, B., Foster, J., 2009. Gold and trace element zonation in pyrite using a laser imaging technique: Implications for the timing of gold in orogenic and carlin-style sediment-hosted deposits. *Econ. Geol.* 104, 635–668.
- Li, R., Chen, H., Xia, X., Yang, Q., Danyushevsky, L.V., Lai, C., 2018. Using integrated in-situ sulfide trace element geochemistry and sulfur isotopes to trace ore-forming fluids: Example from the Mina Justa IOCG deposit (southern Perú). *Ore Geol. Rev.* 101, 165–179.
- Li, J.X., Hu, R., Zhao, C., Zhu, J., Huang, Y., Gao, W., Li, J.W., Zhuo, Y., 2020. Sulfur isotope and trace element compositions of pyrite determined by NanoSIMS and LA-ICP-MS: new constraints on the genesis of the Shuiyindong Carlin-like gold deposit in SW China. *Miner. Depos.* 55, 1279–1298.
- Lin, Z., Sun, X., Peckmann, J., Lu, Y., Xu, L., Strauss, H., Zhou, H., Gong, J., Lu, H., Teichert B., 2016. How sulfate-driven anaerobic oxidation of methane affects the sulfur isotopic composition of pyrite: A SIMS study from the South China Sea. *Chem. Geol.* 440, 26–41.

Losert, J., 1973. Genesis of copper mineralization and associated alterations in the Jurassic volcanics rocks of Buena Esperanza mining area. Publication N°40, Departamento de Geología, Universidad de Chile, Santiago, 104 p.

Losert, J., 1974. Alteration and associated copper mineralization in the Jurassic volcanic rocks of Buena Esperanza mining area (Antofagasta Province, Northern Chile); in Klohn E. (Ed.), Coloquio sobre fenómenos de alteración y metamorfismo en rocas volcánicas e intrusivas, p. 51–85.

Machel, H.G., 2001. Bacterial and thermochemical sulfate reduction in diagenetic settings – old and new insights. *Sed. Geol.* 140, 1–2, 143–175.

Maksaev, V., 1990. Metallogeny, geological evolution, and thermochronology of the Chilean Andes between latitudes 21° and 26° south, and the origin of major porphyry copper deposits. Ph.D. Thesis, Dalhousie University.

Maksaev, V., Zentilli, M., 2002. Chilean strata-bound Cu–(Ag) deposits: an overview; in: Porter, T.M. (Ed.), *Hydrothermal Iron Oxide Copper–Gold & Related Deposits. A Global Perspective*. PGC Publishing, Adelaide, 185–205.

Maksaev, V., Townley, B., Palacios, C., Camus, F., 2007. Metallic ore deposits; in Moreno, T., Gibbons, W. (Eds.), *The Geology of Chile*. The Geological Society, London: 179–199. London.

Marschik, R. and Fontboté, L., 2001. The Punta del Cobre Formation, Punta del Cobre-Candelaria area, northern Chile. *J. South Am. Earth Sci.* 14, 401–433.

Marschik, R., Fontignie, D., Chiaradia, M., Voldet, P., 2003. Geochemical and Sr–Nd–O isotope composition of granitoids of the Early Cretaceous Copiapó plutonic complex (27°30' S), Chile. *J. South. Am. Earth Sci.* 16, 381–398.

Mayer, C.K., Fontboté, L., 1990. The stratiform Ag–Cu deposit El Jardín, Northern Chile; in: Fontboté, L., Amstutz, G.C., Cardozo, M., Cedillo, E. & Frutos, J. (Eds.), *Stratabound ore deposits in the Andes*. Berlin, Springer, 637–646.

Mpodosis, C., Ramos, V., 1990. The Andes of Chile and Argentina; in: Ericksen, E., Cañas Pinochet, T., Reinemund, A. (Eds), *Geology of the Andes and its Relation to Hydrocarbon and Mineral Resources*. Circum-Pacific Council for Energy and Mineral Resources, Earth Science Series 11, 59–90.

Naranjo, J., 1978. Geología de la zona interior de la Cordillera de la Costa entre los 26°20' Sur, Región de Atacama. *Carta Geológica de Chile*, escala 1:100.000. Instituto de Investigaciones Geológicas 34, 48 (in Spanish).

Naranjo, J., Puig, A., 1984. Hojas Taltal y Chañaral, Regiones de Antofagasta y Atacama, escala 1: 250.000, *Carta Geológica de Chile* N° 62–63 (in Spanish).

Niewöhner, C., Hensen, C., Kasten, S., Zabel, M., Schulz, H.D., 1998. Deep sulfate reduction completely mediated by anaerobic methane oxidation in sediments of the upwelling area off Namibia. *Geochim. Cosmochim. Acta* 62, 455–464.

- Nöth S., 1997. High H₂S contents and other effects of thermochemical sulfate reduction in deeply buried carbonate reservoirs: a review. *Geol. Rundsch.* 86, 2, 275–287.
- Ohmoto, H., 1972. Systematics of sulfur and carbon isotopes in hydrothermal ore deposits. *Econ. Geol.* 67, 551–578.
- Ohmoto, H., Goldhaber, M.B., 1997. Sulfur and carbon isotopes; in: Barnes, H.L. (Ed.), *Geochemistry of Hydrothermal Ore Deposit*, 3rd Edn. John Wiley & Sons, New York, pp. 517–611.
- Oliveros, V., Féraud, G., Aguirre, L., Ramírez, L., Fornari, M., Palacios, C., Parada, M., 2008. Detailed ⁴⁰Ar/³⁹Ar dating of geologic events associated with the Mantos Blancos copper deposit, northern Chile. *Miner. Depos.* 43, 3, 281–293.
- Orr, W., 1974. Changes in sulfur content and isotopic-ratios of sulfur during petroleum maturation – study of Big Horn Basin Paleozoic oils. *AAPG Bull.* 58, 11, 2295–2318.
- Orr, W., 1986. Kerogen asphaltene sulfur relationships in sulfur-rich Monterrey oils. *Org. Geochem.* 10, 1-3, 499–516
- Palacios, C. and Definis, A., 1981. Petrología del yacimiento Buena Esperanza, II Región, Norte de Chile. Primer Coloquio sobre volcanismo y metalogénesis, Departamento de Geociencias, Universidad del Norte, Antofagasta, Chile, p. 48–67 (in Spanish).
- Palacios, C., 1990. Geology of the Buena Esperanza Copper-Silver Deposit, Northern Chile; in: Fontboté, L., et al. (Eds.), *Stratabound Ore Deposits in the Andes*. Berlin, Springer-Verlag, p. 313–318.
- Parnell, J. 1993. Bitumens in ore deposits. Special Publication No. 9 of the Society for Geology Applied to Mineral Deposits, Springer-Verlag, 1-6.
- Paton, C., Hellstrom, J., Paul, B., Woodhead, J., Hergt, J., 2011. Iolite: freeware for the visualisation and processing of mass spectrometric data. *J. Anal. At. Spectrom.* 26, 2508–2518.
- Peterson, E., and Mavrogenes, J., 2014. Linking high-grade gold mineralization to earthquake-induced fault-valve processes in the porguera gold deposit, Papua New Guinea. *Geology*, 42, 383–386.
- Pichowiak, S., Buchelt, M., Damm, K.W., 1990. Magmatic activity and tectonic setting of the early stages of the Andean cycle in northern Chile. *Geol. Soc. Am., Sp Pub* 241, 127–144.
- Powell, T. G. and Snowdon, L. R., 1983. A composite hydrocarbon generation model: Implications for evaluation of basins for oil and gas, *Erdol und Kohle* 36, 163–170.
- Powell, T. G., 1984. Some aspects of the hydrocarbon geochemistry of a middle Devonian barrier reef complex, western Canada; in: Palacas, J.G. (Ed.); *Petroleum Geochemistry and Source Rock Potential of Carbonate Rocks AAPG Studies in Geology* 18, 45–62.
- Powell, T.G., 1986. Petroleum geochemistry and depositional setting of lacustrine source rocks. *Mar. Petrol. Geol.* 3, 3, 200–219.

Ramírez, L.E., Palacios, C., Townley, B., Parada, M.A., Sial, A.N., Fernandez-Turries, J.L., Gimeno, D., Garcia-Valles, M., Lehman, B., 2006. The Mantos Blancos copper deposit: an upper Jurassic breccia-style hydrothermal system in the Coastal Range of northern Chile. *Miner. Depos.* 41, 246–258.

del Real, I., Thompson, J.F.H., Simon, A.C., Reich, M., 2020. Geochemical and isotopic signature of pyrite as a proxy for fluid source and evolution in the Candelaria-Punta del Cobre IOCG district Chile. *Econ. Geol. Bull. Soc. Econ. Geol.* 115, 7, 1493–1518.

Rees, C.E., Jenkins, W.J., Monster, J., 1978. The sulfur isotopic composition of ocean water sulphate. *Geochim. Cosmochim. Acta* 43, 377–381.

Reich, M., Kesler, S.E., Utsunomiya, S., Palenik, C.S., Chryssoulis, S.L., Ewing, R.C., 2005. Solubility of gold in arsenian pyrite. *Geochim. Cosmochim. Acta*, 69, 2781–2796.

Reich, M., Palacios, C., Alvear, M., Cameron, E.M., Leybourne, M.I., and Deditius, A., 2009. Iodine-rich waters involved in supergene enrichment of the Mantos de la Luna argentiferous copper deposit, Atacama Desert, Chile. *Mineral. Depos.* 44, 719–722.

Reich, M.; Chryssoulis, S.; Deditius, A.; Palacios, C.; Zuniga, A.; Weldt, M.; Alvear, M., 2010. “Invisible” silver and gold in supergene digenite (CuS). *Geochem. Cosmochim. Acta* 74, 6157–6173.

Reich, M., Palacios, C., Barra, F., Chryssoulis, S., 2013a “Invisible” silver in chalcopyrite and bornite from the Mantos Blancos copper deposit. *Eur. J. Mineral.* 25, 453–460.

Reich, M., Deditius, A., Chryssoulis, S., Li, J.W., Ma, C.Q., Parada, M.A., Barra, F., Mittermayr, F., 2013b. Pyrite as a record of hydrothermal fluid evolution in a porphyry copper system: A SIMS/EMPA trace element study. *Geochim. Cosmochim. Acta* 104, 42–62.

Rieger, A., Schwark, L., Cisternas, M.E., Miller, H., 2008. Society of Economic Geologists, Inc. *Econ. Geol.* 103, 387–404.

Rimmer, S.M., 2004, Geochemical paleoredox indicators in Devonian-Mississippian black shales, Central Appalachian basin, USA. *Chem. Geol.* 206, 372–391.

Rivano, S., Sepulveda, P., Boric, R. y Espiñeira, D., 1993. Hojas Quillota y Portillo, V Región. Servicio Nacional de Geología y Minería, Carta Geológica de Chile, No. 73, mapa escala 1:250.000 (in Spanish).

Román, N., Reich, M., Leisen, M., Morata, D., Barra, F., Deditius, A.P., 2019. Geochemical and micro-textural fingerprints of boiling in pyrite. *Geochim. Cosmochim. Acta* 246, 60–85.

Rowins, S.M., Groves, D.I., McNaughton, N.J., Palmer, M.R., Eldridge, C.S., 1997. A reinterpretation of the role of granitoids in the genesis of neoproterozoic gold mineralization in the Telfer dome, Western Australia. *Econ. Geol. Bull. Soc. Econ. Geol.* 92, 133–160.

Ruíz, C., Aguirre, L., Corvalán, J., Klohn, C., Klohn, E., Levi, B., 1965. Geología y yacimientos metalíferos de Chile. Instituto de Investigaciones Geológicas, Santiago, Chile, 302 p. (in Spanish).

- Ruiz, C., Aguilar, A., Egert, E., Espinosa, W., Peebles, F., Quezada, R. and Serrano, M., 1971. Strata-bound copper sulphide deposits of Chile; in: Proceedings IMA-IAGOD, 7th General Meeting, Tokyo-Kyoto, Japan, 1970. Soc. Min. Geol. Japan, Special Issue 3, pp. 252–260.
- Ruiz, J., Freydier, C., McCandless, T., Chesley, J., 1997. Re-Os isotope systematics from base metal porphyry and Manto-type mineralization in Chile. *Int. Geol. Rev.* 39, 317–324.
- Rye, R.O., and Ohmoto, H., 1974. Sulfur and Carbon Isotopes and Ore Genesis. *Review. Econ. Geol.* 69, 826–842.
- Saric, N., Kreft, C., Huete, C., 2003. Geología del yacimiento Lo Aguirre, Chile. *Rev. Geol. Chile* 30, 317–331 (in Spanish).
- Sasaki, A., Ulriksen, C., Sato, K., Ishihara, S., 1984. Sulphur isotope reconnaissance of porphyry copper and manto type deposits in Chile and the Philippines. *Bull. Geol. Surv. Jpn.* 35, 615–622.
- Sato, T., 1984. Manto type Copper deposits in Chile. *Review. Bull. Geol. Surv. Jpn.* 35, 565–582.
- Sawlowicz, Z., 1990. Primary copper sulfides from the Kupferschiefer, Poland, *Mineral. Depos.* 25, 262–271.
- Seedorff, E., Dilles, J.H., Proffett, J.M. Jr., Einaudi, M.T., Zürcher, L., Stavast, W.J.A., Johnson, D.A., Barton, M.D., 2005. Porphyry deposits: Characteristics and origin of hypogene features; in: Hedenquist, J.W., Thompson, J.F.H., Goldfarb, R.J., Richards, J.P. (Eds.), *Economic Geology 100th Anniversary Volume*, 251–298.
- Seewald, J.S., 2003. Organic-inorganic interactions in petroleum producing sedimentary basins. *Nature* 426, 6964, 327–333.
- Sælen, G., Raiswell, R., Talbot, M.R., Skei, J.M., Bottrell, S.H., 1993. Heavy sedimentary sulfur isotopes as indicators of super-anoxic bottom-water conditions. *Geology* 21, 1091–1094.
- Seo, J.H., Guillong, M., Heinrich, C.A., 2009. The role of sulfur in the formation of magmatic-hydrothermal copper gold deposits. *Earth. Planet. Sci. Lett.* 282, 323–328.
- Sim, M.S., Bosak, T., Ono, S., 2011. Large sulfur isotope fractionation does not require disproportionation. *Science* 333, 74–77.
- Simon, A.C., Ripley, E.M., 2011. The role of magmatic sulfur in the formation of ore deposits. *Rev. Mineral. Geochem.* 73, 513–578.
- Seal, R.R., 2006. Sulfur Isotope Geochemistry of Sulfide Minerals Sulfur Isotope Geochemistry of Sulfide Minerals. *Rev. Mineral. Geochem.* 61, 633–677.
- Sivan, O., Schrag, D.P., Murray, R.W., 2007. Rates of methanogenesis and methanotrophy in deep-sea sediments. *Geobiology* 5, 141–151.
- Strauss, H., 1997. The isotopic composition of sedimentary sulfur through time. Elsevier, v. 132, p. 97–118.

- Tanner, D., Henley, R.W., Mavrogenes, J.A., Holden, P., 2016. Sulfur isotope and trace element systematics of zoned pyrite crystals from the El Indio Au–Cu–Ag deposit, Chile. *Contrib. Mineral. Petrol.* 171, 33.
- Tosdal, R.M., Munizaga, F., 2003. Lead sources in Mesozoic and Cenozoic Andean ore deposits, north-central Chile (30–34° S). *Miner. Depos.* 38, 2, 234–250.
- Tostevin, R., Turchyn, A.V., Farquhar, J., Johnston, D.T., Eldridge, D.L., Bishop, J.K.B., McIlvin, M., 2014. Multiple sulfur isotope constraints on the modern sulfur cycle. *Earth Planet. Sci. Lett.* 396, 14–21.
- Tristá-Aguilera, D., 2007. Génesis de los sulfuros de Cu primarios de los yacimientos estratoligados de Cu del Norte de Chile: el caso del Yacimiento Lince-Estefanía, Distrito Michilla. II Región de Antofagasta, Chile. Ph.D. Thesis Universidad Católica del Norte. Antofagasta, Chile (in Spanish).
- Ulriksen, C., 1979. Regional geology, geochronology, and metallogeny of the Coastal Cordillera between 23°30' and 26°S. Thesis, Dalhousie University, Halifax, Nova Scotia, p 180.
- Vivallo, W., Henríquez, F., 1998. Génesis común de los yacimientos estratoligados y vetiformes de cobre del Jurásico Medio a Superior en la Cordillera de la Costa, Región de Antofagasta. Chile. *Rev. Geol. Chile* 25, 199–228 (in Spanish).
- Westra, G., 1988. La importancia del metamorfismo de carga en la formación de yacimientos de cobre tipo manto: Keynote Address, Congreso Geológico Chileno, V, Santiago, Chile, August 8–12, 1988, Preprint 18 p. (in Spanish).
- Williams-Jones A.E., Heinrich, C.A., 2005. Vapor transport of metals and the formation of magmatic-hydrothermal ore deposits; in: Hedenquist, J.W., Thompson, J.F.H., Goldfarb, R.J., Richards, J.P. (Eds.). *Economic Geology 100th Anniversary Volume*, 1287–1312.
- Wilson, N.S.F., 1998. The role of petroleum in the formation of the Soldado copper deposit, Chile: Hydrothermal replacement of a biodegraded petroleum reservoir. Unpublished Ph.D. thesis, Halifax, Canada, Dalhousie University, 418 p.
- Wilson, S.A., Ridley, W.I., Koenig A.E., 2002. Development of sulfide calibration standards for the laser ablation inductively- coupled plasma mass spectrometry technique. *J. Anal. At. Spectrom.* 17, 406–409.
- Wilson, N., Zentilli, M., 1999. The Role of Organic Matter in the Genesis of the El Soldado Volcanic-Hosted Manto-Type Cu Deposit, Chile. *Econ. Geol.* 94, 1115–1136.
- Wilson, S.A., Ridley, W.I., Koenig A.E., 2002. Development of sulfide calibration standards for the laser ablation inductively- coupled plasma mass spectrometry technique. *J. Anal. At. Spectrom.* 17, 406–409.
- Wilson, N., Zentilli, M., Reynolds, P.H., Boric, R., 2003a. A age of mineralization by basinal fluids at the El Soldado manto-type copper deposit, Chile 40Ar/39Ar geochronology of K-feldspar. *Chem. Geol.* 197, 161–176.

Wilson, N., Zentilli, M., Spiro, B., 2003b. A sulfur, carbon, oxygen, and strontium isotope study of the volcanic-hosted El Soldado manto type copper deposit, Chile: The essential role of bacteria and petroleum. *Econ. Geol.* 98, 163–174.

Wilson, N., Zentilli, M., 2006. Association of pyrobitumen with copper mineralization from the Uchumi and Talcuna districts, central Chile. *Int. J. Coal Geol.* 65, 1, 158–169.

Wood, S.A., 1996. The role of humic substances in the transport and fixation of metals of economic interest (Au, Pt, Pd, U, V). *Ore Geol. Rev.* 11, 1–33.

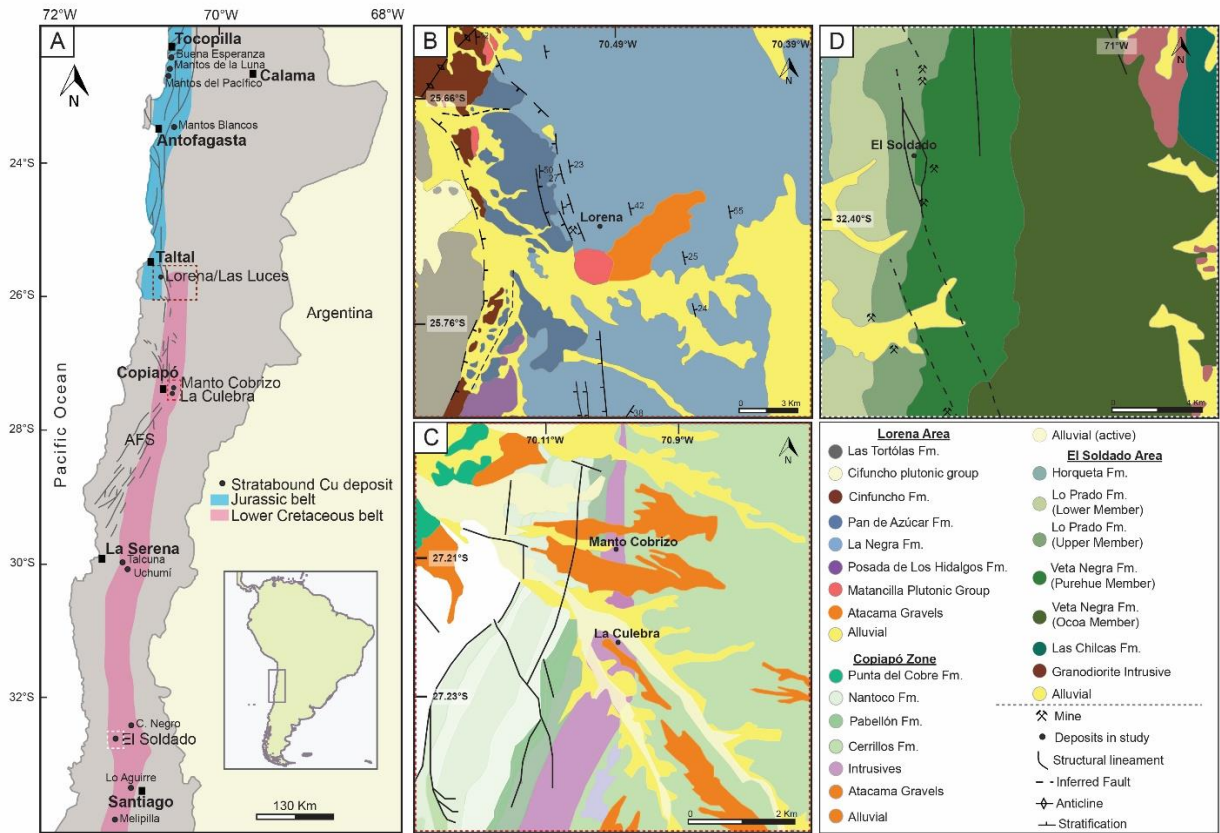
Worden, R.H. and Smalley, P.C., 1996. H₂S-producing reactions in deep carbonate gas reservoirs: Khuff formation, Abu Dhabi. *Chem. Geol.* 133, 1–4, 157–171.

Wortmann, U.G., Bernasconi, S.M., Böttcher, M.E., 2001. Hypersulfidic deep biosphere indicates extreme sulfur isotope fractionation during single-step microbial sulfate reduction. *Geology* 29, 647–650.

Zentilli, M., Boric, R., Munizaga, F. and Graves, M.C., 1994. Petroleum involvement in the genesis of some strata-bound copper deposits of Chile. *Proceedings, 7th Chilean Geological Congress, Concepcion, Chile, II*, 1542–1546.

Zentilli, M., Munizaga, F., Graves, M.C., Boric, R., Wilson, N.S.F., Mukhopadhyay, P.K., Snowdon, L.T., 1997. Hydrocarbon involvement in the genesis of ore deposits: an example in Cretaceous strata-bound (manto-type) copper deposits of central Chile. *Int. Geol. Rev.* 39, 1–21.

4.9. FIGURES



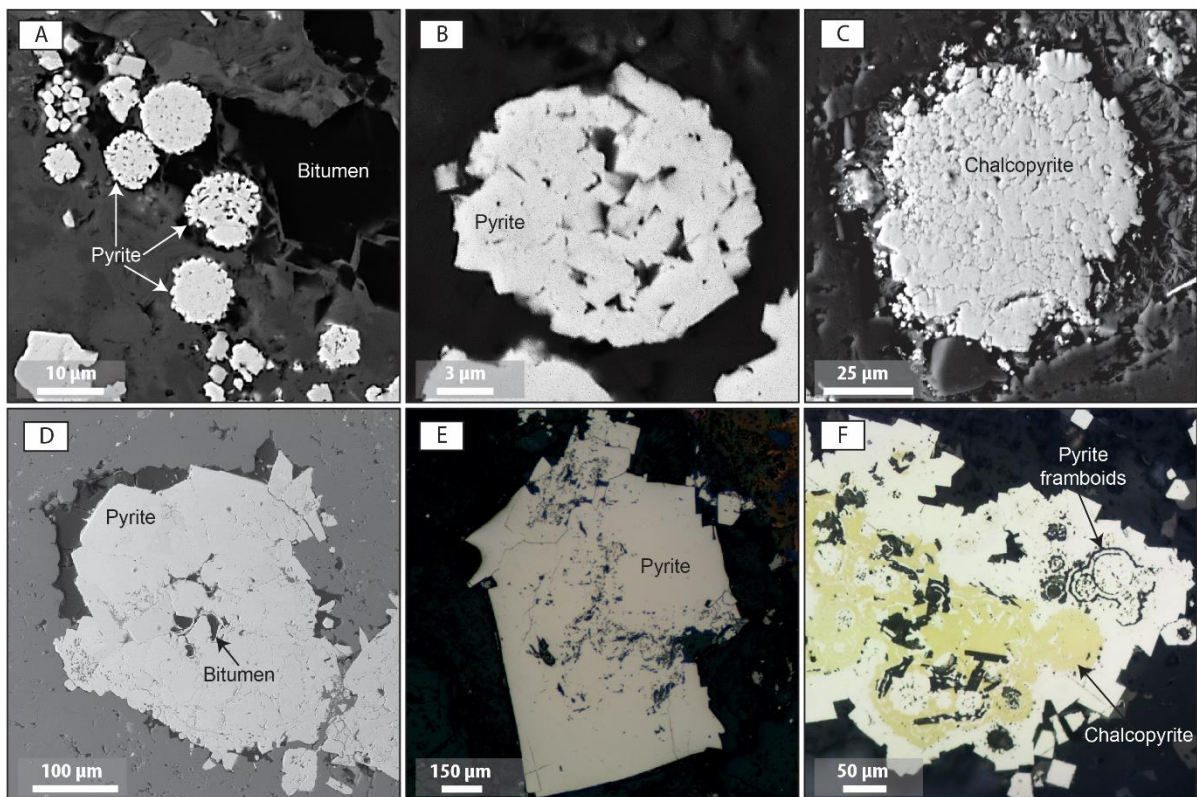


Figure 31. Backscattered electron (BSE) images and reflected polarized light microscopy photomicrographs of pre-ore and ore stage sulfides from the studied deposits. **(A)** Framboids and spherules associated with pyrobitumen. **(B)** Framboids composed of randomly distributed euhedral microcrystals. **(C)** Framboidal pyrite replaced by chalcopyrite, La Culebra deposit. **(D)** Aggregate of pyrite grains forming a rosette-like texture with pyrobitumen at the center, Lorena deposit. **(E)** Representative euhedral pyrite. **(F)** Euhedral pyrite grains with framboidal cores. Framboidal cores are partially replaced by chalcopyrite.

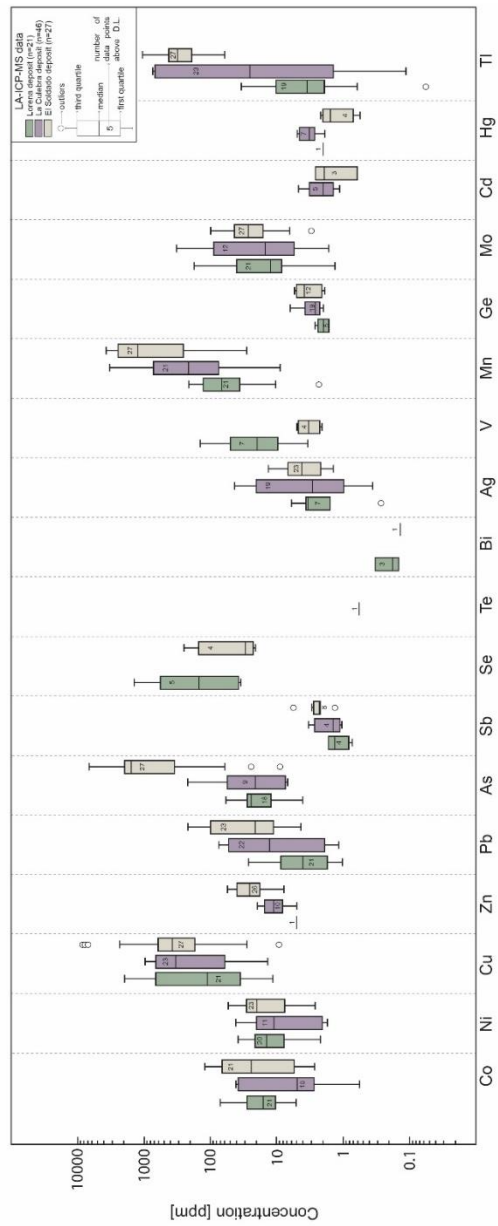


Figure 32. Concentration boxplot for selected minor and trace elements in pyrite from Lorena, La Culebra and the El Soldado stratabound Cu-(Ag) deposits. Data are plotted in parts per million (ppm) on a vertical logarithmic scale. In each boxplot, minimum, median, and maximum concentrations are indicated.

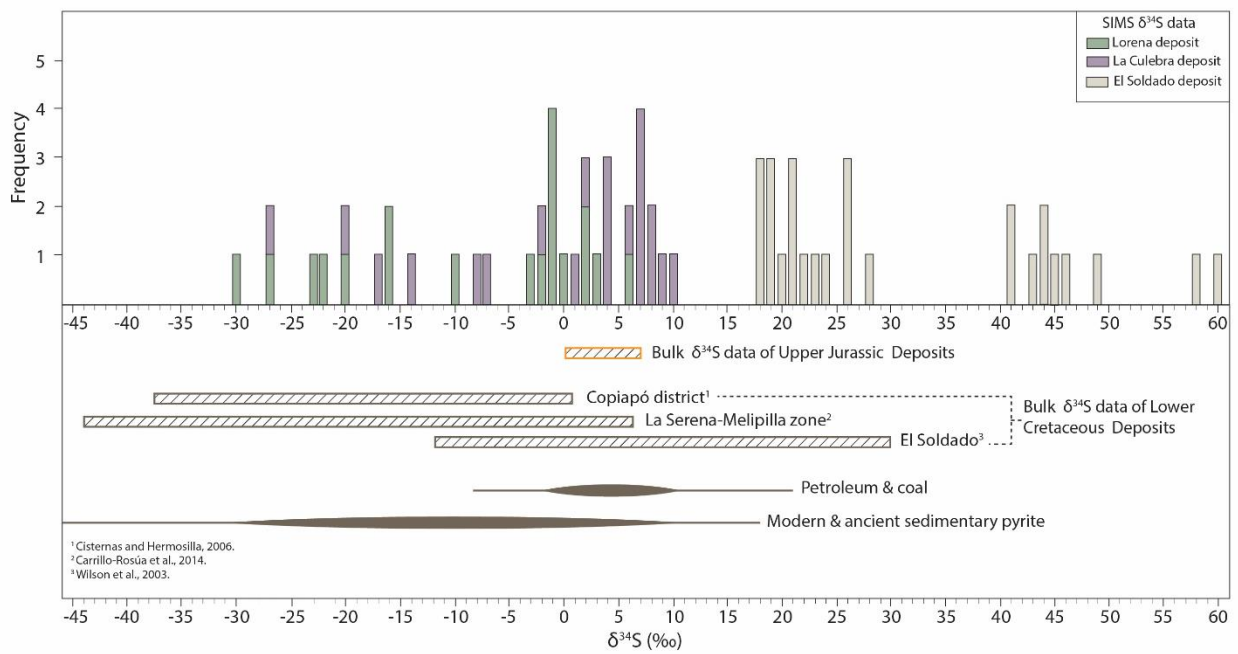


Figure 33. Histogram of in-situ $\delta^{34}\text{S}$ values obtained by secondary ion mass spectrometry (SIMS) of pyrite from the Lorena, La Culebra and El Soldado deposit. Range of previous published sulfur isotope signature are also show as horizontal bars.

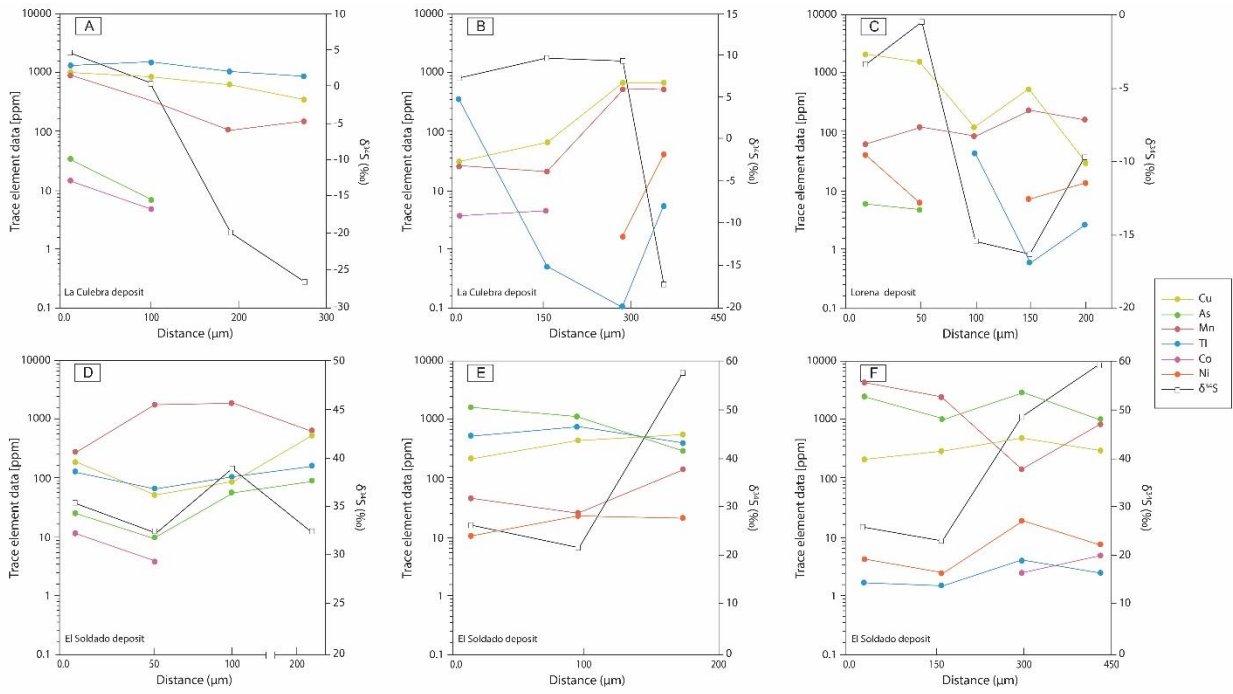


Figure 34. Representative trace element concentrations vs. $\delta^{34}\text{S}$ values for the studied deposits. The horizontal axis represents the distance (μm) from rim to core within pyrite grains where in-situ sulfur isotope analyses were performed. **(A)** and **(B)** Pyrite grains of MTCUL-2D sample from La Culebra deposit **(C)** Representative diagram from Lorena deposit **(D) – (F)** Pyrite grains from the El Soldado deposit (NW-167 sample).

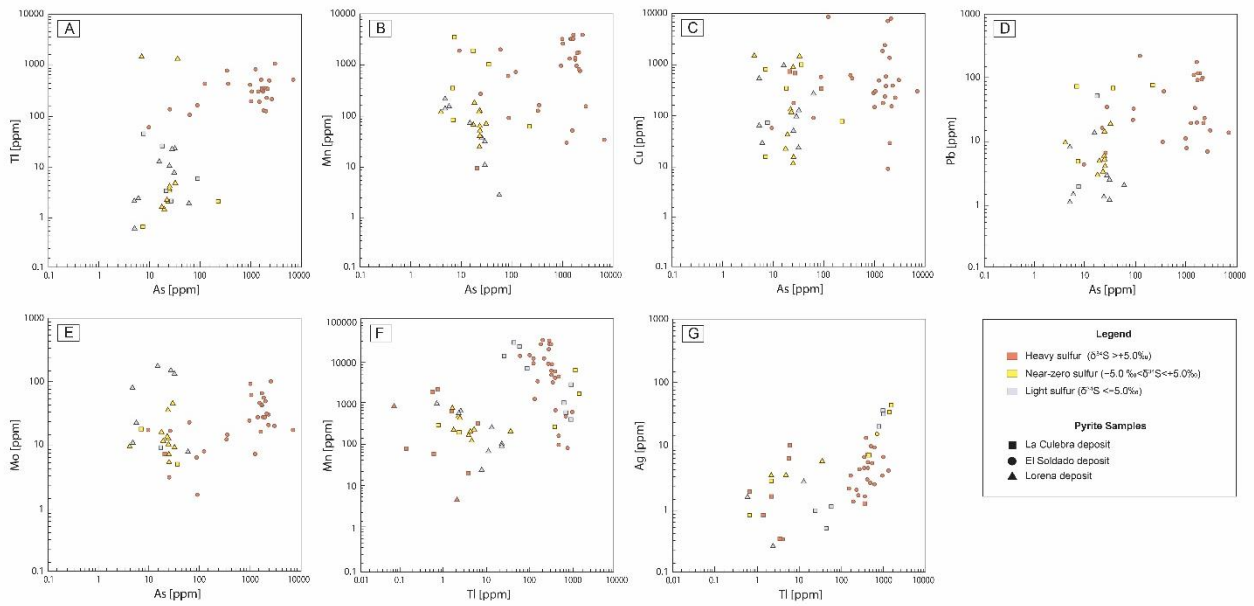


Figure 35. Elemental concentration scatterplots for pyrite from the stratabound Cu-(Ag). **(A)** Tl vs As. **(B)** Mn vs As. **(C)** Cu vs As. **(D)** Pb vs As. **(E)** Mo vs As. **(F)** Mn vs Tl. **(G)** Ag vs Tl. The $\delta^{34}\text{S}$ range is also shown. All concentrations are reported in parts per million (ppm).

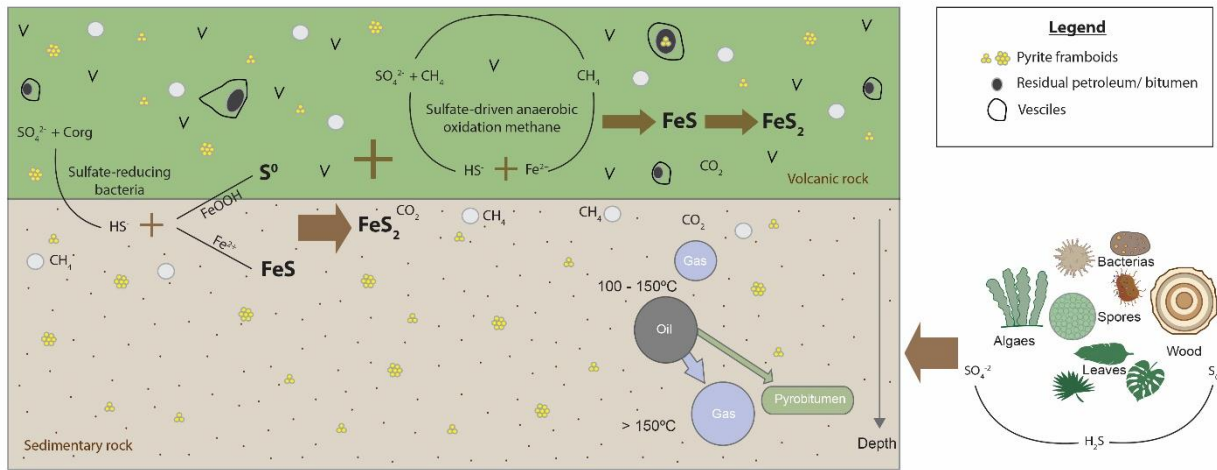


Figure 36. Summary figure showing key processes that led to sulfur fractionation in pyrite from bitumen-bearing stratabound Cu-(Ag) deposits.

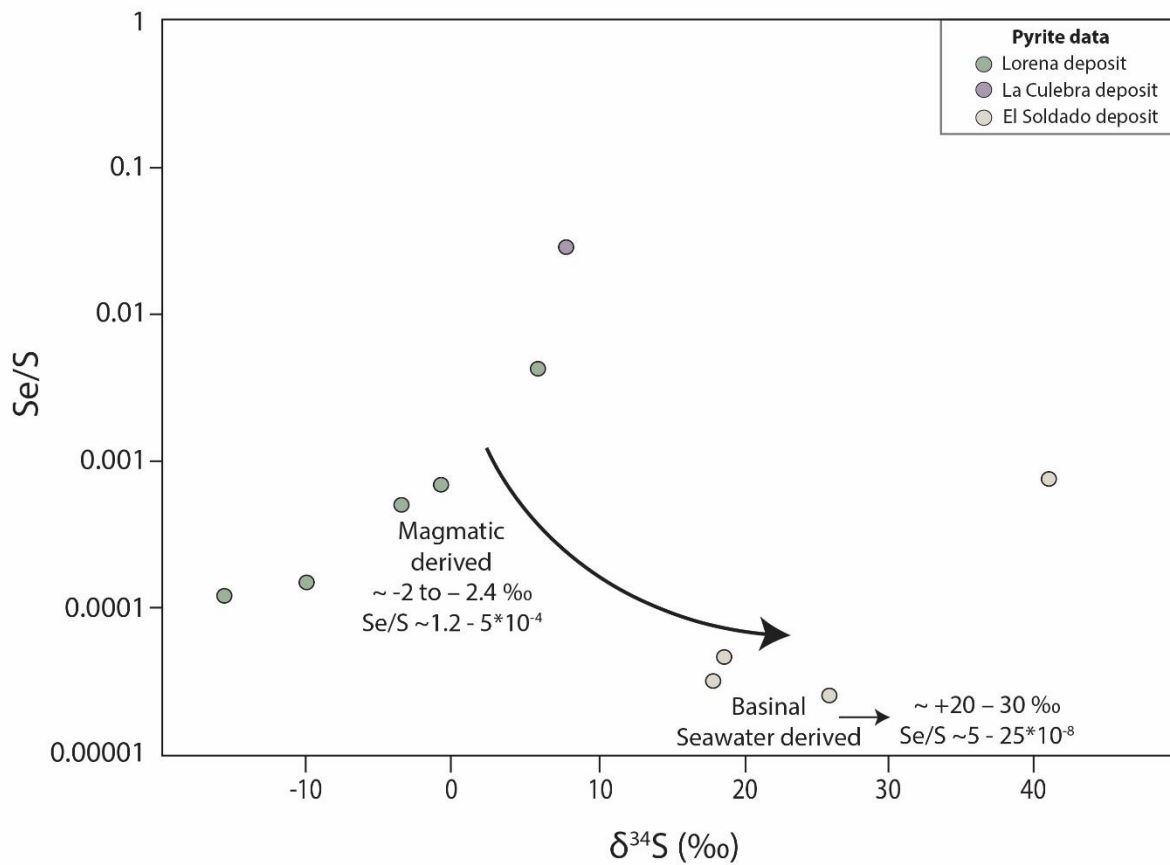


Figure 37. Se/S and $\delta^{34}S$ plot used to evaluate fluid source(s). Higher $\delta^{34}S$ and lower Se/S correlate with basinal derived fluids, whereas lower $\delta^{34}S$ and higher Se/S values correlate with magmatic-derived fluids. Source ranges from Fitzpatrick (2008).

4.10. TABLES

Table 1. Trace element LA-ICP-MS analyses and SIMS sulfur isotope values of pyrite from the Lorena, La Culebra and the El Soldado deposits, Chile. Concentrations are shown in parts per million (ppm) and sulfur isotope ratios are reported as $\delta^{34}\text{S}$ values (in per mil, ‰).

Deposit	$\delta^{34}\text{S}$ (‰)	σ abs (‰)	Sample	V	Mn	Co	Ni	Cu	Zn	Ge	As	Se	Mo	Ag	Cd	Sb	Te	Hg	Tl	Pb	Bi	
				1.1	1.2	0.27	0.98	1.2	2.9	1.2	2.1	14	0.4	0.12	0.39	0.15	0.54	0.3	0.02	0.06	0.05	
Lorena	-29.56	0.23	LO-24-C7-1		10.3	5.1		22.3			29.9		45.1						7.4	1.19		
Lorena	-26.8	0.23	LO-24-C7-2		30.4	11.6	3.3	120			30		132						22.4	2.45		
Lorena	-20.43	0.23	LO-24-C7-4	3.3	133	27.7	12.5	61			5		81						2.07	1.09		
Lorena	-9.89	0.24	LO-24-C3-6		145	21.9	14	28.3		2.06	5.7	40	22.4	0.26					2.33	1.45		
Lorena	-16.42	0.23	LO-24-C3-5	25.4	211	19.6	7.5	530			4.9		10.9	1.56					0.6	7.87	0.182	
Lorena	-15.56	0.24	LO-24-C3-4		76.7	38.5	37.7	117				35	1.31							4.48		
Lorena			LO-24-C4-4		2.56	15.8	9.4	257					7.8						1.89	1.99		
Lorena	-22.33	0.23	LO-24-C4-6		23.9	6.6	2.2	48		2.7	23.4		35.8						10.3	1.33		
Lorena	-23.31	0.23	LO-24-C4-3		34.1	14	9.4	92		1.61	27.2		148				2		21.7	2.89		
Lorena			LO-24-C4-1	19.8	69	56.7	26	930			15.3		173	2.68					12.5	13.6		
Lorena	3.37	0.24	LO-24-C6-3		63	5.2	8.2	21.8			17.2		15.8						1.58	2.82		
Lorena	2.86	0.24	LO-24-C6-4	49	116	32.8	23.4	820			23.4		12.6	3.52					2.09	14		
Lorena	-1.48	0.24	LO-24-C8-1	141	65.7	27.4	14.5	1400			31.5		9	3.55					4.78	18.5		
Lorena	-0.45	0.24	LO-24-C8-2-1		38.6	9.4	16.6	11.3			24.5	230	5.4			1.64			4.23	4		
Lorena	1.78	0.24	LO-24-C8-3		170	14.1	22.2	42			18.5		11.5						1.44	4.76		
Lorena	-0.28	0.24	LO-24-C2-2		50.6	11.61	18.3	15.2			23.8		7.1			1.66			3.52	5.1		
Lorena	-0.54	0.24	LO-24-C3-2	9.9	108.8	27.2	5.2	1520			4		9.6	3.61						9.2	0.143	
Lorena	-3.46	0.24	LO-24-C3-1	9.6	60	70.1	35.1	1920				150	34.5	5.96					34.8	26.3	0.324	
Lorena	-0.01	0.24	LO-24-C5-1		60.3	11.8	16.8	110		1.63	23.7		10.2			1.09			3.85	5.88		
Lorena	-0.35	0.24	LO-24-C5-2		109.5	7.5	7.8	125	5		22.3		13.4			0.73			2.17	3.29		
Lorena	5.84	0.24	LO-24-C1-2		183	20.5	18.4	83		2		1400	1.94						0.058	1.38		
La Culebra	-27.19	0.31	MTCUL-2D-P5-1		142.1			297			3.7		241	20.5			2.7		765	2.74		
La Culebra	-19.77	0.32	MTCUL-2D-P5-2		102.8			595	4.9	2.44			59.5	34.6	1.98		2.64		984	74		
La Culebra			MTCUL-2D-P3-1		1030	1.02		364											89	10		
La Culebra	-13.82	0.32	MTCUL-2D-P3-2	4.97	3320	4.1	1.85	67.9	19.7	2.01	7.5			0.5					43.3	1.83		
La Culebra	-7.79	0.32	MTCUL-2D-P3-3	2.69	1790	6.7	3.9	340	10.3	2.59	17.4		9.1	0.95		1.02			25.1	52		
La Culebra	-7.17	0.33	MTCUL-2D-P3-4	4.02	2770	0.56	2.02	51.5	15.5	1.97				1.1					57.5	3.12		
La Culebra	-17.35	0.32	MTCUL-2D-P8-7		496			579	12.8	2.4			14.1	31.4					1000	0.49		
La Culebra	0.55	0.32	MTCUL-2D-P5-3		328	4.9	8.4	798	8.1	2.23	6.8		17.5	43	1.12		4.89		1447	72.9		
La Culebra	4.45	0.32	MTCUL-2D-P5-4		946	14.6	19.9	953	14.8	2.5	35		5	33.4		1.41		3.6	1274	67		

La Culebra	4.14	0.32	MTCUL-2D-P4-3	57	40.2	10.7	74.1		220		2.84	3.27	2.1	74.6		
La Culebra	3.83	0.32	MTCUL-2D-P4-1	78.5	2.7		15		7		0.79		0.66	4.7		
La Culebra	-2.1	0.32	MTCUL-2D-P1-2	71.9			148	2.76		99.9	7.25	2.2	1.85	404	2.87	
La Culebra	1.74	0.32	MTCUL-2D-P1-3	214			404	2.67		317	15.3	4.7	3.3	674	28.2	
La Culebra	6.6	0.32	MTCUL-2D-C7-P1-P2		37.7	25.2	754	6.2			4.8	10.1		6.15	52.1	
La Culebra	8.42	0.32	MTCUL-2D-C7-P3	8.8	30	12.9	724	4.1	20.8		7.1	0.35		3.36	16	
La Culebra	8.17	0.32	MTCUL-2D-C7-P4		37.5	15.3	655	4	26		16.3	1.59	0.57	2.11	34.2	
La Culebra	7.35	0.32	MTCUL-2D-P2-3	146			60.4	2.9			0.78			1.38	1.89	
La Culebra	7.81	0.32	MTCUL-2D-P2-4	390	0.73		36.1	11.4		9.40E+03	1.92			0.64	0.78	
La Culebra	7.8	0.32	MTCUL-2D-P2-5	349			13.6	10.6	4.6					0.48		
La Culebra	9.04	0.32	MTCUL-2D-P8-5	549			653	2.3			1.22		4.5	364	40.1	
La Culebra	9.65	0.33	MTCUL-2D-P8-4	20.9	4.5		64.6	3.7				1.7		0.51	1.37	
La Culebra	7.23	0.32	MTCUL-2D-P8-3	27.2	3.68	1.7	29.5	1.98						0.112	0.45	
La Culebra			MTCUL-2D-P8-1	2.1	84.9	40.4	41	329	8.2	1.96	87	1.65	6.35	1.39	5.84	32.1
El Soldado	41.02	0.17	NW-167-C9-P1-P2	31.8	21.6	15.5	290	5.1	6670	250	17.2			498	13.6	
El Soldado	28.12	0.15	NW-167-C9-P3	117.1	16.1	28.3	605	21.8	5	329	12	3.48	1.35	759	9.6	
El Soldado	26.06	0.15	NW-167-C2-P1	3680	2.3	3.9	217	43.8	4.9	2500	98.1	1.68	2.11	209	6.8	
El Soldado	23.25	0.15	NW-167-C2-P2	2440		2.6	291	54.5	5.2	1019	60.7	1.62		294		
El Soldado	48.57	0.15	NW-167-C2-P3	142.9	2.9	17.9	484	7.8	4	2890	19.5	4.1		1057	14.6	
El Soldado	59.44	0.15	NW-167-C2-P4	900	5.3	7.5	273	38.4	4.4	930	24	2.62		402	11	
El Soldado	25.73	0.15	NW-167-C1-1	47.8	11.7	12.2	230	20.8	2.5	1560	16.1	2.51		501	19.5	
El Soldado	22.08	0.15	NW-167-C1-3	27.6		23	468	11.2	2.04	1200	7	6.68		807	19.1	
El Soldado	58.45	0.15	NW-167-C1-4	153	42	22.1	533	12	2.53	345	14.5	5.37	1.36	0.55	420	60
El Soldado	18.03	0.15	NW-167-C3-1	710	5.6	22.8	375	19.9		2220	26	20.1	9.5	487	22.8	
El Soldado	17.85	0.15	NW-167-C32-1	911	37.8	20.2	1320	17.1		1910	27.7	4.54	2.2	341	93	
El Soldado	19.82	0.15	NW-167-C3-3	776		13.9	149	17.1		2110	29.9	2.97		337	19	
El Soldado	18.49	0.15	NW-167-C4-2	1285			8.7	17.9		1790	34	54.9	2.6	124.7		
El Soldado	21.3	0.15	NW-167-C4-3	1590			28	23		1910	48.4	2.16	0.6	123		
El Soldado	45.19	0.15	NW-167-C5-1	253	11.2	3.4	169	15.5	3.6	24.7	3.1	3.43	1.9	132.9	6.54	
El Soldado	44.14	0.15	NW-167-C5-2	1780	3.7		55	51		9.2	16.8			59	4.28	

El Soldado	46.32	0.15	NW-167-C5-3	1860			88.6	44	60		22.6			103.1		
El Soldado	43.87	0.2	NW-167-C5-5	568	24.4	7.2	550	24	1.89	85	6.4	1.36		156.9	21.4	
El Soldado	41.28	0.15	NW-167-C6-2	670	74.8	36.1	8.40E+03	26		119	8	9.9	2.3	422	217	
El Soldado	43.32	0.16	NW-167-C6-3	3040	2.59	4.6	141	52.7	2.5	980	90.9	2.06		191	7.7	
El Soldado	20.58	0.15	NW-167-C7-1	3630	59.7	31.5	370	34.1		1654	63.8	6.69		299	90	
El Soldado	20.58	0.15	NW-167-C7-2	3102	120.6	45.4	571	30.3		1634	41.9	7.37	2.23	341	115	0.134
El Soldado	24.5	0.15	NW-167-C7-3	3040	121	54.3	2330	40		1560	43.8	13.4	2.2	318	173	
El Soldado	25.81	0.15	NW-167-C7-4	3019	60.9	12	170	32.1		1449	21	44.5	2.05	188	33	
El Soldado	17.58	0.15	NW-167-C8-1	1629	35.6	20.3	7.80E+03	20.8		2020	30.9	4.31	5.9	1.8	222.6	99
El Soldado	17.58	0.15	NW-167-C8-2	1252	72	21.6	1780	26		1381	26.8	4.51	2.36	294	108	
El Soldado	18.52	0.15	NW-167-C8-3	1231	89	34.5	7000	27		1770	26.8	5.55	2.9	345	115.1	

Notes: bdl = below detection limits; detection limits (ppm) are shown below each element.

Table 2. Statistical summary of LA-ICP-MS data for pyrite from Lorena, La Culebra and the El Soldado deposits, Chile. Trace elements with significant concentrations (in ppm) are shown.

Deposit	Statistical Parameters	Co	Ni	Cu	Zn	Pb	As	Sb	Se	Ag	Mn	Mo	Tl
Lorena	Minimum	5.10	2.20	11.30	5.00	1.09	4.00	0.73	35.00	0.26	2.56	1.31	0.06
	Maximum	70.10	37.70	1920.00	5.00	26.30	58.00	1.66	1400.00	5.96	211.00	173.00	34.80
	Median	15.80	14.25	110.00	5.00	4.00	23.40	1.37	150.00	3.52	65.70	12.60	3.52
	Average	21.67	15.43	394.00	5.00	6.36	21.57	1.28	371.00	3.02	83.88	37.54	7.35
	Count	21.00	20.00	21.00	1.00	21.00	18.00	4.00	5.00	7.00	21.00	21.00	19.00
La Culebra	Minimum	0.56	1.70	13.60	4.90	0.45	6.80	1.02	9400.00	0.35	8.80	1.65	0.11
	Maximum	40.40	41.00	953.00	19.70	74.60	220.00	3.27	9400.00	43.00	3320.00	317.00	1447.00
	Median	4.90	10.70	329.00	11.00	13.00	20.80	1.40	9400.00	2.84	214.00	15.20	25.10
	Average	15.29	12.99	348.07	11.63	26.07	47.50	1.77	9400.00	11.26	615.34	66.08	310.88
	Count	15.00	11.00	23.00	10.00	22.00	9.00	4.00	1.00	19.00	21.00	12.00	23.00
El Soldado	Minimum	2.30	2.60	8.70	7.80	4.28	9.20	1.36	21.00	1.36	27.60	3.10	59.00
	Maximum	121.00	54.30	8400.00	54.50	217.00	6670.00	5.90	250.00	13.40	3680.00	98.10	1057.00
	Median	24.40	20.20	370.00	25.00	21.40	1560.00	2.27	30.00	4.10	1231.00	26.80	318.00
	Average	39.09	20.03	1285.05	28.03	55.61	1486.26	2.68	82.75	4.69	1403.19	32.46	349.34
	Count	21.00	23.00	27.00	26.00	23.00	27.00	8.00	4.00	23.00	27.00	27.00	27.00

CHAPTER 5

CONCLUSIONS

This research is largely motivated by fundamental questions related to ore genesis specifically related to Cu deposits where sulfides are paragenetically related to migrated hydrocarbons. Stratabound or “Manto-type” Cu-(Ag) deposits in Chile provide an ideal setting to study the role of organic matter in metallogenesis. These Upper Jurassic to Lower Cretaceous deposits occur within the Coastal Range of northern and central Chile, and are characterized by the presence of residual petroleum, in the form of bitumen and pyrobitumen, in association with Cu mineralization. The research focused on three districts (Las Luces, Copiapó and El Soldado), and comprised a detailed surface and drill core sample characterization, which included a combination of microanalytical tools including (FE)SEM, EMPA, LA-ICP-MS, μ -XRF, SIMS and synchrotron μ -XRF and XANES analyses.

The data presented in the preceding chapters lead to the following conclusions concerning the timing, genesis, and the role of organic matter in the formation of stratabound Cu-(Ag) deposits in northern and central Chile:

1. Petrographic observations revealed a spatial and temporal relationship between Cu-(Fe) sulfides and pyrobitumen in all studied deposits, i.e., Lorena in the Las Luces district near Taltal, La Culebra and Manto Cobrizo near Copiapó, and the El Soldado deposit near Santiago. Paragenetic studies also suggest that these deposits were formed in two stages, a pre-ore stage and main Cu ore stage. The early pre-ore stage is characterized by the presence of pyrite with minor hematite, in association with pyrobitumen, and widespread, selective albite alteration of andesitic host rocks. The main Cu ore stage is characterized by a chalcopyrite-bornite-chalcocite assemblage with pyrobitumen. Observations at the Lorena deposit indicate the presence of pyrobitumen in both stages, evidencing that multiple pulses of aqueous and hydrocarbon fluids were involved in the formation of this deposit.
2. In the studied deposits, the early stages involved petroleum generation in the sedimentary source rocks, which was mobilized as immiscible droplets by connate waters to the deposition site, usually volcanic units of andesitic composition, with primary and secondary porosity. At Lorena, a first pulse of hydrocarbon injection is evidenced by globular pyrobitumen and pyrite in the volcanic host rocks. Here, vesicles are filled with pyrobitumen, which is partially replaced by Cu-(Fe) sulfides indicating that Cu-bearing hydrothermal fluids interacted with the organic matter and where complexed metals were reduced to precipitate sulfides. In addition, a second pulse of hydrocarbon introduction (or mobilization) is represented by angular pyrobitumen that is intergrown with Cu sulfides and calcite, suggesting that during the main Cu ore stage, hydrocarbons were introduced either as a new, fresh pulse or remobilized from early (globular) pyrobitumen.
3. FE-SEM observations of micro- to nano-scale inclusions of bitumen in pyrite and chalcocite in the Lorena deposit point to a coexistence of aqueous solutions and oil (petroleum) during both the pre-ore and the main Cu ore stage. The formation and stabilization of the water-oil emulsions could have occurred by convection and fluid mixing in the volcano-sedimentary

sequence. Temperature changes were most likely induced by regional low-grade metamorphism, the intrusion of dikes and/or thermal effects related to deep-seated intrusions.

4. Electron microprobe analysis of bitumen in the Lorena deposit reveals significant concentrations of base metals, e.g., high Cu and Fe concentrations (average of 0.16 and 0.1 wt.%, respectively). High concentrations of ligands such as Cl and S are also present in bitumen reaching average values of 0.09 and 0.34 wt.%, respectively.
5. Synchrotron XANES data of sulfur speciation in pyrobitumen suggest that thiophene and elemental compounds are the dominant sulfur species in Lorena, and results are indicative of the presence of organosulfur compounds that can be attributed to an organic. Further, lower sulfur concentrations were observed in bitumen grain rims from Lorena by synchrotron μ -XRF, indicating that these grains were likely in contact with high temperature hydrothermal fluids. This interaction could have caused chemical bond breakage and trigger the loss of external heteroatoms including thiols compounds from pyrobitumen and hence, sulfur from heteroatoms could have been incorporated into the hydrothermal fluid. Some of the S contained in pyrobitumen could have been released during interaction with Cu-bearing hydrothermal fluids contributing, at least partially, to the S budget required for sulfide mineralization from the main ore stage.
6. Trace element geochemistry of pyrite in the studied bitumen-bearing stratabound Cu-(Ag) deposits support their use to fingerprint formation conditions. EMPA and LA-ICP-MS data in pyrite from the Lorena, La Culebra and Manto Cobrizo deposits reveal a geochemical signature characterized by significant concentrations (up to 1000's of ppm) of trace elements, most notably Cu, As, Mn, Pb, Tl, Co, Ni, V, and Mo. These elements occur dominantly in solid solution and/or as submicron-sized inclusions within pyrite. The high concentration of Mn, Mo, V, and Tl in pyrite points to a sedimentary/basinal source or derivation from pyrobitumen, which is usually observed in close association with pyrite in these deposits.
7. Pyrite from stratabound Cu-(Ag) deposits has high Ag/Co and low Co/Cu ratios, and low Co-Ni concentrations in comparison with Andean IOA and IOCG pyrite. These differences are probably related to contrasting physico-chemical conditions of the pyrite-forming fluid, i.e., temperature, redox conditions and source of metals/sulfur. Furthermore, these ratios are characteristic for these deposits and could act as a complementary tool for exploration of stratabound Cu-(Ag), IOCG and IOA deposits within the Coastal Cordillera of central-northern Chile, and possibly elsewhere.
8. In-situ sulfur isotope data of pyrite, obtained by SIMS, provide further insight on the source of sulfur in the studied bitumen-bearing stratabound Cu-(Ag) deposits. The data indicate that the source of sulfur and by interference metals contained in these deposits have a mixed origin, involving a significant (but highly variable) sedimentary component. Furthermore, the high concentrations of Mn (up to 0.14 wt.%), As (up to 0.36 wt.%), and Tl (up to 0.14 wt. %) support a sedimentary/basinal source, which is more prominent at El Soldado deposit, where sulfur from various sources, i.e., basinal brines, seawater, and magmatic-hydrothermal could have been involved.

9. $\delta^{34}\text{S}$ pyrite span over a wide range of values, i.e., between -30 to $+60$ ‰, which involves two main mechanisms during Fe sulfide crystallization: 1) incomplete sulfate reduction in a partially closed system of connate seawater sulfate and 2) sulfate-anaerobic oxidation methane interaction.
10. Geochemical data coupled with in-situ sulfur data of pyrite reveal that high concentrations of Cu, As, Mn and Tl are correlated with the heaviest $\delta^{34}\text{S}_{\text{pyrite}}$ values and their incorporation is probably controlled by different processes including the substitution of Fe^{2+} and S^{2-} in the pyrite structure, metal availability, solubility in the hydrothermal-hydrocarbons and the geological environment of formation.
11. In general, our results support the interaction between pyrobitumen and metal-rich hydrothermal fluids as a key process in the formation of bitumen-bearing stratabound Cu-(Ag) deposits in Chile. Sulfides and bitumen are intimately related in both the pre-ore and ore stage indicating that multiple pulses of both aqueous and hydrocarbon fluids were involved in the ore-forming processes. Further, bitumen is a potential source of metals (e.g., Cu, Tl, Mn, V) and ligands (S), with sulfur and eventually metals possibly derived from a sedimentary source. These data support the notion that pyrobitumen in stratabound Cu-(Ag) deposits played a key role during ore formation as a redox trap for Cu sulfide precipitation, and at least partially, as a source of sulfur and metals.

Final Remarks

The study of the bitumen-bearing stratabound Cu-(Ag) deposits located along the Coastal Cordillera of central-northern Chile (i.e., Lorena, Manto Cobrizo, La Culebra and El Soldado) confirms the key role of organic matter during ore genesis. It is important to emphasize that the genetic model proposed for the Lorena deposit in Chapter 3 would be applicable to the other stratabound deposits associated with bitumen within the belt. A first step involves oil generation within a sedimentary source rock, followed by migration into an andesite host rock. Subsequently, oil was biodegraded forming pyrite during the pre-ore stage, and before the inception of Cu mineralization during the ore-forming stage. Therefore, and according to the evidence presented here, bitumen may have acted not only as a redox trap for Cu mineralization, but eventually as a source of sulfur. For example, some of the S contained in the bitumen could have been used for the formation of pyrite from biodegradation of oil during the pre-ore stage, or released into Cu-bearing hydrothermal fluids as a result of fluid-bitumen interaction during the main Cu stage. In the latter, sulfur could contribute, at least partially, to the S budget required for sulfide mineralization in these deposits. The above could indicate, perhaps, and among other factors, that the amount of bitumen could influence the overall size of stratabound Cu deposits. For example, at El Soldado, the largest and most representative deposit of the belt, studies inferred the presence of a biodegraded petroleum reservoir underlying the deposit during its formation. Therefore, it is likely that a concentration of large amounts of S-rich bitumen may have enhanced processes leading to Cu mineralization, and consequently increasing the Cu resources of the deposit. These factors should be taken into consideration in future studies, and evaluated in detail to better assess the role of organic matter in stratabound Cu-(Ag) deposit in Chile, and possibly elsewhere.

BIBLIOGRAPHY

Ali, M.F., Bukhari, A., Saleem, M., 1983. Trace metals in crude oils from Saudi Arabia. *Ind. Eng. Chem. Prod. Res. Dev.* 22, 691–694.

Anderson, G.M. and Macqueen, R.W., 1982, Ore deposit models-6, Mississippi-Valley type lead-zinc deposits, *Geoscience Canada*, 9, 108–117.

Anderson, G.M., 1991. Organic maturation and ore precipitation in Southeast Missouri. *Econ. Geol.* 86, 909–926.

Barra, F., Reich, M., Selby, D., Rojas, P., Simon, A., Salazar, E.,; Palma, G., 2017. Unraveling the origin of the Andean IOCG clan: A Re-Os isotope approach. *Ore Geol. Rev.* 81, 62–78.

Boric, R., Holmgren, C., Wilson, N.S.F., Zentilli, M., 2002. The Geology of the El Soldado Manto Type Cu (Ag) Deposit, Central Chile; in Porter, T.M. (Ed.), *Hydrothermal Iron Oxide Copper-Gold & Related Deposits: A Global Perspective, Volume 2*; PGC Publishing, Adelaide, 163–184.

Brown, M., Díaz, F., Grocott, F., 1993. Displacement history of the Atacama Fault System 25°00'–27°00'S, northern Chile. *GSA Bull.* 105, 1165–1174.

Camus, F., 1990. Geological characteristics of Strata-bound Deposits Associated with Lacustrine Sediments, Central Chile; in: Fontboté, et al. (Eds.) *Stratabound Ore Deposits in the Andes*. Berlin, Springer-Verlag, p. 449–462.

Carrillo-Rosúa, J., Boyce A., Morales-Ruano, S., Morata, D., Roberts, S., Munizaga, F., Moreno-Rodríguez, V., 2014. Extremely negative and inhomogeneous sulfur isotope signatures in Cretaceous Chilean manto-type Cu-(Ag) deposits, Coastal Range of central Chile. *Ore Geol. Rev.* 56, 3–24.

Charrier, R., Pinto, L., Rodríguez, M.P., 2007. Tectonostratigraphic evolution of the Andean Orogen in Chile in Moreno, T., Gibbons, W. (Eds.), *The Geology of Chile*. The Geological Society, London.

Cisternas, E., Hermosilla, J., 2006. The role of bitumen in strata-bound copper deposit formation in the Copiapó area, Northern Chile. *Miner. Depos.* 41, 339–355.

Colombo, U., Sironi, G., 1961. Geochemical analysis of Italian oils and asphalts, *Geochim. Cosmochim. Acta* 25, 24–51.

Colombo, U., Sironi, G., Fasolo, G.B., Malvano, R., 1964. Systematic neutron activation technique for the determination of trace metals in petroleum. *Anal. Chem.* 36, 802–807.

Cucurella, J., Canut de Bon, C., Cisternas, M.E., 2005. Pyrobitumen related to silver-copper deposits in a Cretaceous volcanic-sedimentary sequence: Talcuna district, Coquimbo, Chile. *Mineral. Polonica* 36, 1, 21–29.

- Cuney, M., 2009. The extreme diversity of uranium deposits. *Miner. Depos.* 44, 3–9.
- Definis, A. 1985. Antecedentes geológicos del yacimiento de cobre Santo Domingo, Taltal y discusión acerca de su relación con un sistema de filones gabrodioríticos. Congreso Geológico Chileno, IV, Antofagasta, Chile, Vol. 2, 3–204, 3–215 (in Spanish).
- Dallmeyer, R.D., Brown, M., Grocott, J., Taylor, G.K., Treolar, P.J., 1996. Mesozoic Magmatic and Tectonic Events within the Andean Plate Boundary, Zone 26°-27°30'S, North Chile: Constraints from $^{40}\text{Ar}/^{39}\text{Ar}$ Mineral Ages. *The Journal of Geology*, University of Chicago, v. 104, 19–40.
- Durieux, C.G., and Brown, A.C., 2007. Geological context, mineralization, and timing of the Juramento sediment-hosted stratiform copper-silver deposit, Salta district, northwestern Argentina. *Miner. Depos.* 42, 879–899.
- Ellrich, J., Hirner, A., Stark, H., 1985. Distribution of trace elements in crude oils from southern Germany. *Chem. Geol.* 48, 313–323.
- Espinoza, S., Véliz, H., Esquivel, J., Arias, J., y Moraga, A., 1996. The Cupriferous Province of the Coastal Range, Northern Chile; in: Camus, F., Sillitoe, R.H., and Petersen, R. (Eds.), *Andean Copper Deposits: New Discoveries, Mineralization, Styles and Metallogeny*. Society of Economic Geologists, Special Publication Number 5, 19–32.
- Fuchs, S., Schumann, D., Williams-Jones, A.E., Vali, H., 2015. The growth and concentration of uranium and titanium minerals in hydrocarbons of the Carbon Leader Reef, Witwatersrand Supergroup, South Africa. *Chem. Geo.* 393–394, 55–66.
- Fuchs, S., Williams-Jones, A.E., Przybylowicz, W.J., 2016. The origin of the gold and uranium ores of the Black Reef Formation, Transvaal Supergroup, South Africa. *Ore Geol. Rev.* 72, 149–164.
- Gaupp, R., Moller, P., Lüders, V., di Primio, R., Littke, R., 2008. Fluids in sedimentary basin: an overview. *Dynamics of Complex Sedimentary Basins - The Example of the Central European Basin System.* 347–365.
- Goldstein, T. and Aizenshtat, Z., 1994. Thermochemical sulfate reduction – a review. *J. Therm. Anal.* 42, 1, 241–290.
- Haggan, T., Parnell, J., Cisterna, M.E., 2003. Fluid history of andesite-hosted CuS-bitumen mineralization, Copiapó district, north central Chile. *J. Geochem. Explor.* 78–79, 631–633.
- Hitchon, B., Filby, R.H., Shah, K.R., 1975. Geochemistry of trace elements in crude oils, Alberta, Canada; in Yen, T.F (Ed.), *The Role of Trace Metals in Petroleum*, Ann Arbor Science Publisher 111–112.
- Hunt, J. M., 1996, *Petroleum Geochemistry and Geology*, Second edition, W.H. Freeman and Company, New York, 743 p.

Jara, J.J., Barra, F., Reich, M., Morata, D., Leisen, M., Romero, R.. 2021. Geochronology and petrogenesis of intrusive rocks in the Coastal Cordillera of northern Chile: Insights from zircon U-Pb dating and trace element geochemistry. *Gondwana Res.* 93, 48–72.

Jones, P., 1975. Trace Elements and Other Elements in Crude Oil- A Literature Review. Report of British Petroleum Research Centre, Sunbury.

Kojima, S., Astudillo, J., Rojo, J.; Tristá, D., Hayashi, K., 2003. Ore mineralogy, fluid inclusion, and stable isotopic characteristics of stratiform copper deposits in the coastal Cordillera of northern Chile. *Miner. Depos.* 38, 208–216.

Kojima, S., Tristá-Aguilera, D., Hayashi, K., 2009. Genetic aspects of the manto-type copper deposits based on geochemical studies of North Chilean deposits. *Resour. Geol.* 59, 1, 87–98.

Khuhawar, M.Y., Mirza, M.A., Jahangir, T.M., 2012. Determination of Metal Ions in Crude Oils; in: Abdul-Raouf, M.E.-S. (Ed.), *Crude Oil Emulsions - Composition Stability and Characterization*. InTech, Croatia, 1-25, doi: 10.5772/36945.

Large, R.R., Bull, S.W., Maslennikov, V.V., 2011. A carbonaceous sedimentary source-rock model for carlin-type and orogenic gold deposits. *Econ. Geol.* 106, 331–358.

Leventhal and Giordano, 1998, Introduction to the roles of Organic Matter in Ore genesis and Exploration: in Kettler, R. M., Giordano, T. H. and Wood, S. Z. (eds.) *Ore genesis and Exploration: The roles of Organic Matter*, SEG Short Course.

Lewan, M., 1984. Factors controlling the proportionality of vanadium to nickel in crude oils. *Geochim. Cosmochim. Acta* 48, 2231–2238.

Lo Mónaco, S., López, L., Rojas, H., Lugo, P., García, D., Gastiel, J., 2007. Applications of electron microprobe analysis (EPMA) in the study of Venezuelan source rocks: La Luna and Querecual Formations. *Fuel* 86, 641–648.

Machel, H.G., 2001. Bacterial and thermochemical sulfate reduction in diagenetic settings – old and new insights. *Sed. Geol.* 140, 1–2, 143–175.

Maksaev, V., Zentilli, M., 2002. Chilean strata-bound Cu–(Ag) deposits: an overview; in: Porter, T.M. (Ed.), *Hydrothermal Iron Oxide Copper–Gold & Related Deposits. A Global Perspective*. PGC Publishing, Adelaide, 185–205.

Maksaev, V., Townley, B., Palacios, C., Camus, F., 2007. Metallic ore deposits; in Moreno, T., Gibbons, W. (Eds.), *The Geology of Chile*. The Geological Society, London: 179–199. London.

Marinovic, N., Smoje, I., Maksaev, V., Hervé, M., Mpodozis, C., 1995. Hoja Aguas Blancas, Región de Antofagasta. Servicio Nacional de Geología y Minería, Carta Geológica de Chile N° 70, 150 p (in Spanish).

Mastalerz, M., Glikson, M., 2000. In-situ analysis of solid bitumen in coal: Examples from the Bowen Basin and the Illinois Basin. *Int. J. Coal Geol.* 42, 207–220.

Mayer, C.K., Fontboté, L., 1990. The stratiform Ag-Cu deposit El Jardín, Northern Chile; in: Fontboté, L., Amstutz, G.C., Cardozo, M., Cedillo, E. & Frutos, J. (Eds.), *Stratabound ore deposits in the Andes*. Berlin, Springer, 637–646.

Migdisov, A.A., Guo, X., Williams-Jones, A.E., Sun, C.J., Vasyukova, O., Sugiyama, I., Fuchs, S., Pearce, K., Roback, R., 2017. Hydrocarbons as ore fluids. *Geochem. Perspect. Lett.* 5, 47–52.

Mossman, D., Nagy, B., Davis, D., 1993. Hydrothermal alteration of organic matter in uranium ores, Elliot Lake, Canada: Implications for selected organic-rich deposits. *Geochim. Cosmochim. Acta* 57, 3251–3259.

Oliveros, V., Féraud, G., Aguirre, L., Ramírez, L., Fornari, M., Palacios, C., Parada, M., 2008. Detailed $^{40}\text{Ar}/^{39}\text{Ar}$ dating of geologic events associated with the Mantos Blancos copper deposit, northern Chile. *Miner. Depos.* 43, 3, 281–293.

Pfaff, K., Hildebrandt, L.H., Leach, D.L., Jacob, D.E., Markl, G., 2010. Formation of the Wiesloch Mississippi Valley-type Zn-Pb-Ag deposit in the extensional setting of the Upper Rhinegraben, SW Germany. *Miner. Depos.* 45, 7, 647–666.

Parnell, J., 1988. Metal enrichments in solid bitumens: a review. *Miner. Depos.* 23, 191–199.

Pichowiak, S., Buchelt, M., Damm, K.W., 1990. Magmatic activity and tectonic setting of the early stages of the Andean cycle in northern Chile. *Geol. Soc. Am. Sp Pub* 241, 127–144.

Ramírez, L.E., Palacios, C., Townley, B., Parada, M.A., Sial, A.N., Fernandez-Turiel, J.L., Gimeno, D., Garcia-Valles, M., Lehmann, B. 2006. The Mantos Blancos copper deposit: an upper Jurassic breccia-style hydrothermal system in the Coastal Range of Northern Chile. *Miner. Depos.* 41, 3, 246.

Ramírez, L.E., Parada, M.A., Palacios, C., Wittenbrink, J. 2008. Magmatic evolution of the Mantos Blancos copper deposit, Coastal Range of northern Chile: insight from Sr-Nd isotope, geochemical data and silicate melt inclusions. *Resour. Geol.* 58, 2, 124–142.

Reich, M., Palacios, C., Alvear, M., Cameron, E.M., Leybourne, M.I., and Deditius, A., 2009. Iodine-rich waters involved in supergene enrichment of the Mantos de la Luna argentiferous copper deposit, Atacama Desert, Chile. *Mineral. Depos.* 44, 719–722.

Reich, M., Chryssoulis, S., Deditius, A., Palacios, C., Zuniga, A., Weldt, M., Alvear, M., 2010. “Invisible” silver and gold in supergene digenite (CuS). *Geochim. Cosmochim. Acta* 74, 6157–6173.

Reich, M., Palacios, C., Barra, F., Chryssoulis, S., 2013. “Invisible” silver in chalcopyrite and bornite from the Mantos Blancos copper deposit. *Eur. J. Mineral.* 25, 453–460.

Rickard, D. T., 1997, Kinetics of pyrite formation by the R2S oxidation of iron(II) monosulphide in aqueous solutions between 25 and 125°C: The rate equation. *Geochim. Cosmochim. Acta.*, 61, 115–134.

Rickard, D. and Luther, G. W., 1997, Kinetics of pyrite formation by the H₂S oxidation of iron (II) mono sulphide in aqueous solutions between 25 and 125°C: The mechanism, *Geochim. Cosmochim. Acta.* 61, 1, 135–147.

Rieger, A., Schwark, L., Cisternas, M.E., Miller, H., 2008. Society of Economic Geologists, Inc. *Econ. Geol.* 103, 387–404.

Robb, L.J., Meyer, F.M., 1995. The Witwatersrand Basin, South Africa: Geological framework and mineralization processes. *Ore Geol. Rev.* 10, 67–94.

Rogers, G., Hawkesworth, J., 1989. A geochemical traverse across the North Chilean Andes: evidence for crust generation from the mantle wedge. *Earth Planet. Sci. Lett.* 91, 271–285.

Ruíz, C., Aguirre, L., Corvalán, J., Klohn, C., Klohn, E., Levi, B., 1965. Geología y yacimientos metalíferos de Chile. Instituto de Investigaciones Geológicas, Santiago, Chile, 302 p. (in Spanish).

Ruiz, C., Aguilar, A., Egert, E., Espinosa, W., Peebles, F., Quezada, R. and Serrano, M., 1971. Strata-bound copper sulphide deposits of Chile. In: *Proceedings IMA-IAGOD, 7th General Meeting, Tokyo-Kyoto, Japan, 1970. Soc. Min. Geol. Japan, Special Issue 3*, pp. 252–260.

Saintilan, N.J., Spangenberg, J.E., Chiaradia, M., Chelle-Michou, C., Stephens, M.B., Fontboté, L., 2019. Petroleum as source and carrier of metals in epigenetic sediment-hosted mineralization. *Sci. Rep.* 9, 8283.

Sato, T. 1984. Manto type Copper deposits in Chile- a Review. *Bull Geol. Surv. Jpn.* 35, 565–582.

Scheuber, E., Andriessen, P., 1990. The kinematic and geodynamic significance of the Atacama Fault Zone, northern Chile. *J. Struct. Geol.* 12, 243–257.

Scheuber, E., González, G., 1999. Tectonics of Jurassic-Early Cretaceous magmatic arc of the north Chilean Coastal Cordillera (22°–26°S). A story of crustal deformation along a convergent plate boundary. *Tectonics* 18, 895–910.

Scheuber, E., Bogdanic, T., Jensen, A., Reutter, K.J., 1994. Tectonic development and magmatism since the Jurassic. In: Reutter, K.-J., Scheuber, E., Wigger, P. (Eds.), *Tectonics of Southern Central Andes Structure and Evolution of an Active Continental Margin*. Springer, Heidelberg, pp. 121–140.

Spirakis C.S., 1996. The roles of organic matter in the formation of uranium deposits in sedimentary rocks. *Ore Geol. Rev.* 11, 53–69.

Sun, Y.Z., Püttmann, W., 2000. The role of organic matter during copper enrichment in Kupferschiefer from the Sangerhausen basin, Germany. *Org. Geochem.* 31, 11, 1143–1161.

- Szmihelsky, M., Steele-MacInnis, M., Bain, W., Falck, H., Adair, R., Campbell, B., Dufrane, A., Went, A., Corlett, H. 2021. Mixing of brine with oil triggered sphalerite deposition at Pine Point, Northwest Territories, Canada. *Geology* 49, 5, 488–492.
- Tristá-Aguilera, D., Barra, F., Ruíz, J., Morata, D., Talavera-Mendoza, O., Kojima, S., Ferraris, F. 2006. Re-Os isotope systematics for the Lince-Estefanía deposit: constraints on the timing and source of copper mineralization in a stratabound copper deposit, Coastal Cordillera of Northern Chile. *Miner. Depos.* 41, 99–105.
- Tosdal, R.M., Munizaga, F. 2003. Lead sources in Mesozoic and Cenozoic Andean ore deposits, north-central Chile (30–34° S). *Miner. Depos.* 38, 2, 234–250.
- Vivallo, W., Henriquez, F. 1998. Génesis común de los yacimientos estratoligados y vetiformes de cobre del Jurásico Medio a Superior en la Cordillera de la Costa, Región de Antofagasta, Chile. *Andean Geol.* 25, 2, 199–228. (in Spanish).
- Watkinson, P., 2007. Deposition from Crude Oils in Heat Exchangers. *Heat Transfer Eng.* 28, 177–184.
- Wilson, N.S.F., 1998. The role of petroleum in the formation of the Soldado copper deposit, Chile: Hydrothermal replacement of a biodegraded petroleum reservoir. Unpublished Ph.D. thesis, Halifax, Canada, Dalhousie University, 418 p.
- Wilson, N., Zentilli, M., 1999. The Role of Organic Matter in the Genesis of the El Soldado Volcanic-Hosted Manto-Type Cu Deposit, Chile. *Econ. Geol.* 94, 1115–1136.
- Wilson, N., Zentilli, M., Reynolds, P.H., Boric, R., 2003a. A age of mineralization by basinal fluids at the El Soldado manto-type copper deposit, Chile $^{40}\text{Ar}/^{39}\text{Ar}$ geochronology of K-feldespar. *Chem. Geol.* 197, 161–176.
- Wilson, N., Zentilli, M., Spiro, B., 2003b. A sulfur, carbon, oxygen, and strontium isotope study of the volcanic-hosted El Soldado manto type copper deposit, Chile: The essential role of bacteria and petroleum. *Econ. Geol.* 98, 163–174.
- Wilson, N., Zentilli, M., 2006. Association of pyrobitumen with copper mineralization from the Uchumi and Talcuna districts, central Chile. *Int. J. Coal Geol.* 65, 1, 158–169.
- Wu, Y., Evans, K., Fisher, L.A., Zhou, M., Hu, S., Fougereuse, D., Large, R., Li, J., 2020. Distribution of trace elements between carbonaceous matter and sulfides in a sediment-hosted orogenic gold system. *Geochim. Cosmochim. Acta* 276, 345–362.
- Zentilli, M., Boric, R., Munizaga, F. and Graves, M.C., 1994. Petroleum involvement in the genesis of some strata-bound copper deposits of Chile. *Proceedings, 7th Chilean Geological Congress, Concepcion, Chile, II*, 1542–1546.
- Zentilli, M., Munizaga, F., Graves, M.C., Boric, R., Wilson, N.S.F., Mukhopadhyay, P.K., Snowdon, L.T., 1997. Hydrocarbon involvement in the genesis of ore deposits: an example in Cretaceous strata-bound (manto-type) copper deposits of central Chile. *Int. Geol. Rev.* 39, 1–21.

ANEXXES

ANEXX A

SUPPLEMENTARY MATERIAL OF CHAPTER 2

Assessing the role of bitumen in the formation of stratabound Cu-(Ag) deposits: Insights from the Lorena deposit, Las Luces district, northern Chile

This file include:

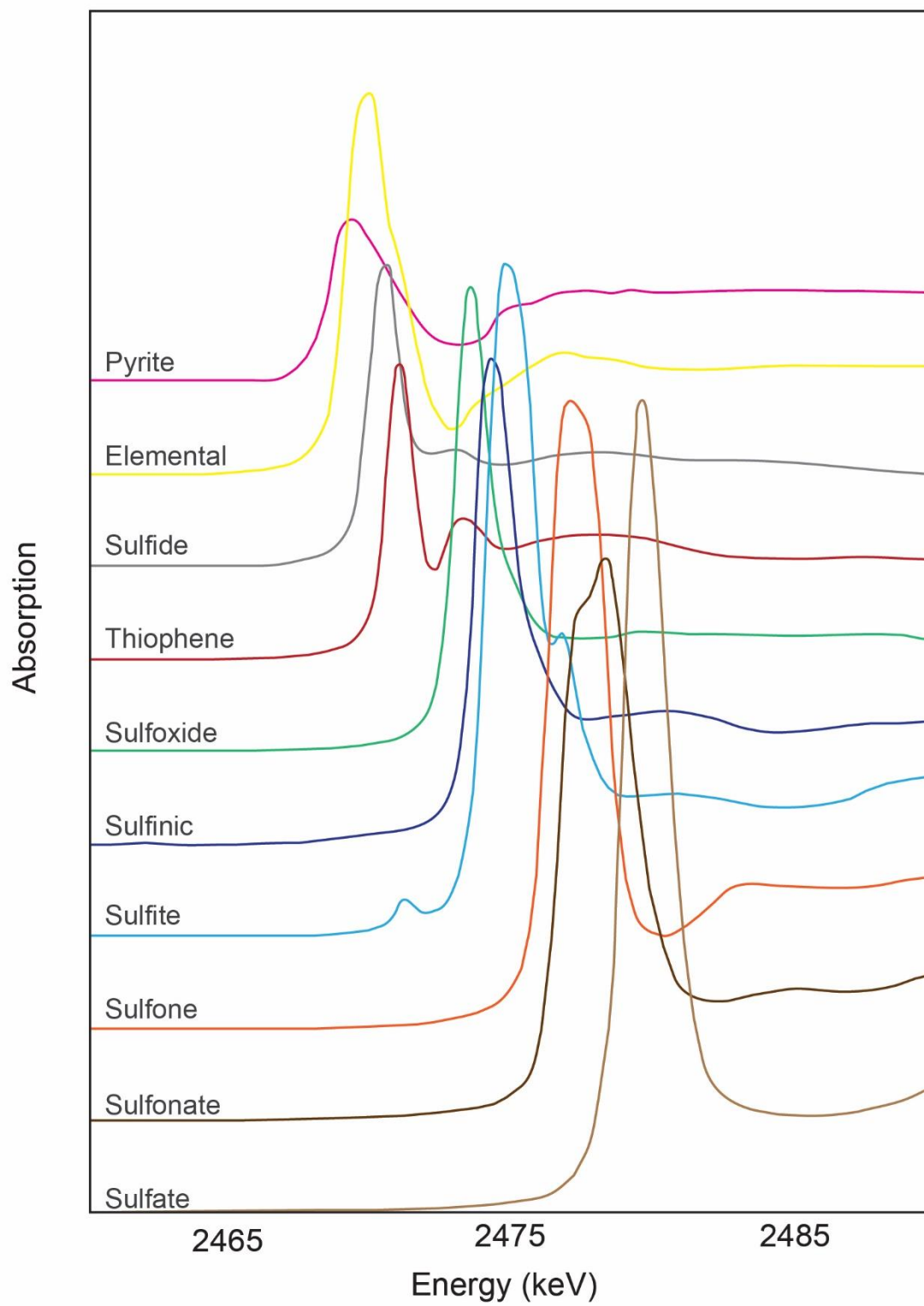
A.1. Sulfur K-edge spectra for sulfur standards (Bolin et al., 2016).

A.2. Representative electron microprobe analyzes (EMPA) data (wt.%) of bitumen in Lorena deposit carried out at Peter Hooper GeoAnalytical Laboratory of Washington State University (WSU), USA and LAMARX Laboratory of the Universidad Nacional de Córdoba, Argentina. b.d.l: below detection limit. Detection limits (wt.%) are shown below each element analyzed.

A.3. Concentration boxplot for selected minor elements in pyrobitumen from Lorena. Electron microprobe analyses (EMPA) including all data are plotted in weight percent (wt.%) on a vertical logarithmic scale. In the boxplot, mean and median concentrations are shown. A circle outlier is a data point above $1.5 \times (75\text{th percentile} - 25\text{th percentile})$ while a square outlier is above $3.0 \times (75\text{th percentile} - 25\text{th percentile})$.

A.4. Boxplot showing the concentration of Fe, Cu, S, Cl, Ag and Au in pyrobitumen plotted as a function of sample depth (LO-62, LO-7-1 and LO-15: intermediate-shallow samples, LO-24: deep sample). All EMPA data are plotted in weight percent (wt.%) on a vertical logarithmic scale. In each boxplot, mean concentrations are marked. A circle outlier is above $1.5 \times (\text{quartile } 3 - \text{quartile } 1)$ while a square outlier is above $3.0 \times (75\text{th percentile} - 25\text{th percentile})$.

A.1. Sulfur K-edge spectra for sulfur standards (Bolin et al., 2016).



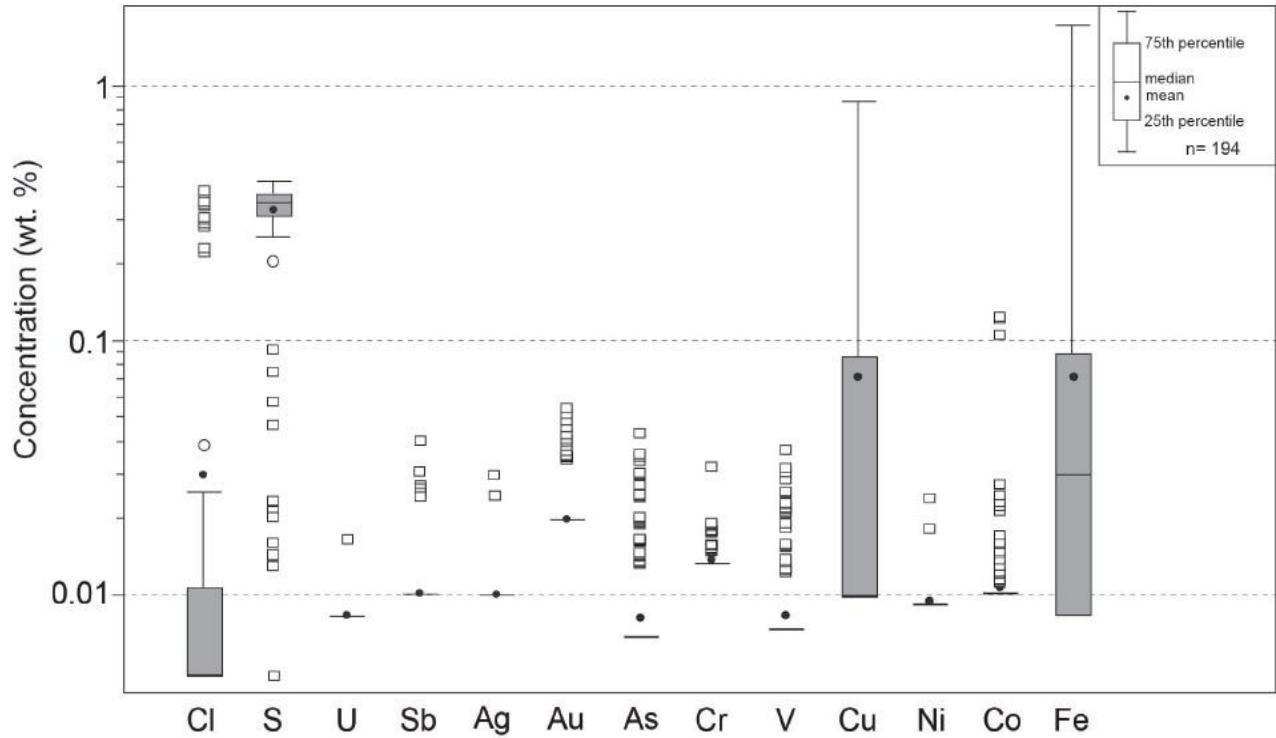
A.2. Representative electron microprobe analyzes (EMPA) data (wt.%) of bitumen in Lorena deposit carried out at Peter Hooper GeoAnalytical Laboratory of Washington State University (WSU), USA and LAMARX Laboratory of the Universidad Nacional de Córdoba, Argentina. b.d.l: below detection limit. Detection limits (wt.%) are shown below each element analyzed.

SAMPLE	Cl	S	U	Sb	Ag	Au	As	Cr	V	Cu	Ni	Co	Fe	Laboratory
D.L	0.017	0.010	0.017	0.02	0.02	0.036	0.013	0.014	0.013	0.021	0.019	0.010	0.017	
ID														
LO-24_Pt2_BIT	0.32	0.21	b.d.l	b.d.l	b.d.l	b.d.l	b.d.l	b.d.l	0.03	0.32	b.d.l	b.d.l	1.74	WSU
LO-24_Pt2_BIT	0.33	0.06	b.d.l	0.08	b.d.l	b.d.l	0.35	WSU						
LO-24_Pt2_BIT	0.26	0.05	b.d.l	0.07	b.d.l	b.d.l	0.44	WSU						
LO-24_Pt2_BIT	0.25	0.02	b.d.l	0.07	b.d.l	b.d.l	0.27	WSU						
LO-24_Pt6-2_BIT	0.01	0.32	b.d.l	0.12	WSU									
LO-24_Pt6-2_BIT	b.d.l	0.31	b.d.l	0.06	WSU									
LO-24_Pt6-2_BIT	b.d.l	0.35	b.d.l	0.02	WSU									
LO-24_Pt6-2_BIT	b.d.l	0.36	b.d.l	b.d.l	0.03	b.d.l	0.03	WSU						
LO-24_Pt6-2_BIT	b.d.l	0.33	b.d.l	0.05	WSU									
LO-24_Pt9_BIT	0.34	0.08	b.d.l	0.87	b.d.l	0.12	0.10	WSU						
LO-24_Pt9_BIT	0.39	0.10	b.d.l	0.64	b.d.l	b.d.l	0.19	WSU						
LO-24_Pt14-1_BIT	b.d.l	0.31	b.d.l	0.02	WSU									
LO-24_Pt14-2_BIT	0.40	0.02	b.d.l	0.40	b.d.l	b.d.l	0.04	WSU						
LO-24_Pt14-2_BIT	0.33	0.02	b.d.l	b.d.l	b.d.l	0.05	b.d.l	0.02	b.d.l	0.26	b.d.l	b.d.l	0.04	WSU
LO-24_Pt14-2_BIT	0.30	0.01	b.d.l	0.23	b.d.l	b.d.l	0.03	WSU						
LO-24_Pt14-2_BIT	b.d.l	0.32	b.d.l	0.07	b.d.l	b.d.l	0.02	WSU						
LO-24_Pt16_BIT	b.d.l	0.36	b.d.l	0.08	WSU									
LO-24_Pt16_BIT	b.d.l	0.35	b.d.l	WSU										
LO-24_Pt17_BIT	b.d.l	0.26	b.d.l	0.03	WSU									
LO-24_Pt17_BIT	b.d.l	0.30	b.d.l	b.d.l	b.d.l	b.d.l	b.d.l	0.02	b.d.l	b.d.l	b.d.l	b.d.l	0.04	WSU
LO-24_Pt21_BIT	0.31	0.02	b.d.l	0.42	b.d.l	0.12	0.05	WSU						
LO-24_Pt21_BIT	0.35	0.02	b.d.l	0.23	b.d.l	b.d.l	0.04	WSU						
LO-24_Pt26_BIT	b.d.l	0.33	b.d.l	WSU										
LO-24_Pt26_BIT	b.d.l	0.35	b.d.l	WSU										
LO-24_Pt30_BIT	b.d.l	0.41	b.d.l	0.02	WSU									
LO-24_Pt30_BIT	0.01	0.37	b.d.l	WSU										
LO-7-1_Pt5_BIT	b.d.l	0.35	b.d.l	WSU										
LO-7-1_Pt5_BIT	b.d.l	0.32	b.d.l	WSU										
LO-7-1_Pt5_BIT	b.d.l	0.33	b.d.l	WSU										
LO-7-1_Pt9_BIT	b.d.l	0.35	b.d.l	WSU										
LO-7-1_Pt9_BIT	b.d.l	0.33	b.d.l	WSU										
LO-7-1_Pt9_BIT	b.d.l	0.34	b.d.l	0.02	b.d.l	b.d.l	WSU							
LO-7-1_Pt12_BIT	b.d.l	0.39	b.d.l	b.d.l	b.d.l	0.04	b.d.l	b.d.l	b.d.l	0.23	b.d.l	b.d.l	b.d.l	WSU
LO-7-1_Pt12_BIT	0.02	0.33	b.d.l	0.28	b.d.l	b.d.l	0.02	WSU						
LO-7-1_Pt12_BIT	b.d.l	0.32	b.d.l	0.03	b.d.l	WSU								
LO-7-1_Pt14_BIT	b.d.l	0.34	b.d.l	WSU										
LO-7-1_Pt14_BIT	b.d.l	0.32	b.d.l	WSU										
LO-7-1_Pt14_BIT	b.d.l	0.35	b.d.l	0.10	b.d.l	WSU								
LO-7-1_Pt19_BIT	b.d.l	0.37	b.d.l	0.03	b.d.l	b.d.l	WSU							
LO-7-1_Pt19_BIT	b.d.l	0.36	b.d.l	b.d.l	0.03	b.d.l	WSU							
LO-7-1_Pt19_BIT	b.d.l	0.36	b.d.l	b.d.l	b.d.l	b.d.l	b.d.l	0.02	b.d.l	b.d.l	b.d.l	b.d.l	b.d.l	WSU
LO-7-1_Pt19_BIT	b.d.l	0.31	b.d.l	WSU										
LO71-30-Bi-3	b.d.l	0.37	b.d.l	b.d.l	b.d.l	b.d.l	0.02	b.d.l	b.d.l	0.22	b.d.l	b.d.l	0.05	LAMARX
LO71-30-Bi-4	0.02	0.38	b.d.l	0.13	b.d.l	b.d.l	0.03	LAMARX						
LO71-30-Bi-5	b.d.l	0.38	b.d.l	b.d.l	b.d.l	0.04	b.d.l	b.d.l	b.d.l	0.06	b.d.l	b.d.l	0.04	LAMARX
LO71-30-Bi-6	b.d.l	0.38	b.d.l	0.05	b.d.l	b.d.l	b.d.l	LAMARX						
LO71-31-Bi-7	0.01	0.34	0.02	b.d.l	b.d.l	0.06	b.d.l	LAMARX						
LO71-31-Bi-8	0.02	0.37	b.d.l	0.10	b.d.l	0.02	b.d.l	LAMARX						
LO71-31-Bi-9	0.01	0.37	b.d.l	b.d.l	b.d.l	b.d.l	b.d.l	0.02	b.d.l	0.04	b.d.l	b.d.l	b.d.l	LAMARX
LO71-31-Bi-10	b.d.l	0.43	b.d.l	LAMARX										
LO71-31-Bi-11	b.d.l	0.39	b.d.l	0.15	b.d.l	b.d.l	0.02	LAMARX						
LO71-33-Bi-16	0.01	0.38	b.d.l	b.d.l	b.d.l	b.d.l	b.d.l	b.d.l	0.02	0.05	b.d.l	b.d.l	b.d.l	LAMARX
LO71-33-Bi-17	b.d.l	0.39	b.d.l	b.d.l	b.d.l	b.d.l	0.02	b.d.l	b.d.l	b.d.l	b.d.l	0.01	b.d.l	LAMARX
LO71-33-Bi-18	b.d.l	0.38	b.d.l	LAMARX										
LO71-33-Bi-19	b.d.l	0.37	b.d.l	LAMARX										
LO71-33-Bi-20	b.d.l	0.36	b.d.l	0.02	LAMARX									
LO71-33-Bi-21	b.d.l	0.38	b.d.l	LAMARX										
LO71-34-Bi-22	b.d.l	0.36	b.d.l	LAMARX										
LO71-34-Bi-23	0.02	0.37	b.d.l	0.02	b.d.l	LAMARX								
LO71-34-Bi-24	b.d.l	0.35	b.d.l	0.02	b.d.l	b.d.l	b.d.l	LAMARX						

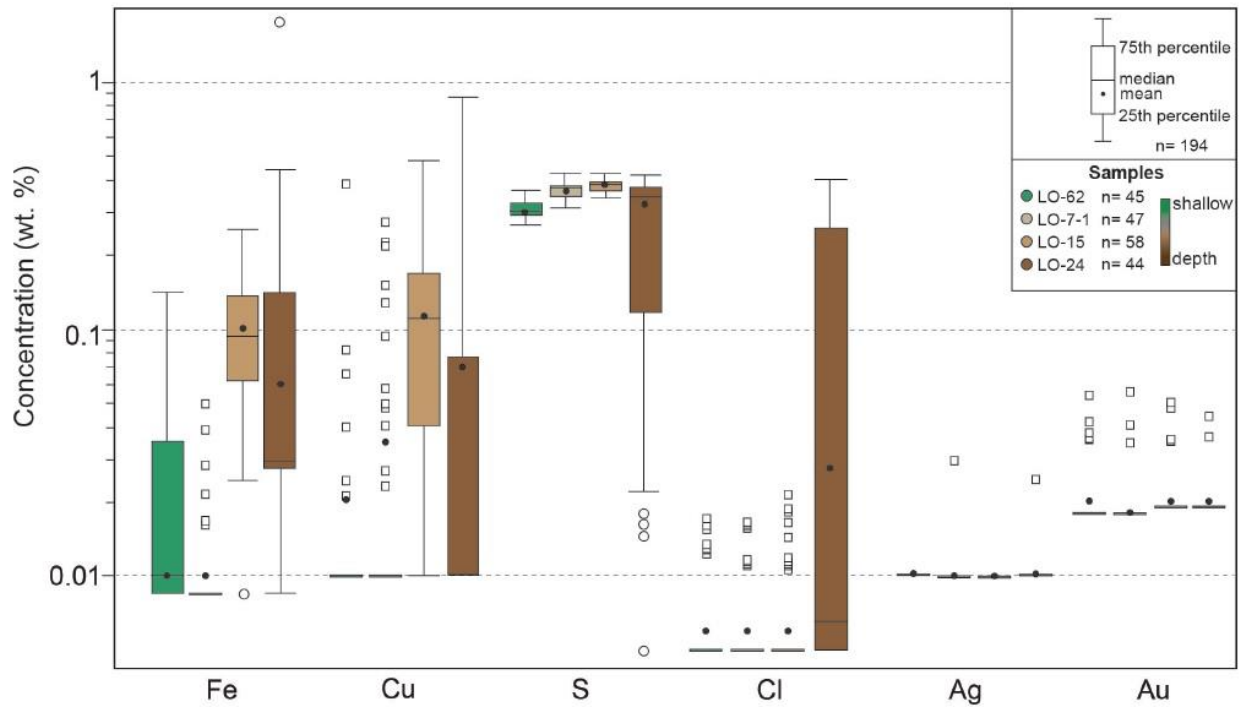
LO71-34-Bi-25	0.01	0.37	b.d.1	0.03	b.d.1	LAMARX									
LO71-34-Bi-26	b.d.1	0.34	b.d.1	b.d.1	b.d.1	b.d.1	b.d.1	b.d.1	0.01	b.d.1	b.d.1	b.d.1	b.d.1	LAMARX	
LO71-38-Bi-27	b.d.1	0.37	b.d.1	b.d.1	b.d.1	b.d.1	b.d.1	b.d.1	0.02	0.02	b.d.1	b.d.1	b.d.1	LAMARX	
LO71-38-Bi-28	b.d.1	0.37	b.d.1	b.d.1	b.d.1	b.d.1	b.d.1	b.d.1	0.02	0.03	b.d.1	b.d.1	b.d.1	LAMARX	
LO71-38-Bi-29	b.d.1	0.39	b.d.1	LAMARX											
LO71-38-Bi-30	0.01	0.37	b.d.1	b.d.1	b.d.1	b.d.1	b.d.1	b.d.1	0.02	b.d.1	b.d.1	b.d.1	0.01	b.d.1	LAMARX
LO71-38-Bi-31	b.d.1	0.38	b.d.1	LAMARX											
LO71-38-Bi-32	b.d.1	0.32	b.d.1	LAMARX											
LO71-38-Bi-33	b.d.1	0.39	b.d.1	b.d.1	b.d.1	b.d.1	b.d.1	0.01	b.d.1	b.d.1	b.d.1	b.d.1	b.d.1	LAMARX	
LO71-38-Bi-34	b.d.1	0.37	b.d.1	LAMARX											
LO71-42-Bi-40	b.d.1	0.37	b.d.1	LAMARX											
LO71-42-Bi-41	b.d.1	0.37	b.d.1	LAMARX											
LO71-42-Bi-42	b.d.1	0.40	b.d.1	LAMARX											
Lo15-13-Bi-1	b.d.1	0.38	b.d.1	b.d.1	b.d.1	0.04	b.d.1	b.d.1	b.d.1	0.14	b.d.1	b.d.1	0.21	LAMARX	
Lo15-13-Bi-2	0.01	0.39	b.d.1	0.09	b.d.1	b.d.1	0.18	LAMARX							
Lo15-13-Bi-3	b.d.1	0.35	b.d.1	b.d.1	b.d.1	b.d.1	b.d.1	0.02	b.d.1	b.d.1	0.07	b.d.1	b.d.1	0.25	LAMARX
Lo15-20-Bi-12	b.d.1	0.38	b.d.1	0.13	b.d.1	b.d.1	0.11	LAMARX							
Lo15-20-Bi-13	b.d.1	0.37	b.d.1	0.12	b.d.1	b.d.1	0.13	LAMARX							
Lo15-20-Bi-14	b.d.1	0.39	b.d.1	0.01	0.20	LAMARX									
Lo15-20-Bi-15	b.d.1	0.37	b.d.1	0.02	0.05	b.d.1	b.d.1	0.19	LAMARX						
Lo15-20-Bi-16	b.d.1	0.37	b.d.1	0.36	b.d.1	b.d.1	0.15	LAMARX							
Lo15-20-Bi-17	0.02	0.39	b.d.1	0.02	0.48	b.d.1	0.02	0.14	LAMARX						
Lo15-20-Bi-18	b.d.1	0.40	b.d.1	0.22	b.d.1	b.d.1	0.05	LAMARX							
Lo15-14-Bi-19	0.01	0.38	b.d.1	0.02	b.d.1	b.d.1	b.d.1	LAMARX							
Lo15-14-Bi-20	b.d.1	0.39	b.d.1	LAMARX											
Lo15-14-Bi-21	b.d.1	0.36	b.d.1	0.02	b.d.1	b.d.1	b.d.1	b.d.1	LAMARX						
Lo15-14-Bi-22	0.01	0.40	b.d.1	b.d.1	b.d.1	b.d.1	b.d.1	0.02	b.d.1	b.d.1	b.d.1	b.d.1	0.03	b.d.1	LAMARX
Lo15-14-Bi-30	b.d.1	0.40	b.d.1	0.01	0.14	b.d.1	b.d.1	0.09	LAMARX						
Lo15-14-Bi-31	b.d.1	0.34	b.d.1	0.06	b.d.1	b.d.1	0.12	LAMARX							
Lo15-14-Bi-32	b.d.1	0.35	b.d.1	0.03	b.d.1	b.d.1	0.24	LAMARX							
Lo15-10-Bi-33	b.d.1	0.39	b.d.1	0.06	b.d.1	b.d.1	0.03	LAMARX							
Lo15-10-Bi-34	0.01	0.40	b.d.1	b.d.1	b.d.1	b.d.1	b.d.1	0.03	b.d.1	b.d.1	0.18	b.d.1	b.d.1	0.04	LAMARX
Lo15-10-Bi-35	0.01	0.39	b.d.1	b.d.1	b.d.1	b.d.1	b.d.1	0.02	b.d.1	b.d.1	b.d.1	b.d.1	b.d.1	0.08	LAMARX
Lo15-10-Bi-36	b.d.1	0.40	b.d.1	0.04	b.d.1	0.02	0.04	LAMARX							
Lo15-10-Bi-37	0.02	0.39	b.d.1	0.11	b.d.1	b.d.1	0.07	LAMARX							
Lo15-10-Bi-38	b.d.1	0.37	b.d.1	0.03	b.d.1	b.d.1	0.09	LAMARX							
Lo15-15-Bi-44	b.d.1	0.34	b.d.1	0.09	b.d.1	b.d.1	0.06	LAMARX							
Lo15-15-Bi-45	0.01	0.39	b.d.1	b.d.1	b.d.1	b.d.1	b.d.1	0.03	b.d.1	b.d.1	0.05	b.d.1	b.d.1	0.04	LAMARX
Lo15-15-Bi-46	b.d.1	0.38	b.d.1	b.d.1	b.d.1	b.d.1	b.d.1	0.03	b.d.1	0.01	0.06	b.d.1	b.d.1	0.03	LAMARX
Lo15-15-Bi-47	b.d.1	0.40	b.d.1	0.13	b.d.1	b.d.1	0.06	LAMARX							
Lo15-15-Bi-48	b.d.1	0.35	b.d.1	b.d.1	b.d.1	b.d.1	b.d.1	0.02	b.d.1	b.d.1	b.d.1	b.d.1	b.d.1	0.03	LAMARX
Lo15-9-Bi-49	b.d.1	0.39	b.d.1	0.02	0.12	b.d.1	b.d.1	0.22	LAMARX						
Lo15-9-Bi-50	0.01	0.38	b.d.1	0.02	0.12	b.d.1	b.d.1	0.17	LAMARX						
Lo15-9-Bi-51	b.d.1	0.40	b.d.1	0.04	b.d.1	b.d.1	0.02	b.d.1	b.d.1	b.d.1	0.12	b.d.1	b.d.1	0.14	LAMARX
Lo15-9-Bi-52	b.d.1	0.35	b.d.1	0.30	b.d.1	b.d.1	0.18	LAMARX							
Lo15-9-Bi-54	0.01	0.38	b.d.1	b.d.1	b.d.1	0.05	b.d.1	0.08	LAMARX						
Lo15-9-Bi-55	b.d.1	0.42	b.d.1	0.09	LAMARX										
Lo15-9-Bi-56	0.01	0.36	b.d.1	0.02	0.17	b.d.1	b.d.1	0.13	LAMARX						
Lo15-8-Bi-63	0.01	0.40	b.d.1	0.12	b.d.1	0.01	0.15	LAMARX							
Lo15-8-Bi-64	b.d.1	0.36	b.d.1	0.04	b.d.1	b.d.1	0.09	LAMARX							
Lo15-8-Bi-65	b.d.1	0.40	b.d.1	b.d.1	b.d.1	b.d.1	b.d.1	0.02	0.02	b.d.1	0.03	b.d.1	0.02	0.11	LAMARX
Lo15-8-Bi-66	0.01	0.35	b.d.1	b.d.1	b.d.1	b.d.1	b.d.1	0.04	b.d.1	b.d.1	0.04	b.d.1	b.d.1	0.11	LAMARX
Lo15-8-Bi-67	b.d.1	0.38	b.d.1	0.17	b.d.1	b.d.1	0.11	LAMARX							
Lo15-8-Bi-68	b.d.1	0.36	b.d.1	0.05	b.d.1	0.02	0.18	LAMARX							
Lo15-16-Bi-69	b.d.1	0.37	b.d.1	LAMARX											
Lo15-16-Bi-70	b.d.1	0.39	b.d.1	0.02	LAMARX										
Lo15-16-Bi-71	b.d.1	0.41	b.d.1	0.04	b.d.1	b.d.1	0.07	LAMARX							
Lo15-16-Bi-72	b.d.1	0.39	b.d.1	0.05	b.d.1	b.d.1	0.07	LAMARX							
Lo15-16-Bi-73	0.02	0.41	b.d.1	0.30	b.d.1	b.d.1	0.11	LAMARX							
Lo15-16-Bi-74	b.d.1	0.38	b.d.1	b.d.1	b.d.1	b.d.1	0.05	b.d.1	b.d.1	0.02	0.11	b.d.1	b.d.1	0.11	LAMARX
Lo15-16-Bi-75	b.d.1	0.34	b.d.1	0.11	b.d.1	b.d.1	0.10	LAMARX							
Lo15-16-Bi-76	0.01	0.38	b.d.1	0.02	0.15	b.d.1	b.d.1	0.10	LAMARX						
Lo15-16-Bi-77	b.d.1	0.36	b.d.1	0.20	b.d.1	b.d.1	0.11	LAMARX							
Lo15-6-Bi-88	b.d.1	0.38	b.d.1	0.16	b.d.1	b.d.1	0.08	LAMARX							
Lo15-6-Bi-89	b.d.1	0.37	b.d.1	b.d.1	b.d.1	b.d.1	b.d.1	0.02	b.d.1	0.23	b.d.1	0.01	0.07	LAMARX	
Lo15-6-Bi-90	b.d.1	0.35	b.d.1	0.17	b.d.1	b.d.1	0.06	LAMARX							
Lo15-6-Bi-91	0.02	0.36	b.d.1	0.42	b.d.1	b.d.1	0.07	LAMARX							
Lo15-7-Bi-92	b.d.1	0.38	b.d.1	b.d.1	b.d.1	b.d.1	b.d.1	0.02	b.d.1	b.d.1	0.17	b.d.1	b.d.1	0.13	LAMARX
Lo15-7-Bi-93	b.d.1	0.37	b.d.1	0.03	b.d.1	b.d.1	b.d.1	b.d.1	b.d.1	b.d.1	0.29	b.d.1	b.d.1	0.12	LAMARX
Lo15-7-Bi-94	0.01	0.40	b.d.1	0.17	b.d.1	b.d.1	0.08	LAMARX							
Lo15-7-Bi-96	b.d.1	0.38	b.d.1	b.d.1	b.d.1	0.04	b.d.1	b.d.1	b.d.1	b.d.1	0.24	b.d.1	b.d.1	0.11	LAMARX
LO62-1-Bi-01	0.02	0.29	b.d.1	LAMARX											
LO62-1-Bi-02	0.01	0.27	b.d.1	LAMARX											

LO62-1-Bi-03	b.d.1	0.31	b.d.1	b.d.1	b.d.1	b.d.1	b.d.1	b.d.1	0.01	b.d.1	b.d.1	b.d.1	b.d.1	LAMARX
LO62-1-Bi-04	b.d.1	0.29	b.d.1	b.d.1	b.d.1	b.d.1	b.d.1	0.02	b.d.1	0.01	b.d.1	b.d.1	b.d.1	LAMARX
LO62-1-Bi-05	0.01	0.29	b.d.1	LAMARX										
LO62-7-Bi-06	b.d.1	0.35	b.d.1	b.d.1	b.d.1	b.d.1	0.04	b.d.1	b.d.1	b.d.1	b.d.1	b.d.1	b.d.1	LAMARX
LO62-7-Bi-07	b.d.1	0.30	b.d.1	b.d.1	b.d.1	b.d.1	b.d.1	0.02	b.d.1	b.d.1	b.d.1	b.d.1	b.d.1	LAMARX
LO62-7-Bi-08	b.d.1	0.29	b.d.1	b.d.1	b.d.1	b.d.1	b.d.1	b.d.1	0.02	b.d.1	b.d.1	b.d.1	b.d.1	LAMARX
LO62-7-Bi-09	0.01	0.30	b.d.1	LAMARX										
LO62-7-Bi-10	b.d.1	0.32	b.d.1	b.d.1	b.d.1	b.d.1	0.04	b.d.1	b.d.1	b.d.1	b.d.1	b.d.1	b.d.1	LAMARX
LO62-7-Bi-11	b.d.1	0.28	b.d.1	0.03	b.d.1	b.d.1	b.d.1	LAMARX						
LO62-2-Bi-12	b.d.1	0.36	b.d.1	b.d.1	b.d.1	0.05	b.d.1	b.d.1	b.d.1	b.d.1	b.d.1	0.02	0.03	LAMARX
LO62-2-Bi-13	0.02	0.32	b.d.1	b.d.1	b.d.1	b.d.1	0.03	b.d.1	b.d.1	b.d.1	b.d.1	b.d.1	0.02	LAMARX
LO62-2-Bi-14	0.02	0.34	b.d.1	b.d.1	b.d.1	b.d.1	0.02	b.d.1	0.02	b.d.1	b.d.1	0.01	0.02	LAMARX
LO62-2-Bi-15	b.d.1	0.33	b.d.1	0.01	0.02	LAMARX								
LO62-4-Bi-16	b.d.1	0.28	b.d.1	0.02	b.d.1	b.d.1	0.11	LAMARX						
LO62-4-Bi-17	b.d.1	0.27	b.d.1	0.39	b.d.1	b.d.1	0.14	LAMARX						
LO62-4-Bi-18	b.d.1	0.30	b.d.1	b.d.1	b.d.1	b.d.1	b.d.1	b.d.1	0.01	0.03	b.d.1	b.d.1	0.05	LAMARX
LO62-4-Bi-19	b.d.1	0.29	b.d.1	0.09	LAMARX									
LO62-10-Bi-20	b.d.1	0.29	b.d.1	0.07	b.d.1	b.d.1	0.03	LAMARX						
LO62-10-Bi-21	b.d.1	0.28	b.d.1	0.04	b.d.1	b.d.1	b.d.1	LAMARX						
LO62-10-Bi-22	b.d.1	0.27	b.d.1	LAMARX										
LO62-10-Bi-23	b.d.1	0.30	b.d.1	b.d.1	b.d.1	b.d.1	0.03	b.d.1	b.d.1	0.08	b.d.1	b.d.1	0.04	LAMARX
LO62-13-Bi-24	b.d.1	0.32	b.d.1	b.d.1	b.d.1	b.d.1	0.02	b.d.1	0.03	b.d.1	0.02	b.d.1	0.06	LAMARX
LO62-13-Bi-25	b.d.1	0.32	b.d.1	b.d.1	b.d.1	b.d.1	0.03	b.d.1	b.d.1	b.d.1	b.d.1	b.d.1	0.10	LAMARX
LO62-13-Bi-26	b.d.1	0.33	b.d.1	0.13	LAMARX									
LO62-13-Bi-27	b.d.1	0.32	b.d.1	b.d.1	b.d.1	b.d.1	0.02	0.03	0.02	b.d.1	b.d.1	b.d.1	0.07	LAMARX
LO62-13-Bi-28	b.d.1	0.32	b.d.1	0.01	0.07	LAMARX								
LO62-16-Bi-29	b.d.1	0.30	b.d.1	0.03	LAMARX									
LO62-16-Bi-30	b.d.1	0.28	b.d.1	b.d.1	b.d.1	b.d.1	0.02	b.d.1	b.d.1	b.d.1	b.d.1	b.d.1	0.02	LAMARX
LO62-16-Bi-31	b.d.1	0.31	b.d.1	b.d.1	b.d.1	0.04	b.d.1	b.d.1	0.01	b.d.1	b.d.1	b.d.1	b.d.1	LAMARX
LO62-16-Bi-32	b.d.1	0.30	b.d.1	b.d.1	b.d.1	b.d.1	0.04	b.d.1	b.d.1	0.02	b.d.1	b.d.1	b.d.1	LAMARX
LO62-16-Bi-33	b.d.1	0.30	b.d.1	b.d.1	b.d.1	b.d.1	b.d.1	b.d.1	0.02	b.d.1	b.d.1	b.d.1	0.07	LAMARX
LO62-18-Bi-34	b.d.1	0.31	b.d.1	b.d.1	b.d.1	b.d.1	0.03	b.d.1	b.d.1	b.d.1	b.d.1	b.d.1	b.d.1	LAMARX
LO62-18-Bi-35	0.02	0.33	b.d.1	b.d.1	b.d.1	b.d.1	0.03	0.02	b.d.1	b.d.1	b.d.1	b.d.1	b.d.1	LAMARX
LO62-18-Bi-36	b.d.1	0.33	b.d.1	LAMARX										
LO62-18-Bi-37	b.d.1	0.32	b.d.1	b.d.1	b.d.1	b.d.1	b.d.1	b.d.1	0.01	b.d.1	b.d.1	b.d.1	b.d.1	LAMARX
LO62-18-Bi-38	b.d.1	0.32	b.d.1	b.d.1	b.d.1	b.d.1	0.01	0.02	b.d.1	b.d.1	b.d.1	b.d.1	b.d.1	LAMARX
LO62-18-Bi-39	b.d.1	0.31	b.d.1	LAMARX										
LO62-18-Bi-40	0.01	0.31	b.d.1	0.01	b.d.1	LAMARX								
LO62-20-Bi-41	b.d.1	0.30	b.d.1	0.03	LAMARX									
LO62-20-Bi-42	b.d.1	0.29	b.d.1	LAMARX										
LO62-20-Bi-43	b.d.1	0.27	b.d.1	b.d.1	b.d.1	b.d.1	b.d.1	0.02	b.d.1	b.d.1	b.d.1	b.d.1	b.d.1	LAMARX
LO62-20-Bi-44	b.d.1	0.30	b.d.1	0.02	LAMARX									
LO62-20-Bi-45	0.01	0.30	b.d.1	b.d.1	b.d.1	b.d.1	0.04	0.02	b.d.1	b.d.1	b.d.1	b.d.1	0.02	LAMARX
LO-24-7-Bi-01	b.d.1	0.39	b.d.1	b.d.1	b.d.1	b.d.1	0.01	b.d.1	b.d.1	b.d.1	b.d.1	b.d.1	0.25	LAMARX
LO-24-7-Bi-02	0.01	0.39	b.d.1	b.d.1	b.d.1	b.d.1	b.d.1	b.d.1	0.02	b.d.1	b.d.1	b.d.1	0.21	LAMARX
LO-24-7-Bi-03	b.d.1	0.40	b.d.1	b.d.1	b.d.1	0.04	b.d.1	b.d.1	0.01	b.d.1	b.d.1	b.d.1	0.17	LAMARX
LO-24-7-Bi-04	b.d.1	0.37	b.d.1	b.d.1	b.d.1	b.d.1	b.d.1	b.d.1	0.04	b.d.1	b.d.1	0.01	0.15	LAMARX
LO-24-7-Bi-05	0.03	0.42	b.d.1	0.02	b.d.1	b.d.1	0.16	LAMARX						
LO-24-7-Bi-06	b.d.1	0.36	b.d.1	b.d.1	b.d.1	b.d.1	0.03	b.d.1	b.d.1	b.d.1	b.d.1	b.d.1	0.19	LAMARX
LO-24-7-Bi-07	0.01	0.37	b.d.1	b.d.1	b.d.1	b.d.1	0.02	b.d.1	b.d.1	b.d.1	b.d.1	b.d.1	0.13	LAMARX
LO-24-12-Bi-08	b.d.1	0.40	b.d.1	0.05	LAMARX									
LO-24-12-Bi-09	b.d.1	0.38	b.d.1	0.05	LAMARX									
LO-24-12-Bi-10	0.01	0.35	b.d.1	b.d.1	b.d.1	b.d.1	0.02	b.d.1	b.d.1	b.d.1	b.d.1	b.d.1	0.05	LAMARX
LO-24-12-Bi-11	b.d.1	0.41	b.d.1	b.d.1	b.d.1	b.d.1	b.d.1	b.d.1	0.02	b.d.1	b.d.1	b.d.1	0.03	LAMARX
LO-24-25-Bi-12	0.03	0.33	b.d.1	0.15	b.d.1	b.d.1	0.05	LAMARX						
LO-24-25-Bi-13	0.01	0.35	b.d.1	b.d.1	b.d.1	b.d.1	0.04	b.d.1	b.d.1	0.04	b.d.1	b.d.1	0.07	LAMARX
LO-24-25-Bi-14	b.d.1	0.39	b.d.1	b.d.1	b.d.1	b.d.1	b.d.1	b.d.1	0.03	b.d.1	b.d.1	b.d.1	0.07	LAMARX
LO-24-25-Bi-15	0.01	0.36	b.d.1	0.07	LAMARX									
LO-24-25-Bi-16	0.04	0.34	b.d.1	0.03	b.d.1	0.06	LAMARX							
LO-24-25-Bi-17	0.02	0.34	b.d.1	0.04	b.d.1	b.d.1	0.07	LAMARX						

A.3. Concentration boxplot for selected minor elements in pyrobitumen from Lorena. Electron microprobe analyses (EMPA) including all data are plotted in weight percent (wt.%) on a vertical logarithmic scale. In the boxplot, mean and median concentrations are shown. A circle outlier is a data point above $1.5 \times (75\text{th percentile} - 25\text{th percentile})$ while a square outlier is above $3.0 \times (75\text{th percentile} - 25\text{th percentile})$.



A.4. Boxplot showing the concentration of Fe, Cu, S, Cl, Ag and Au in pyrobitumen plotted as a function of sample depth (LO-62, LO-7-1 and LO-15: intermediate-shallow samples, LO-24: deep sample). All EMPA data are plotted in weight percent (wt.%) on a vertical logarithmic scale. In each boxplot, mean concentrations are marked. A circle outlier is above $1.5 \times$ (quartile 3- quartile 1) while a square outlier is above $3.0 \times$ (75th percentile - 25th percentile).



ANEXX B

SUPPLEMENTARY MATERIAL OF CHAPTER 3

Trace element geochemistry of pyrite from bitumen-bearing stratabound Cu-(Ag) deposits, northern Chile

This file include:

B.1. Electron probe microanalysis (EPMA) data of pyrite from stratabound Cu-(Ag) deposits, Chile. Concentrations are reported in weight percent (wt.%). Detection limits (in wt.%) are shown below each element. LO: Lorena deposit; MTCUL: La Culebra deposit; MTC: Manto Cobrizo deposit. b.d.l: below detection limit.

B.2. Laser ablation inductively coupled plasma mass spectrometry (LA-ICP-MS) analyses of Ag, Au, Cu, Bi, Hg, Tl, Pb, Zn, Se, Te, As, Sb, Ge, Cd, In, Sn, Co, Ni, Mn, Cr, V and Mo of pyrite from stratabound Cu-(Ag) deposits, Chile. Concentrations are reported in parts per million (ppm). Detection limits (in ppm) are shown below each element. LO: Lorena deposit; MTCUL: La Culebra deposit; MTC: Manto Cobrizo deposit. b.d.l: below detection limit.

B.1. Electron probe microanalysis (EPMA) data of pyrite from stratabound Cu-(Ag) deposits, Chile. Concentrations are reported in weight percent (wt.%). Detection limits (in wt.%) are shown below each element. LO: Lorena deposit; MTCUL: La Culebra deposit; MTC: Manto Cobrizo deposit. b.d.l: below detection limit.

Sample	S	Fe	Co	Ni	Cu	Au	Ag	Zn	As	Sb	Se	Te	Hg	Pb	Bi	Total
	0.01	0.01	0.04	0.01	0.02	0.02	0.02	0.02	0.02	0.02	0.02	0.02	0.03	0.03	0.03	
Lorena (Las Luces district)																
LO-24	54.11	46.67	bdl	bdl	0.09	bdl	100.87									
LO-24	53.30	46.76	bdl	bdl	0.09	bdl	bdl	bdl	bdl	bdl	0.02	bdl	bdl	bdl	bdl	100.18
LO-24	54.54	46.64	bdl	0.01	0.38	bdl	bdl	0.02	0.03	bdl	bdl	bdl	bdl	bdl	bdl	101.62
LO-24	54.92	46.76	bdl	0.02	0.03	bdl	bdl	bdl	101.73							
LO-24	54.10	46.43	bdl	bdl	0.24	bdl	bdl	bdl	0.03	bdl	bdl	bdl	bdl	bdl	bdl	100.80
LO-24	54.19	46.77	bdl	bdl	0.06	0.06	bdl	bdl	0.05	bdl	bdl	bdl	bdl	bdl	bdl	101.13
LO-24	54.31	46.77	bdl	bdl	0.04	0.04	bdl	0.02	bdl	bdl	bdl	0.02	bdl	0.03	bdl	101.23
LO-24	53.47	46.64	bdl	bdl	0.09	bdl	bdl	bdl	0.05	bdl	bdl	bdl	bdl	bdl	bdl	100.25
LO-24	54.43	47.04	bdl	bdl	0.10	bdl	bdl	0.03	0.04	bdl	bdl	bdl	bdl	bdl	bdl	101.64
LO-24	54.17	47.01	bdl	bdl	bdl	bdl	bdl	bdl	0.03	bdl	bdl	bdl	0.06	bdl	bdl	101.27
LO-24	54.07	46.82	bdl	bdl	bdl	bdl	bdl	0.02	0.02	bdl	bdl	bdl	bdl	bdl	bdl	100.93
LO-24	54.08	46.65	bdl	bdl	0.02	bdl	bdl	0.02	0.06	0.02	bdl	bdl	0.12	bdl	bdl	100.98
LO-24	54.70	46.92	bdl	bdl	0.05	bdl	bdl	0.02	0.05	bdl	bdl	0.03	bdl	bdl	bdl	101.77
LO-24	54.39	46.70	bdl	bdl	bdl	bdl	bdl	bdl	0.02	bdl	bdl	bdl	bdl	bdl	bdl	101.11
LO-24	54.65	46.52	bdl	bdl	0.02	0.04	bdl	bdl	bdl	bdl	bdl	bdl	0.06	bdl	bdl	101.29
LO-24	54.39	46.71	bdl	bdl	0.40	bdl	bdl	bdl	0.03	bdl	bdl	bdl	bdl	bdl	bdl	101.53
LO-24	54.20	46.76	bdl	bdl	0.05	bdl	101.01									
LO-24	54.36	46.69	bdl	bdl	0.05	0.05	0.02	0.02	0.03	bdl	bdl	bdl	bdl	bdl	bdl	101.22
LO-24	54.14	46.27	bdl	bdl	0.05	0.04	bdl	bdl	0.06	bdl	bdl	0.02	bdl	bdl	bdl	100.59
LO-24	52.32	46.77	bdl	bdl	0.06	bdl	bdl	0.02	bdl	bdl	bdl	bdl	0.04	bdl	bdl	99.19
LO-24	52.25	46.94	bdl	0.01	0.04	bdl	0.04	bdl	bdl	99.28						
LO-24	51.50	46.48	bdl	bdl	bdl	bdl	bdl	bdl	0.18	bdl	bdl	bdl	bdl	bdl	bdl	98.15
LO-24	52.04	46.38	0.08	bdl	bdl	bdl	bdl	bdl	0.14	bdl	bdl	bdl	bdl	bdl	bdl	98.63
LO-24	51.98	46.54	bdl	bdl	bdl	bdl	bdl	bdl	0.13	bdl	bdl	bdl	bdl	bdl	bdl	98.64
LO-24	51.88	46.91	bdl	0.03	bdl	bdl	bdl	bdl	0.18	bdl	bdl	bdl	bdl	bdl	0.04	99.03
LO-24	52.28	46.50	bdl	bdl	0.04	bdl	98.81									

Copiapó District

MTCUL-1C	53.38	46.28	bdl	bdl	bdl	0.03	bdl	0.02	0.03	bdl	0.02	bdl	bdl	bdl	bdl	99.76
MTCUL-1C	53.53	45.96	0.04	bdl	bdl	bdl	bdl	bdl	0.02	bdl	bdl	bdl	0.07	bdl	bdl	99.62
MTCUL-1C	53.36	45.55	bdl	bdl	bdl	bdl	bdl	0.03	bdl	bdl	bdl	bdl	bdl	bdl	bdl	98.94
MTCUL-1C	53.22	46.23	bdl	bdl	bdl	bdl	bdl	bdl	0.03	bdl	bdl	bdl	bdl	bdl	bdl	99.48
MTCUL-1C	53.38	45.87	bdl	bdl	0.03	bdl	bdl	bdl	0.04	bdl	bdl	0.02	bdl	bdl	bdl	99.33
MTCUL-1C	53.22	45.80	0.03	0.02	bdl	bdl	bdl	bdl	0.04	bdl	bdl	bdl	bdl	bdl	bdl	99.12
MTCUL-1C	53.25	45.55	bdl	bdl	bdl	0.03	bdl	bdl	bdl	bdl	bdl	bdl	0.06	bdl	bdl	98.89
MTCUL-1C	53.04	45.54	bdl	bdl	bdl	bdl	bdl	bdl	0.05	bdl	bdl	bdl	bdl	bdl	bdl	98.63
MTCUL-1C	53.78	46.08	bdl	bdl	bdl	bdl	bdl	bdl	0.02	bdl	bdl	bdl	bdl	bdl	bdl	99.88
MTCUL-1C	52.61	45.67	bdl	bdl	bdl	0.02	bdl	0.02	bdl	bdl	bdl	bdl	0.04	bdl	bdl	98.36
MTCUL-1C	52.95	45.57	bdl	bdl	bdl	bdl	bdl	bdl	0.07	bdl	0.03	bdl	bdl	bdl	bdl	98.61
MTCUL-1C	53.49	45.89	bdl	bdl	bdl	0.05	bdl	bdl	0.05	bdl	bdl	bdl	bdl	bdl	bdl	99.48
MTCUL-1C	53.59	46.17	bdl	bdl	bdl	bdl	bdl	bdl	bdl	bdl	bdl	0.03	bdl	bdl	bdl	99.79
MTCUL-1C	53.54	46.05	bdl	bdl	0.03	bdl	bdl	bdl	0.05	bdl	0.02	bdl	0.04	bdl	bdl	99.73
MTCUL-1C	53.53	45.99	bdl	bdl	bdl	bdl	bdl	bdl	bdl	bdl	0.02	bdl	bdl	bdl	bdl	99.54
MTCUL-1C	53.71	45.91	bdl	bdl	bdl	0.03	bdl	bdl	bdl	bdl	bdl	bdl	bdl	bdl	bdl	99.65
MTCUL-1C	53.64	45.94	bdl	bdl	bdl	bdl	bdl	bdl	0.07	bdl	bdl	0.03	bdl	bdl	bdl	99.68
MTCUL-1C	53.56	45.86	bdl	bdl	bdl	bdl	bdl	bdl	bdl	bdl	bdl	bdl	bdl	bdl	bdl	99.42
MTCUL-1C	53.30	45.25	bdl	bdl	0.02	bdl	bdl	0.02	bdl	bdl	bdl	bdl	bdl	bdl	bdl	98.59
MTCUL-1C	53.48	45.97	0.03	bdl	bdl	0.04	bdl	0.02	bdl	bdl	bdl	bdl	bdl	bdl	bdl	99.54
MTCUL-1C	52.93	46.05	bdl	bdl	0.03	bdl	bdl	0.03	bdl	bdl	bdl	bdl	bdl	bdl	bdl	99.03
MTCUL-1C	53.75	46.33	bdl	bdl	bdl	0.04	bdl	bdl	bdl	bdl	bdl	bdl	0.07	bdl	bdl	100.19
MTCUL-1C	53.10	46.19	bdl	bdl	bdl	bdl	bdl	bdl	bdl	bdl	0.03	bdl	bdl	bdl	bdl	99.32
MTCUL-1C	53.00	45.34	bdl	bdl	bdl	bdl	bdl	bdl	0.02	bdl	bdl	bdl	bdl	bdl	bdl	98.36
MTCUL-1C	53.24	46.30	bdl	bdl	bdl	bdl	bdl	bdl	bdl	0.03	0.02	bdl	bdl	bdl	bdl	99.59
MTCUL-1C	53.27	45.95	bdl	bdl	0.02	0.03	bdl	bdl	0.02	bdl	0.02	bdl	bdl	bdl	bdl	99.31
MTCUL-1C	53.22	45.65	bdl	bdl	bdl	0.06	bdl	0.02	0.05	bdl	bdl	bdl	0.04	0.08	bdl	99.13
MTCUL-1C	53.52	46.09	0.03	bdl	bdl	bdl	bdl	bdl	bdl	bdl	0.02	bdl	bdl	bdl	bdl	99.66
MTCUL-1D	53.58	46.10	bdl	bdl	0.04	bdl	bdl	bdl	bdl	bdl	bdl	bdl	bdl	bdl	bdl	99.72
MTCUL-1D	53.80	46.41	0.03	bdl	bdl	0.05	bdl	bdl	bdl	bdl	bdl	bdl	bdl	bdl	bdl	100.29
MTCUL-1D	53.74	46.14	bdl	bdl	bdl	bdl	bdl	bdl	0.04	bdl	bdl	bdl	bdl	bdl	bdl	99.92
MTCUL-1D	53.40	46.14	bdl	bdl	0.02	0.02	bdl	bdl	0.07	bdl	bdl	bdl	bdl	bdl	bdl	99.65
MTCUL-1D	53.21	46.22	bdl	bdl	bdl	0.03	bdl	0.02	0.04	bdl	bdl	bdl	bdl	bdl	bdl	99.52
MTCUL-1D	53.08	45.97	bdl	bdl	bdl	0.05	bdl	0.02	bdl	bdl	bdl	bdl	bdl	bdl	bdl	99.11
MTCUL-1D	53.12	45.03	bdl	bdl	0.06	bdl	bdl	bdl	0.04	bdl	bdl	bdl	bdl	bdl	bdl	98.25
MTCUL-1D	53.77	46.31	bdl	bdl	0.03	0.05	bdl	bdl	bdl	bdl	bdl	bdl	bdl	bdl	bdl	100.16
MTCUL-1D	54.08	46.49	bdl	bdl	0.09	bdl	bdl	bdl	0.03	bdl	bdl	bdl	0.07	bdl	bdl	100.76
MTCUL-1D	53.00	45.57	bdl	bdl	0.04	bdl	bdl	0.02	0.02	bdl	0.02	bdl	bdl	bdl	bdl	98.67
MTCUL-1D	53.67	46.33	bdl	bdl	0.12	bdl	bdl	bdl	0.04	bdl	bdl	bdl	bdl	bdl	bdl	100.16
MTCUL-1D	53.95	46.52	bdl	bdl	0.08	bdl	bdl	bdl	0.02	bdl	bdl	bdl	bdl	bdl	bdl	100.57
MTCUL-1D	53.89	46.22	bdl	bdl	0.17	bdl	bdl	0.02	bdl	bdl	0.02	0.03	bdl	bdl	bdl	100.35

MTCUL-1D	53.82	46.09	0.04	bdl	0.05	bdl	bdl	bdl	0.04	bdl	bdl	bdl	bdl	bdl	bdl	100.04
MTCUL-2A	53.81	46.64	bdl	0.02	bdl	bdl	bdl	bdl	100.47							
MTCUL-2A	53.69	46.76	bdl	bdl	bdl	0.04	bdl	bdl	0.03	bdl	bdl	bdl	bdl	bdl	bdl	100.52
MTCUL-2A	53.48	45.73	bdl	bdl	bdl	bdl	bdl	bdl	0.02	bdl	bdl	0.03	bdl	bdl	bdl	99.26
MTCUL-2A	53.38	46.32	bdl	bdl	0.16	bdl	0.03	0.02	bdl	bdl	bdl	bdl	bdl	bdl	bdl	99.91
MTCUL-2A	53.76	46.62	0.05	bdl	bdl	bdl	bdl	0.03	bdl	bdl	bdl	bdl	bdl	bdl	bdl	100.46
MTCUL-2A	53.47	46.34	bdl	bdl	bdl	bdl	bdl	0.04	0.03	bdl	bdl	bdl	bdl	bdl	bdl	99.88
MTCUL-2A	53.07	46.38	bdl	bdl	bdl	0.05	bdl	0.02	0.02	bdl	0.02	0.04	bdl	bdl	bdl	99.59
MTCUL-2A	53.28	46.24	bdl	bdl	bdl	99.52										
MTCUL-2A	53.54	46.22	0.03	bdl	0.13	bdl	bdl	bdl	0.03	bdl	bdl	bdl	bdl	bdl	bdl	99.95
MTCUL-2A	53.36	46.26	bdl	bdl	0.14	bdl	bdl	bdl	0.03	bdl	bdl	0.02	bdl	bdl	bdl	99.81
MTCUL-2A	53.63	46.10	bdl	bdl	0.23	0.02	bdl	bdl	0.03	bdl	bdl	bdl	bdl	bdl	bdl	100.02
MTCUL-2A	54.72	46.78	bdl	bdl	0.03	bdl	bdl	bdl	0.04	bdl	bdl	bdl	bdl	bdl	bdl	101.57
MTCUL-2A	54.12	46.70	0.03	bdl	bdl	bdl	100.85									
MTCUL-2A	53.95	46.66	0.04	bdl	0.03	bdl	bdl	bdl	0.02	bdl	bdl	bdl	bdl	bdl	bdl	100.70
MTCUL-2A	54.58	46.81	bdl	bdl	0.02	bdl	0.04	bdl	bdl	101.45						
MTCUL-2A	54.23	46.87	bdl	bdl	bdl	0.04	bdl	0.02	0.02	bdl	bdl	bdl	bdl	bdl	bdl	101.18
MTCUL-2A	54.09	46.98	0.03	bdl	0.02	bdl	0.02	bdl	0.04	bdl	bdl	bdl	0.07	bdl	bdl	101.26
MTCUL-2A	54.09	46.54	bdl	bdl	bdl	100.63										
MTCUL-2A	53.98	46.99	bdl	bdl	bdl	bdl	bdl	bdl	0.04	bdl	bdl	bdl	bdl	bdl	0.05	101.06
MTCUL-2A	54.08	46.89	0.04	bdl	0.03	bdl	bdl	bdl	0.05	bdl	0.02	bdl	bdl	bdl	bdl	101.10
MTCUL-2A	54.04	46.80	bdl	bdl	0.03	bdl	bdl	bdl	100.87							
MTCUL-3B	52.97	46.99	bdl	0.02	0.06	bdl	bdl	100.05								
MTCUL-3B	52.61	47.05	0.06	bdl	0.03	bdl	bdl	bdl	99.75							
MTCUL-3B	52.87	46.81	bdl	bdl	0.14	bdl	bdl	bdl	99.81							
MTCUL-3B	52.80	46.85	bdl	bdl	0.08	bdl	0.02	bdl	bdl	bdl	bdl	bdl	bdl	bdl	bdl	99.75
MTCUL-3B	52.61	46.33	bdl	bdl	0.03	bdl	bdl	bdl	98.97							
MTCUL-3B	52.98	46.75	bdl	bdl	0.06	bdl	0.05	bdl	bdl	99.84						
MTCUL-3B	53.13	47.08	bdl	0.05	0.09	bdl	bdl	bdl	100.35							
MTCUL-3B	53.05	46.92	bdl	bdl	0.03	bdl	bdl	bdl	100.00							
MTCUL-3B	52.36	46.70	0.09	0.02	bdl	bdl	bdl	99.16								
MTCUL-3B	52.68	46.99	bdl	bdl	bdl	bdl	bdl	bdl	0.05	bdl	bdl	bdl	bdl	bdl	bdl	99.72
MTCUL-3B	52.78	46.67	0.15	0.06	0.05	bdl	bdl	bdl	99.71							
MTCUL-3B	51.12	45.72	0.05	bdl	bdl	bdl	bdl	bdl	3.35	bdl	bdl	bdl	bdl	bdl	bdl	100.25
MTCUL-3B	52.52	46.50	bdl	bdl	bdl	0.03	bdl	bdl	bdl	99.05						
MTCUL-3B	52.76	46.95	0.06	bdl	bdl	bdl	99.77									
MTCUL-3B	53.44	47.11	bdl	bdl	bdl	100.55										
MTCUL-2D	51.47	46.89	bdl	bdl	bdl	bdl	0.02	bdl	0.04	bdl	bdl	bdl	bdl	bdl	0.03	98.46
MTCUL-2D	51.10	45.96	0.07	bdl	bdl	bdl	bdl	bdl	2.63	bdl	bdl	bdl	bdl	bdl	bdl	99.76
MTCUL-2D	49.61	44.67	0.05	bdl	bdl	bdl	bdl	bdl	5.22	0.09	bdl	bdl	bdl	bdl	bdl	99.64

MTCUL-2D	52.19	46.96	bdl	0.02	0.02	bdl	bdl	bdl	0.08	bdl	bdl	bdl	bdl	bdl	99.27
MTCUL-2D	52.02	46.73	bdl	bdl	bdl	bdl	bdl	bdl	0.40	bdl	bdl	bdl	bdl	bdl	99.15
MTCUL-2D	50.27	45.24	bdl	bdl	0.02	bdl	bdl	0.02	4.08	0.06	bdl	bdl	bdl	bdl	99.69
MTCUL-2D	51.89	46.88	bdl	bdl	bdl	bdl	bdl	bdl	0.11	bdl	bdl	bdl	0.05	bdl	98.92
MTCUL-2D	51.07	46.09	bdl	bdl	bdl	bdl	bdl	bdl	2.26	bdl	bdl	bdl	bdl	bdl	99.42
MTCUL-2D	52.07	46.88	0.08	bdl	0.03	bdl	bdl	bdl	0.10	bdl	bdl	bdl	bdl	bdl	99.16
MTCUL-2D	51.75	46.92	bdl	bdl	bdl	bdl	bdl	bdl	0.32	bdl	bdl	bdl	bdl	bdl	98.99
MTCUL-2D	52.07	46.80	0.07	0.01	bdl	0.04	bdl	98.99							
MTCUL-2D	52.42	46.65	bdl	0.01	bdl	bdl	bdl	0.02	0.03	bdl	bdl	bdl	bdl	bdl	99.13
MTCUL-2D	52.43	46.69	0.06	bdl	0.03	bdl	99.21								
MTCUL-2D	52.70	46.98	bdl	99.68											
MTCUL-2D	52.04	46.80	0.06	bdl	0.13	bdl	99.02								
MTCUL-2D	52.05	46.47	0.06	0.03	0.03	bdl	bdl	bdl	0.03	bdl	bdl	bdl	bdl	bdl	98.66
MTCUL-2D	51.65	46.48	0.07	0.02	0.02	bdl	0.05	bdl	98.30						
MTCUL-2D	52.59	46.77	bdl	99.36											
MTCUL-2D	52.77	46.79	bdl	0.01	0.05	bdl	99.62								
MTCUL-2D	52.45	46.47	bdl	0.03	0.10	bdl	99.05								
MTCUL-2D	52.33	46.53	0.06	0.01	0.13	bdl	0.09	99.15							
MTCUL-2D	52.69	47.09	bdl	99.78											
MTCUL-2D	52.34	46.72	bdl	bdl	0.08	bdl	bdl	0.03	bdl	bdl	bdl	bdl	bdl	bdl	99.18
MTC- 9	52.24	45.43	bdl	bdl	1.44	bdl	99.11								
MTC- 9	53.39	45.19	0.07	bdl	2.23	bdl	100.87								
MTC- 9	52.82	45.30	bdl	bdl	1.08	bdl	99.21								
MTC-10	53.13	46.24	bdl	bdl	0.13	bdl	0.02	bdl	0.04	bdl	0.04	bdl	bdl	bdl	99.60
MTC-10	52.84	46.25	bdl	bdl	0.33	bdl	bdl	0.02	0.06	bdl	bdl	bdl	bdl	bdl	99.50
MTC-10	53.75	46.41	bdl	bdl	0.10	bdl	bdl	0.02	bdl	bdl	bdl	bdl	bdl	bdl	100.28
MTC-10	54.21	46.50	bdl	bdl	0.12	bdl	100.83								
MTC-10	52.73	45.65	bdl	bdl	1.45	bdl	bdl	0.02	bdl	bdl	bdl	bdl	0.05	bdl	99.90
MTC-10	53.96	46.14	bdl	bdl	0.08	0.03	bdl	bdl	0.04	bdl	bdl	bdl	bdl	bdl	100.24
MTC-10	53.52	44.60	bdl	bdl	0.61	bdl	bdl	0.03	bdl	bdl	bdl	0.02	bdl	bdl	98.79
MTC-10	53.96	46.60	bdl	bdl	0.10	bdl	100.66								
MTC-10	53.58	45.98	bdl	bdl	0.04	bdl	bdl	bdl	0.05	bdl	bdl	bdl	bdl	bdl	99.65
MTC-10	54.14	46.71	bdl	bdl	0.21	bdl	bdl	bdl	0.02	bdl	bdl	bdl	0.04	bdl	101.12
MTC-10	54.03	45.95	bdl	0.02	0.30	bdl	bdl	bdl	0.02	bdl	0.02	bdl	bdl	bdl	100.34
MTC-10	54.19	46.19	bdl	bdl	0.14	bdl	bdl	bdl	0.03	bdl	bdl	bdl	0.16	bdl	100.71
MTC-10	54.06	46.80	bdl	bdl	0.25	bdl	bdl	bdl	bdl	bdl	0.02	bdl	0.04	bdl	101.17
MTC-10	53.92	46.21	bdl	bdl	0.08	bdl	bdl	bdl	bdl	0.02	bdl	bdl	bdl	bdl	100.23
MTC-10	54.71	46.73	bdl	bdl	0.10	bdl	bdl	bdl	0.05	bdl	bdl	bdl	bdl	bdl	101.59
MTC-10	54.29	46.82	bdl	bdl	0.04	0.04	bdl	101.19							
MTC-10	54.14	46.61	0.03	bdl	0.02	0.04	bdl	100.84							
MTC-10	53.48	45.91	bdl	bdl	1.43	bdl	0.09	bdl	100.91						

MTC-12	52.97	44.66	0.06	bdl	2.87	bdl	bdl	0.14	0.10	bdl	bdl	bdl	bdl	bdl	bdl	100.80
MTC-12	53.55	46.91	bdl	bdl	0.30	bdl	bdl	bdl	bdl	bdl	bdl	bdl	bdl	bdl	bdl	100.76
MTC-12	53.63	47.06	bdl	bdl	0.36	bdl	bdl	bdl	bdl	bdl	bdl	bdl	bdl	bdl	bdl	101.05
MTC-12	53.24	46.94	bdl	bdl	0.17	bdl	bdl	bdl	bdl	bdl	bdl	bdl	bdl	bdl	bdl	100.36
MTC-12	53.36	46.95	bdl	bdl	0.38	bdl	bdl	0.02	bdl	bdl	bdl	bdl	bdl	bdl	bdl	100.71
MTC-12	53.41	46.50	bdl	bdl	0.83	bdl	bdl	bdl	bdl	bdl	bdl	bdl	bdl	bdl	bdl	100.74
MTC-12	52.80	45.54	0.06	0.01	1.50	bdl	bdl	0.10	0.03	bdl	bdl	bdl	bdl	bdl	bdl	100.04
MTC-12	52.76	46.77	0.14	0.01	0.22	bdl	bdl	0.02	bdl	bdl	bdl	bdl	bdl	bdl	bdl	99.93

Minimum	49.61	44.60	0.03	0.01	0.02	0.02	0.02	0.02	0.02	0.02	0.02	0.02	0.04	0.03	0.03	98.15
Maximum	54.92	47.11	0.15	0.01	2.87	0.06	0.03	0.14	5.22	0.09	0.04	0.04	0.16	0.09	0.05	101.77
Median	53.38	46.49	0.05	0.01	0.08	0.04	0.02	0.02	0.04	0.03	0.02	0.03	0.05	0.08	0.04	99.79
Average	53.25	46.37	0.06	0.01	0.24	0.04	0.02	0.03	0.28	0.04	0.02	0.03	0.06	0.07	0.04	99.94
Count	156.00	156.00	32.00	18.00	91.00	27.00	6.00	35.00	77.00	5.00	18.00	13.00	24.00	3.00	3.00	156.00

B.2. Laser ablation inductively coupled plasma mass spectrometry (LA-ICP-MS) analyses of Ag, Au, Cu, Bi, Hg, Tl, Pb, Zn, Se, Te, As, Sb, Ge, Cd, In, Sn, Co, Ni, Mn, Cr, V and Mo of pyrite from stratabound Cu-(Ag) deposits, Chile. Concentrations are reported in parts per million (ppm). Detection limits (in ppm) are shown below each element. LO: Lorena deposit; MTCUL: La Culebra deposit; MTC: Manto Cobrizo deposit. b.d.l: below detection limit.

Sample	Ag	Au	Bi	Hg	Tl	Pb	Zn	Se	Te	As	Sb	Ge	Cd	In	Sn	Co	Ni	Mn	Cr	V	Mo	Cu
	0.12	0.02	0.05	0.30	0.02	0.06	2.90	14.00	0.54	2.10	0.15	1.20	0.39	0.02	0.15	0.27	0.98	1.20	2.70	1.10	0.40	1.20
Lorena (Las Luces district)																						
LO-24	bdl	bdl	bdl	bdl	0.15	0.82	28.40	bdl	bdl	bdl	bdl	bdl	bdl	bdl	0.51	40.80	36.30	2970.00	bdl	bdl	bdl	52.0
LO-24	bdl	bdl	bdl	bdl	21.4	2.98	bdl	bdl	bdl	29.10	bdl	3.40	bdl	0.03	bdl	21.10	16.00	551.00	bdl	bdl	311.00	38.3
LO-24	bdl	bdl	bdl	bdl	23.1	1.17	bdl	bdl	bdl	834.00	bdl	2.40	bdl	bdl	bdl	4.51	3.30	18.70	bdl	bdl	373.00	32.2
LO-24	7.60	bdl	2.49	bdl	bdl	58.90	42.00	bdl	bdl	bdl	bdl	bdl	bdl	bdl	bdl	99.00	56.00	2040.00	bdl	299.00	bdl	6.70E+03
LO-24	17.80	bdl	3.58	2.51	0.41	122.00	24.50	bdl	bdl	bdl	bdl	bdl	bdl	bdl	bdl	251.00	123.00	664.00	bdl	99.00	bdl	1960.00
LO-24	bdl	bdl	bdl	bdl	126.7	0.72	4.40	bdl	bdl	939.00	3.74	2.30	bdl	bdl	bdl	bdl	bdl	46.30	bdl	bdl	186.00	5.90
LO-24	0.99	bdl	bdl	bdl	97.7	0.26	bdl	bdl	bdl	1897.00	5.33	2.80	bdl	bdl	bdl	bdl	bdl	47.70	bdl	bdl	283.00	224.00
LO-24	1.16	bdl	bdl	bdl	105.7	bdl	bdl	bdl	bdl	1370.00	4.26	2.50	bdl	bdl	bdl	bdl	3.80	64.30	bdl	bdl	361.00	203.00
LO-24	0.55	bdl	bdl	bdl	102.4	6.77	bdl	bdl	bdl	2660.00	11.1	bdl	bdl	bdl	bdl	0.89	bdl	16.70	bdl	bdl	98.20	86.20
LO-24	0.26	bdl	bdl	bdl	57.6	21.50	bdl	bdl	bdl	2540.00	9.4	bdl	bdl	bdl	bdl	5.41	3.00	68.50	bdl	80.80	71.20	249.00
LO-24	0.29	bdl	bdl	bdl	54.6	1.83	bdl	bdl	bdl	1620.00	5.91	2.69	bdl	bdl	bdl	1.06	1.28	13.20	bdl	1.80	115.80	61.00
LO-24	0.63	bdl	0.06	bdl	3.69	3.71	bdl	bdl	bdl	27.30	0.56	2.11	bdl	bdl	0.22	15.90	11.50	45.40	bdl	bdl	422.00	119.00
LO-24	0.64	bdl	bdl	bdl	2.13	2.00	bdl	bdl	bdl	52.60	bdl	bdl	bdl	bdl	bdl	5.40	2.10	7.60	bdl	bdl	42.30	460.00
LO-24	bdl	bdl	bdl	bdl	2.25	0.58	bdl	bdl	bdl	69.00	bdl	bdl	bdl	bdl	bdl	1.50	bdl	9.40	bdl	bdl	46.70	360.00
LO-24	0.26	bdl	bdl	bdl	1.73	6.51	bdl	bdl	bdl	73.50	0.91	2.40	bdl	bdl	bdl	7.02	11.60	10.50	bdl	bdl	43.10	37.00
LO-24	bdl	bdl	bdl	bdl	bdl	1.42	bdl	bdl	bdl	bdl	bdl	bdl	bdl	0.25	bdl	bdl	bdl	bdl	bdl	bdl	bdl	3.11E+05
LO-24	bdl	discarded	bdl	bdl	1.58	2.82	bdl	bdl	bdl	17.20	bdl	bdl	bdl	bdl	bdl	5.20	8.20	63.00	bdl	bdl	15.80	21.80
LO-24	3.52	discarded	bdl	bdl	2.09	14.00	bdl	bdl	bdl	23.40	bdl	bdl	bdl	bdl	bdl	32.80	23.40	116.00	bdl	49.00	12.60	820.00
LO-24	bdl	discarded	bdl	bdl	7.40	1.19	bdl	bdl	bdl	29.90	bdl	bdl	bdl	bdl	bdl	5.10	23.40	10.30	bdl	bdl	45.10	22.30
LO-24	3.52	discarded	bdl	bdl	22.40	2.45	bdl	bdl	bdl	30.00	bdl	bdl	bdl	bdl	bdl	11.60	3.30	30.40	bdl	bdl	132.00	120.00
LO-24	bdl	discarded	bdl	bdl	2.07	1.09	bdl	bdl	bdl	5.00	bdl	bdl	bdl	bdl	bdl	27.70	12.50	133.00	bdl	3.30	81.00	61.00
LO-24	bdl	discarded	bdl	bdl	4.78	18.50	bdl	bdl	bdl	31.50	bdl	bdl	bdl	bdl	bdl	27.40	14.50	65.70	bdl	141.00	9.00	1400.00
LO-24	bdl	discarded	bdl	bdl	4.23	4.00	bdl	230.00	bdl	24.50	1.64	bdl	bdl	bdl	bdl	9.40	16.60	38.60	bdl	bdl	5.40	11.30
LO-24	3.55	discarded	bdl	bdl	1.44	4.76	bdl	bdl	bdl	18.50	bdl	bdl	bdl	bdl	bdl	14.10	22.20	170.00	bdl	bdl	11.50	42.00
LO-24	bdl	discarded	bdl	bdl	0.06	1.38	bdl	1400.00	bdl	bdl	bdl	2.00	bdl	bdl	bdl	20.50	18.40	183.00	bdl	bdl	1.94	83.00
LO-24	bdl	discarded	bdl	bdl	3.52	5.10	bdl	bdl	bdl	23.80	1.66	bdl	bdl	bdl	bdl	11.61	18.30	50.60	bdl	bdl	7.10	15.20
LO-24	bdl	discarded	bdl	bdl	2.33	1.45	bdl	40.00	bdl	5.70	bdl	2.06	bdl	bdl	bdl	21.90	14.00	145.00	bdl	bdl	22.40	28.30
LO-24	bdl	discarded	0.18	bdl	0.60	7.87	bdl	bdl	bdl	4.90	bdl	bdl	bdl	bdl	bdl	19.60	7.50	211.00	bdl	25.40	10.90	530.00
LO-24	0.26	discarded	bdl	bdl	bdl	4.48	bdl	35.00	bdl	bdl	bdl	bdl	bdl	bdl	bdl	38.50	37.70	76.70	bdl	bdl	1.31	117.00
LO-24	1.56	discarded	0.14	bdl	bdl	9.20	bdl	bdl	bdl	4.00	bdl	bdl	bdl	bdl	bdl	27.20	5.20	108.80	bdl	9.90	9.60	1520.00
LO-24	bdl	discarded	0.32	bdl	34.80	26.30	bdl	150.00	bdl	bdl	bdl	bdl	bdl	bdl	bdl	70.10	35.10	60.00	bdl	9.60	34.50	1920.00
LO-24	3.61	discarded	bdl	bdl	1.89	1.99	bdl	bdl	bdl	58.00	bdl	bdl	bdl	bdl	bdl	15.80	9.40	2.56	bdl	bdl	7.80	257.00
LO-24	5.96	discarded	bdl	bdl	10.30	1.33	bdl	bdl	bdl	23.40	bdl	2.70	bdl	bdl	bdl	6.60	2.20	23.90	bdl	bdl	35.80	48.00
LO-24	bdl	discarded	bdl	bdl	21.70	2.89	bdl	bdl	bdl	27.20	bdl	1.61	bdl	bdl	bdl	14.00	9.40	34.10	bdl	bdl	148.00	92.00
LO-24	bdl	discarded	bdl	bdl	12.50	13.60	bdl	bdl	bdl	15.30	bdl	bdl	bdl	bdl	bdl	56.70	26.00	69.00	bdl	19.80	173.00	930.00
LO-24	bdl	discarded	bdl	bdl	3.85	5.88	bdl	bdl	bdl	23.70	1.09	1.63	bdl	bdl	bdl	11.80	16.80	60.30	bdl	bdl	10.20	110.00
LO-24	2.68	discarded	bdl	bdl	2.17	3.29	5.00	bdl	bdl	22.30	0.73	bdl	bdl	bdl	bdl	7.50	7.80	109.50	bdl	bdl	13.40	125.00

Copiapó district

MTCUL-2A	21.20	bdl	bdl	0.41	713	11.60	9.80	bdl	bdl	bdl	bdl	2.90	bdl	bdl	0.60	1.58	8.90	1397.00	bdl	71.50	2.16	973.00
MTCUL-2A	0.94	bdl	bdl	bdl	197	0.66	6.70	bdl	bdl	bdl	bdl	bdl	bdl	bdl	0.51	bdl	2600.00	bdl	88.50	1.30	112.10	
MTCUL-2A	2.22	bdl	bdl	0.56	48.7	84.00	38.60	bdl	bdl	530.00	2.82	3.40	bdl	bdl	0.38	22.80	7.10	285.00	bdl	50.90	3.20	92.00
MTCUL-2A	2.22	bdl	bdl	0.95	113.4	29.90	11.90	bdl	bdl	42.90	bdl	bdl	bdl	bdl	0.41	15.20	18.90	359.00	bdl	72.70	1.47	127.40
MTCUL-2A	1.47	bdl	bdl	bdl	73.6	81.90	bdl	bdl	bdl	bdl	bdl	bdl	bdl	bdl	bdl	5.10	bdl	144.00	bdl	bdl	4.50	74.00
MTCUL-2A	bdl	bdl	bdl	bdl	7.87	4.79	bdl	bdl	bdl	bdl	bdl	bdl	bdl	bdl	bdl	53.40	7.30	8.10	bdl	bdl	19.20	11.90
MTCUL-2A	0.57	bdl	bdl	bdl	3.07	1.48	bdl	bdl	bdl	bdl	bdl	bdl	bdl	bdl	bdl	85.30	24.50	24.30	bdl	bdl	8.60	45.00
MTCUL-2A	0.93	bdl	bdl	bdl	73.3	131.90	bdl	bdl	bdl	bdl	1.13	3.00	bdl	bdl	0.97	16.90	7.40	152.00	bdl	bdl	bdl	327.00
MTCUL-2A	0.81	0.02	bdl	bdl	69.7	149.70	bdl	bdl	bdl	bdl	1.99	2.24	bdl	bdl	bdl	46.10	10.10	69.30	bdl	bdl	7.90	149.80
MTCUL-2A	0.72	0.04	bdl	bdl	1.98	387.00	bdl	bdl	bdl	37.20	18.4	2.30	bdl	bdl	bdl	220.00	82.40	14.70	bdl	bdl	76.40	163.00
MTCUL-2A	13.00	0.05	bdl	bdl	543	5.70	bdl	bdl	1.70	bdl	bdl	4.40	bdl	bdl	bdl	bdl	1140.00	bdl	bdl	bdl	550.00	
MTCUL-2A	32.00	bdl	bdl	2.14	635	1.85	18.30	bdl	bdl	bdl	bdl	bdl	bdl	bdl	bdl	bdl	2690.00	bdl	bdl	bdl	406.00	
MTCUL-2A	0.71	0.02	bdl	0.95	155	147.00	bdl	bdl	bdl	8.30	0.84	2.19	bdl	bdl	bdl	0.31	bdl	23.10	bdl	bdl	102.00	77.00
MTCUL-2A	76.40	0.02	bdl	4.32	904	82.00	20.00	bdl	bdl	bdl	bdl	2.04	bdl	bdl	bdl	bdl	2.10	4400.00	bdl	bdl	2.90	1272.00
MTCUL-2A	0.31	bdl	bdl	bdl	27.8	1.39	bdl	bdl	bdl	bdl	bdl	bdl	bdl	bdl	bdl	1.50	bdl	251.00	bdl	bdl	bdl	12.80
MTCUL-2A	2.89	bdl	bdl	bdl	28.1	194.00	15.10	bdl	bdl	74.00	3.64	2.58	bdl	bdl	bdl	145.40	35.00	53.00	bdl	9.30	31.30	114.00
MTCUL-2A	0.33	bdl	bdl	bdl	31.6	1.78	bdl	bdl	bdl	bdl	bdl	2.41	bdl	bdl	bdl	1.66	1.80	135.30	bdl	bdl	bdl	24.70
MTCUL-2A	bdl	bdl	bdl	bdl	56.3	7.04	bdl	bdl	bdl	bdl	bdl	2.55	bdl	bdl	bdl	195.00	53.40	28.90	bdl	bdl	7.90	16.30
MTCUL-2A	0.33	bdl	bdl	bdl	52.5	3.66	4.60	bdl	bdl	bdl	bdl	1.71	bdl	bdl	bdl	162.30	31.40	90.90	bdl	bdl	14.50	19.90
MTCUL-2A	0.42	bdl	bdl	bdl	42.3	1.90	bdl	190.00	bdl	bdl	bdl	2.07	bdl	bdl	bdl	224.00	48.30	11.50	bdl	bdl	6.09	14.20
MTCUL-1C	7.41	bdl	bdl	5.2	79.5	62.40	bdl	bdl	bdl	21.60	9.80	bdl	bdl	0.08	bdl	80.00	66.00	111.00	bdl	20.70	3.70	169.00
MTCUL-1C	24.90	bdl	bdl	15.8	184	428.00	bdl	bdl	bdl	132.00	28.00	bdl	25.00	bdl	bdl	460.00	297.00	402.00	bdl	109.00	23.00	830.00
MTCUL-1C	2.26	bdl	bdl	bdl	77.9	bdl	bdl	bdl	bdl	bdl	bdl	bdl	6.00	bdl	bdl	bdl	223.00	bdl	bdl	bdl	49.10	
MTCUL-1C	1.11	bdl	bdl	bdl	178	bdl	bdl	bdl	bdl	bdl	bdl	bdl	bdl	bdl	bdl	bdl	261.00	bdl	12.10	bdl	213.00	
MTCUL-1C	bdl	bdl	bdl	bdl	40.2	1.49	6.90	bdl	bdl	bdl	bdl	bdl	bdl	bdl	bdl	bdl	5.50	293.00	bdl	bdl	bdl	43.00
MTCUL-1C	1.04	bdl	0.11	7.1	5.67	750.00	bdl	27.00	bdl	281.00	26.60	3.80	bdl	0.06	bdl	27.30	72.00	10.10	bdl	4.10	12.60	471.00
MTCUL-1C	0.28	bdl	bdl	bdl	4.8	7.80	bdl	bdl	bdl	bdl	1.68	bdl	bdl	bdl	bdl	16.50	10.40	39.00	bdl	6.30	4.10	73.00
MTCUL-1C	bdl	bdl	bdl	bdl	bdl	1.56	bdl	bdl	bdl	bdl	bdl	bdl	bdl	bdl	bdl	8.50	16.00	15.10	bdl	bdl	bdl	53.50
MTCUL-1C	bdl	bdl	bdl	bdl	0.165	0.16	bdl	bdl	bdl	bdl	bdl	2.70	4.30	bdl	bdl	2.55	bdl	4.04	bdl	bdl	bdl	43.10
MTCUL-1C	bdl	bdl	bdl	bdl	0.085	0.16	bdl	bdl	bdl	bdl	bdl	2.92	bdl	bdl	bdl	1.40	bdl	13.10	bdl	bdl	bdl	14.50
MTCUL-1C	bdl	bdl	bdl	bdl	0.204	0.24	bdl	bdl	bdl	bdl	bdl	3.50	3.60	bdl	bdl	bdl	bdl	5.30	bdl	bdl	bdl	1.22
MTCUL-1C	bdl	bdl	bdl	bdl	0.073	0.90	bdl	bdl	bdl	bdl	bdl	3.50	2.80	bdl	bdl	1.98	2.30	5.30	bdl	1.67	bdl	16.90
MTCUL-1C	bdl	bdl	bdl	bdl	0.207	0.43	bdl	bdl	bdl	bdl	bdl	2.40	1.70	bdl	bdl	1.29	4.90	13.80	bdl	bdl	bdl	15.90
MTCUL-1C	bdl	bdl	bdl	bdl	0.6	0.53	bdl	bdl	bdl	bdl	0.48	1.92	1.77	bdl	bdl	0.98	4.60	20.00	bdl	bdl	bdl	16.40
MTCUL-1C	1.52	bdl	bdl	bdl	14.8	bdl	bdl	50.00	bdl	bdl	bdl	bdl	bdl	bdl	bdl	bdl	bdl	52.70	bdl	bdl	bdl	9.70
MTCUL-1C	1.76	bdl	bdl	bdl	4.06	14.60	15.60	bdl	bdl	bdl	2.35	bdl	bdl	bdl	bdl	13.30	9.10	36.00	bdl	16.30	19.50	70.00
MTCUL-1C	1.11	bdl	bdl	bdl	72	4.97	bdl	50.00	bdl	bdl	bdl	bdl	1.80	bdl	bdl	5.10	bdl	860.00	bdl	7.20	bdl	102.00
MTCUL-1C	bdl	bdl	bdl	bdl	3.3	2.74	bdl	bdl	bdl	bdl	bdl	bdl	bdl	bdl	0.63	7.60	20.80	108.00	bdl	20.50	1.54	50.10
MTCUL-1C	16.70	bdl	bdl	8.9	460	125.00	bdl	160.00	bdl	bdl	bdl	6.80	bdl	bdl	bdl	12.70	57.00	68.00	bdl	bdl	39.20	650.00
MTCUL-1C	bdl	bdl	bdl	bdl	86	18.70	bdl	130.00	bdl	bdl	bdl	bdl	bdl	bdl	bdl	bdl	bdl	216.00	bdl	bdl	45.80	364.00
MTCUL-1C	14.40	bdl	bdl	6.7	409	140.00	bdl	200.00	bdl	bdl	bdl	bdl	bdl	bdl	bdl	10.90	57.00	96.00	bdl	bdl	25.60	470.00
MTCUL-1C	0.54	bdl	bdl	bdl	54.6	64.50	bdl	bdl	bdl	bdl	bdl	3.60	bdl	bdl	bdl	bdl	bdl	30.80	bdl	bdl	21.2	748.00
MTCUL-1C	28.20	0.05	bdl	25.5	441	412.00	bdl	bdl	bdl	74.00	6.80	bdl	bdl	0.06	13.00	5.30	7.70	4990.00	bdl	9.30	8.00	115.00
MTCUL-1C	3.20	bdl	bdl	bdl	17	80.00	24.00	bdl	bdl	13.20	4.30	bdl	1.10	0.05	bdl	455.00	127.00	74.00	bdl	15.00	13.00	95.00

MTC-10	3.75	bdl	bdl	1.1	0.77	27.30	bdl	bdl	bdl	bdl	bdl	bdl	bdl	bdl	33.60	bdl	43.10	bdl	bdl	2.90	1970.00	
MTC-10	3.68	bdl	bdl	bdl	1.46	36.00	bdl	bdl	bdl	11.30	bdl	bdl	bdl	bdl	50.00	10.40	178.00	bdl	bdl	13.10	710.00	
MTC-10	7.90	bdl	bdl	bdl	2.11	92.00	bdl	bdl	bdl	65.00	3.70	bdl	bdl	bdl	63.00	bdl	54.90	bdl	bdl	13.80	6.90E+03	
MTC-10	15.60	bdl	bdl	bdl	0.72	256.00	bdl	bdl	bdl	bdl	bdl	bdl	bdl	bdl	bdl	bdl	69.00	bdl	bdl	bdl	3.25E+05	
MTC-10	15.50	bdl	bdl	bdl	1.17	218.00	bdl	bdl	bdl	bdl	7.50	bdl	bdl	0.56	bdl	15.00	bdl	3160.00	bdl	bdl	bdl	2.00E+05
MTC-10	15.90	bdl	bdl	bdl	bdl	259.00	bdl	bdl	bdl	bdl	bdl	bdl	bdl	0.90	bdl	bdl	bdl	bdl	bdl	bdl	3.00E+05	
MTC-10	bdl	bdl	bdl	bdl	0.48	8.70	bdl	bdl	bdl	bdl	bdl	bdl	bdl	bdl	2.90	bdl	104.60	bdl	bdl	3.70	31.50	
MTC-10	1.57	bdl	bdl	bdl	6.51	97.70	11.30	bdl	bdl	13.60	1.73	bdl	0.48	bdl	bdl	51.70	4.10	1085.00	bdl	bdl	2.14	840.00
MTC-10	1.13	bdl	bdl	bdl	2.42	83.00	8.70	bdl	bdl	8.50	bdl	bdl	bdl	bdl	1.30	28.20	bdl	1240.00	bdl	bdl	3.90	240.00
MTC-10	1.46	bdl	bdl	bdl	1.46	27.40	bdl	bdl	bdl	bdl	bdl	bdl	bdl	bdl	55.90	13.10	613.00	bdl	bdl	5.30	218.00	
MTC-10	6.40	bdl	bdl	bdl	bdl	34.50	bdl	bdl	bdl	bdl	bdl	bdl	bdl	bdl	57.00	bdl	409.00	bdl	bdl	bdl	4.20E+03	
MTC-10	0.91	bdl	bdl	bdl	0.165	7.90	bdl	bdl	bdl	bdl	bdl	bdl	bdl	bdl	18.10	bdl	8.80	bdl	bdl	5.50	280.00	
MTC-10	3.69	bdl	bdl	bdl	13.81	23.20	bdl	bdl	bdl	44.20	bdl	bdl	bdl	bdl	35.40	4.90	69.20	bdl	bdl	235.00	1160.00	
MTC-10	bdl	bdl	bdl	bdl	14.56	1.62	bdl	bdl	bdl	32.30	bdl	bdl	bdl	bdl	bdl	1.04	bdl	73.40	bdl	bdl	8.50	55.00
MTC-10	8.49	bdl	bdl	bdl	63.4	102.70	bdl	bdl	bdl	99.00	4.50	bdl	bdl	bdl	bdl	73.00	45.00	100.00	bdl	bdl	5.90	4.80E+03
MTC-10	4.11	0.15	bdl	bdl	bdl	37.60	27.70	bdl	bdl	bdl	bdl	bdl	bdl	bdl	49.00	bdl	8450.00	bdl	bdl	bdl	1390.00	
MTC-10	2.30	bdl	bdl	bdl	bdl	19.60	26.90	bdl	bdl	bdl	bdl	bdl	bdl	bdl	23.00	48.00	5730.00	bdl	bdl	bdl	1340.00	
MTC-10	bdl	bdl	bdl	bdl	bdl	12.80	bdl	bdl	bdl	bdl	bdl	bdl	bdl	bdl	1.81	3.40	bdl	2.41E+04	bdl	bdl	bdl	37.00
MTC-10	14.00	bdl	bdl	bdl	1.53	255.00	bdl	bdl	bdl	bdl	bdl	bdl	bdl	bdl	16.40	bdl	1.10E+04	bdl	bdl	bdl	1.21E+05	
MTC-10	4.90	bdl	bdl	bdl	7.1	60.00	bdl	bdl	bdl	58.00	5.00	8.40	bdl	bdl	31.00	bdl	18.10	bdl	bdl	3.70	2400.00	
MTC-10	16.60	bdl	0.21	3.8	22.7	303.00	bdl	bdl	bdl	87.00	15.90	11.00	bdl	0.09	bdl	132.00	31.00	125.00	bdl	bdl	2.70	2.89E+04
MTC-10	6.00	bdl	bdl	bdl	0.52	81.00	bdl	bdl	bdl	bdl	bdl	8.50	bdl	bdl	bdl	36.10	9.00	406.00	bdl	bdl	25.30	4290.00
MTC-10	4.40	bdl	bdl	bdl	0.77	57.80	bdl	bdl	bdl	bdl	bdl	9.20	bdl	bdl	bdl	83.00	10.50	341.00	bdl	bdl	11.00	670.00
MTC-10	bdl	bdl	bdl	bdl	0.26	5.47	bdl	bdl	bdl	110.00	2.76	4.70	bdl	bdl	bdl	10.80	11.00	40.00	bdl	bdl	33.6	9.10
MTC-10	0.91	bdl	bdl	bdl	0.134	37.50	bdl	bdl	bdl	bdl	bdl	4.30	bdl	bdl	bdl	41.70	bdl	171.20	bdl	bdl	3.00	108.00
MTC-10	2.76	bdl	bdl	bdl	0.207	33.20	16.40	bdl	bdl	bdl	bdl	3.50	bdl	bdl	bdl	43.40	6.50	956.00	bdl	bdl	1.67	830.00
MTC-10	3.89	bdl	bdl	2.2	bdl	38.50	bdl	bdl	bdl	bdl	bdl	5.80	bdl	bdl	bdl	38.60	bdl	29.70	bdl	bdl	15.00	2030.00
MTC-10	12.10	bdl	0.35	2.3	214	148.00	bdl	bdl	bdl	44.00	5.40	9.20	bdl	bdl	bdl	96.00	42.00	140.00	bdl	bdl	bdl	3040.00
MTC-10	12.80	bdl	0.52	bdl	61.2	126.00	bdl	bdl	bdl	66.00	3.90	8.00	bdl	bdl	bdl	105.00	48.00	851.00	23	88.00	7.10	3280.00
MTC-10	1.19	0.09	bdl	bdl	0.26	51.20	19.50	bdl	bdl	bdl	bdl	6.10	bdl	bdl	bdl	38.00	11.80	4550.00	bdl	bdl	0.75	511.00

Minimum	0.26	0.02	0.06	0.41	0.06	0.16	4.40	27.00	1.70	4.00	0.48	1.61	0.48	0.03	0.22	0.31	1.28	2.56	23.00	1.67	0.75	1.22
Maximun	76.40	0.15	3.58	25.50	904.00	750.00	42.00	1400.00	1.70	2660.00	28.00	11.00	25.00	0.90	13.00	460.00	297.00	24100.00	23.00	299.00	422.00	325000.00
Median	2.49	0.05	0.27	2.41	7.64	9.20	16.00	140.00	1.70	34.75	3.74	2.75	2.30	0.08	0.62	19.60	12.50	76.70	23.00	20.15	12.60	127.40
Average	6.43	0.06	0.80	5.14	70.67	59.36	17.56	221.83	1.70	276.02	5.87	3.79	4.86	0.23	1.98	46.83	26.55	864.91	23.00	47.92	50.02	12210.51
Count	76	8	10	18	100	107	22	12	1	52	35	46	10	9	10	95	75	109	1	28	81	111

ANEXX C

SUPPLEMENTARY MATERIAL OF CHAPTER 4

*Isotopic signature of pyrite from bitumen-bearing stratabound Cu-(Ag) deposits, northern Chile:
Implications for fluid source and mineralization processes*

This file include:

Figures C.1 – C.3

Figure C.1. BSE images showing pyrite grains from Lorena deposit analyzed by SIMS. In-situ sulfur isotope values are shown.

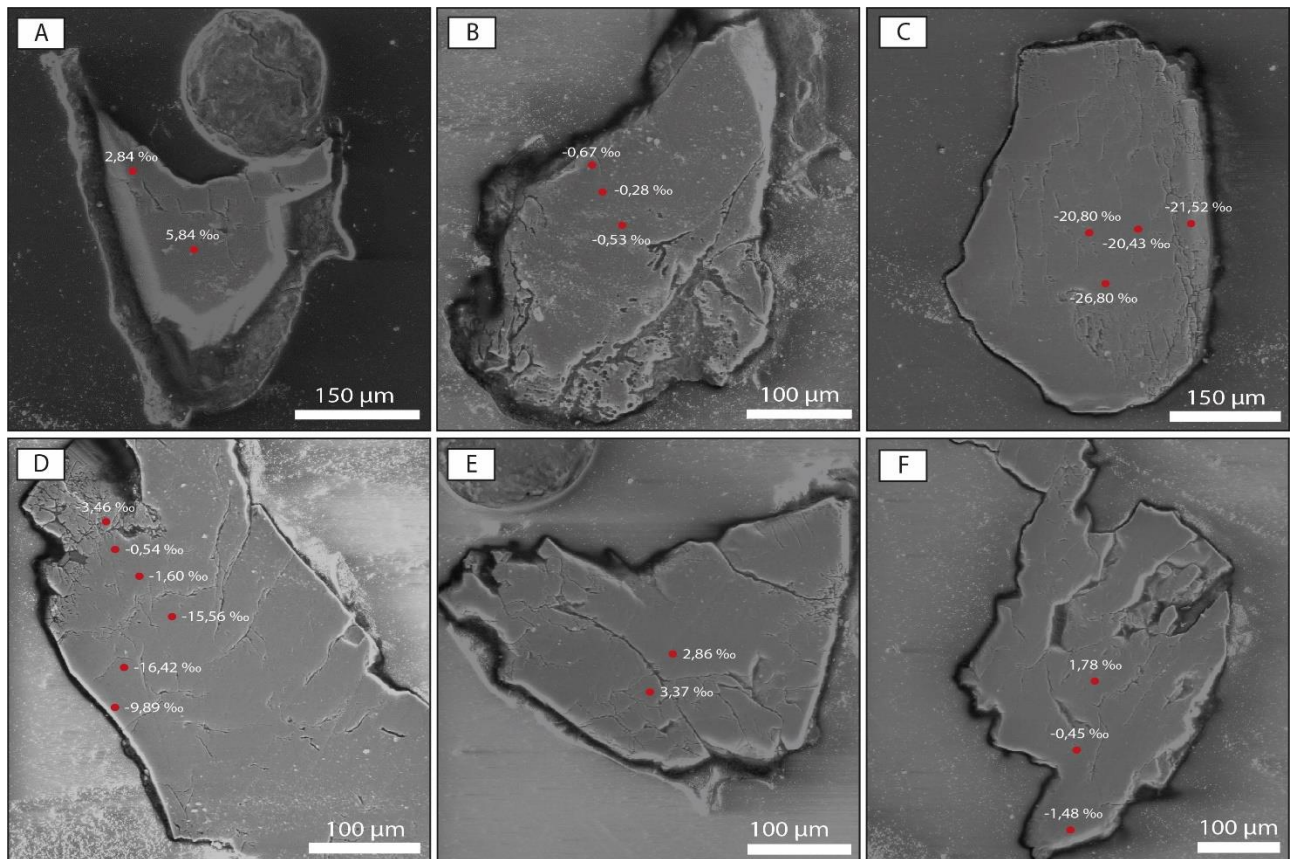


Figure C.2. BSE images showing pyrite grains from La Culebra deposit analyzed by SIMS. In-situ sulfur isotope values are shown.

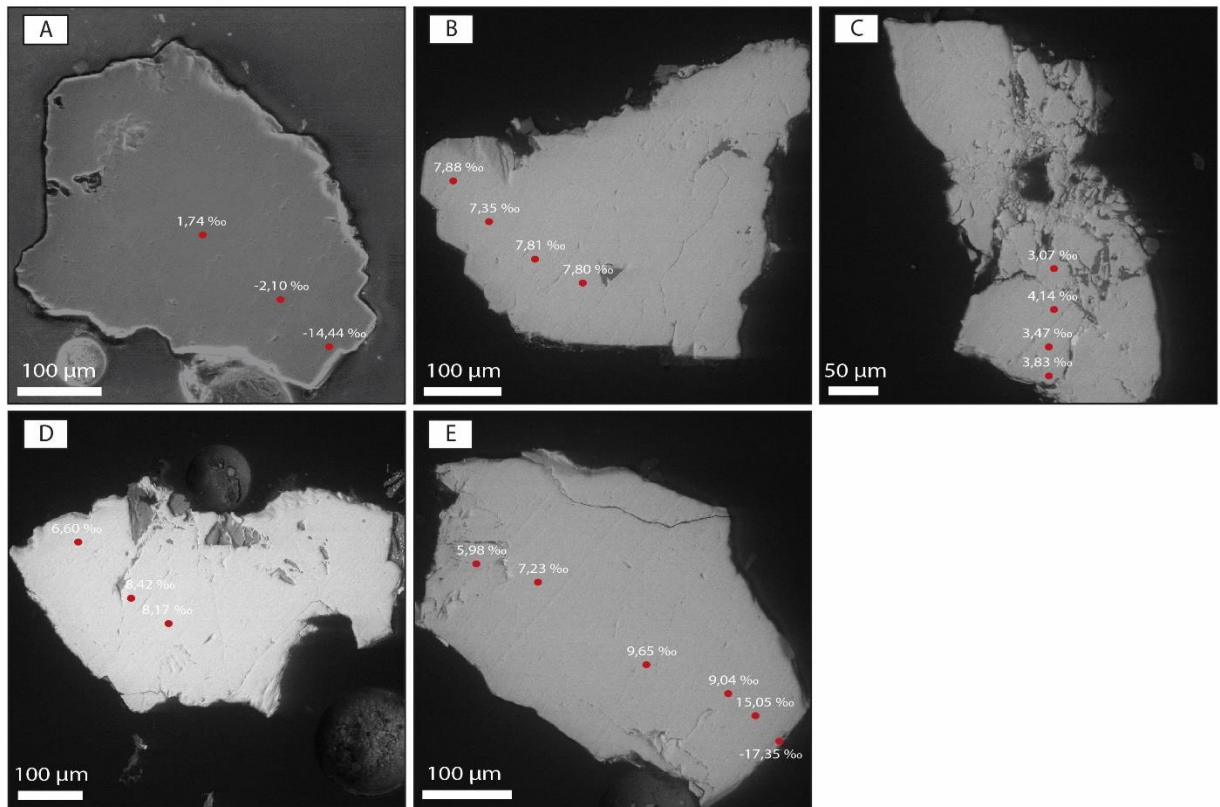


Figure C.3. BSE images showing pyrite grains from the El Soldado deposit analyzed by SIMS. In-situ sulfur isotope values are shown.

